

**Crystallization  
&  
Encapsulation  
in multicomponent mixtures**

**Marloes Reus**



**Crystallization**  
**&**  
**Encapsulation**  
in multicomponent mixtures

**Marloes Anne REUS**  
**2016**



# Crystallization & Encapsulation in multicomponent mixtures

PROEFSCHRIFT

ter verkrijging van de graad van doctor  
aan de Technische Universiteit Delft,  
op gezag van de Rector Magnificus Prof. ir. K.C.A.M Luyben,  
voorzitter van het College voor Promoties,  
in het openbaar te verdedigen op vrijdag 18 maart 2016 om 12:30 uur  
door

Marloes Anne REUS

Scheikundig ingenieur, Technische Universiteit Delft  
geboren te Heiloo, Nederland.

Dit proefschrift is goedgekeurd door de promotoren:  
Prof. Dr. A.E.D.M. van der Heijden and Prof. Dr. ir. J.H. ter Horst

Samenstelling promotiecommissie:

|                                    |                                       |
|------------------------------------|---------------------------------------|
| Rector Magnificus                  | Voorzitter                            |
| Prof. Dr. A.E.D.M. van der Heijden | Technische Universiteit Delft         |
| Prof. Dr. ir. J.H. ter Horst       | University of Strathclyde Glasgow, UK |

Onafhankelijke leden:

|                              |                                |
|------------------------------|--------------------------------|
| Prof. Dr. D. Poncelet        | Oniris Nantes, France          |
| Prof. Dr. G. Coquerel        | Université de Rouen, France    |
| Prof. Dr. T. Leyssens        | Université de Louvain, Belgium |
| Dr. R.M. Geertman            | Janssen Pharmaceutica, Belgium |
| Prof. Dr. ir. A. Schmidt-Ott | Technische Universiteit Delft  |

|                            |  |
|----------------------------|--|
| Prof. Dr. ir. B.J. Boersma | Technische Universiteit Delft,<br>reservelid |
|----------------------------|--|



Dit werk is financieel ondersteund door TNO Defense and Security.

ISBN: 978-94-6299-311-2

Cover image & design: M.A. Reus

Copyright © 2016 by M.A. Reus

All rights reserved. No part of the material protected by this copyright notice may be reproduced or utilized in any form or by any means, electronic or mechanical, including photocopying, recording or by any information storage and retrieval system, without the prior permission of the author.

Printed in the Netherlands by Ridderprint B.V.

*Ajeto*

---

# Summary

Many products from chemical industries, such as consumer products, pharmaceuticals, food products and fine chemicals industries (e.g. energetic materials, pigments, fertilizers), constitute particulate products. The functionality of these products depends among others on the properties of its constituents, their interactions and their distribution in the product. Sometimes pure solids lack a desired functionality of the final product and other compounds need to be added to achieve the desired product. For example, controlled release of medicines is a common reason to apply a thin protective layer around the active pharmaceutical ingredient (API), or the shelf life of a product can be extended by applying a protective layer around the target material. For the production of both the final product and the particles it contains, a suitable process needs to be developed, taking into account all demands (e.g. purity, bioavailability, controlled release function, yield) and limitations (e.g. temperature sensitivity, reactivity, toxicity) of the specific system. Producing multicomponent particulate products involves the use of multicomponent mixtures. These components can interact with each other in many different ways, ranging from the formation of (pseudo) polymorphs and polymeric structures to the stabilization or isolation of a component, which are discussed in the introductory **Chapter 1**. A suitable process for the handling of such mixtures must be able to control what happens to each individual component, as well as to the combination of them. Additionally, the process must operate at conditions at which the materials do not undergo unwanted reactions, e.g. degradation. Only if such control is available to sufficient extent, can the product gain the right conformation that enables all desired functionalities. However, such control cannot be gained without understanding the possible interactions between the components.

vii

In this dissertation crystallization and microencapsulation processes are used to produce multicomponent particulate products with different functionalities (improved stability, controlled release, protection from environment, etc.) and their performance is assessed. Additionally, the interactions between the components in the processes are addressed. In this context, we investigated the crystallization in multicomponent mixtures as well as microencapsulation of various compounds. Model compounds from various industrial fields (e.g. food, pharmaceutical and energetic material industries) are used to illustrate the wide applicability of the tested processes.

---

For the design of production processes for solid materials from multicomponent mixtures, the phase diagram of such systems is essential information. Currently used methods (e.g. equilibrium concentration (EqC) and temperature variation (TV) methods) are either slow, labor intensive, or require the temperature to be changed. In multicomponent mixtures, often phase diagrams at a single temperature are desired. In **Chapter 2** we develop the solvent addition (SA) method, which determines the isothermal solubility of a compound in the mother phase as a function of composition by the addition of solvent. Our method is validated by comparison with the EqC and TV methods of obtained solubility data of p-hydroxybenzoic acid (pHBA) in acetic acid. Additionally, suggestions are given to arrive at a proper value for the addition rate for other systems. The technique is then applied to multicomponent systems, comprising either 2 solvents and a solute (e.g. anti-solvent crystallization), or 1 solvent and 2 solutes (e.g. co crystallization). It was shown that the SA method is highly suited for determining phase boundaries in multicomponent systems.

In some cases, a compound can incorporate solvent molecules into its crystal structure as regular building blocks, adopting another crystal structure with different properties (e.g. solubility) from the pure crystal. In API's, a change in solubility means a change in bioavailability. Therefore, the formation of such pseudo-polymorphs (also called solvates) must be carefully controlled. Such control can be achieved by using solvent mixtures, where the composition determines which solid state crystallizes or dissolves, due to the change in activity of the solvent mixture. Transitions between different solvated states of pHBA are investigated in **Chapter 3**, by determining the ternary phase diagrams of pHBA in various binary solvent mixtures. The ternary diagrams were used to construct a quaternary phase diagram, which can be used to investigate more complex solubility behavior.

In principle, encapsulated crystalline particles can be produced by using well-controlled concomitant crystallization. However, this encapsulation step, driven by heterogeneous nucleation of the second compound on the first, does not always occur. In **Chapter 4** a novel technique, electrospray crystallization (EC), is used to overcome this problem. In EC, solutions are sprayed from small nozzles and a strong electric field is used for the creation of an aerosol. Each droplet of the aerosol acts as a micron-sized evaporative crystallizer. The information from the phase diagrams is used to aid in the design of the process. The concentration is largely responsible for the distribution of the solids in the resulting particles, where the compound with the higher concentration relative to its solubility ends up at the outside of the

particle. This technique can be used as a simple, direct process for the production and in-situ encapsulation of crystalline materials that dissolve in the same solvent. Comparing the resulting particles with those from a concomitant cooling crystallization experiment shows that, regardless of their behavior in cooling crystallization, the compounds are forced to crystallize in a single particle in the confined volume created by the electrospray process.

In an EC process many factors (e.g. type of solvent, concentration of solute, configuration of the setup) play a role in achieving a smooth operation of the process, as well as good product quality. To arrive at the combination of these factors that leads to the desired material, three main challenges are identified and suggestions are provided of how to overcome them (**Chapter 5**). First, the operation window for the electrospray crystallization process is very small. The concentration of the solute is the main variable to be tuned, next to the operating parameters of a regular electrospray process. Second, material losses can be very high, especially when premature crystallization occurs at the nozzle tips. It was found that this encrustation was a large contributor. Preventing this from happening will greatly increase the yield of the process. Third, it depends on the requirements of the product how the created particles are best collected, which has implications for the design of the process. The challenges and suggested solutions are combined in a comprehensible design diagram, to increase the efficiency in process design and thereby to lower the threshold for more research into this technique.

Encapsulated solution droplets can be applied in a new nucleation rate measurement technique, that can provide valuable information for the production of small crystals. In **Chapter 6**, we therefore encapsulated small volumes (12 and 194 nL) of fenofibrate (Fen) in heptane (Hep) solutions in a transparent shell of calcium alginate, in order to observe the crystallization inside such small volumes. From these observations, information about the nucleation and growth rates was obtained. The growth rate of crystals decreased rapidly over time due to the depletion of the supersaturation. It was found that only a fraction of the droplets crystallized, which is attributed to the presence of heterogeneous particles in the encapsulated droplets. The fraction of particles with heterogeneous particles was used in the estimation of the nucleation rates, which in turn yielded the kinetic and thermodynamic nucleation rate parameters. The core-shell configuration is very suitable for the investigation of crystallization kinetics and has the potential to be used for studying heterogeneous nucleation.

---

Another application of microencapsulation is found in the food industry, where often very complex mixtures are processed. For use in meat analog structuring, vital wheat gluten (WG) and soy protein isolate (SPI) are mixed with water and other ingredients, after which at high temperatures the gluten are subjected to low shear, in order to form a meat-like structure. However, due to instant fibrilization of the gluten upon contact with water, material losses of the entire composition are significant. In **Chapter 7** we produce, by means of a dripping technique, matrix type particles with a core of vital wheat gluten (WG) and a shell of hydrogel. In this configuration, the WG is prevented from instant fibrilization upon contact with water, and released at conditions of high temperature and low shear. Two hydrogels, alginate (Alg) and  $\kappa$  carrageenan (Car), were used as wall material. While the Alg particles are easy to produce using the encapsulator, they were not able to release the gluten at the processing conditions. The Car particles required the use of additional oil for spherification, but were able to release the WG under the desired process conditions. After the release at process conditions, the WG encapsulated in Car was still able to form fibers.

x

In energetic materials applications, a coating may be used to protect the material from moisture, oxygen or other reactive species. Since coatings often decrease the explosive performance of the material, very thin layers are desired, provided they are impervious. **Chapter 8** deals with the application of layers with a thickness in the order of nanometers. Atomic layer deposition (ALD) of inorganic coatings is applied to particles suspended in a fluidized bed. In ALD, the coating is applied monolayer by monolayer, in a cyclic manner. ALD lends itself excellently for application in fluidized beds, since the gaseous precursors can be brought to the core particles in the gas flow already required to keep the particles fluidized. Micro-particles of ammonium chloride were encapsulated with  $\text{Al}_2\text{O}_3$  and ZnO using this technique to prevent contact with ambient moisture. Aluminum (Al) micro-particles are coated with  $\text{MgF}_2$  to both protect it from moisture and to activate the Al for burning. It was found that the precursors penetrated into the porous structure of the micro-particles, where they deposited. This resulted in lower layer thicknesses found on top of the particle surface and with that a lower performance than expected. However, it excellently shows the atomic nature of the process.

In this thesis we produced multicomponent particulate products by means of crystallization and microencapsulation processes, to realize a variety of applications.

The findings in this thesis can help to efficiently study multicomponent phase diagrams, as well as control the formation of (pseudo-)polymorphs by use of multicomponent mixtures. This aids the development of novel crystallization processes, like concomitant electrospray crystallization, that meet the requirements of innovative products on the one hand and low energy consumption and waste production on the other. In the production of small particles, to achieve e.g. higher dissolution rates of APIs with a low solubility, crystallization in confined volumes is an indispensable technique, since it can be easily integrated in production processes. Encapsulating droplets of solution in transparent hydrogels aids in the understanding of the crystallization at such small scales and the information gained as such opens the possibility of controlling the nucleation and growth inside confined volumes. Moreover, use of the hydrogel coating allows for a more thorough investigation of how functionalization of the coating, e.g. by adding surfactants, can enhance or delay crystallization. Such extra functionalization is not only valuable in crystallization research. Other industries can benefit from multifunctional encapsulates, where the coating not only protects the core, but also aids in the usage of it, for example, where a protective coating around an energetic core contains activating additives that increase the explosive performance. As such, the knowledge gained in this thesis is very widely applicable.

---

# Samenvatting

Veel producten uit de chemische industrie, zoals consumptiegoederen, medicijnen, voedingsmiddelen en fijnchemicaliën (bijvoorbeeld energetische materialen, pigmenten of meststoffen) bevatten vaste deeltjes. De functionaliteit van deze producten is onder andere afhankelijk van de eigenschappen van de bestanddelen, de interacties ertussen en hun verdeling over het product. In sommige gevallen mist een pure stof de gewenste functionaliteit van het product en moeten andere componenten worden toegevoegd om dit te realiseren. Gecontroleerde vrijgave van medicijnen in het lichaam is een veel voorkomende reden om een dun, beschermend laagje aan te brengen rondom het actieve farmaceutische ingrediënt (API). Ook kan bijvoorbeeld de houdbaarheid van een product worden verlengd door een beschermend laagje aan te brengen. Voor de productie van zowel het eindproduct als de deeltjes die daarin voorkomen moet een geschikt proces worden ontwikkeld. Hierbij moet rekening gehouden worden met alle eisen (zoals zuiverheid, biologische beschikbaarheid, gecontroleerde vrijgave, opbrengst) en beperkingen (zoals temperatuur gevoeligheid, reactiviteit, toxiciteit) van het systeem in kwestie. De productie van multi-componentenproducten met vaste deeltjes impliceert het werken met multi-componentenmengsels. Er zijn veel verschillende interacties mogelijk tussen de componenten, variërend van de vorming van (pseudo-)polymorfen en polymeerstructuren tot de stabilisering of isolatie van een component. Dit wordt beschreven in **Hoofdstuk 1**.

Een geschikt proces voor het bewerken van dit soort mengsels moet kunnen regelen wat er gebeurt met elke individuele component, zowel als met de combinatie van de componenten. Daarnaast moet het proces kunnen werken bij omstandigheden waarbij de materialen geen ongewenste reacties, zoals ontleding, ondergaan. Alleen als dergelijke controle voldoende aanwezig is, kan het product de juiste conformatie aannemen, dat alle gewenste functies bevat. Echter, deze controle kan niet worden verkregen zonder kennis over de mogelijke interacties tussen de componenten.

In dit proefschrift worden kristallisatie en micro-encapsulatie processen gebruikt om multi-componentenproducten met vaste deeltjes erin te produceren, die verschillende functionaliteiten hebben (verbeterde stabiliteit, gecontroleerde vrijgave, bescherming van de omgeving, etc.). Daarnaast wordt de prestatie van de deeltjes en processen getest en worden de interacties tussen de componenten in de processen besproken. In deze context hebben wij zowel de kristallisatie in multi-componentenmengsels onderzocht, als de

---

micro-encapsulatie van verschillende stoffen. Modelstoffen uit verschillende industrieën (bijvoorbeeld voedsel, medicijnen en energetische materialen industrieën) zijn gebruikt om de wijde toepasbaarheid van de processen te illustreren.

Voor het ontwerp van productieprocessen voor vaste materialen uit multi-componentenmengsels geeft het fase-diagram van dergelijke systemen essentiële informatie. Huidige methodes die gebruikt worden om fase-diagrammen te bepalen (zoals de evenwichtsconcentratie (EqC) en temperatuur variatie (TV) methodes) zijn langzaam, arbeidsintensief, of behoeven een temperatuurverandering. In multi-componentenmengsels is het echter vaak gewenst om een fase-diagram bij vaste temperatuur te hebben. In **Hoofdstuk 2** ontwikkelen wij de oplosmiddeltoevoegingsmethode (SA), die de oplosbaarheid van een stof in de moederloog bepaalt als een functie van de samenstelling door de toevoeging van oplosmiddel. Onze methode is gevalideerd door de met de SA methode gemeten oplosbaarheidsdata van p-hydroxybenzoëzuur (pHBA) in azijnzuur te vergelijken met die gemeten door de EqC en TV methodes. Daarnaast geven we suggesties om voor andere systemen een geschikte toevoegingssnelheid te kiezen. De methode wordt dan toegepast op multi-componentensystemen met 2 oplosmiddelen en een opgeloste stof (bijvoorbeeld anti-solvent kristallisatie) en met 1 oplosmiddel en 2 opgeloste stoffen (bijvoorbeeld co-kristallisatie). Daarmee laten we zien dat de SA methode zeer geschikt is voor het bepalen van oplosbaarheden in multi-componentensystemen.

xiv

In sommige gevallen kan een stof de moleculen van het oplosmiddel in zijn kristalstructuur verwerken als regelmatige bouwsteen, waardoor een andere kristalstructuur wordt aangenomen met verschillende eigenschappen (zoals oplosbaarheid) dan het pure kristal. In API's betekent een verandering in oplosbaarheid een verandering in biologische beschikbaarheid. Daarom is het belangrijk dat er controle is over de vorming van dit soort pseudo-polymorfen (ook solvaten genoemd). Zulke controle kan worden verkregen door gebruik te maken van mengsels van oplosmiddelen, waarbij de samenstelling van het mengsel bepaalt welke vaste vorm kristalliseert of oplost, door de verandering in de activiteit van het mengsel. In **Hoofdstuk 3** worden overgangen tussen de verschillende gesolvateerde vormen van pHBA onderzocht, door de ternaire fase-diagrammen te bepalen van pHBA in verschillende binaire oplosmiddelmengsels. De ternaire fase-diagrammen zijn vervolgens gebruikt voor het construeren van quaternair fase-diagram, dat kan worden gebruikt om nog complexer oplosbaarheidsgedrag te bestuderen.

In principe kunnen geëncapsuleerde kristallijne deeltjes worden gemaakt door goed gecontroleerde gelijktijdige kristallisatie uit te voeren. Echter, deze encapsulatiestap vindt niet altijd plaats, omdat hiervoor de tweede kristalliserende component heterogeen moet nucleëren op de eerste. In **Hoofdstuk 4** gebruiken wij een nieuwe techniek, electrospray kristallisatie (EC), om dit probleem te verhelpen. In EC worden oplossingen gespreoid uit een kleine spuitstuk, waarbij een sterk elektrisch veld wordt gebruikt voor het creëren van een aerosol. Elk druppeltje in de aerosol is in feite een minuscule verdampingskristallisator. De informatie uit fasediagrammen wordt gebruikt bij het ontwerp van het proces. De concentratie is de voornaamste factor die de distributie van de vaste stoffen in de uiteindelijke deeltjes bepaalt, waarin de stof met de hogere concentratie vergeleken met zijn oplosbaarheid zich meer aan de buitenkant van het deeltje bevindt. Dit is een simpel, direct proces voor het produceren en in-situ encapsuleren van kristallijne materialen die in hetzelfde oplosmiddel oplossen. Als de deeltjes worden vergeleken met die verkregen uit een koelkristallisatie proces wordt duidelijk dat, ongeacht het gedrag van de stoffen tijdens koelkristallisatie, ze worden geforceerd om in één enkel deeltje te kristalliseren in het beperkte volume gecreëerd door het electrospray proces.

In een EC proces spelen vele factoren (zoals type oplosmiddel, concentratie van de opgeloste stof, configuratie van de opstelling) een rol in het ongestoord opereren van het proces, zowel als in het verkrijgen van een kwalitatief goed product. Om tot een combinatie van deze factoren te komen die tot het gewenste materiaal leiden, zijn er in **Hoofdstuk 5** drie belangrijke uitdagingen geïdentificeerd en worden er oplossingen voor voorgesteld. Ten eerste is het toepassingskader voor het electrospray kristallisatieproces erg klein. De concentratie van de opgeloste stof is de belangrijkste variabele om te worden afgestemd, naast de parameters van een gewoon electrospray proces. Ten tweede is het materiaalverlies groot, vooral wanneer voortijdige kristallisatie plaatsvindt op de spuitstuk. De opbrengst van het proces kan sterk worden vergroot door deze afzetting te voorkomen. Ten derde hangt het van de producteisen af hoe de geproduceerde deeltjes het best opgevangen kunnen worden, wat implicaties heeft voor het ontwerp van het proces. De uitdagingen en voorgestelde oplossingen daarvoor zijn gecombineerd in een ontwerpdiagram, dat het ontwerp van electrospray kristallisatieprocessen efficiënter maakt en daarmee de drempel verlaagt voor meer onderzoek in deze techniek.

---

Geëncapsuleerde druppels met oplossing kunnen worden toegepast in een nieuwe meettechniek voor de nucleatiesnelheid, die waardevolle informatie kan verschaffen voor de productie van kleine kristallen. In **Hoofdstuk 6** hebben we daarom kleine volumes (12 en 194 nL) van fenofibraat (Fen) in heptaan (Hep) oplossingen geëncapsuleerd in een omhulsel van calcium alginaat, om zo de kristallisatie in zulke kleine volumes te kunnen observeren. Uit deze waarnemingen is informatie gehaald over de nucleatie en groeisnelheden van de kristallen. De groeisnelheid van de kristallen nam snel af in de tijd door het uitputten van de oververzadiging in de druppels. Slechts in een fractie van de druppels vond kristallisatie plaats, wat wordt toegeschreven aan de aanwezigheid van heterogene deeltjes in de geëncapsuleerde druppels. De fractie druppels met heterogene deeltjes is gebruikt bij het afleiden van de nucleatiesnelheden, die op hun beurt de kinetische en thermodynamische nucleatiesnelheidsparameters geven. De encapsulatie van druppels oplossing is een goede methode om kristallisatiekinetiek te bestuderen en biedt de mogelijkheid om heterogene nucleatie te bestuderen.

*xvi* In de voedingsindustrie, waar vaak met zeer complexe mengsels wordt gewerkt, kan men een andere toepassing van micro-encapsulatie vinden. Voor het gebruik in de structurering van vleesvervangers worden gluten (WG) en eiwitten geïsoleerd uit soja (SPI) gemengd met water en andere ingrediënten, waarna het mengsel op hoge temperatuur wordt onderworpen aan een afschuifprofiel, om een vleesachtige structuur te maken. Echter, doordat gluten instantaan vezels vormen als het met water in contact komt, zijn de materiaalverliezen van het hele mengsel hoog. In **Hoofdstuk 7** produceren we matrix-type deeltjes met een kern van gluten en een omhulsel van hydrogel, door middel van een druppeltechniek. In deze configuratie wordt deze vezelvorming van de WG tijdens de mengstap voorkomen en wordt de WG weer vrijgegeven bij hoge temperatuur en onder invloed van het afschuifprofiel. Twee hydrogels, alginaat (Alg) en  $\kappa$ -carrageenan (Car) zijn gebruikt voor het omhulsel. Hoewel de Alg deeltjes gemakkelijk te produceren waren met de druppeltechniek, waren ze niet in staat om de WG weer vrij te geven bij de procesomstandigheden. Voor het produceren van de Car deeltjes was de toevoeging van olie nodig om de deeltjes bolvormig te maken, maar deze deeltjes waren goed in staat om de WG weer vrij te geven. Vezelvorming was wel weer mogelijk na ontsnapping van de WG uit de hydrogel.

In toepassingen met energetische materialen kan een coating worden aangebracht om het materiaal te beschermen tegen vocht, zuurstof of andere

reactieve stoffen. Aangezien coatings vaak de explosieve prestaties van het materiaal verminderen, zijn dunne lagen gewenst, zolang ze ondoordringbaar zijn. **Hoofdstuk 8** behandelt de toepassing van laagjes met een dikte van enkele nanometers. Anorganische coating lagen worden aangebracht op deeltjes die gesuspenderd zijn in een fluïde bed met 'Atomic Layer Deposition' (ALD). In het ALD proces wordt de coating op cyclisch wijze monolaag voor monolaag aangebracht op de deeltjes. Dit proces leent zich uitstekend voor combinatie met een fluïde bed, omdat de precursors in de gasfase naar de deeltjes kunnen worden getransporteerd door de gasstroom die al aanwezig is voor het fluïdiseren van de deeltjes. Met deze techniek zijn microdeeltjes van ammonium chloride geëncapsuleerd met aluminiumoxide en zinkoxide, om ze te beschermen tegen vocht. Aluminium microdeeltjes zijn geëncapsuleerd met magnesiumfluoride, voor bescherming tegen vocht, alsmede voor het activeren van de verbranding van de deeltjes. De precursors reikten tot diep in de poreuze structuur van de deeltjes, waar zij ook werden afgezet. Dit resulteerde in een kleinere laagdikte en daarmee in mindere prestaties van de coating. Echter, het laat duidelijk de schaal zien waarop ALD werkt.

In dit proefschrift hebben we met kristallisatie- en encapsulatieprocessen producten gemaakt bestaande uit meerdere componenten, waarvan sommige vaste stoffen waren, om een grote variëteit aan toepassingen te realiseren.

De vindingen voortgekomen uit dit werk kunnen helpen om zowel fase-diagrammen van multi-componentensystemen efficiënter te bestuderen, als de vorming van (pseudo)polymorfen controleren door middel van het gebruik van mengsels bestaande uit meerdere componenten. Dit baat de ontwikkeling van nieuwe kristallisatie processen, zoals gelijktijdige electrospray kristallisatie, die aan de ene kant de producteisen tegemoet komen van innovatieve producten en aan de andere kant lage energieconsumptie en afvalproductie hebben. In de productie van kleine deeltjes, bijvoorbeeld om de oplosbaarheid van API's met een lage oplosbaarheid te verhogen, is kristallisatie in beperkte volumes een onmisbare techniek, omdat het gemakkelijk geïntegreerd kan worden in huidige productieprocessen. Het encapsuleren van druppels oplossing in transparante hydrogels bevordert het begrip van kristallisatie op dergelijke kleine schaal en de informatie die daaruit voortkomt geeft de mogelijkheid om kristal-nucleatie en groei in de beperkte volumes te controleren. Bovendien maakt het gebruik van hydrogel coatings dieper onderzoek mogelijk over wat voor effect functionele oppervlakken hebben op de kristallisatie, bijvoorbeeld door het toevoegen van oppervlakte-actieve stoffen aan de coating die de kristallisatie kunnen uitstellen of juist

---

bevorderen. Dergelijke extra functionaliteiten zijn niet alleen waardevol in kristallisatieonderzoek. Andere industrieën kunnen ook profiteren van multifunctionele geëncapsuleerde deeltjes, waar de coating niet alleen de kern beschermt, maar ook het gebruik ervan bevordert. Een voorbeeld hiervan is een coating die een energetisch deeltje zowel beschermt als activeert. Zodoende is de kennis uit dit proefschrift zeer breed toepasbaar.

# Content

|   |             |
|---|-------------|
| <b>Summary</b>  | <b>vii</b>  |
| <b>Samenvatting</b>   | <b>xiii</b> |
| <br>  |             |
| <b>Chapter 1</b>  |             |
| <b>General introduction</b>   | <b>25</b>   |
| 1.1. Introduction   | 27          |
| 1.2. Crystallization  | 28          |
| 1.3. Encapsulation  | 31          |
| 1.4. Thesis outline   | 33          |
| 1.5. References   | 36          |
| <br>  |             |
| <b>Chapter 2</b>  |             |
| <b>Solubility determination from clear points upon solvent addition</b> | <b>41</b>   |
| 2.1. Introduction   | 43          |
| 2.2. Experimental section   | 44          |
| 2.3. Results  | 46          |
| 2.4. Discussion   | 56          |
| 2.5. Conclusion   | 58          |
| 2.6. References   | 59          |

---

## Chapter 3

### **Understanding solvate formation in mixed solvents** 63

- 3.1. Introduction 65
- 3.2. Materials and Methods 66
- 3.3. Results and discussion 67
- 3.4. Conclusions 79
- 3.5. References 80

## Chapter 4

### **Concomitant crystallization for in-situ encapsulation of organic materials** 83

- 4.1. Introduction 85
- 4.2. Potential concomitant crystallization mechanisms 86
- 4.3. Experimental 87
- 4.4. Results and Discussion 89
- 4.5. Conclusions 102
- 4.6. References 103

xx

## Chapter 5

### **Electrospray crystallization: challenges in process design, operation and control** 107

- 5.1. Introduction 109
- 5.2. Materials and methods 110
- 5.3. Results and discussion 111
- 5.4. Conclusions 126
- 5.5. References 127

## Chapter 6

### **Crystal nucleation of fenofibrate in encapsulated solution droplets** **131**

- 6.1. Introduction 133
- 6.2. Materials and Methods 133
- 6.3. Results and discussion 136
- 6.4. Conclusions 147
- 6.5. References 148

## Chapter 7

### **Immobilization of gluten in spherical matrices of food -grade hydrogels** **153**

- 7.1. Introduction 155
- 7.2. Materials and Methods 156
- 7.3. Results and Discussion 159
- 7.4. Conclusion 168
- 7.5. References 170



## Chapter 8

### **Improved particle properties through microencapsulation by gas-phase deposition in fluidized beds** **173**

- 8.1. Introduction 175
- 8.2. Materials and methods 177
- 8.3. Results and Discussion 180
- 8.4. Conclusions 194
- 8.5. References 195

---

## **Chapter 9**

### **Conclusions** **199**

- 9.1. Obtaining multicomponent phase diagrams 201
- 9.2. Crystallization in small volumes 201
- 9.3. Protective encapsulants 202

## **Chapter 10**

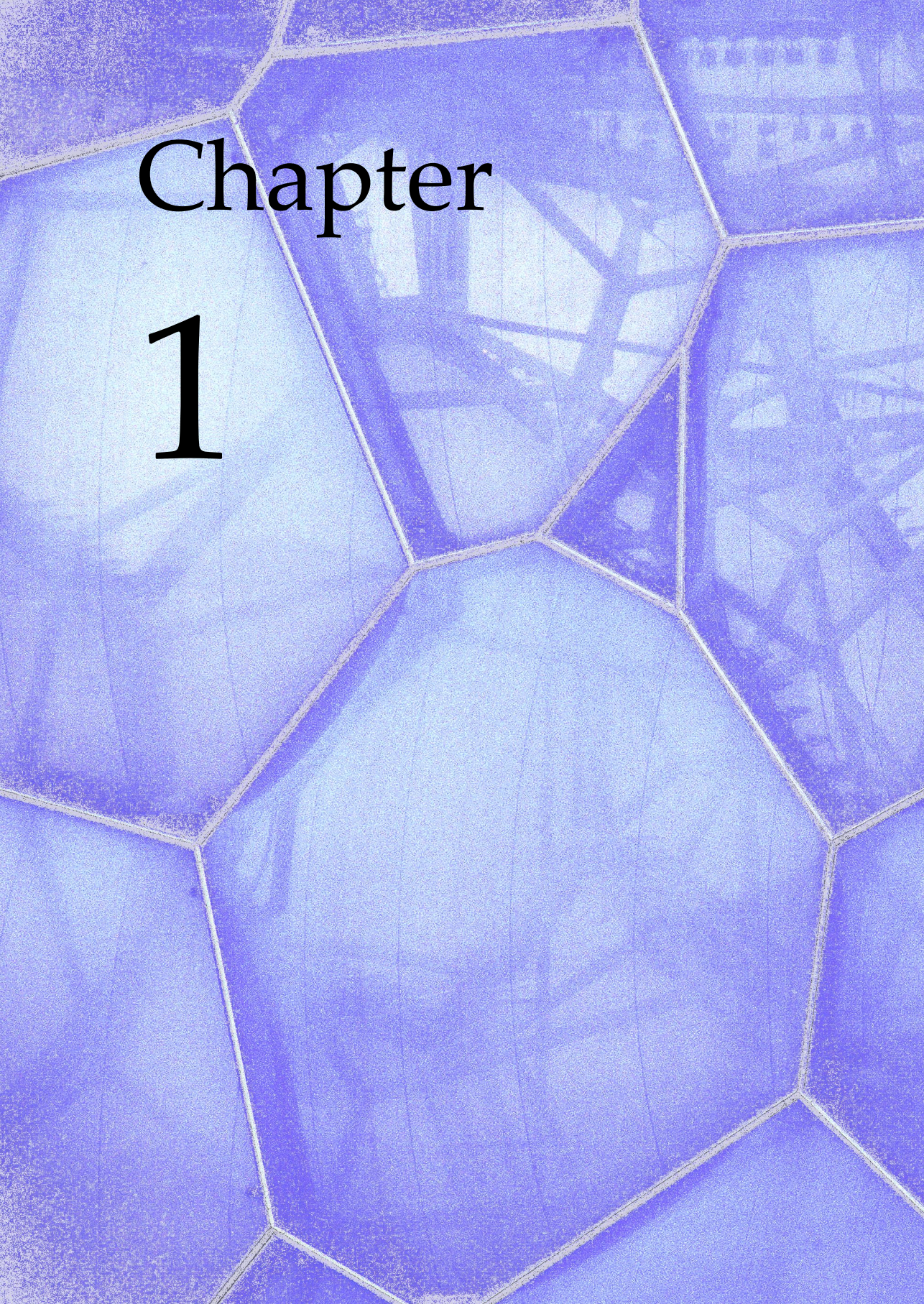
### **Recommendations** **205**

- 10.1. Applications 207
- 10.2. Research 208

### **Addendum** **213**

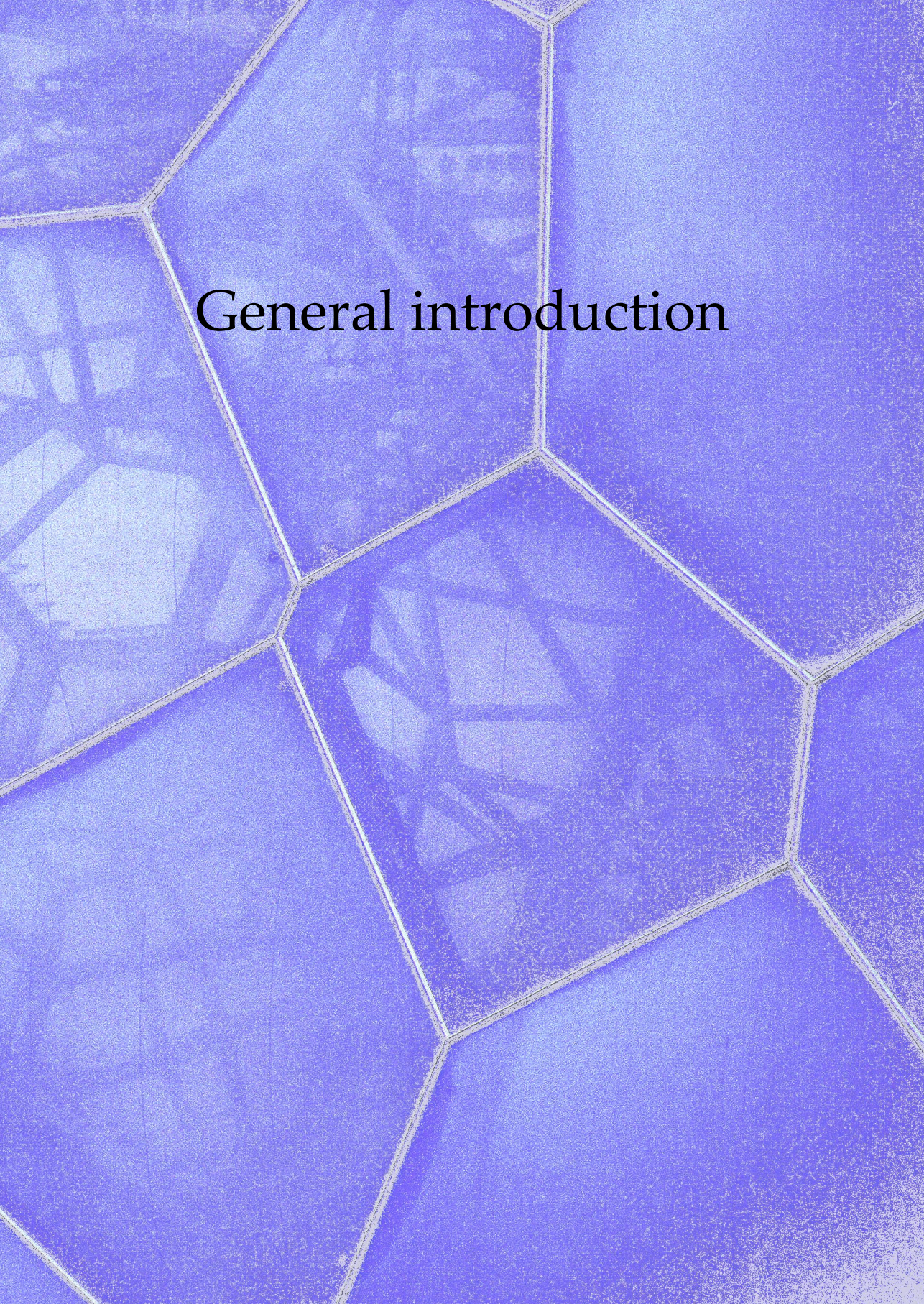
- Acknowledgements 215
- Resume 221
- Publications 222





Chapter

1



# General introduction



## 1.1. Introduction

About 70% of all chemical compounds produced in industry are solids<sup>1</sup>, which are often obtained in the form of powders. The Cambridge Dictionary defines a powder as *“a solid substance that consists of extremely small pieces, is soft and easy to divide, and often has the same shape as the container that it is in”*<sup>2</sup>. They are found especially in the consumer products, pharmaceuticals, food products and fine chemicals industries (e.g. explosives, pigments, fertilizers). These powders have certain functionalities, depending on the properties (e.g. size, size distribution, shape, purity) of their constituent particles. The production process of these powders must therefore be designed to control the particle properties<sup>3</sup>. This is mainly done during the crystallization step of the production process, by which the particles are produced and separated from by-products of the reaction phase. In this step, particle formation occurs due to a change in solubility conditions of the solute in its solvent. Due to the nature of crystallization, even in a single processing step a high purity of the crystals (>99%) can be obtained<sup>4</sup>. Control of shape, size and size distribution is possible by proper equipment design and operation.

However, not all the required particle functionalities can be obtained by controlling the aforementioned particle properties. In pharmaceutical compounds, such functionalities may involve low bioavailability, bad taste, premature dissolution, or shelf life. Other issues that cannot be overcome by using the pure material involve protection from the environment (mainly from oxygen or moisture), handling issues (e.g. of sticky materials) or isolation from reactive species. For such functionalities, more complex materials need to be designed, which comprise more than one component<sup>3</sup>. Microencapsulation of particles is one of the ways in which most of the aforementioned functionalities can be tuned towards the preferred specifications. In microencapsulation, the particle is surrounded by a uniform solid layer of another compound, or is entrapped in a solid mixture of wall material as a suspension<sup>5</sup>. There are many types of microencapsulation processes (both physical and chemical)<sup>6</sup> and more emerge due to increasing demand of particles with increasingly complex functionalities at lower (energy) cost.

In the production of particulate products, mixtures are handled that comprise multiple components (solutes, solvents)<sup>3,7</sup>. The possible interactions between the different components are as numerous as the functionalities that can be achieved. In crystallization processes, such interactions express themselves in the form of solubility, (pseudo) polymorphism, growth rate, etc. In encapsulation mixtures, these interactions express themselves in reactions

(e.g. cross-linking of a polymer, undesired side reaction), stabilizing or activating functions, isolation, etc. Additionally, the type of processing can have an effect on the materials used in them. A thorough understanding of these interactions is required to systematically arrive at the best core-shell combination, as well as the best process, for each product. In this thesis we make multicomponent particulate products with different functions (improved stability, immobilized solutions for small scale crystallization research, controlled release, protection from environment and activation) by various crystallization and microencapsulation processes, and investigate aforementioned interactions between the components and the effect of the processing on them. Model compounds are used from various industrial fields to illustrate the wide applicability of the tested processes.

## 1.2. Crystallization

One of the most used separation techniques is that of crystallization. Apart from separating products from the reaction phase, solid product is created. The crystalline material is of very high purity already after a single processing step.

### 1.2.1. Phase diagram

One of the essential pieces of information for the design of a crystallization process is the phase diagram of the compound to be crystallized with the mother phase<sup>8-11</sup>. The mother phase can be the impure melt of the desired compound, or a solution of the compound in a solvent<sup>12</sup>. From the phase diagram several system properties can be deduced, among which the solubility of the compound in the mother phase, the crystal yield under certain operation conditions and which (pseudo) polymorph persists under certain conditions<sup>12, 13</sup>.

In **Figure 1.1**, a schematic example is given of an isobaric phase diagram of a compound in a solvent. At high temperature and low concentrations the solution is undersaturated; all of the compound will be dissolved and a clear solution is obtained. Moving across the solubility line to high concentrations and low temperatures, the solution is supersaturated. In this region, crystals appear (nucleation) and are suspended in the remaining solution<sup>13</sup>. The nucleation of crystals, however, does not occur directly upon crossing the solubility line. The solution requires a high enough supersaturation for nucleation to occur<sup>13</sup>. The metastable zone limit is the line where the solution reached such a high supersaturation, that crystals can start to appear. The region between the solubility lines and metastable zone limits is called the metastable zone. In this region, the solution is supersaturated, but no nucle-

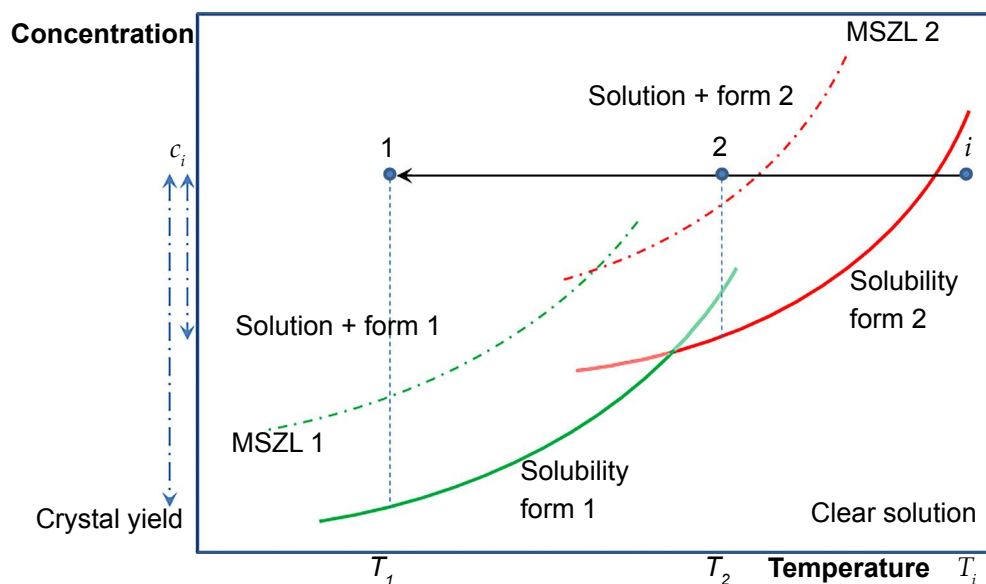


**Figure 1.1:** Schematic example of solubility lines of a polymorphic compound in a solvent. The green lines correspond to the temperature dependent solubility and metastable zone limit of form 1, the red lines to the solubility and metastable zone limit of form 2. Point  $i$  is a starting point of a crystallization experiment with concentration  $c_i^*$  at  $T = T_i$ . Points 1 and 2 are end points of cooling crystallization experiments with initial concentrations  $c_i$  but with different end temperatures ( $T_1$  and  $T_2$ ), resulting in different crystal yields.

ation takes place, only growth<sup>13</sup>.

The compound in **Figure 1.1** exhibits polymorphism, i.e. the ability to form different crystal structures with different properties from the same molecules<sup>14-17</sup>. Due to the different properties (this can be shape, solubility, etc.) of the polymorphs, it is of utmost importance to consistently produce the polymorph with favorable properties. For example, a polymorph with a higher water solubility may be favored in the pharmaceutical industry, since the compound may then have a higher bioavailability<sup>16-19</sup>. The green lines in the diagram correspond to the temperature dependent solubility and metastable zone limit of form 1, the red lines to form 2. The two polymorphs have different solubilities in the solvent and from the diagram it can be seen that form 1 is the thermodynamically stable form at lower temperatures, while form 2 is stable at higher temperatures. If in a cooling crystallization experiment with starting composition  $c_i$  and temperature  $T_i$  (point  $i$  in **Figure 1.1**) a solution is cooled from the undersaturated state to  $T_1$ , following the black arrow, form 1 crystallizes. In case the same solution is brought from the undersaturated state to the  $T_2$ , form 2 will crystallize. Control over the nucleation of the poly-

morph is very important<sup>17</sup>, especially if a metastable form is desired, since it is more likely that in the growth phase this polymorph persists<sup>20</sup>. Therefore, obtaining the phase diagram of the system to optimize is an essential step in the design of the process. Knowledge about phase diagrams is even more important in case of multicomponent systems, since the interaction of the components with each other, e.g. in the form of co-crystallization or solvate formation, can lead to very different products<sup>15, 17</sup>.

## 1.2.2. Crystallization techniques

There are various ways of bringing a system from the undersaturated state to a supersaturated one, in order to induce nucleation. From **Figure 1.1** it is clear that reducing temperature or concentration will eventually lead to crystallization. Cooling crystallization is mainly used when the solubility is a strong function of temperature, while evaporation of solvent is used for systems with a lower dependency on temperature<sup>15</sup>. Such choices are made based on the possible crystal yield compared to the energy requirement of the process.

The yield is determined by the difference in initial solution composition and the solubility at the final temperature<sup>21</sup>. In the cooling crystallization experiments in **Figure 1.1** the yield  $Y_{cr}$  can be calculated using **Eq. (1.1)**:

$$Y_{cr} = m_{solvent} \cdot (c_i - c_f) \quad (1.1)$$

Where  $m_{solvent}$  is the amount of solvent (e.g. in kg) and  $c_i$  and  $c_f$  are the concentrations (e.g. in  $\text{kg}_{\text{solute}}/\text{kg}_{\text{solvent}}$ ) of solute in the mother liquor at the start and end of the experiment, respectively.  $c_i$  corresponds to the composition in point  $x_i$  in **Figure 1.1**, while  $c_f$  corresponds to the solubility at the end temperature ( $T_1$  or  $T_2$ ). Since the solubility of form 2 is higher than that of form 1, the crystal yield  $Y_{cr}$  of form 2 will be lower than that of form 1. In evaporative crystallization, the evaporated solvent needs to be taken into account for the yield calculations. In case hydrates are formed, the crystal water should be taken into account<sup>21</sup>.

When only very low concentrations of the dissolved compound are present, evaporative and cooling crystallization require too much energy input. In these cases, either precipitation or anti-solvent crystallization may be used<sup>15</sup>. Here another solute or solvent is added, through which the solubility of the compound in the multicomponent mixture drops dramatically and crystallization takes place. The principles of crystallization by cooling, evaporation, precipitation or addition of anti-solvent are well known and already applied in batch tanks or in various types of continuous crystallizers<sup>22</sup>. However, the demand for novel products also drives the development of new applications

of these principles. For specialty products, novel crystallization processes can provide the desired product quality (e.g. in terms of crystal size, size distribution, reproducibility)<sup>23, 24</sup>. In continuous crystallization the control over size and size distribution of the crystals has already been addressed to a certain extent, as well as the reproducibility<sup>22</sup>. However, continuous processing does not answer the requirements of currently emerging products in the sense of multicomponent particulate product formation or the production of (sub )micron sized crystals. For such advanced purposes, crystallization processes need to be redesigned<sup>24</sup>. Additional benefits of redesigning crystallization processes are potential cost and energy savings.

### 1.3. Encapsulation

Final formulations of particulate products, regardless of the industry they are produced in, often comprise mixtures of different components<sup>25</sup>. Each component brings its own properties to this mixture and has its own function in the product. A combination of some specific components can yield additional benefits, due to special interactions between them<sup>25, 26</sup>. Benefits gained from combining materials in a formulation range from property assisting perks (e.g. an active pharmaceutical ingredient (API) can be mixed with a suitable excipient to improve the dissolution of the API<sup>26, 27</sup>), to fully controlled multiple transport and release particles, which are currently mainly found in experimental medicine<sup>28</sup>.

#### 1.3.1. Configurations

For the more basic enhancements, simply mixing a number of ingredients may be sufficient<sup>29</sup>. However, when a more specific enhancement is desired, like controlled release or activation, powders need to be created of which

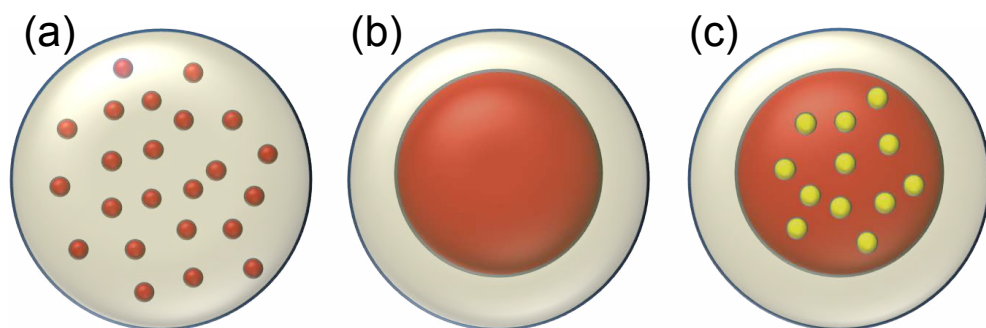


**Figure 1.2:** Variations of encapsulated compounds, with (a) matrix configuration, (b) core-shell configuration and (c) a combination of matrix and core-shell configuration.

each particle consists of multiple solids, to improve the contact between the different components. In case of controlled release particles, the solids need to be distributed over the particle in a very specific way; the component to be transported and released should be entirely surrounded by its protective shell until the release conditions are met<sup>30-32</sup>. These particles can be made in two basic configurations, as a matrix particle (**Figure 1.2(a)**) or as core-shell particle (**Figure 1.2(b)**)<sup>7, 33</sup>. Combinations of these configurations are also possible, as can be seen from **Figure 1.2(c)**, where the core in a core-shell particle contains another compound. This way, different functionalities can be combined, e.g. controlled release and activation. Any number of shells is possible, though the larger the number of components, the more complex the process becomes to produce them.

### 1.3.2. Processing

In the production of encapsulated particles, the handling and control of complex multicomponent systems is the main challenge. Many processes, both physical and chemical and combinations thereof, have been investigated for encapsulation<sup>6, 34</sup>. Physical processes comprise crystallization, spray drying and variations thereof, extrusion and fluidized bed (FB) coating, which allow for efficient process integration, since some of these processes are already used for purification or drying of the produced material<sup>13, 35</sup>. Examples of chemical processes are coacervation, self-assembly processes and liposome entrapment. These processes require addition of multiple steps and possibly extra separation steps to the process<sup>6</sup>. The type of process that should be chosen depends largely on the materials and functions they are applied to, which means that the process should be tailored to the intended product. For producing matrix materials, extrusion is a popular, low cost option, since the core and shell materials only need to be mixed<sup>36</sup>. For core-shell particles with thin layers, on the other hand, self-assembly systems are more viable, since the coating needs to be applied very carefully<sup>37</sup>.

In most cases the core material is produced and pretreated prior to the coating step<sup>7</sup>. However, in some cases attempts can be made to combine the production of both the core and the shell in a single processing step. Control over the coating process is mostly obtained by varying conditions like temperature, pressure, flow rate and concentration of materials. In some industries, though, the extent to which these parameters can be changed is limited due to the sensitivity of the product to a certain variable. For example, biological materials, pharmaceuticals, energetic materials and foods are often unstable at higher temperatures. Further, with food and biological materials the processing is mostly restricted to watery environments<sup>38, 39</sup>, while other solvents may render these materials unfit for use. Such limitations reduce

the list of potential encapsulation processes dramatically. In the field of energetic materials the number of limitations stacks, since the molecules of which these materials consist can be sensitive to increased temperature, rapidly changing pressure, friction, sparks, etc.<sup>40, 41</sup>. The consequences, in case of erroneous processing, are also more severe with these substances, since an explosion might occur. Therefore, encapsulation processes need to be tailored to the system in question, where the demands of the final product are taken into account, as well as the safety of the processing and the potential deactivation of the product<sup>7, 41</sup>.

## 1.4. Thesis outline

In this thesis the production of particulate products is explored by investigating the crystallization of pure and mixed organic substances as well as the encapsulation or immobilization of various compounds to achieve certain special effects. Model compounds are used from various industrial fields to illustrate the wide applicability of the tested processes.

There to, various aspects of crystallization in multicomponent mixtures are discussed. To gain more insight into phase diagrams of multicomponent systems, the solubility of the compound in the mixture must be determined, which can be done in various ways<sup>12, 42-44</sup>. However, currently used methods for determining solubility are either slow, labor intensive or rely on the variation of temperature, while often a multicomponent phase diagram is desired at constant temperature. **Chapter 2** describes a novel method of determining the solubility of organic compounds in a solvent or solvent mixture at constant temperature, utilizing solvent addition.

Performing crystallization in solvent mixtures can lead to the formation of different pseudo-polymorphs, where solvent molecules are incorporated into the crystal lattice as regular building blocks<sup>14, 15</sup>. Such solvate formation influences properties of the resulting crystals in terms of solubility, stability, etc. It is therefore of utmost importance to control the formation of such structures. **Chapter 3** describes how changing the composition of solvent mixtures allows to control the resulting crystal form after crystallization. This is done for ternary systems (1 solute + 2 solvents) and a quaternary system (1 solute + 3 solvents), in which either 1 or 2 of the solvents can be integrated in the crystal lattice.

When a multicomponent mixture consists of 2 solutes and a solvent, the crystallization of the solutes can be controlled in a special manner, in which the one component nucleates later than the other. In such a controlled sys-

tem, heterogeneous nucleation can occur, where the second compound crystallizes on the surface of the first. This way, the crystallization process can be used for encapsulation. However, not all combinations of compounds show heterogeneous nucleation<sup>45, 46</sup>. In **Chapter 4** electrospray crystallization is used to combine such solids in a single particle, regardless of the tendency towards heterogeneous nucleation.

Electrospray crystallization is a promising technique for producing small crystals with a narrow size distribution, leading to many improvements, such as dissolution rate and stability<sup>27, 47</sup>. However, many challenges need to be overcome to arrive at successful operation of such a process. The operation window of the process is very small, since a balance needs to be found between many parameters. Additionally, material losses arise, due to e.g. premature crystallization. The handling of the final product is also subject to various considerations. **Chapter 5** comments on such difficulties encountered during electrospray crystallization and provides strategies to either prevent or solve these difficulties.

In small volumes of solution, such as obtained e.g. in electrospray crystallization, the crystallization kinetics may be different from those in larger volumes<sup>48</sup>. To gain a better understanding of the crystal nucleation and growth in small volumes, in **Chapter 6** small droplets of solution are encapsulated in a transparent shell. Inside these particles, cooling crystallization experiments are performed to derive the scale dependent kinetics.

Additionally, the production and application of core-shell and matrix type encapsulates in the food and energetic materials industries are explored. Nowadays, meat analogs are an increasingly welcome alternative to meat<sup>49, 50</sup>. A novel process was developed that improves the mouthfeel of the meat analog by creating meat-like structures through the application of shear stress on a suspension containing soy protein isolate (SPI) and vital wheat gluten (WG)<sup>51</sup>. However, during the mixing of the ingredients with water, the gluten instantly fibrillize, forming a sticky gel. This premature fibrillization leads to material losses. In **Chapter 7**, the gluten powder is immobilized in biopolymers in a matrix type configuration, to prevent the instant fibrillization and thereby improve the mixing of the components prior to the shearing step.

In matrix type encapsulates, the wall material constitutes a relatively large part of the product. In some applications, e.g. energetic materials, this can have a high impact on the performance of the product. In such a case, if a coating is required, the aim is to keep it as thin as possible, so as to keep the impurity effect small. This automatically leads to a core-shell configuration

of the encapsulates. **Chapter 8** deals with the application of very thin layers, i.e. in the order of nanometers, onto micro particles of various materials by the use of atomic layer deposition (ALD) in a fluidized bed<sup>52, 53</sup>.

## 1.5. References

1. Front Matter. In *Industrial Crystallization Process Monitoring and Control*, Wiley-VCH Verlag GmbH & Co. KGaA **2012**; pp I-XXII.
2. Powder. <http://dictionary.cambridge.org/dictionary/english/powder> (27 October),
3. *Particulate Products*. 1 ed.; Springer International Publishing: Switzerland, **2014**; p 469.
4. Mullin, J. W., *Crystallization*. 3 ed.; Butterworth-Heinemann Ltd.: Oxford, **1993**.
5. Poncelet, D., Microencapsulation: fundamentals, methods and applications. In *Surface Chemistry in Biomedical and Environmental Science*, Blitz, J.; Gun'ko, V., Eds. Springer Netherlands **2006**; Vol. 228, pp 23-34.
6. Caruso, F., Nanoengineering of Particle Surfaces. *Advanced Materials* **2001**, 13, 11-22.
7. Oxley, J., Chapter 4 - Overview of Microencapsulation Process Technologies. In *Microencapsulation in the Food Industry*, Gaonkar, A. G.; Vasisht, N.; Khare, A. R.; Sobel, R., Eds. Academic Press: San Diego, **2014**; pp 35-46.
8. Haas, C.; Drenth, J., Understanding protein crystallization on the basis of the phase diagram. *Journal of Crystal Growth* **1999**, 196, 388-394.
9. Chiarella, R. A.; Davey, R. J.; Peterson, M. L., Making Co-Crystals The Utility of Ternary Phase Diagrams. *Crystal Growth & Design* **2007**, 7, 1223-1226.
10. Crocker, L. S.; Ge, Z.; Abraham, A.; Hartman, R.; Xu, J., An Etoricoxib Phase Diagram: Hemihydrate and Anhydrate. *Organic Process Research & Development* **2003**, 7, 958-961.
11. Veessler, S.; Revalor, E.; Bottini, O.; Hoff, C., Crystallization in the Presence of a Liquid-Liquid Phase Separation. *Organic Process Research & Development* **2006**, 10, 841-845.
12. Mullin, J. W., 3 - Solutions and solubility. In *Crystallization (Fourth Edition)*, Mullin, J. W., Ed. Butterworth-Heinemann: Oxford, **2001**; pp 86-134.
13. Schwartz, A. M.; Myerson, A. S., 1 - Solutions and solution properties. In *Handbook of Industrial Crystallization (Second Edition)*, Myerson, A. S., Ed. Butterworth-Heinemann: Woburn, **2002**; pp 1-31.
14. Mullin, J. W., 1 - The crystalline state. In *Crystallization (Fourth Edition)*, Mullin, J. W., Ed. Butterworth-Heinemann: Oxford, **2001**; pp 1-31.
15. Myerson, A. S.; Ginde, R., 2 - Crystals, crystal growth, and nucleation. In *Handbook of Industrial Crystallization (Second Edition)*, Myerson, A. S., Ed. Butterworth-Heinemann: Woburn, **2002**; pp 33-65.
16. Kulkarni, S. A.; McGarrity, E. S.; Meekes, H.; ter Horst, J. H., Isonicotinamide self-association: the link between solvent and polymorph nucleati-

on. *Chemical Communications* **2012**, 48, 4983-4985.

17. Ymén, I., Introduction to the Solid State – Physical Properties and Processes. In *Solid State Characterization of Pharmaceuticals*, John Wiley & Sons, Ltd **2011**; pp 1-34.

18. Kobayashi, Y.; Ito, S.; Itai, S.; Yamamoto, K., Physicochemical properties and bioavailability of carbamazepine polymorphs and dihydrate. *International Journal of Pharmaceutics* **2000**, 193, 137-146.

19. Tipduangta, P.; Takeddin, K.; Fábíán, L.; Belton, P.; Qi, S., A New Low Melting-Point Polymorph of Fenofibrate Prepared via Talc Induced Heterogeneous Nucleation. *Crystal Growth & Design* **2015**, 15, 5011-5020.

20. Mullin, J. W., 6 - Crystal growth. In *Crystallization (Fourth Edition)*, Mullin, J. W., Ed. Butterworth-Heinemann: Oxford, **2001**; pp 216-288.

21. Bennett, R. C., 5 - Crystallizer selection and design. In *Handbook of Industrial Crystallization (Second Edition)*, Myerson, A. S., Ed. Butterworth-Heinemann: Woburn, **2002**; pp 115-140.

22. Kirwan, D. J.; Orella, C. J., 11 - Crystallization in the pharmaceutical and bioprocessing industries. In *Handbook of Industrial Crystallization (Second Edition)*, Myerson, A. S., Ed. Butterworth-Heinemann: Woburn, **2002**; pp 249-266.

23. Ambrus, R.; Radacsi, N.; Szunyogh, T.; van der Heijden, A. E. D. M.; ter Horst, J. H.; Szabó-Révész, P., Analysis of submicron-sized niflumic acid crystals prepared by electrospray crystallization. *Journal of Pharmaceutical and Biomedical Analysis* **2013**, 76, 1-7.

24. Radacsi, N.; van der Heijden, A. E. D. M.; Stankiewicz, A. I.; ter Horst, J. H., Nanoparticle generation by intensified solution crystallization using cold plasma. *Chemical Engineering and Processing* **2013**, 71, 51-58.

25. Merkus, H.; Meesters, G. H., Introduction. In *Particulate Products*, Merkus, H. G.; Meesters, G. M. H., Eds. Springer International Publishing **2014**; Vol. 19, pp 1-19.

26. Paus, R.; Prudic, A.; Ji, Y., Influence of excipients on solubility and dissolution of pharmaceuticals. *International Journal of Pharmaceutics* **2015**, 485, 277-287.

27. Radacsi, N.; Ambrus, R.; Szunyogh, T.; Szabó-Révész, P.; Stankiewicz, A.; van der Heijden, A.; ter Horst, J. H., Electrospray Crystallization for Nanosized Pharmaceuticals with Improved Properties. *Crystal Growth & Design* **2012**, 12, 3514-3520.

28. Zhang, L.; Zeng, Z.; Hu, C.; Bellis, S. L.; Yang, W.; Su, Y.; Zhang, X.; Wu, Y., Controlled and targeted release of antigens by intelligent shell for improving applicability of oral vaccines. *Biomaterials* **2016**, 77, 307-319.

29. Jannin, V.; Rodier, J.-D.; Musakhanian, J., Polyoxylglycerides and

glycerides: Effects of manufacturing parameters on API stability, excipient functionality and processing. *International Journal of Pharmaceutics* **2014**, 466, 109-121.

30. Ma, G., Microencapsulation of protein drugs for drug delivery: Strategy, preparation, and applications. *Journal of Controlled Release* **2014**, 193, 324-340.

31. Wieland-Berghausen, S.; Schote, U.; Frey, M.; Schmidt, F., Comparison of microencapsulation techniques for the water-soluble drugs nitenpyram and clomipramine HCl. *Journal of Controlled Release* **2002**, 85, 35-43.

32. Elzoghby, A. O.; Abo El-Fotoh, W. S.; Elgindy, N. A., Casein-based formulations as promising controlled release drug delivery systems. *Journal of Controlled Release* **2011**, 153, 206-216.

33. Singh, M. N.; Hemant, K. S. Y.; Ram, M.; Shivakumar, H. G., Microencapsulation: A promising technique for controlled drug delivery. *Research in Pharmaceutical Sciences* **2010**, 5, 65-77.

34. Jacobs, I. C., Chapter 30 - Process Scale-up Considerations for Microencapsulation Processes. In *Microencapsulation in the Food Industry*, Gaonkar, A. G.; Vasisht, N.; Khare, A. R.; Sobel, R., Eds. Academic Press: San Diego, **2014**; pp 391-398.

35. Frey, C., Chapter 7 - Fluid Bed Coating-Based Microencapsulation. In *Microencapsulation in the Food Industry*, Gaonkar, A. G.; Vasisht, N.; Khare, A. R.; Sobel, R., Eds. Academic Press: San Diego, **2014**; pp 65-79.

36. Harrington, J.; Schaefer, M., Chapter 8 - Extrusion-Based Microencapsulation for the Food Industry. In *Microencapsulation in the Food Industry*, Gaonkar, A. G.; Vasisht, N.; Khare, A. R.; Sobel, R., Eds. Academic Press: San Diego, **2014**; pp 81-84.

37. van Ommen, J. R.; Yurteri, C. U.; Ellis, N.; Kelder, E. M., Scalable gas-phase processes to create nanostructured particles. *Elsevier* **2010**, 8, 572 - 577.

38. MariaIns, R.; Maria HelenaAndrade, S.; MarcosAkira, d. Ä. Å., Encapsulation Technologies for Modifying Food Performance. In *Innovation in Food Engineering*, CRC Press **2009**; pp 223-275.

39. Cross, J.; Wood, L., Purifying water for biotechnology: A case study. *Process Biochemistry* **1994**, 29, 449-453.

40. Meyer, R.; Köhler, J.; Homburg, A., B. In *Explosives*, Wiley-VCH Verlag GmbH & Co. KGaA **2003**; pp 23-48.

41. Schmidt, E.; Nastke, R.; Heintz, T.; Niehaus, M.; Teipel, U., Size Enlargement. In *Energetic Materials*, Wiley-VCH Verlag GmbH & Co. KGaA **2005**; pp 183-223.

42. Hermanto, M. W.; He, G.; Tjahjono, M.; Chow, P. S.; Tan, R. B. H.;

Garland, M., Calibration of dielectric constant measurements to improve the detection of cloud and clear points in solution crystallization. *Chemical Engineering Research and Design* **2011**, 89, 2613-2619.

43. Vellema, J.; Hunfeld, N. G. M.; Van den Akker, H. E. A.; ter Horst, J. H., Avoiding crystallization of lorazepam during infusion. *European Journal of Pharmaceutical Sciences* **2011**, 44, 621-626.

44. Srisanga, S.; ter Horst, J. H., Racemic Compound, Conglomerate, or Solid Solution: Phase Diagram Screening of Chiral Compounds. *Crystal Growth & Design* **2010**, 10, 1808-1812.

45. Tsekova, D. S.; Williams, D. R.; Heng, J. Y. Y., Effect of surface chemistry of novel templates on crystallization of proteins. *Chemical Engineering Science* **2012**, 77, 201-206.

46. Mullin, J. W., 5 - Nucleation. In *Crystallization (Fourth Edition)*, Mullin, J. W., Ed. Butterworth-Heinemann: Oxford, **2001**; pp 181-215.

47. Radacsi, N.; Stankiewicz, A. I.; Creighton, Y. L. M.; van der Heijden, A. E. D. M.; ter Horst, J. H., Electro spray Crystallization for High-Quality Submicron-Sized Crystals. *Chem. Eng. Technol.* **2011**, 34, 624-630.

48. Hammadi, Z.; Candoni, N.; Grossier, R.; Ildefonso, M.; Morin, R.; Veesler, S., Small-volume nucleation. *Comptes Rendus Physique* **2013**, 14, 192-198.

49. Hughes, D., Animal welfare. *British Food Journal* **1995**, 97, 3-7.

50. Steinfeld, H.; Food; Agriculture Organization of the United, N.; Livestock, E.; *Development, Livestock's long shadow : environmental issues and options*. Food and Agriculture Organization of the United Nations: Rome, **2006**.

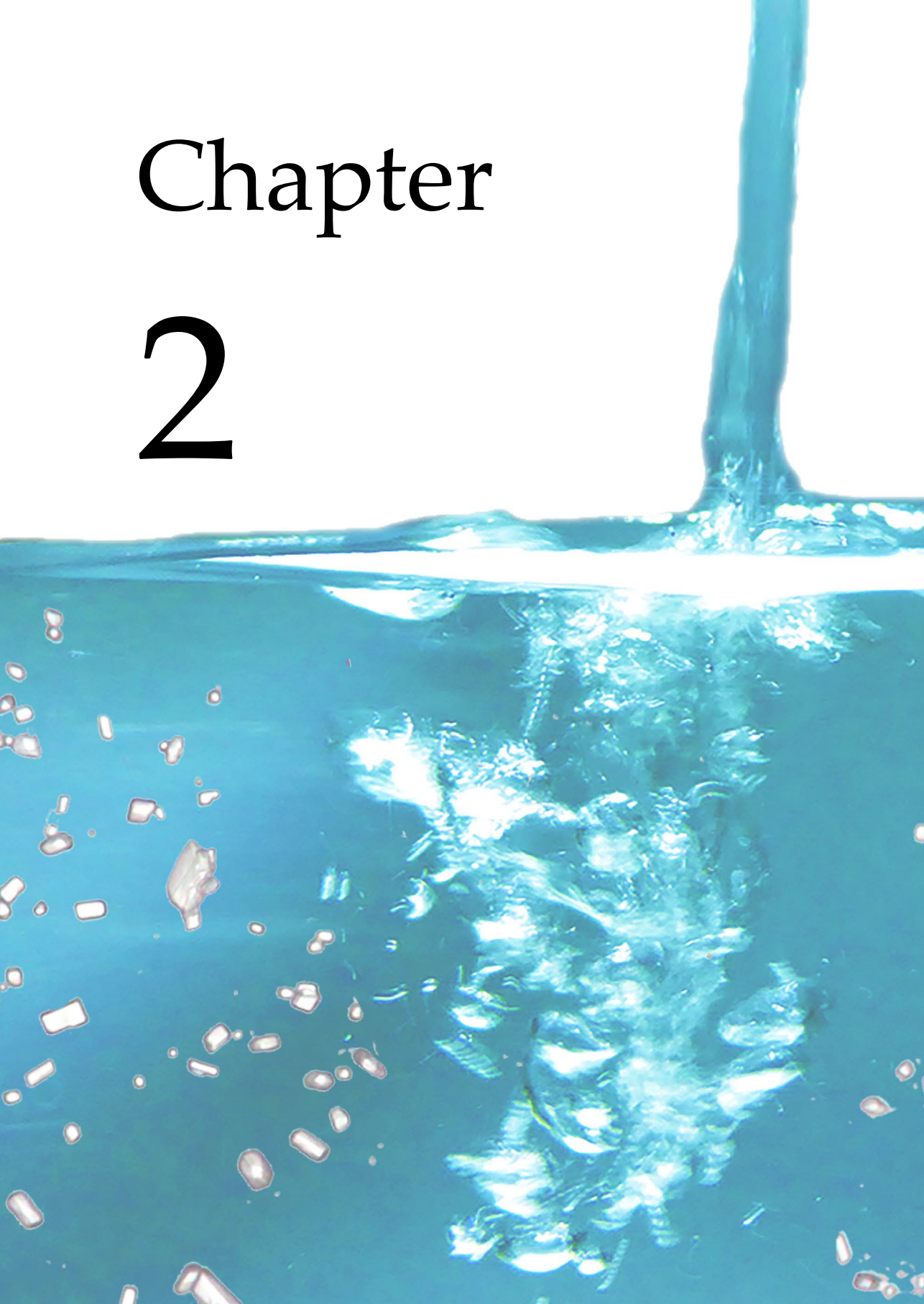
51. Krintiras, G. A.; Göbel, J.; van der Goot, A. J.; Stefanidis, G. D., Production of structured soy-based meat analogues using simple shear and heat in a Couette Cell. *Journal of Food Engineering* **2015**, 160, 34-41.

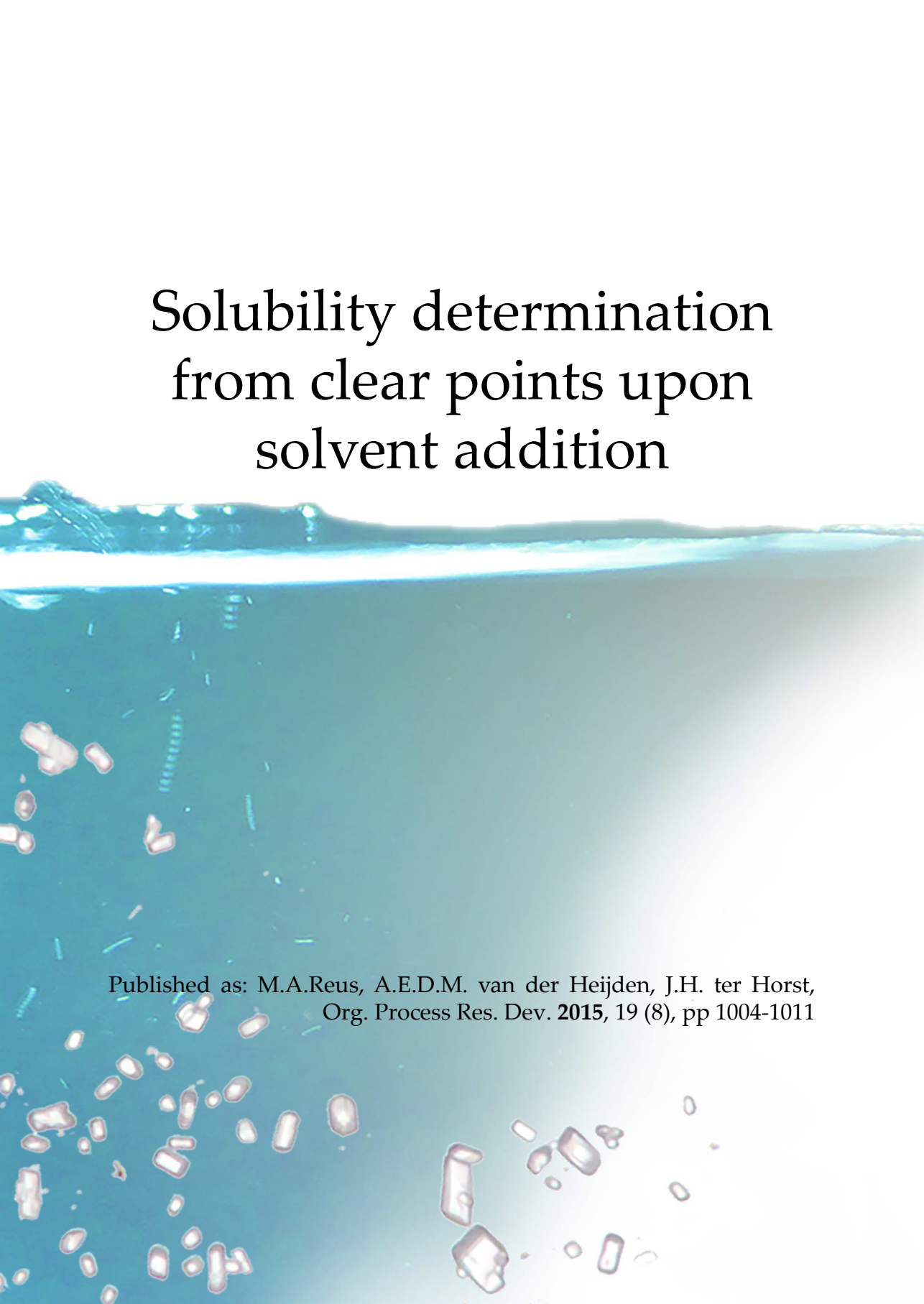
52. Beetstra, R.; Lafont, U.; Nijenhuis, J.; Kelder, E. M.; van Ommen, J. R., Atmospheric Pressure Process for Coating Particles Using Atomic Layer Deposition. *Chemical Vapor Deposition* **2009**, 15, 227 - 233.

53. Valdesueiro, D.; Meesters, G.; Kreutzer, M.; van Ommen, J.R., Gas-Phase Deposition of Ultrathin Aluminium Oxide Films on Nanoparticles at Ambient Conditions. *Materials* **2015**, 8, 1249.

Chapter

2





# Solubility determination from clear points upon solvent addition

Published as: M.A.Reus, A.E.D.M. van der Heijden, J.H. ter Horst,  
*Org. Process Res. Dev.* **2015**, 19 (8), pp 1004-1011

### Abstract

A method is described for determining the solubility of multicomponent crystalline compounds from clear points upon sample dilution at a constant temperature. Clear points are established by continuously adding solvent mixture to a suspension of known composition until a clear solution appears. For validation, this solvent addition method is compared to the traditional equilibrium concentration method at constant temperature and the more recent temperature variation method with which clear point temperatures are determined upon increasing the sample temperature. Solubility data of binary systems (1 solute, 1 solvent) measured using the solvent addition method are obtained relatively quickly compared to the equilibrium concentration method. These solubility data are consistent with those of the temperature variation and the equilibrium concentration method. For the temperature variation method the results are dependent on the heating rate. Likewise, for the solvent addition method they are dependent on the addition rate. Additionally, for ternary systems involving anti-solvent or co-crystals, solubilities are determined at a constant temperature using the solvent addition method. The use of the solvent addition method is especially valuable in the case of solvent mixtures and other complex multi-component systems, in which the temperature variation method cannot be applied easily.

## 2.1. Introduction

In production often a crystallization step is required for purification and final crystalline particulate product formation.<sup>1,2</sup> The solubility or phase diagram of such compounds is essential information for efficient and reliable crystallization process design and operation.<sup>3-6</sup> The phase diagram indicates the most stable phases at specific compositional and temperature conditions<sup>1,4-6</sup>, determines the achievable yield<sup>7</sup> and enables the monitoring of the supersaturation during the crystallization process<sup>7,8</sup>.

Traditionally the solubility is measured through equilibration of a suspension<sup>1</sup>. The solubility is then equal to the concentration in the equilibrated solution, which can be sampled and determined by for example, a gravimetric method or HPLC (**Figure 2.1(a)**). Although the Equilibrium Concentration (EqC) method is widely accepted and considered accurate<sup>1</sup>, it is laborious and time-consuming. Currently, commercial equipment from various suppliers is available that streamlines measurements through a temperature variation (TV) method in which clear points are measured.<sup>9-11</sup> In the TV method the solubility is changed by changing the temperature, until it matches the concentration. A clear point is then the temperature at which, upon increasing the temperature, a suspension turns into a clear solution. **Figure 2.1(b)** shows the principle of a clear point measurement using the TV method. If the heating rate is sufficiently small, the crystal dissolution rate is fast and the clear point can be assumed to be equal to the saturation temperature.<sup>10</sup> This TV method is much less labor intensive, much faster and allows for the measurement of the metastable zone width or induction time in the same measurement.

However, the TV method loses its advantages when solubility data is required at a specific temperature, for example in phase diagrams with multicomponent mixtures in which the solubility is a function of the concentra-

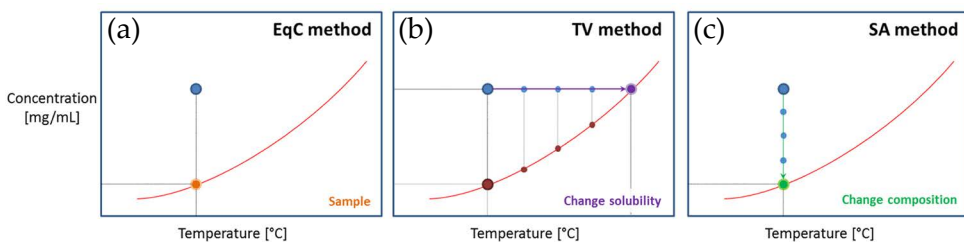


**Figure 2.1:** Different principles for solubility measurements using a certain overall composition (Blue dot). **(a)** EqC method. The equilibrium concentration (orange dot) is determined by analysing the concentration in an equilibrated suspension. **(b)** The purple arrow represents the TV method, where the solubility of the system is changed until it corresponds to the overall concentration. **(c)** The green arrow represents the Solvent Addition (SA) method, where the concentration in the system is continuously decreased until it corresponds to the solubility at constant temperature.

tion of more than 1 component, since the TV method relies on a variable temperature.

Several groups<sup>1, 12-14</sup> reported another method of determining solubility. Instead of increasing the solubility by increasing the temperature, in this Solvent Addition (SA) method the concentration is decreased by adding solvent (**Figure 2.1(c)**). The green arrow represents the SA method. At a constant temperature, starting from a known suspension, solvent is added drop-wise until full dissolution of the material. Also continuous methods have been shown to work, for example by Labarthe et al.<sup>15, 16</sup>, predominantly in multi-component mixtures. However, no account was given as to how parameters like the addition rate must be chosen to obtain reliable data. Additionally, up to now this approach is more labor intensive and time consuming than even the EqC method and is therefore not widely applied. We intensify this method by making the addition continuous instead of quasi static and by using clear point measurements for ease of operation. Additionally, this method can be automated similar to the TV method. We therefore aim to make the method more accessible and more widely applicable.

This method seems particularly useful for determining phase diagrams of complex multicomponent mixtures at constant temperature, since the concentration of each component can be tracked. Here we report the validation of the Solvent Addition method through a study of the solubility of p-hydroxybenzoic acid (pHBA) in acetic acid. Additionally, the influence of the solvent addition rate on the accuracy of the SA measurements is determined. Finally the SA method is applied to two multi-component systems; DL-asparagine (DL-Asn) in water-ethanol mixtures, and the carbamazepine - isonicotinamide (CBZ-INA) co-crystal in the solvent ethanol.

## 2.2. Experimental section

### 2.2.1. Materials

pHBA ( $\geq 99\%$ ), INA ( $\geq 99\%$ ), CBZ (99%), glacial acetic acid, ethanol (100%) and DL-Asn ( $\geq 99\%$ ) were supplied by Sigma Aldrich and used without further purification. Demi water was taken from a Millipore MilliQ system and had a resistivity of approximately 18 M $\Omega$ -cm.

### 2.2.2. Equilibrium concentration method

For the EqC method the same protocol was used as reported by Nordström and Rasmuson<sup>17</sup>, where the solution was equilibrated at a constant temperature in a 100 mL Easymax reactor setup (Mettler Toledo) for 4 days. At various temperatures solution samples of approximately 5 mL were taken with a syringe, weighed and left to evaporate in a fume hood for at least 14 days. When the crystals appeared dry, they were weighed. Two days later

they were weighed again to check for any additional mass loss until the mass was constant.

### 2.2.3. Temperature variation method

A Crystal16 multiple reactor system of Technobis was programmed for three subsequent clear point measurements of 16 samples of 1 mL containing a specific amount of pHBA and solvent. The samples were agitated using magnetic stirrer bars with a stirring rate of 700 rpm. First, the suspension was heated at a rate of  $+0.3^{\circ}\text{C}/\text{min}$ . At some temperature (with an average error of  $\Delta T = 0.8^{\circ}\text{C}$ ), upon heating the light transmission became 100% and this was taken as the clear point. Then the temperature was kept constant for 2 hours at which the solutions remained clear liquids. Upon cooling at a rate of  $0.3^{\circ}\text{C}/\text{min}$  crystallization occurred, always well below the clear point, after which another temperature cycle was performed. For the pHBA phase diagram, the temperature was varied between  $0 - 90^{\circ}\text{C}$ . For determining the influence of the heating rate on the clear point measurements, concentrations of 136.2 and 161.4 mg/mL of pHBA in acetic acid were used in a temperature range of  $0 - 60^{\circ}\text{C}$ .

### 2.2.4. Solvent addition method

For the solvent addition experiments a Crystalline Multiple Reactor setup (Avantium Technologies) was used to provide a constant temperature and stirring rate (300 rpm), and to monitor the dissolution process by video. The starting volume was 2 mL of suspension. The solution was allowed to equilibrate for approximately 30 minutes prior to the solvent addition.

A rough estimate of the upper level of the equilibrium concentration in the co-crystal system was made using the pure component solubilities<sup>18</sup>. If a rough educated guess of the equilibrium concentration was not possible, a small amount of crystalline material was taken and small known amounts of solvent were added in steps until the material is dissolved. The amount of solvent added and the amount of crystalline material lead to an estimate of the solubility. Starting points for other compositions or temperatures in the same system were estimated from neighboring measurements, by either increasing or decreasing the concentration compared to the neighboring measurement. For example, for a solubility measurement at  $30^{\circ}\text{C}$ , a starting composition was used with a concentration of approximately 1.5 times the concentration in the starting composition of the measurement at  $20^{\circ}\text{C}$ . As a rule of thumb the solubility doubles when the temperature increases by  $20^{\circ}\text{C}$ <sup>19</sup>, which was used as a guideline. A relatively dense suspension was chosen as a starting point for the SA measurement, at which the amount of solid added to the solvent was 1.3 to 3 times higher than the rough estimate.

Solvent was added using an Aitecs 2016 syringe infusion pump (volumetric accuracy of  $\pm 2\%$ ). Clear points were determined by visual analysis of

the suspension pictures taken every 30 seconds. This method was preferred over the turbidity measurements in the same device, because of the better detection limit.

For larger scale solvent addition measurements a 100 mL Easymax reactor (Mettler Toledo) was used with overhead stirring (250 rpm), combined with an SP-50 dosing unit. Clear points in the Easymax were determined by FTIR measurements using the ReactIR system (Mettler Toledo) equipped with an AgX probe with diamond tip and an LN<sub>2</sub> MCT detector. Peaks at 1168 cm<sup>-1</sup> and at 1612 cm<sup>-1</sup> were used to monitor the concentration changes of the compound in solution. The concentration remained constant until all crystalline material was dissolved. The start of a concentration decrease marked the clear point, which was determined by the intersection of the horizontal line (constant concentration) and the sloped line (decreasing concentration).

### 2.2.5. Characterization

The crystalline phase was analyzed by X-ray Powder Diffraction (XRPD), using a Bruker AXS D2-Phaser with a Bragg-Brentano focusing geometry and a CuKα1 radiation. Measurements were taken between 5 < 2θ < 50°. An optical microscope (Leica Nikon Optiphot 200) was used for the analysis of the crystal shape.

## 2.3. Results

pHBA is a white crystalline solid and is mostly known for its esters, which are used as preservatives. The SA method was used to determine its solubility in acetic acid. In a small volume ( $V_{start} = 2$  mL), the SA method was applied at 3 different temperatures while using a solvent addition rate of  $R_a = 0.5$  mL/h. While adding acetic acid, the suspension was monitored by video images. From **Figure 2.2** the decreasing suspension density upon solvent addition and the clear point after addition of 0.70 mL of acetic acid are evident. More pictures were recorded during the experiment for accurate determination of the clear point, but are left out of **Figure 2.2** for clarity. The clear point lies between 0.696 and 0.706 mL of added acetic acid, resulting in a solubility of  $94.5 \pm 0.2$  mg/mL.

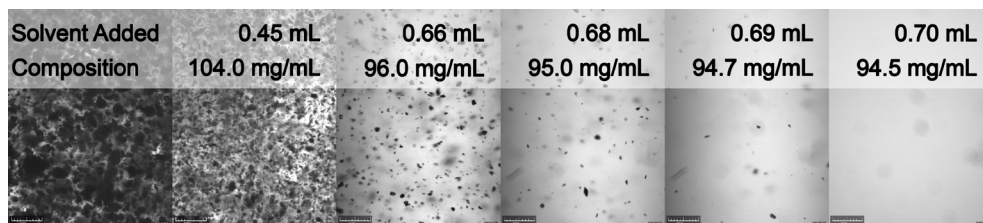


**Figure 2.2:** Visualization of the suspension density decrease of 255.2 mg/mL pHBA in 2 mL acetic acid upon acetic acid addition. After addition of 0.70 mL of acetic acid a clear solution was obtained.

From 2 or 3 measurements per temperature, average clear points were determined at 94.3, 113.7 and 131.7 mg/mL at temperatures of 20, 30 and 40°C, respectively. These data are shown in **Figure 2.3** as green diamonds. The solubilities were reproducible within 0.4 mg/mL.

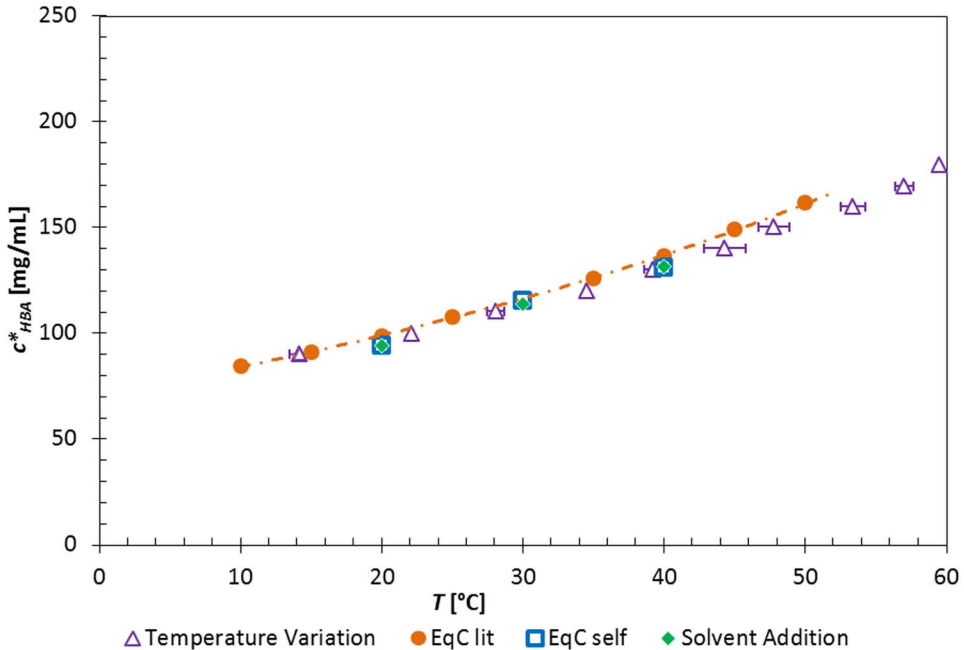


**Figure 2.3:** Phase diagram of pHBA in acetic acid measured by the EqC method (● = literature data<sup>17</sup>, □ = own EqC measurements), TV method (△) and SA method (◆). For the TV and SA methods, heating and addition rates of 0.3°C/min and 0.3 mL/h were used, respectively.

### 2.3.1. Comparison with other solubility measurement methods

For pHBA in acetic acid, the phase diagram was also determined using the TV method (△) and the EqC method (□). Both datasets are in good agreement with each other. The standard deviation in the EqC data is very small, which is expected due to the number of samples taken (15 at each temperature) and the long time allowed for equilibration. In the TV data the standard deviation is somewhat larger, especially at higher temperatures. This larger deviation may be due to the dynamic nature of the measurements and to the number of samples that make up the average (3 clear points were determined per concentration). The SA measurements (◆) are in good agreement with the data obtained by the EqC and TV methods. Additionally, previously measured data by Nordström and Rasmuson<sup>17</sup>, using the EqC method are plotted in **Figure 2.3** (●). Our measurements fit well with these data.

### Heating rate in the TV method

For any solubility measurement using the dynamic techniques (TV and SA), it is mainly important that the rates of change are small enough for the dissolution to keep up with the change. Therefore, with both methods a sensitivity analysis is performed for the pHBA in acetic acid system, where the rates of change are plotted versus the recorded clear points.

Clear point temperatures were measured for pHBA in acetic acid using the TV method. **Figure 2.4(a)** shows the measured clear point as a function of the heating rate ( $R_h$ ). For a concentration of  $c_{HBA} = 136.2$  mg/mL six clear point temperatures were measured, averaging at  $T^c = 39.9^\circ\text{C}$  with a standard deviation of  $0.3^\circ\text{C}$ . It is observed that higher heating rates yield higher clear point temperatures, thus lower apparent solubilities. This is mainly related to the interplay between the overall crystal dissolution rate and the applied heating rate, because the rate of change in the solubility depends on the heating rate. If the heating rate is too high, the dissolution of the crystals is not fast enough to keep up with the increasing solubility, the crystals will ultimately dissolve at a higher temperature. In those cases, a clear point temperature will be measured that is higher than the actual saturation temperature.

Upon decreasing  $R_h$ , the clear point would approach the saturation temperature, as seen in **Figure 2.4(a)**. If the heating rate is sufficiently low the crystals have sufficient time to dissolve and the solution approaches thermodynamic equilibrium at each temperature. Ideally a heating rate close to  $R_h = 0^\circ\text{C}/\text{min}$  would lead to clear point temperatures that are equal to the saturation temperature. A linear extrapolation for the sample with an overall concentration of 136.2 mg/mL leads to a saturation temperature of  $T^* = 38.5 \pm 0.4^\circ\text{C}$  (**Figure 2.4(a)**). Using a heating rate of  $R_h = 0.5^\circ\text{C}/\text{min}$  the measured

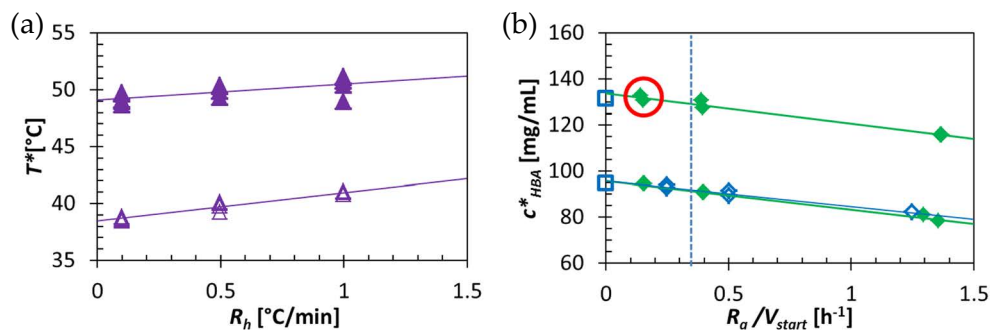


**Figure 2.4:** (a) Influence of heating rate ( $R_h$ ) on clear point temperatures ( $T^*$ ) of pHBA in acetic acid during TV measurements using 2 different concentrations ( $c_{HBA} = 136.2$  mg/mL ( $\Delta$ ) and 161.4 mg/mL ( $\blacktriangle$ )). (b) Influence of addition rate ( $R_a$ ) on clear point concentration of pHBA ( $c^*_{HBA}$ ) in acetic acid during SA measurements at 2 different temperatures ( $T = 20^\circ\text{C}$  and  $40^\circ\text{C}$ ) and at small ( $V_{start} = 2$  mL ( $\blacklozenge$ )) and large scale ( $V_{start} = 40$  mL ( $\diamond$ )). In the right graph our EqC measurements ( $\square$ ) are provided for comparison. For the measurements in the circle an addition rate of 0.3 mL/h was used, the dashed vertical line represents the addition rate of  $R_a = 0.75$  mL/h for a starting volume of 2 mL.

clear point is  $T^c = 39.9^\circ\text{C} \pm 0.3^\circ\text{C}$ ,  $1.4^\circ\text{C}$  higher than the extrapolated saturation temperature. For a sample with an overall concentration of  $161.4 \text{ mg/mL}$  a saturation temperature of  $T^* = 49.1 \pm 0.7^\circ\text{C}$  is extrapolated. Using a  $R_h$  of  $0.5^\circ\text{C}/\text{min}$  the measured clear point is  $T^c = 49.9 \pm 0.4^\circ\text{C}$ ,  $0.8^\circ\text{C}$  higher than the extrapolated saturation temperature. Based on both measurements, we assumed a  $R_h = 0.3^\circ\text{C}/\text{min}$  to provide us with clear point temperatures that fall within  $1.0^\circ\text{C}$  of the actual saturation temperature ( $T^c = 49.7$  and  $39.5^\circ\text{C}$  for the high and low concentrations, respectively). A typical single clear point measurement using this heating rate would take around 1 to 4 hours. Measuring multiple vials simultaneously and including duplo measurements of the same recrystallized samples enables the construction of a solubility line within one day.

#### *Addition rate in the SA method*

Using the SA method clear point concentrations of the same system (pHBA in acetic acid) were measured. The SA method was applied at 2 different temperatures while using solvent addition rates varying from 0.3 to 5.5 mL/h. **Figure 2.4(b)** shows the relation between the addition rate ( $R_a$ ) and the measured clear point concentrations. The clear point concentrations are plotted against the addition rate ( $R_a$ ) divided by the initial volume ( $V_{\text{start}}$ ) to enable the comparison of measurements at different scales. It shows that lower addition rates lead to higher clear point concentrations. Analogous to the trend in the clear point temperature variation with the heating rate, the clear point concentration is determined by a balance between the dissolution rate and the concentration dilution rate, the latter of which depends on the  $R_a$ . In the solvent addition method the Addition Rate ( $R_a$ ) is to some extent the equivalent of the heating rate in the TV method. If the  $R_a$  is too high, the dissolution of the crystals is not fast enough to keep up with the decreasing concentration.

A linear extrapolation for the samples at  $T = 20$  and  $40^\circ\text{C}$  lead to a saturation concentration of  $c_{\text{HBA}}^* = 95.8 \pm 0.6 \text{ mg/mL}$  and  $133.8 \pm 0.9 \text{ mg/mL}$  (**Figure 2.4(b)**). For the equipment, chemicals and 2 mL starting volume, clear point data within 5% of the saturation concentration are obtained at addition rates around  $R_a = 0.75 \text{ mL/h}$  or lower. A typical single clear point measurement using solvent addition, starting with 2 mL to which 4 mL is added, would then take around 2 to 3 hours.

In principle the initial volume should not affect the clear point measured if the appropriate addition rate is used. To test this, SA measurements were performed at  $T = 20^\circ\text{C}$  at a larger scale, in which the starting volume was 40 mL. The corresponding addition rate would then be 15 mL/h. The clear point was determined using FTIR measurements. The peaks at  $1168 \text{ cm}^{-1}$  and at  $1612 \text{ cm}^{-1}$  were used to monitor the concentration changes of the compound in solution. An example of such a measurement is shown in **Figure 2.5**. Upon

addition of acetic acid, in this case with an addition rate of  $R_a = 10$  mL/h, the concentration of pHBA in solution remained constant (saturated), because the dilution was compensated with the dissolution of crystals. After a certain amount was added, the concentration decreased, because all crystals in the suspension were dissolved, which marked the clear point. The precise clear point was determined by the intersection of the slopes. The clear point for this particular measurement was found after addition of 12.5 mL of acetic acid. The concentration of pHBA in the crystallizer is plotted in the same figure and found on the second  $y$ -axis as  $c_{HBA}^* = 0.94$  g/mL.

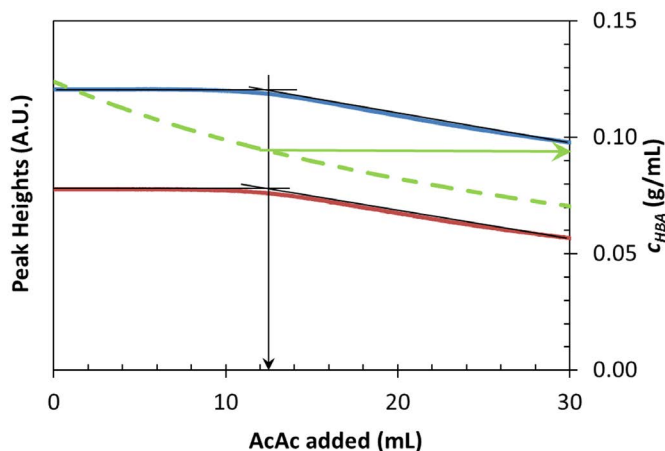


**Figure 2.5:** Trends of IR spectrum peak heights at  $1168\text{ cm}^{-1}$  (blue) and  $1612\text{ cm}^{-1}$  (red) taken during a SA experiment with pHBA in acetic acid at  $20^\circ\text{C}$  with an acetic acid addition rate of  $10\text{ mL/h}$  over a starting volume of  $40\text{ mL}$ . The green dashed data represents the concentration of pHBA in the crystallizer. The clear point in this experiment was determined as  $c_{HBA}^* = 0.940 \pm 0.005\text{ g/mL}$ , after addition of  $12.5\text{ mL} \pm 0.3\text{ mL}$  of acetic acid.

These results, alongside the small scale tests, are shown in **Figure 2.4(b)** and are in good agreement with those of the small scale tests, yielding a clear point at  $R_a/V_{start} = 0\text{ h}^{-1}$  of  $95.9 \pm 0.6\text{ mg/mL}$ . These measurements confirm that similar results are obtained at different scales using different detection techniques with the SA method as long as the same  $R_a/V_{start}$  is used. The method therefore can be used at any scale, as long as the addition rate is chosen accordingly.

#### *Comparing heating and addition rate*

In order to allow the comparison between the TV and SA data in **Figure 2.3**, the rates of change used in both methods should be equivalent at the clear point. For both methods the rate of change can be expressed as the relative dilution rate,  $d(c_i/c_i^*)/dt$  and is assessable at the clear point, i.e. where  $(c_i/c_i^*) = 1$ .

In TV measurements, by changing the temperature, the solubility of the compound ( $c_i^*$ ) is increased in order to completely dissolve the crystals while

the overall composition ( $c_i$ ) remains unchanged. The solubility can be described as an exponential function of the temperature:

$$c_i^*(T) = a \exp(-bT) \quad (2.1)$$

When the composition in the crystallizer does not change, the supersaturation ratio can then be expressed as:

$$\frac{c_i}{c_i^*(T)} = \frac{c_i}{a} \exp(-bT) \quad (2.2)$$

In **eq. 2.1**,  $a$  and  $b$  are fitting parameters. The temperature  $T(t)$  in degrees Celsius is changed over time according to:

$$T = T_0 + R_h t \quad (2.3)$$

Combining **eqs. 2.1** and **2.2** and taking the derivative over time yields the rate of change for TV measurements as a function of the heating rate  $R_h$ :

$$\frac{d(c_i/c_i^*(T))}{dt} = -bR_h (c_i/c_i^*(T)) \quad (2.4)$$

Which shows that the relative dilution rate at  $c/c^* = 1$  is a linear function of the heating rate.

From our experimental data, the fitting parameters were  $a = 70.5$  mg/mL and  $b = 0.0157/^\circ\text{C}$ . Starting at  $T_0 = 20^\circ\text{C}$  with a concentration  $c_i = 131$  mg/mL, the clear point should be reached at  $40^\circ\text{C}$ . Using a heating rate of  $R_h = 0.30^\circ\text{C}/\text{min}$  gives a relative dilution rate of  $d(c_i/c_i^*)/dt = 4.7 \cdot 10^{-3}/\text{min}$ .

In the performed SA measurements, by addition of solvent, the overall concentration of the compound in the vessel ( $c_i$ ) is decreased in order to dissolve the crystals while the solubility remains unchanged. In case of complex multicomponent mixtures where solvent mixtures are added, however, the solubility may change. For the performed SA measurements the supersaturation ratio is expressed via the change in concentration  $c_i(t)$  over time due to the changing volume  $V(t)$  of solvent:

$$\frac{c_i}{c_i^*} = \frac{c_{i,0}}{c_i^*} \cdot \frac{V_0}{V(t)} \quad (2.5)$$

In which  $c_{i,0}$  is the initial concentration of compound in the vial and  $V_0$  is the initial volume of solvent. The volume of solvent in the vial is expressed as:

$$V(t) = V_0 + R_a t \quad (2.6)$$

Substituting eq. 2.5 into 2.4 and taking the derivative over time yields the rate of change for SA measurements:

$$\frac{d(c_i/c_i^*)}{dt} = - \frac{\left(\frac{c_{i,0}}{c_i^*}\right) V_0 R_a}{(V_0 + R_a t)^2} \quad (2.7)$$

Eq. 2.6 shows that at a constant addition rate, the relative dilution rate decreases with increasing sample volume  $V$ . At a temperature of 40°C, the solubility is  $c_i^* = 131$  mg/mL. With an initial volume of  $V_0 = 2$  mL, an initial overall concentration of  $c_0 = 163$  mg/mL, and an addition rate of  $R_a = 0.3$  mL/h (0.005 mL/min, experiments in red circle in **Figure 2.4(b)**) a relative dilution rate of  $2.0 \cdot 10^{-3}/\text{min}$  is calculated at the clear point. This falls in the same order of magnitude as the rate of change in solubility for the TV measurements, which means that the data can fairly be compared. Since the rate of change in the SA measurements is smaller than in the TV measurements, it is not surprising that the accuracy of the SA data is higher. In this system at 40°C, a similar change in supersaturation ratio can be obtained to that of the TV measurement if an addition rate of  $R_a = 0.75$  mL/h (dashed blue line in **Figure 2.4(b)**) is used. The rate of change in supersaturation ratio in that case is  $d(c_i/c_i^*)/dt = 5.0 \cdot 10^{-3}/\text{min}$  at the clear point concentration.

### 2.3.2. The SA method in more complex mixtures

The TV method is the fastest method for obtaining solubility data of pure components in single solvents. However, when multicomponent mixtures are investigated and a phase diagram at a single, fixed temperature is required, the TV method loses its advantages over the SA method. We measured the solubility of crystalline compounds in multicomponent mixtures containing multiple solvents (anti-solvent crystallization) and multiple solutes (co-crystallization).

#### *Phase diagram for anti-solvent crystallization*

Asparagine (Asn) is one of the most common amino acids and appears as a white crystalline solid. It dissolves well in water, but not in alcohols. Therefore, anti-solvent crystallization can be performed with this compound. The phase diagram at  $T = 20^\circ\text{C}$  of DL-Asn in water with ethanol as anti-solvent is determined by the SA method and presented in **Figure 2.6**, where the solubility of DL-Asn in the solvent mixture (green data) is plotted against the solute excluded mass fraction of ethanol,  $x_E$ . The red arrow in **Figure 2.6** demonstrates the measurement method. For the solubility of Asn in the solvent – anti-solvent system water - ethanol, the starting point was chosen such that the mass fraction of Asn in an ethanol-water mixture of low ethanol concentration was approximately equal to the solubility in pure water. The mass fraction of Asn

corresponding to the solubility measured in this measurement was used as a starting point for a measurement with a higher ethanol starting concentration.

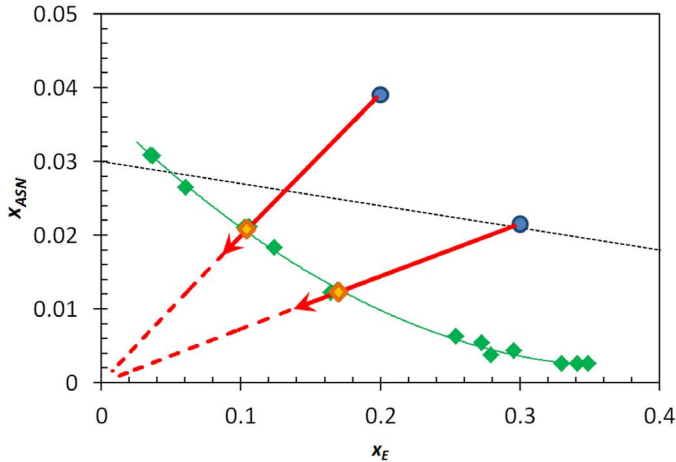


**Figure 2.6:** Solubility of anhydrous DL-Asn in the solvent – anti-solvent system water – ethanol. The measured mass fraction  $x_{ASN}$  of DL-Asn at 20°C is plotted versus the mass fraction  $x_E$  of ethanol on solute free basis. The red arrows indicate the overall composition during the measurement of the clear points (♦) starting at an overall composition in the blue points. The black dashed line represents the addition of pure ethanol to a solution of DL-Asn in water during an anti-solvent crystallization experiment.

If necessary, extra points were added in between compositions of previous measurements. Starting at an overall suspension composition corresponding to the blue point, pure water was added using an addition rate  $R_{a,V} = 1$  mL/h to a 2 mL starting volume. This addition rate is slightly larger than the addition rate applied for the pHBA – acetic acid system in **Figure 2.3**. However, it was found experimentally, using the method displayed in **Figure 2.4** that 1 mL/h was a sufficiently low addition rate. The overall composition then follows the red line towards the origin of the graph. The orange diamond at the point (0.12; 18.6) corresponds to the clear point. The larger spread in data points around an ethanol mass fraction of 0.3 is most likely because in some points the starting suspension was chosen rather close to the solubility line, which slightly decreases the accuracy since interval between the suspension pictures was not decreased.

Additionally, an example is given of the dilution path during an anti-solvent crystallization process that starts with an initial solution with a DL-Asn mass fraction of 0.30 in water, to which pure ethanol is added (black dashed line in **Figure 2.6**). This phase diagram allows for the tracking of supersaturation during anti-solvent crystallization processes and is a valuable tool in determining the optimal amount of ethanol to add to a starting solution in order to achieve a high yield while keeping the added anti-solvent at a minimum. Since DL-Asn forms a monohydrate in water and crystallizes in anhydrous form from ethanol, the crystals in suspensions at 20°C were analysed

by XRPD. Already at ethanol fractions as low as  $x_E = 0.03$  the anhydrous form was the predominant crystal form.

### *Co-crystal Phase Diagram*

Carbamazepine (CBZ) is a drug that suffers from limited bioavailability due to its dissolution behaviour. One of the solutions for this problem is the formation of co-crystals<sup>20</sup>. Isonicotinamide (INA) is a suitable conformer for CBZ<sup>21</sup>. For the reliable crystallization of co-crystals it is important that the composition in the crystallizer lies in the co-crystal region of the phase diagram<sup>18</sup>. A simplified version of the phase diagram of this CBZ-INA co-crystal system in ethanol at  $T = 25^\circ\text{C}$  was determined by ter Horst and Cains<sup>21</sup>. This phase diagram was constructed by fitting the data from TV measurements at different temperatures ( $\blacktriangle$  in **Figure 2.7**) with the Van 't Hoff equation for co-crystals:

$$\ln(x_a x_b) = -\frac{\Delta H}{R} \left( \frac{1}{T} - \frac{1}{T_0} \right) \quad (2.8)$$

Extrapolation of the data to  $T = 20^\circ\text{C}$  leads to a solubility product ( $x_a x_b$ ) =  $37.1 \cdot 10^{-6}$  (the point  $\Delta$  in **Figure 2.7**), which in the ideal case is constant at constant temperature (purple dashed curve). In this method it is assumed that the solutes do not influence each other's pure solubilities in the pure component regions. This means that straight lines, perpendicular to each axis represent the pure component solubilities of INA and CBZ. The pure component solubilities at  $T = 20^\circ\text{C}$  are the result of the extrapolation of the pure component solubility lines determined by the TV method. However, ter Horst et al.<sup>18</sup> also found that the system does not show ideal behaviour in the pure component regions, i.e. the solutes do influence each other's solubility in the pure component region of the phase diagram.

The co-crystal phase diagram was also determined using the SA method. The red arrows in the figure show the measuring protocol used for obtaining the data in the co-crystal region. The method starts by creating a suspension of the co-crystals in solvent by making a starting sample composition of both compounds at their pure component solubility (at  $20^\circ\text{C}$   $x_{INA}^* = 0.028$  and  $x_{CBZ}^* = 0.0045$ , blue point 1) in 2 mL solvent. The pure crystalline forms dissolved, while co-crystallization occurred from this solution, since this composition is located in the co-crystal region and is supersaturated there<sup>18</sup>. With this suspension, solvent addition using pure solvent was started with an addition rate of 0.5 mL/h. However, the suspension was rather dense which resulted in a required added volume for complete dissolution that exceeded the volume of the crystallizer. A new starting mixture of 2 mL was created (blue point 2) having the same composition as the final composition of the previous experiment. This point 2 was the starting point for other clear point measurements, by adding not pure solvent but an undersaturated solution

of one of the pure compounds. In this way, such phase diagrams can be constructed without prior knowledge about their shape.

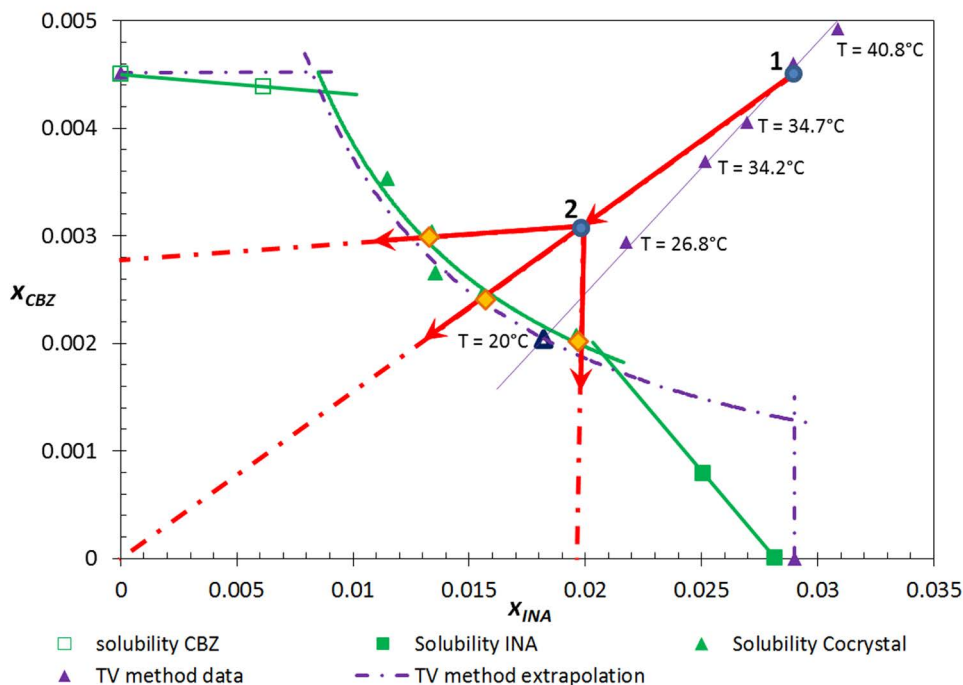


**Figure 2.7:** Phase diagram of the INA-CBZ co-crystal in ethanol. The purple triangles are TV data, the purple dotted lines represent the phase diagram constructed at  $T = 20^\circ\text{C}$  based on the extrapolation from the TV measurements. The green markers represent SA measurements at  $T = 20^\circ\text{C}$ . The blue dots are starting points in the SA methodology, the red arrows depict examples of the dilution path in a number of clear point measurements (♦) measured by the SA method.

The green markers in **Figure 2.7** represent the measurements with the SA method at  $T = 20^\circ\text{C}$ . The co-crystal solubility as well as the pure component solubilities are determined using this method. The data points in the co-crystal region have approximately the same solubility products ( $(x_a x_b) = 39 \cdot 10^{-6} \pm 10^{-6}$ ). The solubility products of the data points in the pure component regions deviate significantly from this value.

In **Figure 2.7**, it can be seen that the TV data and the SA data agree well in the co-crystal region. The results from the methods do deviate significantly in the pure component regions. While the solubility of CBZ is only slightly affected by the presence of INA in the solution, the solubility of INA decreases significantly in the presence of relatively small concentrations of CBZ. To account for these influences with the TV method many measurements are required.<sup>10</sup> The SA method is thus suitable for investigating non-ideal behaviour in multi-component systems.

## 2.4. Discussion

Next to the already accepted methods for determining solubility lines, our SA method proves to be a potential technique. Although our SA method needs as many experiments as the EqC method and is therefore not as efficient as the TV method, the measurements are less laborious and time consuming than the EqC method, with the additional advantage that they can be automated. A crucial point for both the TV and the SA method is the determination of the clear point. In this paper the determination of the clear points was done by turbidity measurements, video images and FTIR concentration measurements for 1 mL, 6 mL and 100 mL samples, respectively. The detection limit for each technique is different and can therefore significantly influence the accuracy of the measurements. For example, turbidity measurements are less accurate at larger sample volumes, making other detection techniques preferable.

One of the challenges in using the SA method, similar to the TV method, is determining the starting composition in the measurement. For systems where no literature data is available, the first starting point must be determined by making a fast estimate of the solubility using a SA measurement with high  $R_{cr}$ , as described in the experimental section. This initial estimate takes up to 30 minutes, including the equilibration time of the suspension prior to the measurement.

The strongest point of the SA method lies in its application in (complex) multi-component mixtures, in which the composition at any 2-phase to 1-phase transition point at a constant temperature can be determined. Additionally, if the solubility is slightly impacted by temperature changes, for instance in salt or protein systems, the SA method can be preferred as well.

**Figure 2.8** displays the schematic quaternary phase diagram of a hypothetical system containing 2 solutes (A and B) and two solvents (S and AS), in which A and B can co-crystallize and AS is an anti-solvent for all solid phases. The pyramid shows the pure components A, B, S and AS at each corner point. The green areas in **Figure 2.8** mark the co-crystal region, the lilac areas mark the regions where the pure components A or B crystallize, the blue areas mark a clear solution and the white areas mark the regions where the co-crystal is present together with either A or B. In the upper left part of **Figure 2.8** the sides of the pyramid are unfolded to show each ternary phase diagram out of which the quaternary phase diagram is built up. This is a hypothetical example of a complex multi-component system where SA is ideally suited to provide information about both the solubility of the solid phases A, B and AB in the solvent mixture (e.g. in a system where A and B are enantiomers). The SA method can be used to determine the phase transitions marked red inside the pyramid. An example of a proposed measurement is given in **Figure 2.8** from the blue dot to pure S. Additionally, a projection of

this measurement is plotted as a red dashed arrow on each face of the fold out. The blue dot is an example of where the solvent addition measurement can be started. The red arrow depicts the solvent addition pathway, where pure solvent is added to the suspension in the co-crystal region but other compositions can be added as well. The orange diamond represents the clear point. The dotted line on the base of the pyramid is a projection of the dilution pathway and meant as a guideline.

The SA method, similar to the TV method, results in an equilibrium composition at a certain temperature. However, in the case of polymorphs, co-crystals or other systems, it is unclear which equilibrium is measured without the use of an additional analysis tool. Especially in the neighborhood of a triphasic domain, the equilibrium composition related to a metastable rather than the stable phase could be determined, for instance due to a smaller dissolution rate of the metastable phase. In the case of Asn, there is a region

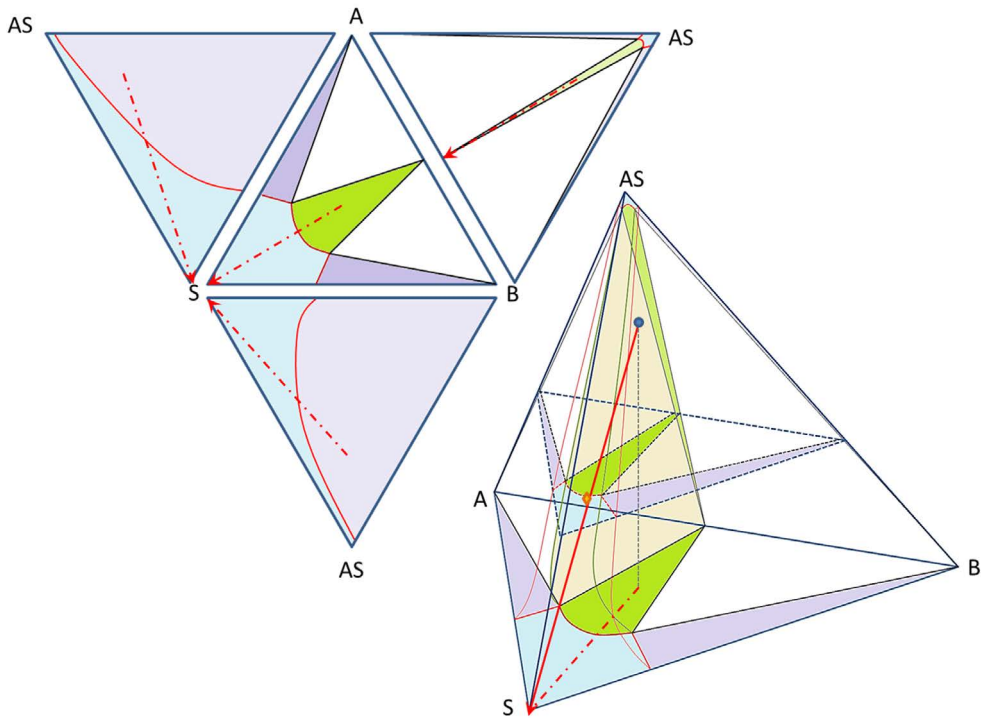


**Figure 2.8:** Quaternary phase diagram of a co-crystallization system in solvent (S) – anti-solvent (AS) mixtures with ternary phase diagrams colored at two different anti-solvent concentrations. Upper left: The phase diagram is unfolded into all ternary phase diagrams. Lower right: The quaternary phase diagram is depicted as a pyramid with the pure components (A, B, S and AS) at its corners. The green areas mark the co-crystal region, the lilac areas mark the regions where the pure components A or B crystallize, the blue areas mark a clear solution and the white areas mark the regions where the co-crystal is present together with either A or B. The red arrow depicts a possible solvent addition pathway, where pure solvent is added to a suspension in the co-crystal region.

in the phase diagram where the hydrate is the stable form and a region where the hydrate and anhydrous form coexist. Care was taken that only the solubility of the anhydrous Asn was measured. This was confirmed by taking XRPD measurements of crystals crystallized under conditions similar (same temperature, same solvent composition, slightly higher solid content) to those during the SA measurements .

Transitions from triphasic to biphasic domains and reversibly can only be followed with the SA method if a detection technique is used that enables identification between the different solid phases. In a triphasic domain with 2 crystalline phases the composition in solution would be in the polysaturated solution point. Addition of solvent would only change the composition in solution when one of the crystalline phases has disappeared (when going from triphasic to biphasic domains). This change can be detected by spectroscopic techniques. IR and Raman spectroscopy can also be used to determine the contents of the solid phases present until dissolution, which would be beneficial if the solid form exhibits polymorphism. In such case the dissolving polymorph can be identified. In systems where the SMT process is fast<sup>2,22</sup>, the transformation can be followed prior to dissolution. In slower systems<sup>23</sup>, the solubility of the metastable polymorph could be measured. Especially when the disappearing phase can be identified, the SA method is an important addition to the currently used methods for determining phase diagrams of complex multicomponent systems.

## 2.5. Conclusion

We found that the solvent addition method produces reliable solubility results for the organic compound p-hydroxybenzoic acid in the solvent acetic acid. The effect of changing the addition rate in solvent addition measurements follows a similar trend to the effect of changing the heating rate in the temperature variation method. Using low enough heating and addition rates, solubility data have been obtained that agree well with the more laborious suspension equilibrium method. The use of the SA method seems especially valuable in the case of solvent mixtures and other multi-component systems, e.g. with multiple solvents or solutes, in which the TV method cannot be applied easily. It was shown that the SA method works well for determining a co-crystal phase diagram as well as a solvent mixture phase diagram for anti-solvent crystallization. The SA measurements for the co-crystal system showed that the pure component solubilities are strongly influenced by the presence of the other component while that of the co-crystal is not. The SA method is therefore a suitable technique to investigate non-idealities in certain multi-component systems.

## 2.6. References

1. Mullin, J. W., *Crystallization*. 3 ed.; Butterworth-Heinemann Ltd.: Oxford, 1993.
2. Dufour, F.; Stichel, B.; Grayson, J. I., Control of Crystal Modification and Crystal Shape by Control of Solid-Solid Transitions during Crystallization and Drying: Two Industrial Case Studies. *Organic Process Research & Development* **2013**, 17, 568-577.
3. Haas, C.; Drenth, J., Understanding protein crystallization on the basis of the phase diagram. *Journal of Crystal Growth* **1999**, 196, 388-394.
4. Chiarella, R. A.; Davey, R. J.; Peterson, M. L., Making Co-Crystals The Utility of Ternary Phase Diagrams. *Crystal Growth & Design* **2007**, 7, 1223-1226.
5. Crocker, L. S.; Ge, Z.; Abraham, A.; Hartman, R.; Xu, J., An Etoricoxib Phase Diagram: Hemihydrate and Anhydrate. *Organic Process Research & Development* **2003**, 7, 958-961.
6. Veessler, S.; Revalor, E.; Bottini, O.; Hoff, C., Crystallization in the Presence of a Liquid-Liquid Phase Separation. *Organic Process Research & Development* **2006**, 10, 841-845.
7. Myerson, A., *Handbook of Industrial Crystallization*. Butterworth Heine-  
mann **2001**.
8. Koutsoukos, P. G.; Kofina, A. N.; Kenellopoulou, D. G., Solubility of salts in water: Key issue for crystal growth and dissolution processes. *Pure Appl. Chem.* **2007**, 79, 825-850.
9. Hermanto, M. W.; He, G.; Tjahjono, M.; Chow, P. S.; Tan, R. B. H.; Garland, M., Calibration of dielectric constant measurements to improve the detection of cloud and clear points in solution crystallization. *Chemical Engineering Research and Design* **2011**, 89, 2613-2619.
10. Vellema, J.; Hunfeld, N. G. M.; Van den Akker, H. E. A.; ter Horst, J. H., Avoiding crystallization of lorazepam during infusion. *European Journal of Pharmaceutical Sciences* **2011**, 44, 621-626.
11. Srisanga, S.; ter Horst, J. H., Racemic Compound, Conglomerate, or Solid Solution: Phase Diagram Screening of Chiral Compounds. *Crystal Growth & Design* **2010**, 10, 1808-1812.
12. Mullin, J. W.; Sipek, M., Solubility and density isotherms for potassium aluminum sulfate-water-alcohol systems. *Journal of Chemical & Engineering Data* **1981**, 26, 164-165.
13. Marchand, P.; Lefebvre, L.; Perez, G.; Counioux, J. J.; Coquerel, G., Theoretical and Experimental Interpretation of the Signals From ITA. *Journal of Thermal Analysis and Calorimetry* **2002**, 68, 37-47.
14. Marchand, P.; Lefebvre, L. c.; Querniard, F.; Cardinaël, P.; Perez, G.; Counioux, J.-J.; Coquerel, G., Diastereomeric resolution rationalized by

phase diagrams under the actual conditions of the experimental process. *Tetrahedron: Asymmetry* **2004**, 15, 2455-2465.

15. Labarthe, E.; Bougrine, A. J.; Delalu, H.; Berthet, J.; Counioux, J. J., Equilibrium study between condensed phases by isoplethic thermal analysis when a miscibility gap is observed. *Journal of Thermal Analysis and Calorimetry* **2009**, 95, 135-139.

16. Berthet, J.; Tenu, R.; Counioux, J. J., Construction d'un conductimetre adapte a la determination des diagrammes d'equilibre solide-liquide. Application a l'etude de l'isotherme 65°C du systeme  $H_2O-NaCl-CaCl_2-SrCl_2$ . *Thermochimica Acta* **1983**, 68, 145-154.

17. Nordström, F. L.; Rasmuson, Å. C., Phase equilibria and thermodynamics of p-hydroxybenzoic acid. *Journal of Pharmaceutical Sciences* **2006**, 95, 748-760.

18. ter Horst, J. H.; Deij, M. A.; Cains, P. W., Discovering New Co-Crystals. *Crystal Growth & Design* **2009**, 9, 1531-1537.

19. Muller, F. L.; Fielding, M.; Black, S., A Practical Approach for Using Solubility to Design Cooling Crystallisations. *Organic Process Research & Development* **2009**, 13, 1315-1321.

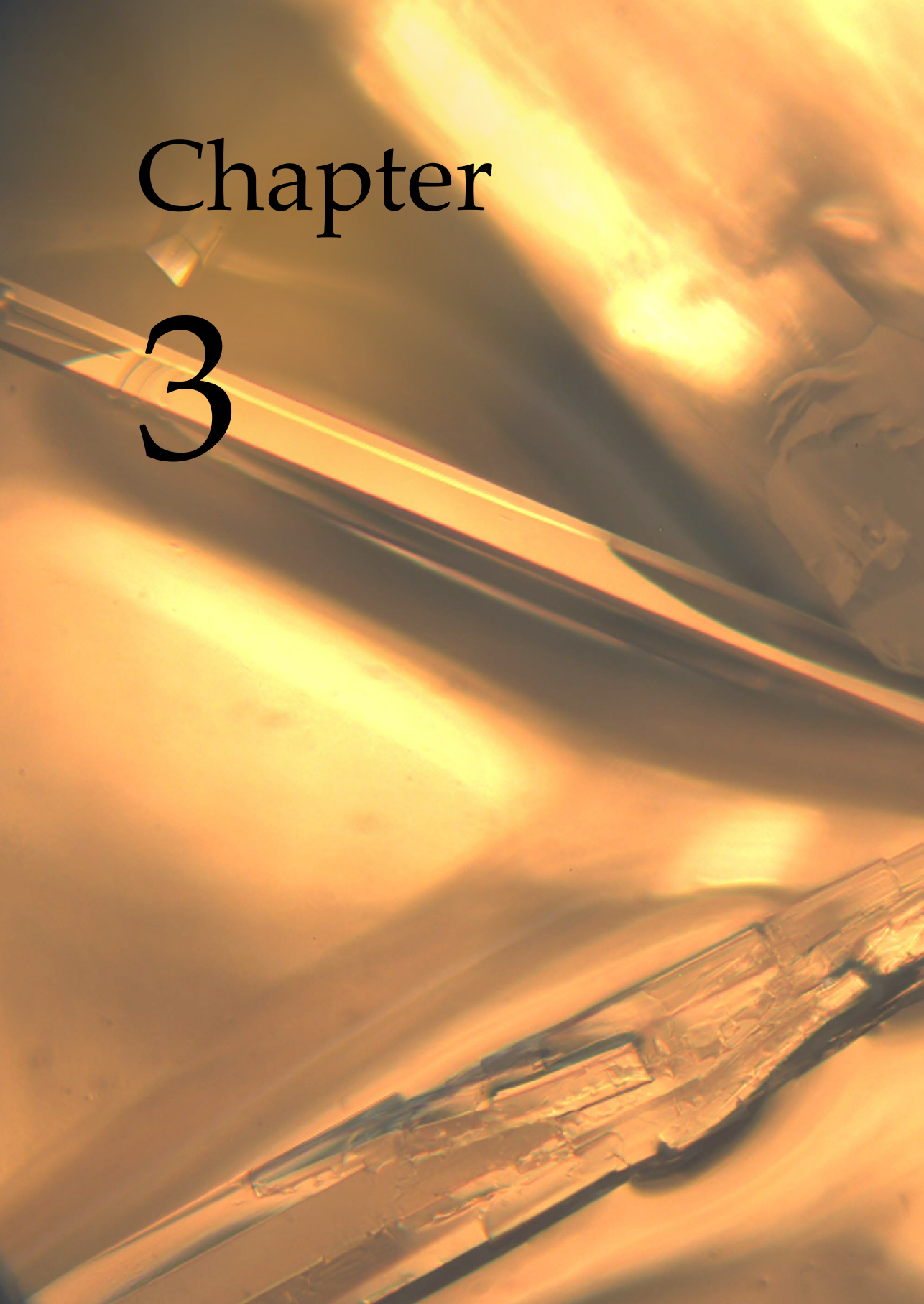
20. Good, D. J.; Rodríguez-Hornedo, N., Solubility Advantage of Pharmaceutical Cocrystals. *Crystal Growth & Design* **2009**, 9, 2252-2264.

21. ter Horst, J. H.; Cains, P. W., Co-Crystal Polymorphs from a Solvent-Mediated Transformation. *Crystal Growth & Design* **2008**, 8, 2537-2542.

22. Hao, H.; Barrett, M.; Hu, Y.; Su, W.; Ferguson, S.; Wood, B.; Glennon, B., The Use of in Situ Tools To Monitor the Enantiotropic Transformation of p-Aminobenzoic Acid Polymorphs. *Organic Process Research & Development* **2012**, 16, 35-41.

23. Wang, G.; Ma, Y.; Wang, Y.; Hao, H.; Jiang, Y., Investigation of Solution-Mediated Phase Transformation of Cefuroxime Acid to Its Acetonitrile Solvate. *Organic Process Research & Development* **2015**.





Chapter

3



Understanding solvate  
formation in mixed  
solvents

**Abstract**

Control over solvate formation can be achieved by the use of solvent mixtures. Knowledge of the phase diagrams of such multicomponent mixtures is of vital importance for such control. Ternary phase diagrams of p-hydroxybenzoic acid in binary solvent mixtures of water, acetone and acetic acid were determined at constant temperature, using the solvent addition method. Changes in solubility trends in these systems often indicated the emergence of a different solvated state of the crystal, e.g. a hydrate. The solubility data, along with slurry measurements, were used to construct a quaternary phase diagram of p-hydroxybenzoic acid in the ternary solvent mixture.

### 3.1. Introduction

Pharmaceutical compounds can occur in various solid forms, such as crystalline forms of the pure compound and solvates, in which solvent molecules are incorporated into the crystal lattice as regular building blocks<sup>1</sup>. Product properties (e.g. stability, bioavailability, shelf life) can differ significantly between these solid states. For example, the solubility in water of theophylline hydrate is much smaller than that of the anhydrous form<sup>2</sup>. Therefore, a specific form with the desired properties is chosen for industrial production.

Control over the formation of these different solid forms is of vital importance, and can be achieved by optimizing the crystallization process in a specific solvent, known to produce the desired solid form<sup>1, 3, 4</sup>. However, in some cases the solvent cannot be chosen; for example when the solvent is part of the reaction mixture during compound synthesis. In such cases control of the formation of the desired solid form can be achieved by adjusting the solvent activity<sup>5, 6</sup>.

The objective of this work is to control the crystallization of specific solvated states of organic compounds by the adjustment of the solvent activity, which is achieved by addition of a co-solvent. We used p-hydroxybenzoic acid (pHBA) as model compound (see **Figure 3.1**), which has various crystal forms, including a hydrate, an anhydrous and various solvated forms.

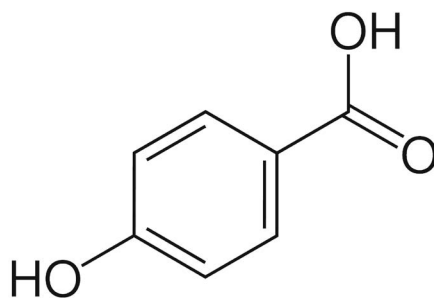


**Figure 3.1:** Molecular structure of p-hydroxybenzoic acid

First, the solubility of the compound in the pure solvents is determined using the temperature variation (TV) method described in **Chapter 2.2**<sup>7</sup>. Then the solubility of pHBA in various mixtures of these solvents at 20°C are determined by the solvent addition (SA) method described in **Chapter 2.2**<sup>7</sup>, along with the solvated state at each solubility point. These ternary phase diagrams are then combined to estimate a quaternary phase diagram of pHBA in mixtures of three solvents.

## 3.2. Materials and Methods

### 3.2.1. Materials

p-Hydroxybenzoic acid ( $\geq 99\%$ ), glacial acetic acid, and acetone (100%) were purchased from Sigma Aldrich and used without further purification. Demi water was taken from a Millipore MilliQ system and had a resistivity of approximately 18 M $\Omega$ ·cm.

### 3.2.2. Methods

#### *Solubility*

The temperature dependent solubility was determined using the temperature variation method as in **Chapter 2.2**<sup>7</sup>, with heating and cooling rates of 0.3°C/min.

The solubility at constant temperature in the ternary phase diagrams was determined using the solvent addition method as in **Chapter 2.2**<sup>7</sup>, with an addition rate of 0.5 mL/h. The phase diagrams with multiple solvents were scanned, starting from the saturation concentration in the pure solvents at a specific temperature. More anhydrous solute was added to create a suspension and subsequently, the other solvent was added to that. From the found clear point concentration ( $\bullet$  in **Figure 3.2(a)**), the same actions were repeated, until either no more clear points were found, or the data sets met. A schematic of this tactic is given in **Figure 3.2(a)**. In **Figure 3.2(b)** two examples are given of concentration profiles in the crystallizer during a measurement in water-acetone mixtures; one starting from a suspension of pHBA in pure

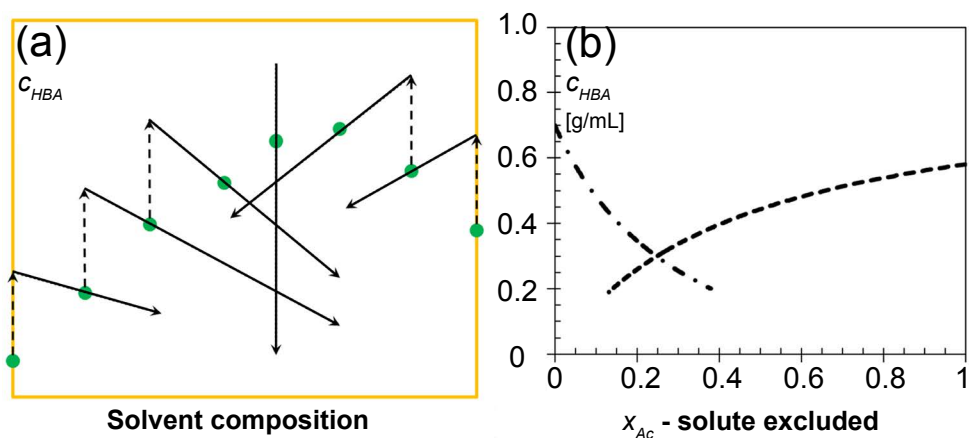


**Figure 3.2:** (a) Tactics for scanning a ternary phase diagram at constant temperature using the SA method. The solid arrows represent the solvent addition path. (b) Examples of actual solvent addition paths of pHBA in water-acetone mixtures, starting at suspensions prepared in the pure solvents.

water (- · -), the other from a suspension of pHBA in pure acetone (- - -). Although the addition paths in **Figure 3.2(a)** are indicated as straight lines, due to the different molar masses of the solvents the addition paths are curves, as demonstrated in **Figure 3.2(b)**. Due to the curved nature of the addition profile, it is possible that no clear point is encountered when the measurement is performed close to the maximum saturation concentration. Additional points in the phase diagram can be obtained by preparing a suspension in a solvent mixture with the desired composition and subsequently adding the same solvent mixture to this suspension.

### *Slurry measurements*

A Crystal16 multiple reactor system of Avantium Technologies was programmed to stabilize the temperature at 20°C for 16 samples of 1 mL containing a specific amount of pHBA solvent mixtures. After 2 days of equilibration, the samples were analyzed for crystal structures.

### 3.2.3. Analysis

To determine which crystal form dissolved during the SA experiments, new samples were created with a higher concentration of pHBA than its measured solubility in a certain solvent mixture. After recrystallization and equilibration at a specific temperature, the suspension was filtered. A Leica Nikon Optiphot 200 microscope was used to visualize the shape of the resulting crystals. XRPD was used for crystal structure analysis. The measurements were performed with a Bruker-AXS D2-Phaser diffractometer, equipped with a Lynxeye detector. The pattern scan was made in the range  $5 \leq 2\theta \leq 50^\circ$ , using a step size of  $0.02^\circ\theta$ . The radiation is  $\text{CuK}\alpha 1$  (0.15406 nm).

## 3.3. Results and discussion

### 3.3.1. Solubility in and crystallization from single solvents

For pHBA, among others a monohydrate, two anhydrous forms and an acetone solvate (pHBA:Ac 2:1) have been reported<sup>8,9</sup>. The hydrate is estimat-

**Table 3.1:** pHBA forms found after recrystallization from various solvents at  $T = 20^\circ\text{C}$ , with their enthalpy of fusion, melting and transition temperature.

| Solvent     | pHBA<br>crystal form | Symbol                | $\Delta_{fus}H$<br>[J/mol] <sup>7,10</sup> | $T_m$<br>[K] | $T_t$<br>[K] <sup>8</sup> |
|-------------|----------------------|-----------------------|--|--------------|---------------------------|
| Water       | Hydrate              | pHBA·H <sub>2</sub> O | $16 \cdot 10^3$                            | 485          | 340                       |
| Acetone     | Hemi-solvate         | pHBA·0.5Ac            | $27 \cdot 10^3$                            | 468          | 323                       |
| Acetic acid | Anhydrous-I          | pHBA                  | $28 \cdot 10^3$                            | 488          | -                         |

ed to be stable up to 67°C in water, the acetone solvate up to 50°C in acetone<sup>9</sup>. In our experiments at  $T = 20^\circ\text{C}$ , pHBA crystallized from water as the monohydrate (pHBA·H<sub>2</sub>O), from acetone as a hemi-solvate (pHBA·0.5Ac) and from acetic acid the anhydrous form, see **Table 3.1**. Additionally, the enthalpy of fusion  $\Delta_{fus}H$ , melting temperature  $T_m$  and transition temperature to the anhydrous form  $T_t$  are given. The crystals are shown in **Figure 3.3**.

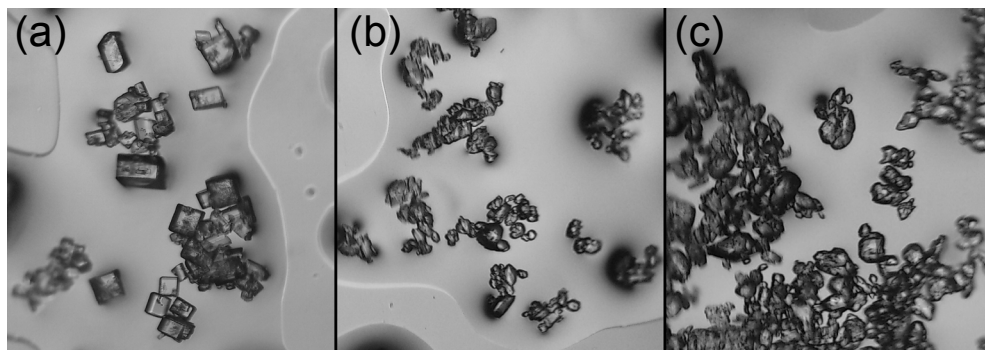


**Figure 3.3:** Various crystal forms of pHBA. (a) The hydrate recrystallized from water, (b) The acetone hemi-solvate recrystallized from acetone, (c) The anhydrous form recrystallized from acetic acid.

The solubility of pHBA was determined in three pure solvents (water (W), acetic acid (AA) and acetone (Ac)). At  $T = 20^\circ\text{C}$ , the solubility of the anhydrous form in pure AA is 0.096 g/mL, the solubility of the hemi-solvate in pure Ac is 0.31 g/mL and the solubility of the monohydrate in W is 0.0044 g/mL. For all systems no indications for a crystal phase change were observed in the temperature range of 10 - 50°C. The van 't Hoff plot is shown in **Figure 3.4**, derived from the solubility data via:

$$\ln(x) = -\frac{\Delta H}{R} \left( \frac{1}{T} - \frac{1}{T_0} \right) \quad (3.1)$$

Additionally, the ideal solubility of the anhydrate is given in the same figure. The heat of fusion and the melting temperature of the hemi-solvate ( $\Delta_{fus}H_{solv} = 27 \cdot 10^3$  J/mol,  $T_{m,solv} = 468$  K<sup>8</sup>) do not differ much from those of the anhydrous form ( $\Delta_{fus}H_{anh} = 28 \cdot 10^3$  J/mol,  $T_{m,anh} = 488$  K<sup>8</sup>), which means that the ideal solubility line of the hemi-solvate is similar to that of the anhydrous form. The ideal solubility of the monohydrate, however, is higher due to its low heat of fusion ( $\Delta_{fus}H_{hyd} = 16 \cdot 10^3$  J/mol,  $T_{m,hyd} = 485$  K<sup>10</sup>).

The measured solubility of pHBA·H<sub>2</sub>O in water is much smaller than ideal, which indicates that the hydrate is very stable in water. This is attributed to the strong intermolecular bonding in the crystal, resulting from the hydrogen bonding of the water with multiple pHBA molecules<sup>8,9</sup>. On the contrary,

the measured solubilities of pHBA in acetic acid and of pHBA·0.5Ac acetone are higher than the ideal solubility. This points to weaker intermolecular bonding, especially in the case of the acetone solvate, which was shown by Nordström et al.<sup>8</sup>. By comparing the measured solubility of the solid states of pHBA in their pure solvents to their ideal solubility, it appears that the extent of hydrogen bonding between the molecules in the crystal largely determines the stability of the compound. However, the solvent in which the crystals are immersed also has an influence on their stability. The extent to which the solvent has an influence on the stability of the solid states is not clear from these data, but can be investigated by changing the solvent composition.

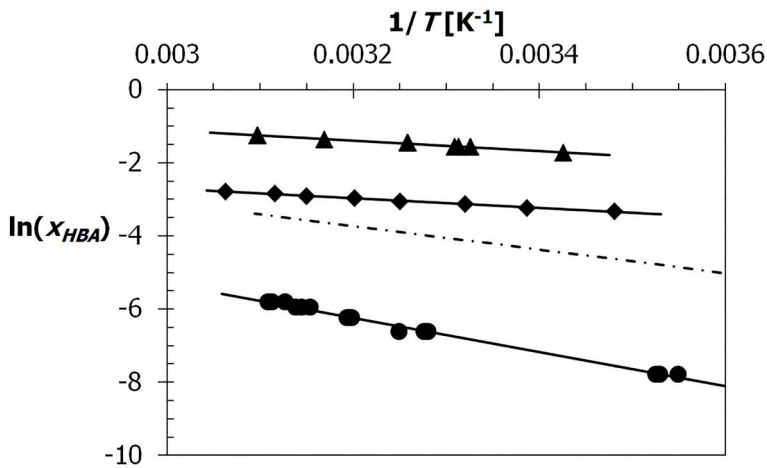


**Figure 3.4:** van't Hoff plot anhydrous pHBA in pure solvents, determined using the TV method. The solvents used are acetone (▲), acetic acid (◆) and water (●). The ideal solubility of pHBA calculated with the van't Hoff equation (— · —) is given.

### 3.3.2. Binary solvent mixtures

In a system with two solvents and a solute, the temperature dependent solubility can be represented in a prism, formed by the composition of the ternary system on the horizontal plane and the temperature on the perpendicular axis. In **Figure 3.5** a schematic of such a phase diagram is given. On the two solute-solvent temperature planes, the temperature dependent solubility of the solute in each pure solvent is given (····). Such solubility curves were determined in **Section 3.3.1**. The blue area represents the ternary phase diagram of the solute in the solvent mixtures at a constant temperature, in which the solid lines plot the phase boundaries. In the example, the compound crystallizes as a solvate with solvent 1 and as anhydrous crystals from solvent 2. The red lines in this ternary phase diagram separate the are-

as where solids are present from the area where a clear solution is the stable phase. These lines can be determined using the SA method.

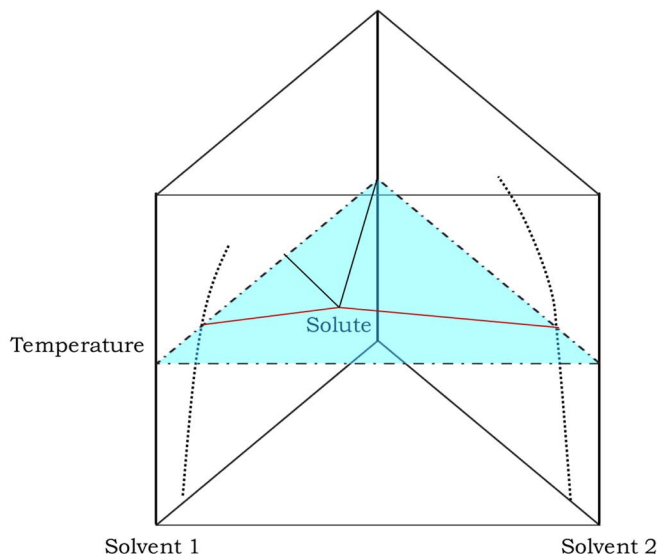


**Figure 3.5:** Schematic of temperature dependent phase diagrams of systems consisting of a solute and two solvents. On the vertical planes, the temperature dependent solubility of the solute in each pure solvent is given (····). The blue area represents the ternary phase diagram of the solute in the solvent mixtures at a constant temperature  $T$ , in which the solid lines indicate the phase boundaries.

The black lines in **Figure 3.5** separate the compositional regions in which different solid states are in equilibrium with the solution. These compositional regions are elaborated in **Figure 3.6**, which shows a ternary phase diagram at constant temperature of a system with a solute (A) and two solvents (S1 and S2), in which the solute forms a solvate with solvent 1 ( $A \cdot S1$ )<sup>11</sup>. The points  $\alpha$  and  $\beta$  represent the solubility of the solute in solvent 1 and 2, respectively. Point  $\gamma$  depicts the stoichiometry of the solvate and point  $\delta$  represents the composition where three phases can coexist at the lowest possible concentration of the solute. In each part of the diagram, the stable phases are depicted. At low concentrations of solute, a clear solution (L) is the stable phase. Upon increasing the concentration of solute, a suspension is formed. At higher concentrations of solvent 1, the solid in the suspension is the solvate ( $A \cdot S1$ ), while at higher concentrations of solvent 2, right of the line  $\delta - \text{Solute}$ , the solid is the anhydrous form (A). At very high concentrations of solute, above the line  $\gamma - \delta$  and left of the line  $\delta - \text{Solute}$ , there is not enough of solvent 1 to form solvate crystals with all the solute molecules. Therefore, a mixture of solvate and anhydrous form will be present there.

If the solubility of compound is very low in a solvent, points  $\alpha$ ,  $\beta$  and  $\delta$  are often located very near to the solvent axis. Hence, it is possible to zoom in on the figure and plot the data in a square instead of triangular diagram, with the solvent composition on the  $x$ -axis. The solvent composition can then be expressed on a solute-free basis.

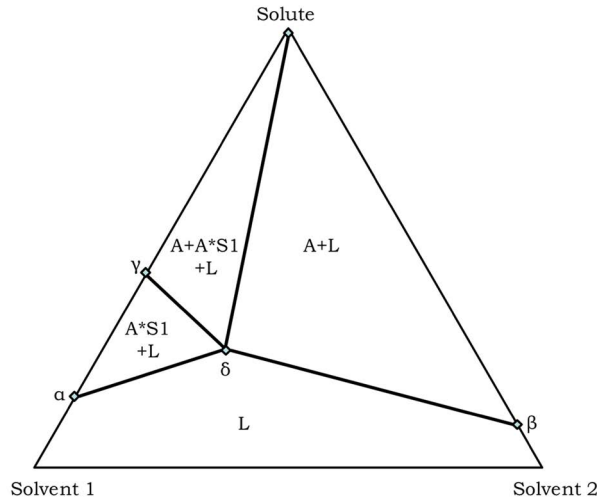


**Figure 3.6:** Ternary phase diagram of a solute with two solvents, in which the solute forms a solvate with solvent 1 (A\*S1). The points  $\alpha$  and  $\beta$  represent the solubility of the solute in solvent 1 and 2, respectively. Point  $\gamma$  depicts the stoichiometry of the solvate and point  $\delta$  represents the composition where three phases can coexist at the lowest possible concentration of the solute.

The solubility of pHBA was determined at 20°C in three different solvent mixtures: Ac – AA, W – AA and W – Ac. From these data, combined with data from XRPD measurements, the three ternary phase diagrams were constructed.

#### *Acetone-acetic acid*

In **Figure 3.7(a)** the solubility of pHBA at 20°C is shown as a function of the solute excluded AA mole fraction  $x_{AA}$  in Ac - AA mixtures. At 20°C, in pure AA the anhydrate is most stable and its solubility is 0.096 g/mL, while in acetone, the hemi-solvate is most stable and its solubility is 0.31 g/mL. Adding small amounts of AA would increase the solubility of the hemi-solvate in the solvent mixture, because the relative stability of the hemi-solvate is smaller in acetic acid. This is attributed to a rise in activity of pHBA in solution as a consequence of the equilibrium<sup>12</sup>. This can be seen in **Figure 3.7**, in which the solubility of pHBA at 20°C is shown as a function of the solute-excluded AA fraction  $x_{AA}$  in Ac - AA mixtures.

Starting from pure AA as a solvent, increasing the Ac fraction increases the solubility of the anhydrate. At an AA mole fraction of around  $x_{AA} = 0.14$  there is a maximum of the pHBA solubility.

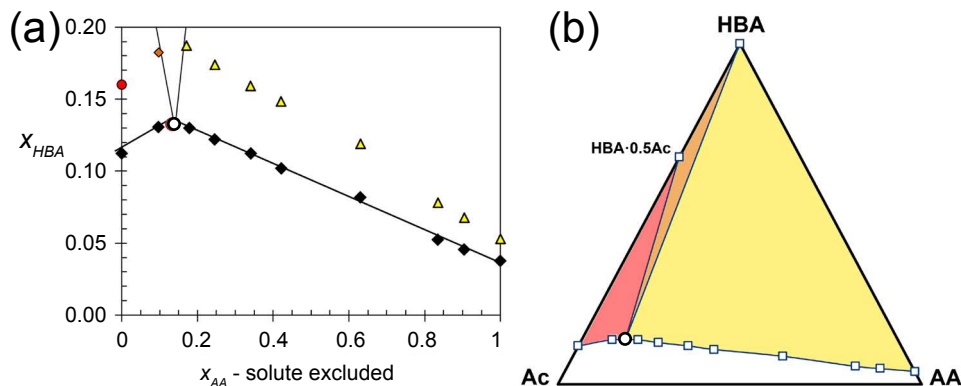


**Figure 3.7:** (a) The solubility of pHBA in Ac-AA mixtures at 20°C, where the mole fraction of acetic acid is given on solute-free basis. The ○ represents the polysaturated point. XRPD data from recrystallized samples in the indicated points identified pHBA·0.5Ac (●) and pHBA (▲) and mixtures thereof (◆). (b) Ternary phase diagram of pHBA in Ac-AA mixtures at 20°C. The colors indicate which solid form was determined using XRPD upon recrystallization in that composition.

72

XRPD analysis of pHBA recrystallized from solutions having slightly higher concentrations than the solubility determined that the anhydrous form crystallizes predominantly from the higher acetic acid mole fractions (▲ in **Figure 3.7(a)**), while at lower mole fractions the solvate form pHBA·0.5Ac exists (● in **Figure 3.7(a)**). Around the maximum solubility point a mixture of solvate and anhydrate is obtained (◆ in **Figure 3.7(a)**). At the maximum solubility point indicated by the black circle in **Figure 3.7(a)** and (b) the mole fraction of pHBA is  $0.13 \pm 0.01$  and that of acetic acid is  $0.12 \pm 0.01$ . If we assume that the maximum solubility point corresponds to the polysaturated point at which the solution and the two solid phases are in equilibrium we can construct the ternary phase diagram in **Figure 3.7(b)**, in which the solid phases in equilibrium with the solution are indicated using the same colors as in **Figure 3.7(a)**.

The ternary phase diagram shows that both the pure anhydrous form and the pure acetone solvate can be obtained, depending on the composition of the solvent mixture. The anhydrous form is stable in the largest part of the phase diagram, which is in agreement with the results from the pure solvent solubility measurements. Both from the presence of two solubility trends and XRPD results, the existence of two different solid forms in the system

was expected. This is in good agreement with the expectations discussed earlier.

#### Water-acetic acid

In **Figure 3.8(a)** the solubility of p-HBA at 20°C is plotted as a function of the AA fraction  $x_{AA}$  in water – acetic acid mixtures. At 20°C in water, the hydrate is most stable and the solubility is 0.0044 g/mL, which is low compared to the other forms. Adding small amounts of the acetic acid increases the solubility of the monohydrated, due to a change in activity of the water molecules. Similar to the case in the AA-Ac system, we expect a polysaturated point for this mixed solvent system. A smooth solubility trend is observed up to around  $x_{AA} = 0.75$ , where it shows a slight bend. Such a change could suggest that the polysaturated point of hydrate and anhydrous pHBA lies around this point.

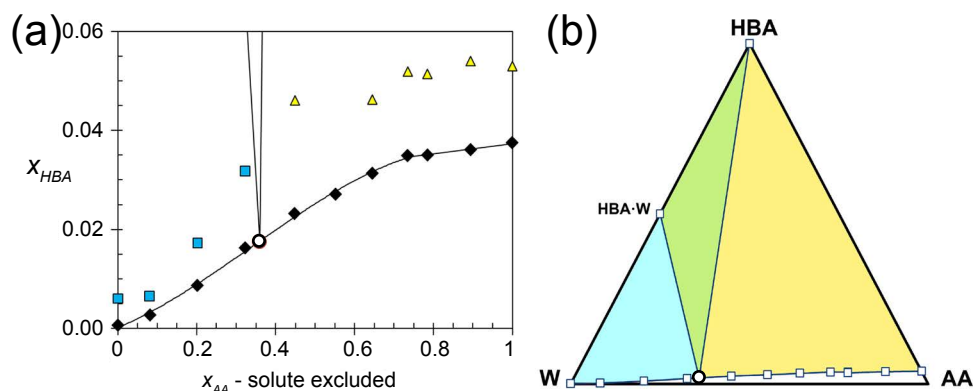


**Figure 3.8:** (a) The solubility of pHBA in W-AA mixtures at 20°C, where the mole fraction of acetic acid is given on solute-free basis. The  $\circ$  represents the polysaturated point. XRPD data from recrystallized points indicate pHBA-H<sub>2</sub>O ( $\blacksquare$ ) and pHBA ( $\blacktriangle$ ). (b) Ternary phase diagram of pHBA in mixtures of acetic acid (AA) and water at 20°C. The colors indicate which solid form was determined using XRPD upon recrystallization.

XRPD analysis of recrystallized pHBA at various solvent mixtures, however, determined that the hydrate only crystallized up to AA fractions of  $x_{AA} = 0.32$  ( $\blacksquare$  in **Figure 3.8(a)**). From acetic acid mole fractions of  $x_{AA} = 0.45$  and higher, the anhydrous form was crystallized ( $\blacktriangle$  in **Figure 3.8(a)**). From these XRPD measurements, the polysaturated point was estimated to lie around an acetic acid mole fraction of  $x_{AA} = 0.36 \pm 0.05$ , with a mole fraction of pHBA of  $0.018 \pm 0.002$ .

In one isolated case, pHBA crystallized from a solution with  $x_{AA} = 0.32$  and  $x_{HBA} = 0.016$  was different from both the hydrate and anhydrous forms. The patterns are shown in **Figure 3.9** and it is clear that the middle pattern (form

x), belonging to the crystals from the  $x_{AA} = 0.32$  mixture is not a mixture of hydrate and anhydrate. It was also observed that crystals resulting from a recrystallization from the solvent mixture with  $x_{AA} = 0.32$  were significantly larger in size than the crystals from any other composition. Recrystallizing more samples from this composition each time led to the hydrate, and form x could not be reproduced. Therefore, we consider form x as a metastable form and treat the point at  $x_{AA} = 0.32$  and  $x_{HBA} = 0.016$  as the polysaturated point between the hydrate and the solution.

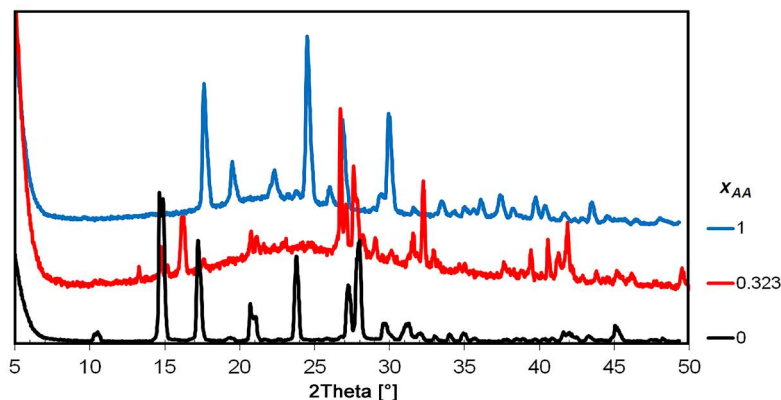


**Figure 3.9:** XRPD patterns of hydrate (bottom), anhydrous form (top) and unknown form crystallized at  $x_{AA} = 0.32$  (middle).

In the phase diagram in **Figure 3.8**, it is shown that both the anhydrous form and the monohydrate of pHBA exist in water-acetic acid mixtures. From the ternary phase diagram it is seen that the hydrate is the stable form even at relatively high mole fractions of acetic acid, compared to the acetone solvate. However, there was no agreement between the solubility trends and the XRPD measurements about the location of the polysaturated point. Zhu et al.<sup>6</sup> found that the location of polysaturated points between solvated states do not have to coincide with the transition points between solubility trends, which shows that this is not an isolated case.

#### *Water-acetone*

Last, **Figure 3.10(a)** shows the solubility of pHBA at 20°C as a function of the Ac fraction  $x_{Ac}$  in W-Ac mixtures. At the lowest acetone fractions, the hydrate is the most stable form, and at the highest acetone fractions the hemi-solvate. Three solubility trends are visible: 1) from pure water to  $x_{Ac} = 0.3$ ; 2) from  $x_{Ac} = 0.3$  to the maximum at  $x_{Ac} = 0.73$ ; and 3) from  $x_{Ac} = 0.73$  to pure acetone. This indicates that there may be three different stable phases crystallizing along the solvent compositions.

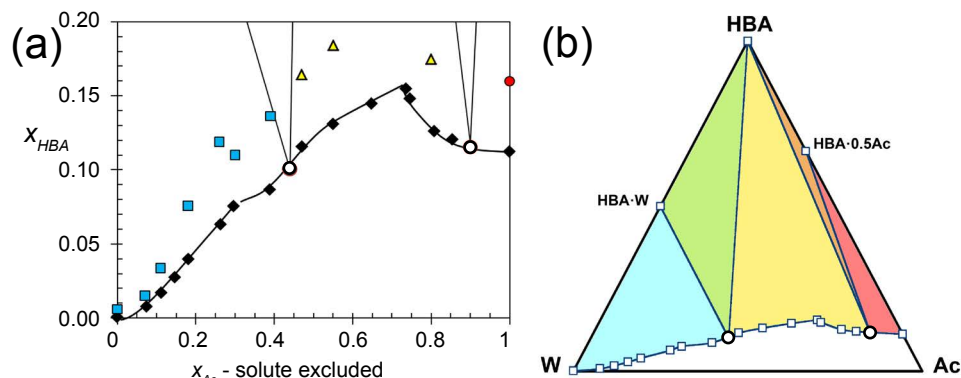


**Figure 3.10:** (a) The solubility of pHBA in W-Ac mixtures at 20°C, where the mole fraction of acetone is given on solute-free basis. The  $\circ$  represent the polysaturated points. XRPD data from recrystallized points indicate pHBA $\cdot$ H<sub>2</sub>O ( $\square$ ), pHBA ( $\triangle$ ) and pHBA $\cdot$ 0.5Ac ( $\bullet$ ). (b) Ternary phase diagram of pHBA in W-Ac mixtures at 20°C. The colors indicate which solid form was determined upon recrystallization using XRPD.

Interestingly, the XRPD analysis of recrystallized pHBA in **Figure 3.11** shows that the form in the center region of the phase diagram in **Figure 3.10** is anhydrous pHBA. Apparently under these mixed solvent conditions at 20°C both the solvate and the hydrate are less stable than the anhydrate.

The relation between the obtained solid phases and the solvent mixture composition suggests that there are 2 polysaturated points in this system. It also suggests that, like in the W-AA system, the polysaturated points are located at different positions than suggested by the solubility trends. The

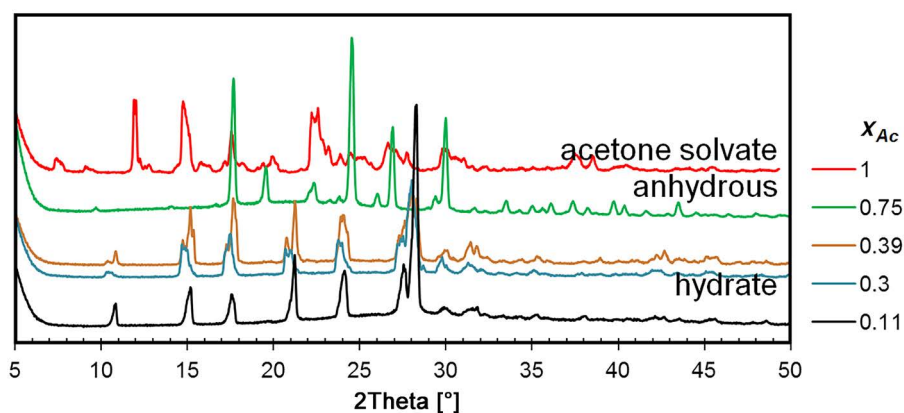


**Figure 3.11:** XRPD patterns of pHBA crystals after recrystallization from different water-acetone mixtures. At  $x_{Ac} = 1$ , the acetone solvate is crystallized, at  $x_{Ac} = 0.75$  the anhydrous form and at  $x_{Ac} \leq 0.39$  the hydrate is crystallized.

hydrate crystallized up to Ac fractions of  $x_{Ac} = 0.38$  (■ in **Figure 3.10(a)**). The anhydrous form was found in the region  $0.43 \leq x_{Ac} \leq 0.85$  (▲ in **Figure 3.10(a)**). Therefore, the polysaturated point describing the equilibrium at 20°C between solution, hydrate and anhydrate was estimated at a composition of  $x_{Ac} = 0.4 \pm 0.02$  and  $x_{HBA} = 0.1 \pm 0.01$ . Only from pure acetone the hemi-solvate crystallized (● in **Figure 3.10(a)**). This led to an estimate of the second polysaturated point, between the anhydrous region and the solvate region, of  $x_{Ac} = 0.79 \pm 0.05$  and  $x_{HBA} = 0.12 \pm 0.02$ .

In the phase diagram in **Figure 3.10**, a competition is shown between three stable states: the hydrate form, the acetone hemi-solvate, and the anhydrous form in between. This indicates a strong effect of the solvent on the prevailing solid state, which relates to the activity of the species in solution. Adding water to acetone drastically increases the activity of acetone, and vice versa. The effect of acetic acid on the activity of water and acetone in the previous phase diagrams was only minor compared to that. This can explain the appearance of the region where the anhydrous form is most stable. At low acetone fractions, through addition of acetone the water activity in the solution increases, yielding an increased solubility, or lower stability, of the hydrate. At a certain solvent composition ( $x_{Ac} = 0.4$  in **Figure 3.10**) the water activity reaches a value where the hydrate can not be crystallized anymore. At high acetone fractions, upon addition of water, a similar process happens, where the acetone activity at which the hemi-solvate can not be crystallized anymore is reached at  $x_{Ac} = 0.85$ . In the region between  $0.43 \leq x_{Ac} \leq 0.85$ , it is therefore the anhydrous form that is most stable.

The three solubility trends suggested the presence of three forms in the system. However, as with the W-AA system, XRPD measurements showed that the location of the polysaturated points was different. The solubility trends in the middle region are attributed to the non-ideality of the system.

### 3.3.3. Ternary solvent mixture

The ternary phase diagrams determined in **Section 3.3.2** can be used to construct a quaternary phase diagram of pHBA in a mixture of the three solvents water, acetic acid and acetone at 20°C. This phase diagram takes the shape of a pyramid with the ternary phase diagrams at its sides and the ternary phase diagram of the three miscible solvents as bottom plane. **Figure 3.12** shows the quaternary phase diagram, with horizontal planes that show the stable phases at different concentrations of pHBA. The bottom plane, where  $x_{HBA} = 0$ , only contains a single liquid phase, since the solvents are miscible in all compositional ranges. In the pyramid, the plane of  $x_{HBA} = 0.10$  is given. Other planes are given as cross sections in the ternary diagrams below, at pHBA mole fractions of 0.125, 0.15, 0.30 and 0.66. In the quater-

nary phase diagram, clear solution is depicted as white areas. The horizontal planes are interpolated from the ternary phase diagrams at the sides of the pyramid.

Upon addition of anhydrous pHBA to the ternary solvent mixtures until  $x_{HBA} = 0.05$  and  $x_{HBA} = 0.10$ , it can be seen that at high mole fractions of acetone a clear solution prevails. At low acetone fractions, the hydrate (blue) and the anhydrous form (yellow) are expected at higher mole fractions of water and acetic acid, respectively. At these low concentrations of acetone, a mixture of hydrate and anhydrous form (green) is located between acetic acid fractions of approximately  $0.32 \leq x_{AA} \leq 0.36$ . Increasing the mole fraction of pHBA further, until  $x_{HBA} = 0.125$ , the first acetone hemi-solvate (red) appears at high mole fractions of acetone. Additionally, the region of solvent mixtures at which the anhydrous phase is in equilibrium with the solution increases drastically in size, at the expense of clear solution. At  $x_{HBA} = 0.30$  the mixed regions have grown at the expense of the pure solids. Above mole fractions of  $x_{HBA} = 0.5$ , the region where only hydrate is in equilibrium with solution disappears entirely, which follows from the stoichiometry. The same goes for the acetone hemi-solvate above mole fractions of  $x_{HBA} = 0.66$ . In such cases not enough water or acetone is present to form their corresponding pseudo-polymorphs with all the pHBA present. Above these points, the pseudo-polymorphs always exist in a mixture with the anhydrous form.

Slurry measurements combined with XRPD analysis of the resulting crystals were performed to identify the stable crystal forms at each composition. The measurements are depicted as diamonds, with the color indicating the solid form identified. At  $x_{HBA} = 0.125$ , the small region between the acetone hemi-solvate - liquid region and the clear solution region was found to result in anhydrous pHBA crystals. At  $x_{HBA} = 0.15$  no clear solution is present anymore. Furthermore, a region emerged in which a mixture of acetone hemi-solvate and anhydrous form (orange) co-exist with the solution, even though it is not easily visible in the phase diagram. From this point up to  $x_{HBA} = 1$  at each solvent composition solids are present. While the phase regions in the planes of the quaternary phase diagram are largely extrapolated from the ternary datasets, they are validated by the slurry measurements. From these measurements we found that at least some of the equilibrium lines, e.g. between anhydrous pHBA and the mixture of anhydrous pHBA and hemi-solvate, are curved. However, possible curvatures of the equilibrium lines are not exactly known and remain estimations. Therefore, this diagram can be used to plan additional measurements, e.g. using solvent addition, to determine the exact trends.

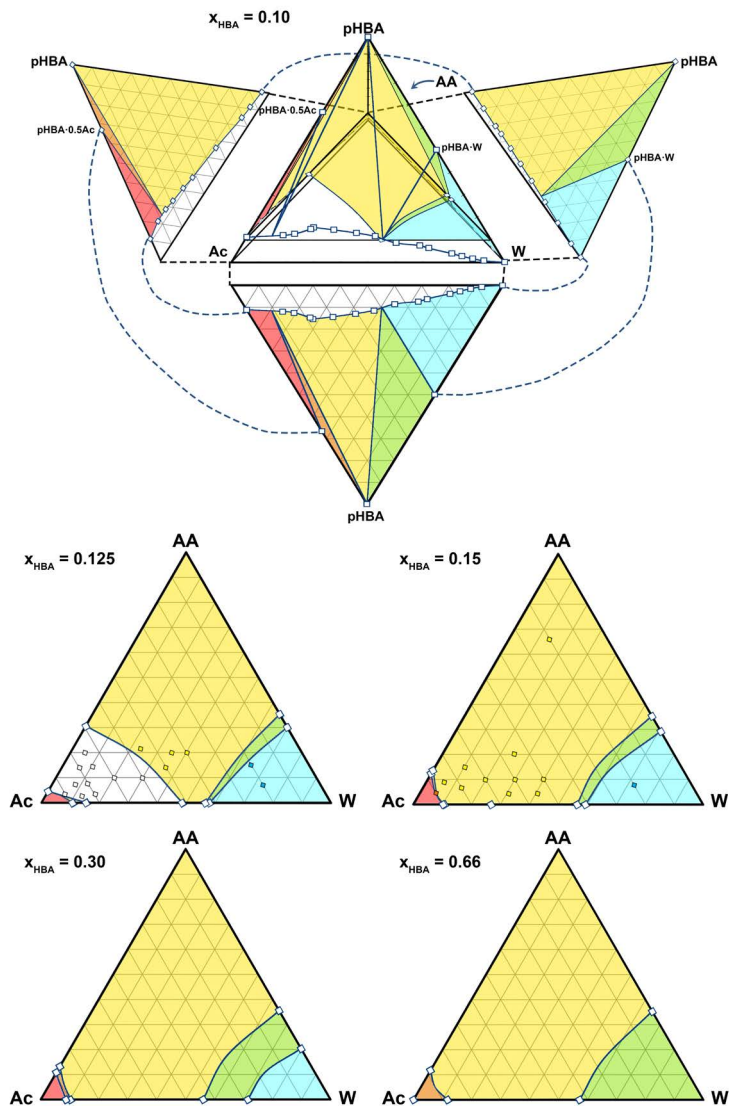


**Figure 3.12:** Quaternary phase diagram of pHBA in water, acetone and acetic acid, with the cross section of  $x_{\text{HBA}} = 0.10$  given in the pyramid. The colors represent the regions in which solid phases are in equilibrium with the solution: Red is acetone solvate, yellow corresponds to anhydrous pHBA and blue to the hydrate. Orange and green are mixtures of anhydrous pHBA with the acetone solvate and the hydrate, respectively. Cross sections at  $x_{\text{HBA}} = 0.125$ , 0.15, 0.30 and 0.66 show the development of each region for increasing mole fractions of pHBA. The diamonds in the cross sections at  $x_{\text{HBA}} = 0.125$  and  $x_{\text{HBA}} = 0.15$  are XRPD measurements, using the same color coding as the diagrams themselves.

The results obtained in this study show that solvent mixtures can be used for control over solvate formation. Since the relative stability of solvated forms is related to the activity of species in the solution, a correct choice of co-solvents can be used to effectively mitigate the formation of a solvate. The water-acetone system most clearly showed that, even in a solvent mixture containing only species that form solvated states with the compound, the right composition of the solvent mixture can still yield the anhydrous form. In the case of pHBA in water-acetone mixtures, the effect of one solvent on the activity of the other is dramatic, which most likely is the cause for the anhydrous form to appear. In the quaternary phase diagram, which was interpolated from the three ternary phase diagrams, slurry measurements showed that this interpolation is valid. However, curvatures of the equilibrium lines must be confirmed by measurements, for which the solvent addition method is very suitable.

### 3.4. Conclusions

The compositional regions for formation of various solvated states of pHBA crystalline phases were investigated. To find the phase boundaries in ternary phase diagrams of pHBA in solvent mixtures, the solvent addition method was used, with which the saturation concentrations at constant temperature were determined as function of the composition of the solvent mixture. For pHBA in mixtures of water, acetone and acetic acid, for which multiple solvated states could be formed along the solvent composition, a change in solubility trend was observed. However, the transition point does not necessarily coincide clearly with such a change, as was indicated by XRPD analysis of recrystallized samples. In mixtures of water and acetone, both of which form solvates with pHBA, anhydrous pHBA was obtained from a range of compositions between  $0.43 \leq x_{Ac} \leq 0.85$ , which is attributed to the dramatic effect of each solvent on the activity of the other. Additionally, the ternary phase diagrams were combined to construct a quaternary phase diagram, which was validated by XRPD analysis of crystalline samples from slurry measurements.

### 3.5. References

1. Ymén, I., Introduction to the Solid State – Physical Properties and Processes. In *Solid State Characterization of Pharmaceuticals*, John Wiley & Sons, Ltd **2011**; pp 1-34.
2. G. M. Edwards, H.; Lawson, E.; de Matas, M.; Shields, L.; York, P., Metamorphosis of caffeine hydrate and anhydrous caffeine. *Journal of the Chemical Society, Perkin Transactions 2* **1997**, 1985-1990.
3. Meenan, P. A.; Anderson, S. R.; Klug, D. L., 3 - The influence of impurities and solvents on crystallization. In *Handbook of Industrial Crystallization (Second Edition)*, Myerson, A. S., Ed. Butterworth-Heinemann: Woburn, **2002**; pp 67-100.
4. Kulkarni, S. A.; McGarrity, E. S.; Meekes, H.; ter Horst, J. H., Isonicotinamide self-association: the link between solvent and polymorph nucleation. *Chemical Communications* **2012**, 48, 4983-4985.
5. Chavez, K. J.; Rousseau, R. W., Solubility and Pseudopolymorphic Transitions in Mixed Solvents: Sodium Naproxen in Methanol-Water and Ethanol-Water Solutions. *Crystal Growth & Design* **2010**, 10, 3802-3807.
6. Zhu, H.; Yuen, C.; Grant, D. J. W., Influence of water activity in organic solvent + water mixtures on the nature of the crystallizing drug phase. 1. Theophylline. *International Journal of Pharmaceutics* **1996**, 135, 151-160.
7. Reus, M. A.; van der Heijden, A. E. D. M.; ter Horst, J. H., Solubility Determination from Clear Points upon Solvent Addition. *Organic Process Research & Development* **2015**, 19, 1004-1011.
8. Nordström, F. L.; Rasmuson, Å. C., Phase equilibria and thermodynamics of p-hydroxybenzoic acid. *Journal of Pharmaceutical Sciences* **2006**, 95, 748-760.
9. Heath, E. A.; Singh, P.; Ebisuzaki, Y., Structure of p-hydroxybenzoic acid and p-hydroxybenzoic acid-acetone complex (2/1). *Acta Crystallographica Section C* **1992**, 48, 1960-1965.
10. Luo, Y.-H.; Xu, B.; Sun, B.-W., Investigation of supramolecular syntheses of p-hydroxybenzoic acid (PHBA): Comparison of its hydrate, co-crystal and salt. *Journal of Crystal Growth* **2013**, 374, 88-98.
11. Coquerel, G., Crystallization of molecular systems from solution: phase diagrams, supersaturation and other basic concepts. *Chemical Society Reviews* **2014**, 43, 2286-2300.
12. Gould, P. L.; Howard, J. R.; Oldershaw, G. A., The effect of hydrate formation on the solubility of theophylline in binary aqueous cosolvent systems. *International Journal of Pharmaceutics* **1989**, 51, 195-202.



Chapter

4



# Concomitant crystallization for in-situ encapsulation of organic materials

Published as: M.A.Reus, G. Hoetmer, A.E.D.M. van der Heijden,  
J.H. ter Horst, Chem. Eng. Proc. **2014**, 80, pp 11-20

## Abstract

Concomitant crystallization leads to process intensification through the synergistic combination of the partial processes of particle formation and encapsulation within a single process step. Both cooling and electro-spray crystallization in multi-component solutions were used to create (sub-)micron sized particles of different crystalline materials. Concentrations were varied to control core and shell material. Depending on the relative initial concentrations used, concomitant electrospray crystallization of isonicotinamide and caffeine leads to encapsulated particles. Only limited encapsulation was achieved during concomitant cooling crystallization. Concomitant cooling crystallization of cyclotrimethylenetrinitramine (RDX)–2,4,6-trinitrotoluene (TNT) resulted in separate RDX and TNT particles. Using electro-spray crystallization, spherical nano-particles were produced, for which the component distribution within the particles could not be determined. Whereas crystallization from bulk solvent starts with a nucleus that grows gradually outward, whereby heterogeneous growth of a coating material on this core particle is not guaranteed, it appears that crystallization from evaporating solvent droplets starts at the surface of the droplets, and moves gradually inward. The resulting RDX–TNT powders have been tested for impact and friction sensitivity. The impact sensitivity has decreased compared to the raw materials, and the friction sensitivity did not change.

## 4.1. Introduction

Application of microencapsulation to organic products has achieved several successes. In the field of energetic materials the sensitivity of an explosive, i.e. tendency to ignite due to external influences like shock or friction, is a serious safety issue<sup>1,2</sup>. In various studies the sensitivity of energetic materials was reduced, while maintaining their effectiveness, by encapsulating the product with a less sensitive energetic material<sup>3,4</sup>. In pharmaceutical research the transport of active pharmaceutical ingredients (API's) inside the human body is of major importance for the effectiveness of the drugs<sup>5</sup>. Rosenkranz et al.<sup>6</sup> achieved controlled release properties by encapsulating crystals of the protein BSA with paraffin, thereby retarding the dissolution of the compound.

In all aforementioned studies the core particles were preformed, and then seeded into a crystallization process of the coating material. As crystallization is already used for the particle formation and purification, intensification in the functional domain<sup>7</sup> by combining the encapsulation with the existing process step leads to several advantages. For example, direct core-shell formation reduces the number of processing steps, potentially leading to a compact, safe, energy-efficient, and environment-friendly sustainable process<sup>8</sup>.

The integration results in the processing of complex solutions with two or more solutes. The crystallization of these solutes must be controlled in a way that they crystallize subsequently, the resulting particles consisting of both component layers. If the concentrations in this process are chosen such that one of the solutes nucleates before the other is supersaturated, the nucleation behavior of the second solute can be influenced. Instead of nucleating at its own metastable zone limit, forming new particles, the second solute can heterogeneously nucleate on the surface of the first. Therefore, control is required over heterogeneous nucleation behavior, which is one of the major challenges in nucleation research<sup>9</sup>. We aim to crystallize particles that act as heterogeneous templates, onto which other particles form in the same processing step. We investigate how the crystal formation occurs in both cooling and electrospray crystallization processes.

Two model systems were investigated, the combination of the pharmaceutical compounds caffeine (CAF) and isonicotinamide (INA), and the combination of the energetic compounds cyclotrimethylenetrinitramine (RDX) and 2,4,6-trinitrotoluene (TNT). For the RDX-TNT system, it is important for safety reasons that the sensitivity of the explosive formulation is reduced. The resulting materials have been tested on composition, crystal shape, size and size distribution. Additionally, the energetic materials have been tested regarding their impact and friction sensitivity.

## 4.2. Potential concomitant crystallization mechanisms

With an aim to crystallize heterogeneous template particles and subsequently deposit particles of other compounds in the same processing step, the crystallization of both compounds from their complex solutions, containing multiple solutes, must be controlled. This concomitant crystallization process is studied in two different ways. Concomitant cooling crystallization is used to show the crystallization behavior in the free environment of bulk solvent, where it is imperative that the solutes have a certain affinity towards each other, in order to form particles consisting of both materials. With “affinity” we mean the effectiveness of the interaction between the different crystalline materials, with high affinity resulting in heterogeneous nucleation of one crystalline material onto the surface of previously formed crystals of the other. This requires a low interfacial energy between the crystalline material and the previously formed template crystal. Also the degree of structural and chemical match of these phases can be an important factor. **Figure 4.1** shows the possible mechanisms for a concomitant cooling crystallization process. In mechanism C1, where the compounds have a high affinity for each other, compound B heterogeneously nucleates on the surface of the previously crystallized compound A, thereby encapsulating this compound. In mechanism C2, where the affinity is low, compound B does not heterogeneously nucleate onto compound A, leading to separate particles of A and B.

In order to reduce the dependence on the affinity between compounds on the resulting material, concomitant electrospray crystallization is used to

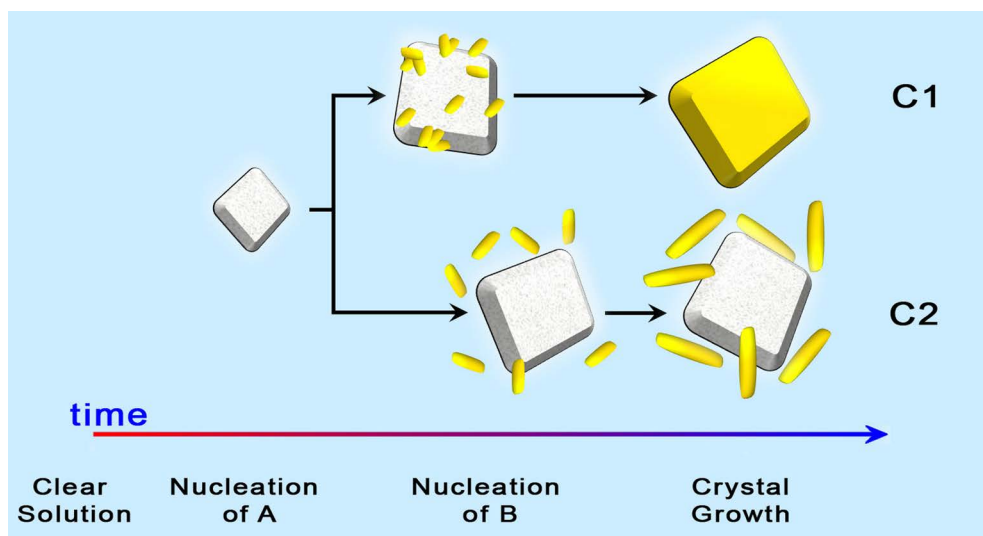


**Figure 4.1:** Possible mechanisms in concomitant cooling crystallization. In mechanism C1 heterogeneous nucleation takes place of B onto A, leading to encapsulation, in mechanism C2 A and B form separate particles.

study crystallization in a small confined space. Electrospray crystallization, similar to cold plasma crystallization<sup>10</sup>, uses an alternative energy form to intensify the crystallization process. In electrospray crystallization<sup>11</sup> the solvent is dispersed in tiny, charged droplets using a high electric field, and subsequently fully evaporated, leading to the formation of small particles. **Figure 4.2** shows the possible mechanisms of particle formation in concomitant electrospray crystallization. In mechanism E1 compound A heterogeneously nucleates onto compound B, on the inside of the droplet. After removal of all solvent compound A is encapsulated by compound B. In mechanism E2 compound A does not heterogeneously nucleate onto compound B and no encapsulation will take place. However, due to the decreasing droplet size, particles will be formed consisting of both materials. Here it is tested whether concomitant electrospray crystallization always forms small particles consisting of multiple solids, where this cannot be achieved with concomitant cooling crystallization.

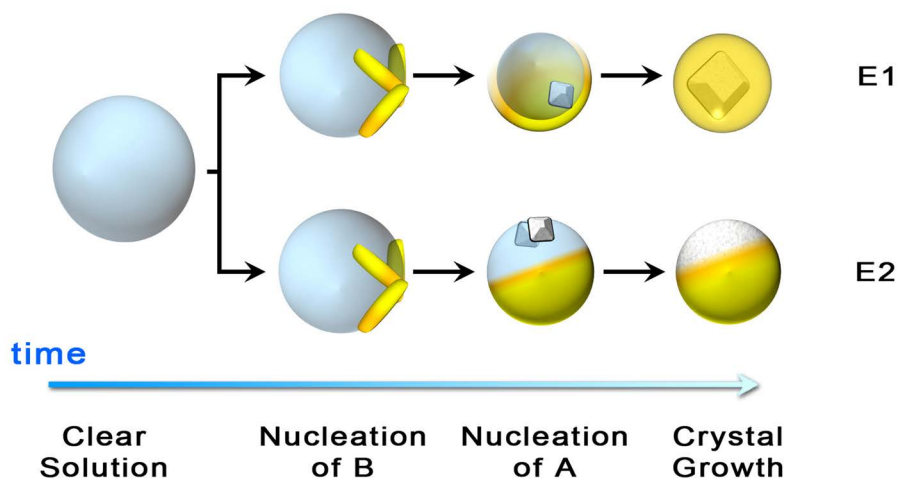


**Figure 4.2:** Possible mechanisms in concomitant electrospray crystallization. In mechanism E1 heterogeneous nucleation takes place of A onto B, leading to encapsulation, in mechanism E2 particles are formed consisting of both A and B, but no real encapsulation takes place.

## 4.3. Experimental

### 4.3.1. Chemicals

INA (>99%) and anhydrous CAF (>99%) were purchased from Sigma Aldrich. The solvent used for these compounds was 92.5% ethanol. Ethanol (100%) was purchased from Sigma Aldrich and was diluted with ultrapure water in order to increase the caffeine solubility. TNT (2,4,6-trinitrotoluene) and class 2 RDX (cyclotrimethylenetrinitramine) were purchased from

Chemring Nobel A.S., Norway. Acetone was used as solvent for these compounds. Acetone (99.8%) was purchased from Merck.

### 4.3.2. Cooling crystallization

The solubility of the compounds in the solvent and the metastable zone width (MSZW) of the solutions were determined using the temperature variation method in **Section 2.2**. Resulting data were used to determine relative concentrations, to be used in cooling and electrospray crystallization experiments.

Concomitant cooling crystallization experiments were conducted using the Crystalline multiple reactor setup (Avantium B.V.). Vials of 8 mL with solutions containing multiple solutes were subjected to a preset temperature profile, to fully dissolve and subsequently crystallize the solutions. A camera recorded the crystallization process.

### 4.3.3. Electrospray crystallization

In the electrospray setup, shown in **Figure 4.3(l)**, a smooth flow tapered tip (Nordson Engineered Fluid Dispensing) functioned as a nozzle. The inner diameter of the nozzle was 0.61 mm. A syringe pump (Aitecs 2016 Advanced Syringe Pump) was used to produce a constant flow rate of solution through the nozzle. The flow rate was varied between 0.5 and 1.5 mL/h. The counter electrode (a grounded steel plate) was set at working distances of 3 – 7 cm from the nozzle. A bipolar DC power supply (FUG Elektronik HCN 140M-12500) was used to generate the electric field between the nozzle and the counter electrode required to reach the stable cone-jet mode<sup>12, 13</sup> (**Figure 4.3(r)**). The required voltage for these experiments ranged from  $\pm 3.5 - 7$  kV,

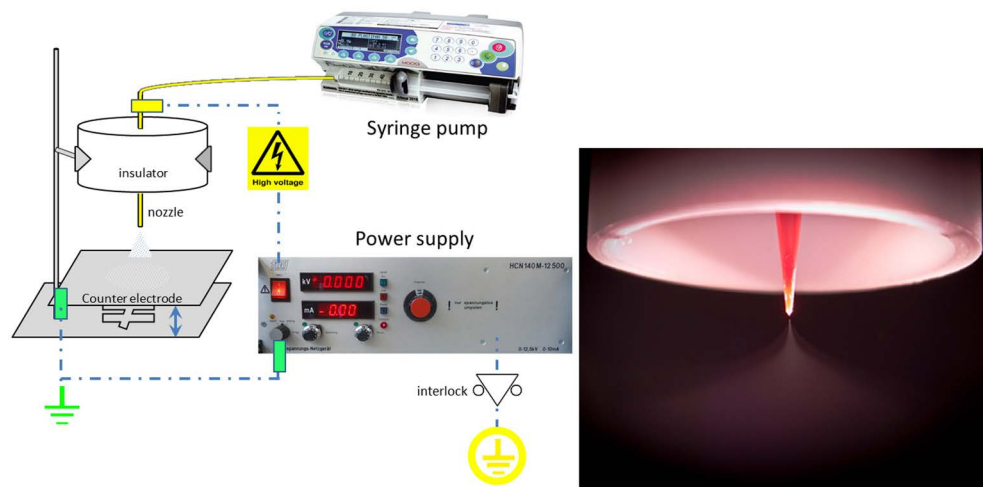


**Figure 4.3:** Schematic of electrospray setup with single nozzle (l) and close up of spray in cone jet mode (r).

depending on the solution, its flow rate and the working distance. The applied potential was positive for the INA–CAF system and negative for the TNT–RDX system.

#### 4.3.4. Characterization

Different microscopes were used for the analysis of the resulting particles. For the relatively large INA–CAF particles an optical microscope (Leica Nikon Optiphot 200) was used, for the energetic materials RDX–TNT a Leica LMBM microscope. Closer inspection of the particles resulting from electro-spray crystallization was done with a scanning electron microscope (SEM), JEOL JSM5400. For closer inspection of the energetic particles a FEI Nova NanoSEM 650 was used.

XRPD was used for the characterization of the particle structures. For the INA–CAF particles a Bruker AXS-D5005 diffractometer was used as in **Section 2.2**. For the RDX–TNT samples a Bruker D8 Advance Diffractometer was used.

The BAM Fallhammer and Friction Apparatus tests, recommended in the UN-recommendations for the transport of dangerous goods<sup>14</sup>, were used to determine the impact and friction sensitivity of the energetic samples produced by electro-spray crystallization. For the impact sensitivity test a BAM Fallhammer device was used (according to the international guidelines EC A.14 and UN 3(a)(ii))<sup>14</sup>. The volume of the samples was approximately 40 mm<sup>3</sup>. The friction sensitivity was determined by a BAM Friction Apparatus (according to the international guidelines EC A.14 and UN 3(b)(i))<sup>14</sup>. The quantity of the test sample is 10 mm<sup>3</sup>. The temperature during the tests ranged from 20 to 23°C.

## 4.4. Results and Discussion

### 4.4.1. Crystallization of pure compounds

#### *Cooling crystallization*

Cooling crystallization experiments were performed using the pure compounds from their respective solvents. The resulting crystals are shown in **Figure 4.4**. TNT and CAF crystals have a strongly elongated, needle-like morphology, while the RDX and INA crystals are more compact.

Solubility and metastable zone width (MSZW) of these compounds were determined. The solubility of TNT ( $c_{TNT}^* = 840$  mg/mL at  $T = 20^\circ\text{C}$ ) in acetone is more than 10 times larger than that of RDX ( $c_{RDX}^* = 60$  mg/mL at  $T = 20^\circ\text{C}$ ). Similarly, the solubility of INA ( $c_{INA}^* = 180$  mg/mL at  $T = 20^\circ\text{C}$ ) in 92.5% ethanol is more than 10 times larger than that of CAF ( $c_{CAF}^* = 15$  mg/mL at  $T = 20^\circ\text{C}$ ).

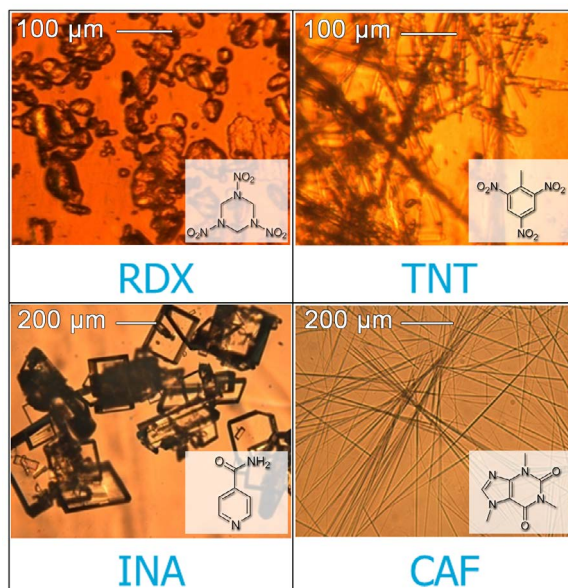


**Figure 4.4:** Molecular structures and crystals after cooling crystallization of the compounds used: INA and CAF from 92.5% ethanol, and TNT and RDX from acetone.

### *Electrospray crystallization*

Electrospray crystallization experiments were conducted using the pure compounds from their respective solvents, to assess the difference between products from cooling and electrospray crystallization. As opposed to the plate-shaped crystals from cooling crystallization, INA particles from electrospray experiments are rather spherical (**Figure 4.5(a)**).

The structure of these particles indicates that they consist of smaller INA crystals, agglomerated in such a way that they adopt the shape of the solvent droplet. CAF resulting from electrospray forms needle-like crystals agglomerated into spherical particles (**Figure 4.5(b)**). When using electrospray crystallization, RDX keeps its compact shape (**Figure 4.5(c)**). Electrosprayed particles of TNT, however, have a spherical, droplet-like shape (**Figure 4.5(d)**). During the experiments, it was observed that crystals are growing around the nozzle tips. These crystals make up for up to 50% of the material losses in this process.

### *Cooling versus electrospray crystallization*

Comparing **Figure 4.4** and **Figure 4.5** it follows that electrospray crystallization leads to strikingly different particle morphologies when compared to those from cooling crystallization. A significant difference lies in the particle size. The particles resulting from cooling crystallization are rather large (up to several hundreds of micrometers) and the size distribution is broad. From electrospray crystallization the particles are much smaller (in the lower

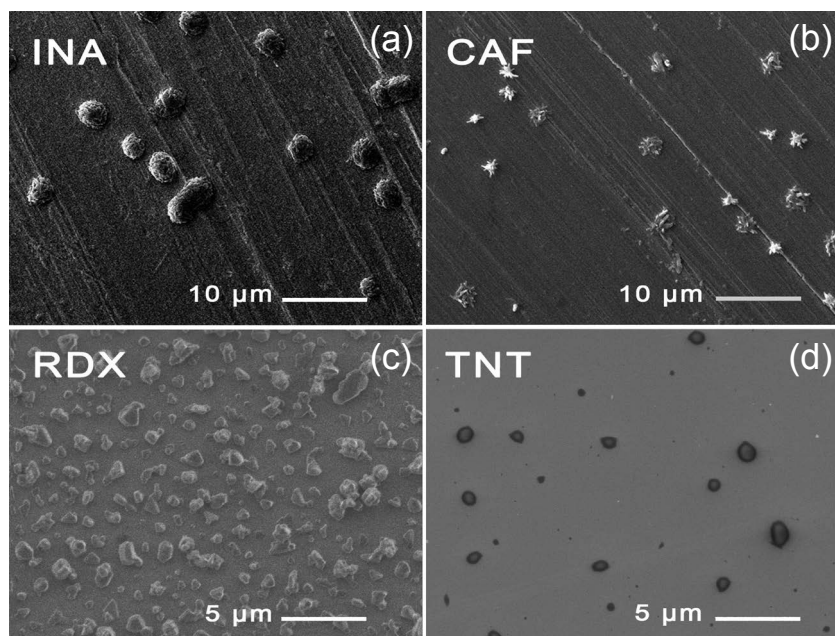


**Figure 4.5:** Particles of pure compounds INA and CAF from 92.5% ethanol, RDX (courtesy of N. Radacsi) and TNT from acetone, resulting from electro spray crystallization.

micron to submicron range) and the size distribution is narrow. This is inherent to the nature of the electro spray process. The solution emerging from the nozzle is divided into micron-sized droplets with the help of the electric field. No agglomeration takes place between the nozzle and the counter electrode, since all the droplets carry a charge of the same sign and thus repel each other<sup>15</sup>. Each droplet functions as a micro-scale evaporative crystallizer and as all droplets are approximately equally sized and contain equal concentrations of the solutes, the resulting particles cannot have a broad size distribution. Additionally, the particle morphologies that are obtained from the electro spray process are different compared to the cooling crystallization results. In cooling crystallization the crystals grow unhindered by any boundaries in the bulk solution, while in electro spray crystallization the growth is restricted to the volume of the droplets. The majority of the particles resulting from electro spray has a spherical shape. Since crystal growth does not occur outside the droplets, but inside where the solution is present, this phenomenon can be attributed to the spherical nature of the droplets.

Interestingly, in case of CAF the particles seem to be of a more spherulitic shape where needles protrude from a center in all directions, while TNT, which in cooling crystallization is also needle shaped, does not. The electro spray crystallization process thus appears to have an influence on the resulting particle shapes and sizes of crystalline compounds, when compared to cooling crystallization of the same compounds from the same solvents. Possibly this is due to the different solubilities of the compounds; whereas

CAF has a rather low solubility in its solvent, the solubility of TNT in its respective solvent is very high. In evaporating droplets with the same rate of evaporation, a high solubility of the compound leads to a faster generation of supersaturation. This in turn leads to faster nucleation and growth rates which results in spherical particles.

#### 4.4.2. Concomitant cooling crystallization

After the crystallization experiments with pure compounds, concomitant crystallization experiments were conducted. In such experiments two solutes are present in the solution, which means that we deal with a ternary system instead of a binary one, as in the pure component cases. A co-crystal screening of the compounds was performed according to the method proposed by ter Horst<sup>16</sup>, which did not give evidence for the existence of co-crystals of either INA-CAF or TNT-RDX.

In the concomitant cooling crystallization experiments, the concentrations of both solutes were chosen such that the first compound (the core) nucleates before the second (the coating) is supersaturated. The previously measured solubility lines and MSZWs of the compounds were used to plan the desired experiments. **Figure 4.6** shows an example of a concomitant crystallization experiment with RDX and TNT. Here the starting concentrations are chosen such that both compounds are dissolved at the start of the experiment (at  $t = t_0$ ) at a temperature  $T = 30^\circ\text{C}$ . At this temperature the concentration of RDX is close to saturation. The concentration of RDX, the core material, is chosen at 74 mg/mL, and that of TNT, the coating, at 770 mg/mL. Upon cooling, the RDX reaches supersaturation just after  $T < 30^\circ\text{C}$ , while TNT then is still undersaturated. At  $t = t_1$ , RDX reaches its metastable zone limit at  $19^\circ\text{C}$  and starts crystallizing. At this point TNT is close to saturation. At  $t = t_2'$ , while RDX crystals grow, TNT is supersaturated in the metastable zone and may start heterogeneous nucleation on the RDX crystals, before reaching its own metastable zone limit. However, if no heterogeneous nucleation takes place on the RDX surface, TNT will form its own separate crystals at  $t = t_2$ . Crystal growth occurs until the experiment is finished at  $t_c$ .

##### *INA-CAF system*

We found that INA influences the solubility and crystallization behavior of CAF in the solvent, making the process deviate from the predicted crystallization scheme using pure component solubilities. This deviation has been determined by using small amounts of each compound in the solubility determination of the other. The presence of CAF did not significantly influence the solubility of the INA. **Figure 4.7** shows that the presence of INA (0.2 g/mL) increases the solubility of CAF by approximately 1.5 times, as can be seen from the difference between the solubility lines of CAF (blue markers (◇) and (▲)).

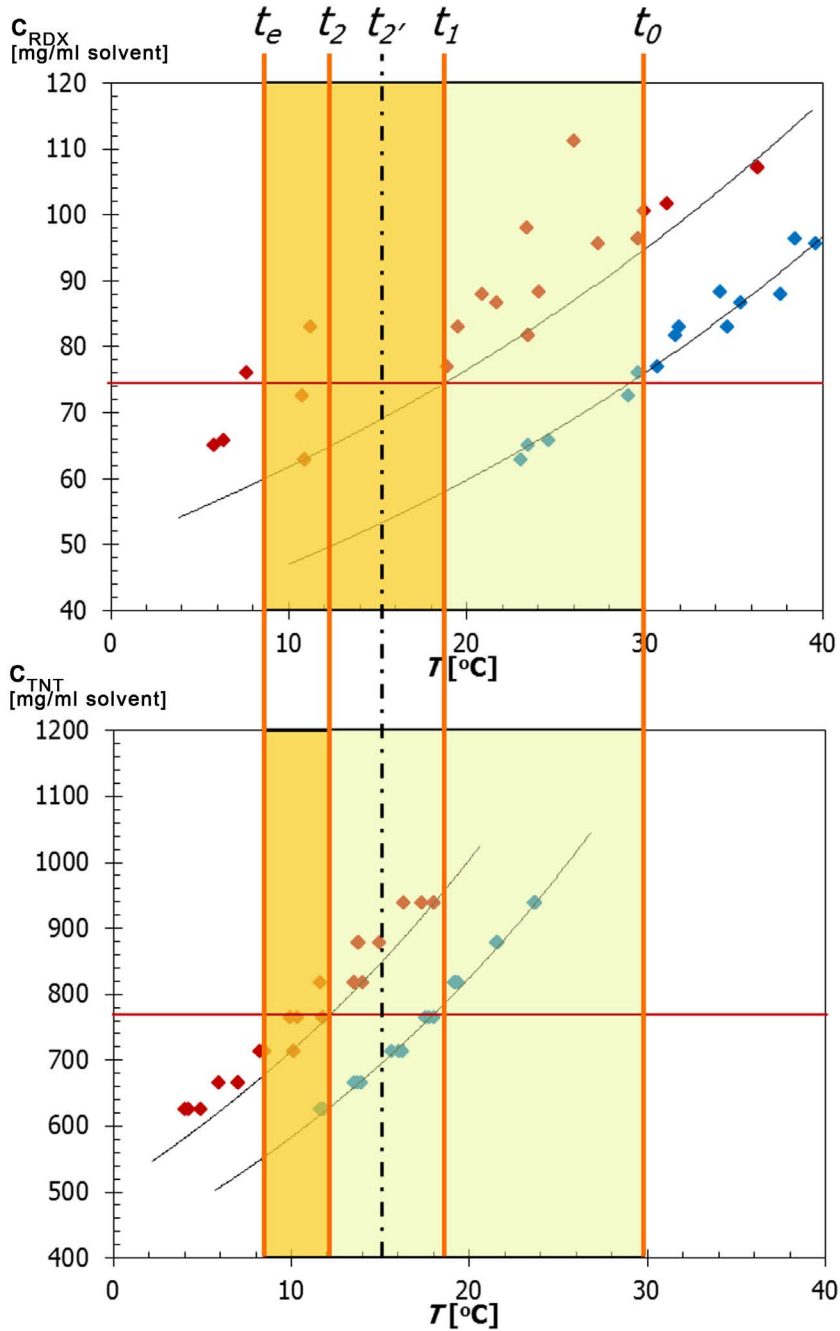


**Figure 4.6:** Solubility lines (♦) and MSZW (♦) of RDX (upper) and TNT (lower) in acetone. The MSZ limit is drawn on the high temperature side of the MSZW, according to Kadam et al.<sup>17</sup>. The different parts of a concomitant cooling crystallization experiment are depicted in the graphs ( $t_0 - t_e$ ).

The MSZ limit (red markers ( $\blacktriangle$ )) of CAF also shifted to higher concentrations when INA was added. For the clarity of the picture the MSZ limit of pure CAF is not shown. In a pure 0.04 g/mL CAF solution, CAF is expected to crystallize around  $T = 33^\circ\text{C}$  using a cooling rate of  $0.3^\circ\text{C}/\text{min}$ . However, in the presence of INA such a solution is only barely supersaturated at this temperature and crystallization of CAF can only be expected around  $T = 21^\circ\text{C}$ . The measured increase of the solubility of CAF in ethanol in the presence of INA is due to interactions between INA and CAF in solution<sup>18</sup>.

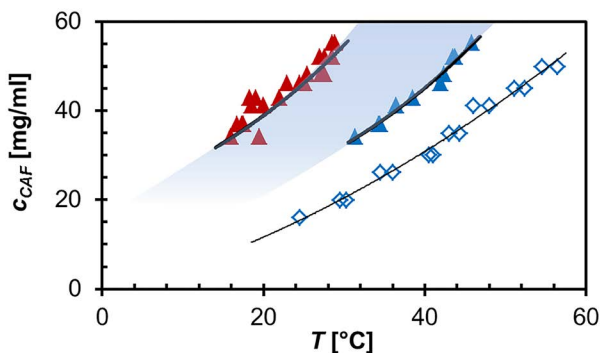


**Figure 4.7:** Solubility line of pure CAF in 92.5% ethanol ( $\diamond$ ) and solubility line ( $\blacktriangle$ ) and metastable zone limit ( $\blacktriangle$ ) of CAF with a small amount of INA ( $c_{\text{INA}} = c_{\text{INA}}^*$  at  $T = 31^\circ\text{C}$ ) added to the solution. The cooling rate was  $0.3^\circ\text{C}/\text{min}$ .

In order to assess the heterogeneous nucleation behavior of these compounds, seeding experiments have been conducted. Solutions of CAF in their metastable zone were seeded with INA crystals. Upon further cooling, where crystallization of both INA and CAF is taking place, and subsequent separation of the crystals from the mother liquor, particles were obtained. Some deposition of CAF on specific surfaces of INA has been observed, vis-

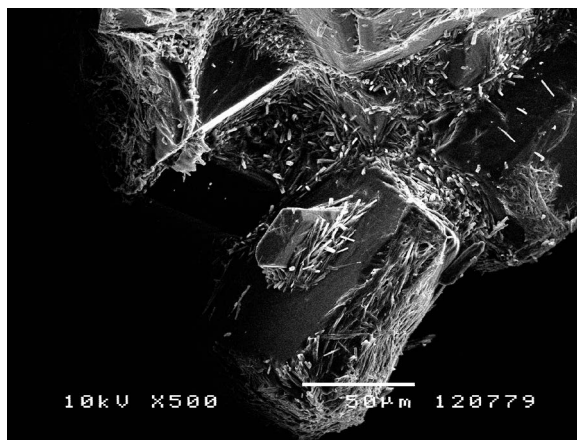


**Figure 4.8:** Large INA seed crystals with some small, needle-like CAF crystals attached to their surfaces, indicating that heterogeneous nucleation of CAF on the INA crystal surface took place.

ible in **Figure 4.8**, indicating that these materials follow mechanism C1 of **Figure 4.1**. Some INA crystals have been observed to be entirely covered by a layer of CAF, but most seeds had a coverage similar to the one in **Figure 4.8**. In the experiment leading to this sample approximately  $0.1 \text{ cm}^3$  of INA seeds were added to a 3 mL supersaturated solution of CAF. At the end of the process approximately 5 mg/mL of CAF was crystallized, leading theoretically to a full coverage of CAF on the INA seeds in the order of  $1 \text{ }\mu\text{m}$  thickness. In the calculation of this coverage we made a rough estimation of the average particle size by measuring the particles in the SEM pictures. The surface equivalent diameter was estimated to be  $50 \text{ }\mu\text{m}$ . Whereas the thickness of the CAF deposited on the INA seeds is in the expected order of magnitude, not the entire crystal is covered.

#### *RDX-TNT system*

In experiments using RDX and TNT no influences on either the solubility or the MSZW have been observed. During concomitant cooling crystallization experiments with TNT and RDX the process was followed with a camera (**Figure 4.9**). It was observed that TNT did not crystallize before reaching its own metastable zone limit. Therefore we suspected that no heterogeneous nucleation took place of TNT onto RDX crystals. After the experiments, inspection of the resulting suspension under the microscope showed separate crystals of TNT and separate crystals of RDX in the solution (**Figure 4.10**). From An et al.<sup>4</sup> this was already expected, since they also found that TNT had a low tendency to nucleate on the surface of RDX particles from solution without help of additives.

RDX and TNT consecutively nucleate in a cooling crystallization experiment with properly chosen concentrations (**Figure 4.9**). However, TNT does not nucleate before it has reached its own metastable zone limit. After the experiments, inspection of the resulting suspension under the microscope showed separate crystals of TNT and separate crystals of RDX in the solution (**Figure 4.10**).

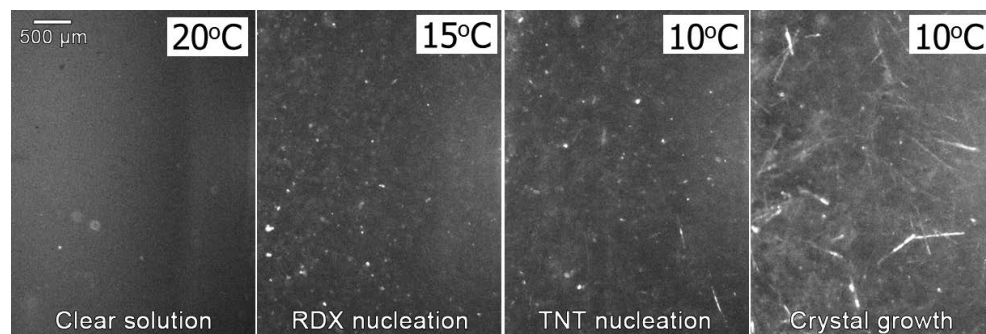


**Figure 4.9:** Concomitant cooling crystallization of a TNT-RDX solution in acetone. RDX nucleates at  $T = 15^\circ\text{C}$ , while TNT nucleates at  $T = 10^\circ\text{C}$ .

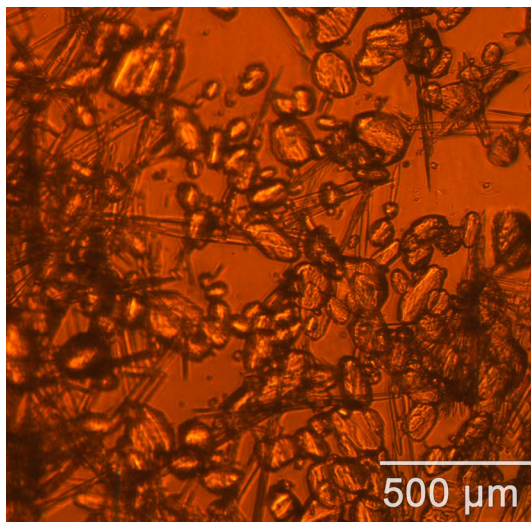


**Figure 4.10:** TNT and RDX crystals from concomitant cooling crystallization. Separate needle-shaped TNT crystals are loosely dispersed between separate compact crystals of RDX.

From the concomitant crystallization experiments it follows that different solutes can be combined into a single particle, but this is not necessarily the case. Due to the free medium, in concomitant cooling crystallization the interaction between the crystalline compounds is an important factor. In concomitant cooling crystallization of RDX and TNT large, separate particles are the result, with a broad size distribution. These materials follow mechanism C2 from **Figure 4.1**, indicating a low affinity between these two compounds.

#### 4.4.3. Concomitant electrospray crystallization

Similar to concomitant cooling crystallization, for concomitant electrospray the concentrations of both compounds have to be chosen in a way that one compound nucleates before the other. Again the previously measured solubility and MSZW data were used. Here, however, we used a different approach compared to concomitant cooling crystallization, since evaporation rather than cooling is the main driver of the crystallization process. A relative concentration,  $y_i$ , of compound  $i$  is defined:

$$y_i = \frac{c_i^0}{c_i^*} \quad (4.1)$$

Where  $y_i$  is the relative concentration of compound  $i$  in the solution, which is equivalent to  $S_i$  (undersaturation ratio),  $c_i^0$  is the initial concentration of that compound in mg/mL solvent and  $c_i^*$  is the solubility of that compound in the solvent, in the presence of any concomitant crystallization compounds, at 20°C. As the electrospray process is conducted at room temperature, the  $y_i$  of each component is chosen below 1, ensuring full dissolution of the com-

pounds prior to the process.  $y_{RDX} = 1$  corresponds to  $c_{RDX}^0 = 60$  mg/mL, because  $c_{RDX}^* = 60$  mg/mL. Analogous for  $y_{TNT} = 1$ ,  $c_{TNT}^0 = 840$  mg/mL. Therefore, concentrations of RDX and TNT are always chosen below 60 mg/mL and 840 mg/mL respectively. However, absolute concentrations must also be taken into consideration. It has been observed that the compounds with lower solubilities can still produce a stable spray when the relative concentration is very high ( $y_i > 0.50$ ). The compounds with high solubilities can often not exceed  $y$ -values of 0.15 – 0.3 before destabilizing the spray.

In **Figure 4.11** the process is depicted to be isothermal (at  $T = 20^\circ\text{C}$ ). Although evaporation is the main distinguishing factor for this process compared to cooling crystallization, the temperature of the droplet could decrease substantially. Evaporation of the solvent costs energy, which is supplied by the droplet, resulting in a substantial but currently unknown decrease in temperature. This causes a decrease in solubility for both compounds and can lead to crystallization at different  $y$ -values. We did not account for this in the sequence of crystallization events.

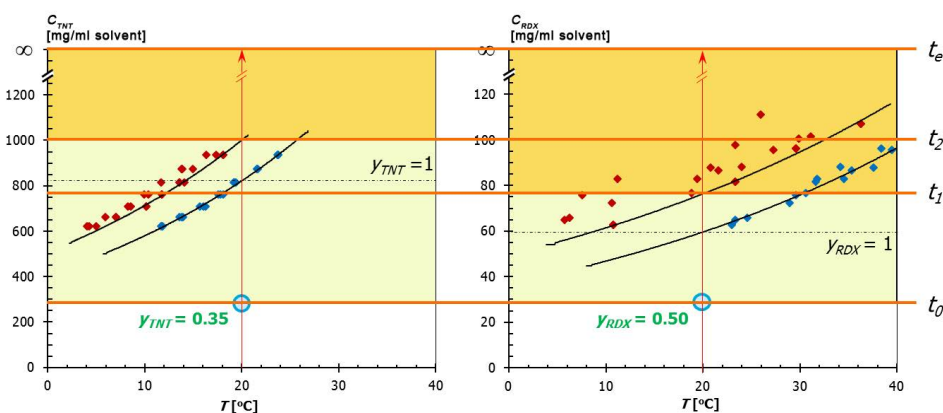


**Figure 4.11:** Solubility lines ( $\blacklozenge$ ) and MSZW ( $\blacklozenge$ ) of TNT (left) and RDX (right) in acetone. The MSZ limit is drawn on the high temperature side of the MSZW, according to Kadam et al.<sup>17</sup>. The dashed lines represent the relative concentration of  $y_i = 1$  of each compound (solubility at  $20^\circ\text{C}$ ). The different events in a concomitant electrospray crystallization experiment are depicted, with the initial concentrations ( $\bullet$ ) and the crystallization events over time ( $t_0 - t_e$ ).

In **Figure 4.11** an example is shown of how concentrations are chosen in a concomitant electrospray crystallization experiment and how the process will develop in terms of crystallization events. Evaporation of the solvent changes the  $y$ -values of both compounds in the solution by the same rate. In the example, the relative concentrations of the compounds are chosen as  $y_{TNT} = 0.35$  and  $y_{RDX} = 0.50$ . The moment that a droplet emerges from the cone jet is defined here as  $t = t_0$ . From this moment evaporation takes place and the solution concentrates, leading first to the crossing of the solubility line of RDX and then to its crystallization starting around  $t = t_1$ . After further evap-

oration TNT reaches its metastable zone limit, while RDX growth takes place. Only at  $t = t_2$  will TNT start nucleating. Thereafter, crystal growth of both materials will continue to take place until the solvent is completely evaporated and a dry particle is the result at  $t = t_e$ .

#### INA-CAF system

The results from various experiments with INA and CAF are given in **Figure 4.12**. XRPD analyses of the INA and CAF samples confirmed the presence of both materials in all samples. In **Figure 4.12** INA can be identified by the darker parts and CAF by the lighter parts, as determined by EDX analysis. For a moderate  $y_{INA}$  (0.3) in combination with a low  $y_{CAF}$  (0.1) (**Figure 4.12(a)**), it can be seen that the surface of the rather spherical particle consists largely of agglomerated plates of INA, with a few small needles of CAF protruding from it (indicated by blue arrows). When both  $y_{INA}$  and  $y_{CAF}$  are low ( $y_i = 0.1$ ) the CAF and INA are not easy to distinguish from one another; they rather seem to be randomly dispersed in the particle (**Figure 4.12(c)**). For high  $y_{CAF}$  (0.9) and low  $y_{INA}$  (0.1) (**Figure 4.12(d)**), bigger needle-like CAF crystals arise from the surface of smaller INA cores. For moderate  $y_{INA}$  and high  $y_{CAF}$  (0.3 and 0.9 respectively) (**Figure 4.12(b)**), CAF needles are found on the surface of the INA cores.

The amounts of solid CAF and INA present in the particles visible in each picture in **Figure 4.12** coincide with what we expect from the amounts we

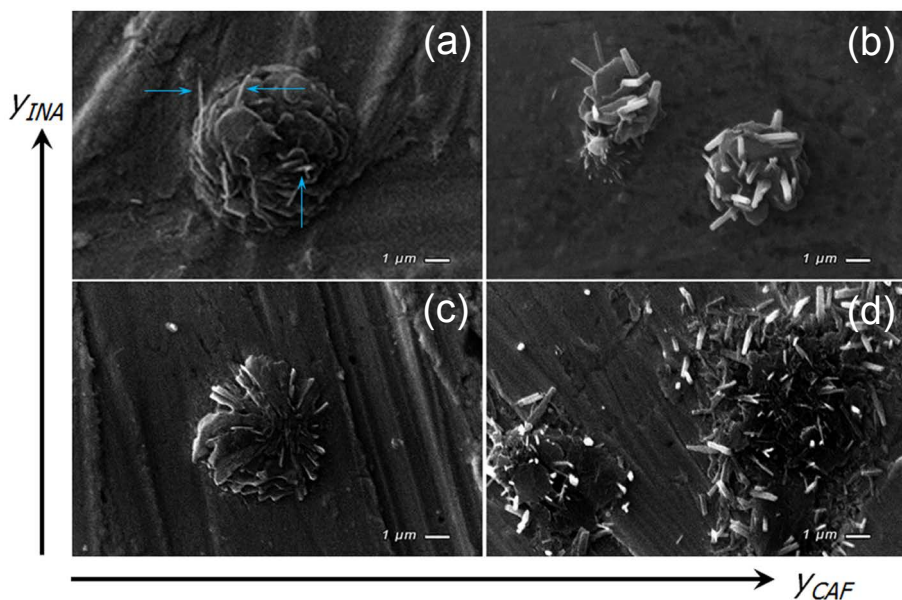


**Figure 4.12:** Resulting particles from concomitant electrospay crystallization experiments using different relative concentrations of INA and CAF. (a)  $y_{CAF} = 0.1$ ,  $y_{INA} = 0.3$ , (b)  $y_{CAF} = 0.9$ ,  $y_{INA} = 0.3$ , (c)  $y_{CAF} = 0.1$ ,  $y_{INA} = 0.1$ , (d)  $y_{CAF} = 0.9$ ,  $y_{INA} = 0.1$ .

used in each experiment. In the top left picture there is only a very small amount of CAF visible. Due to INA having a solubility in the solvent approximately 10 times higher than CAF, using the relative concentrations of  $y_{CAF} = 0.1$  and  $y_{INA} = 0.3$  raises the expectation of reaching about 30 times more INA than CAF in the resulting particles. Analogous to the other pictures, it follows the expectations that in the bottom right picture of **Figure 4.12** we find approximately equal amounts of both solids.

Remarkable observations in concomitant electrospray crystallization are the changing particle morphologies between different combinations of  $y_{INA}$  and  $y_{CAF}$ . The compound with the higher  $y$ -value (higher relative concentration) is mostly found on the surface of the resulting particles, indicating that the process follows mechanism E1 from **Figure 4.2**. This relation between relative concentrations of the compounds and their location in the resulting crystals shows that the compound crystallizing first, i.e. the one with the higher  $y$ -value, is found predominantly on the outside of the particle. This in turn supports the idea that crystallization in an evaporating droplet starts at the surface of this droplet, with an inward direction of crystal growth. Therefore, it is not surprising that in **Figure 4.13** hollow caps result from the electrospray using  $y_{INA} = 0.1$  and  $y_{CAF} = 0.5$ . The caps mainly consist of INA; CAF is not present in large amounts. The hole in the hollow cap, which was observed in all particles in this sample, is possibly created due to evaporation of the solvent and breakage after crystallization.

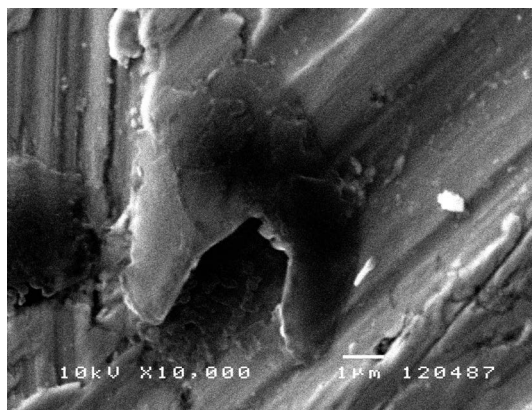


**Figure 4.13:** Hollow cap of INA resulting from electrospray experiments.

#### *RDX-TNT system*

In experiments with TNT and RDX different relative concentrations were also expected to lead to different particle morphologies. However, as both compounds emerged from the spray as spherical particles, in experiments combining the compounds no distinction could be made, not even by SEM analysis. What is clear from **Figure 4.14** is that the particles that are created are of submicron size. The particles have a narrow size distribution. With concomitant electrospray crystallization of TNT and RDX the mechanism

could not be made since it was not possible to determine the distribution of the solids in the particles.

XRPD analysis of the pure energetic materials resulting from electro spray returned results that did not coincide to a large extent with TNT or RDX in the databases, the same was true for the concomitant electro spray samples. However, the samples from concomitant electro spray crystallization had powder patterns that consisted of both pure component powder patterns.

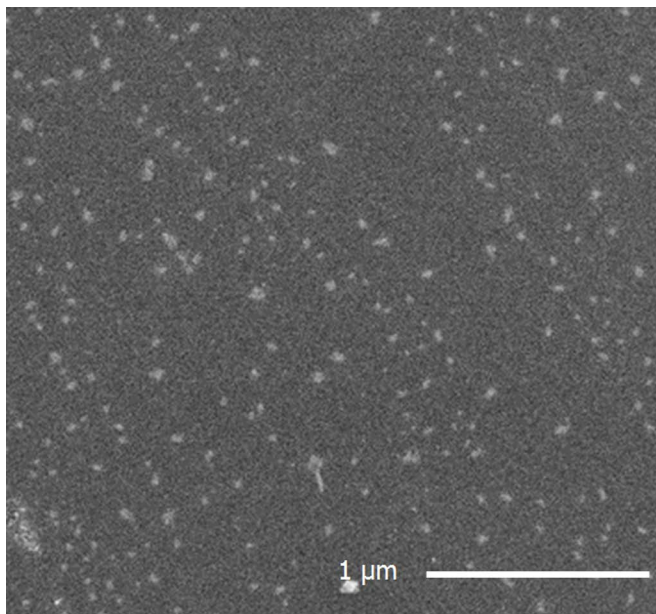


**Figure 4.14:** Particles resulting from concomitant electro spray crystallization of TNT ( $y = 0.05$ ) and RDX ( $y = 0.9$ ) from acetone.

Because the powder patterns did not coincide with the database patterns, additional IR analysis was performed on the samples. The IR spectra of the resulting energetic powders have shown that both TNT and RDX are present in the concomitantly electro sprayed powders. However, the comparison of the IR spectra from the electro sprayed TNT and RDX samples with the raw materials show that the electro spray process has not only changed the physical appearance of the materials. In the electro sprayed samples there are aromatic compounds with different substitutions than TNT present. In TNT from electro spray also nitro-groups with a different environment than TNT make their appearance. It is likely that TNT has been degrading into DNT (dinitrotoluene) and other decomposition products. The presence of aromatics in the RDX sample is remarkable, as RDX itself is aliphatic. It may be due to residuals of TNT from the tubing or due to possible degradation of RDX. It should be noted that the intensity of the extra peaks in the RDX sample, compared to the intensity of pure TNT spectra, suggested that residual TNT is not likely solely responsible for the change.

The energetic materials resulting from concomitant electro-spray crystallization were tested on their impact and friction sensitivity, in order to assess whether the goal of a reduction in sensitivity was achieved by the electro-spray process. The results in **Table 4.1** show that the electro-spray samples are much less sensitive than the raw material RDX, with impact and friction sensitivities of 4 Nm and 120 N, respectively. Instead, the sensitivity of the samples closely resembles that of the raw material TNT (impact and friction sensitivity 15 Nm and > 360 N, respectively), which is the least sensitive of the two raw materials. For the sample containing  $y_{TNT} = 0.15$  and  $y_{RDX} = 0.05$  this is fairly logical, since this yields particles containing > 90 wt% TNT.

**Table 4.1:** Impact and friction sensitivities of electro-sprayed RDX and TNT samples and of the raw materials.

| Electrosprayed | $y_{TNT}$ | $y_{RDX}$ | Impact [Nm] | Friction [N] |
|----------------|-----------|-----------|-------------|--------------|
|                | 0.15      | 0.05      | 15          | >360         |
|                | 0.10      | 0.10      | -           | >360         |
|                | 0.05      | 0.80      | 15          | >360         |
| Raw materials  |           |           | Impact [Nm] | Friction [N] |
| RDX            | -         | -         | 4           | 120          |
| TNT            | -         | -         | 15          | >360         |

However also the sample containing  $y_{TNT} = 0.05$  and  $y_{RDX} = 0.80$ , yielding particles containing approximately 50 wt% RDX, had impact and friction sensitivities resembling that of TNT. These samples do not have impact and friction sensitivity values closer to RDX, which indicates that the concomitant electro-spray process has a positive effect on the sensitivity of these materials and thus on the safety of the product.

#### 4.4.4. Concomitant cooling versus concomitant electro-spray crystallization

Concomitant electro-spray crystallization results in particles consisting of the two solutes each time, even if the solutes do not combine into a single particle during cooling crystallization. This can be attributed to the confined medium of the droplets from which all solvent is evaporated. The particle morphology can be influenced by changing the relative concentrations of the compounds. However, the choice for concentrations of both compounds is limited among others by their solubilities. The  $y$ -values, and thus the absolute concentrations, are linked both to the composition of the final product and to the choice for core and coating material. Therefore, for compounds with similar solubility, the core and coating material can be chosen freely, but in the final product there will be more coating material than core. When the solubilities differ a lot, the core and coating materials can still be chosen. However, then it leads either to very little core with an excess of coating material, or to an excess of core material with only a small amount of coating lay-

er. Electro spray dynamics also play a role: The relative concentration should be kept low enough to prevent crystallization before the droplet leaves the cone-jet. However, absolute concentrations must also be taken into consideration. It has been observed that the compounds with lower solubilities can still produce a stable spray when the relative concentration is very high. The compounds with a high solubility can often not exceed  $y$ -values of 0.10 – 0.3 before destabilizing the spray. The electro spray process is known to work well for fluids with properties (e.g. conductivity, viscosity, density) within certain ranges. It is likely that at too high mass fractions of solute, the fluid properties change so much that they exceed the optimal operation window of the electro spray process.

## 4.5. Conclusions

We show that concomitant crystallization can be used to intensify particle formation and encapsulation processes in the functional domain by reducing the number of processing steps. It has potential to combine different solutes into a single particle, but it does not necessarily lead to encapsulation. Due to the free medium, in concomitant cooling crystallization the affinity between the solutes is an important factor: experiments with TNT and RDX yield large, separate particles, with a broad size distribution. In experiments with INA and CAF the solubility and MSZW of CAF were influenced, delaying its crystallization. However, in seeding experiments deposition of CAF onto INA crystals was observed.

Due to the nature of the electro spray process, in electro spray crystallization submicron sized particles are obtained with a narrow size distribution. Different particle morphologies are obtained compared to those obtained from cooling crystallization. For the system INA–CAF there is evidence that the nucleation starts from the surface of the droplets, with crystal growth in the inward direction.

Due to the confined medium of the droplets from which all solvent has evaporated, concomitant electro spray crystallization results in particles consisting of the two solutes each time, even if they do not combine into a single particle during cooling crystallization. The particle morphology can be influenced by changing relative concentrations of the compounds, albeit within certain limits.

TNT–RDX powders resulting from concomitant electro spray crystallization have impact and friction sensitivity values not exceeding those of the TNT starting material, even at higher concentrations of RDX. With TNT being the less sensitive of the starting material, one can say that an overall reduction in sensitivity is achieved, and thus safer material is obtained by concomitant electro spray crystallization.

## 4.6. References

1. Agrawal, J. P., Recent trends in high-energy materials. *Progress in Energy and Combustion Science* **1998**, *24*, 1-30.
2. van der Heijden, A.; ter Horst, J.; Kendrick, J.; Kim, K. J.; Kröber, H.; Simon, F.; Teipel, U., Crystallization. In *Energetic Materials*, Wiley-VCH Verlag GmbH & Co. KGaA 2005; pp 53-157.
3. Kim, K. J.; Kim, H. S., Coating of Energetic Materials using Crystallization. *Chemical Engineering & Technology* **2005**, *28*, 946-951.
4. An, C. W.; Li, F.-S.; Song, X.-L.; Wang, Y.; Guo, X.-D., Surface coating of RDX with a Composite of TNT and an Energetic-Polymer and its Safety Investigation. *Propellants, Explosives, Pyrotechnics* **2009**, *34*, 400-405.
5. Waterman, K. C.; Goeken, G. S.; Konagurthu, S.; Likar, M. D.; MacDonald, B. C.; Mahajan, N.; Swaminathan, V., Osmotic capsules: A universal oral, controlled-release drug delivery dosage form. *Journal of Controlled Release* **2011**, *152*, 264-269.
6. Rosenkranz, K.; Kasper, M. M.; Werther, J.; Brunner, G., Encapsulation of irregularly shaped solid forms of proteins in a high-pressure fluidized bed. *The Journal of Supercritical Fluids* **2008**, *46*, 351-357.
7. Van Gerven, T.; Stankiewicz, A., Structure, Energy, Synergy, Time—The Fundamentals of Process Intensification. *Industrial & Engineering Chemistry Research* **2009**, *48*, 2465-2474.
8. Stankiewicz, A. I.; Moulijn, J. A., *Re-engineering the Chemical Processing Plant: Process Intensification*. CRC Press: New York, **2003**.
9. Davey, R. J.; Schroeder, S. L. M.; ter Horst, J. H., Nucleation of Organic Crystals—A Molecular Perspective. *Angewandte Chemie International Edition* **2013**, *52*, 2166-2179.
10. Radacsi, N.; Heijden, A. E. D. M. v. d.; Stankiewicz, A. I.; Horst, J. H. t., Nanoparticle generation by intensified solution crystallization using cold plasma. *Chemical Engineering and Processing* **2013**, *71*, 51-58.
11. Radacsi, N.; Stankiewicz, A. I.; Creighton, Y. L. M.; Heijden, A. E. D. M. v. d.; Horst, J. H. t., Electrospray Crystallization for High-Quality Submicron-Sized Crystals. *Chem. Eng. Technol.* **2011**, *34*, 624-630.
12. Grace, J. M.; Marijnissen, J. C. M., A review of liquid atomization by electrical means. *J. Aerosol Sci.* **1994**, *25*, 1005-1019.
13. Arnanthigo, Y.; Yurteri, C. U.; Biskos, G.; Marijnissen, J. C. M.; Schmidt-Ott, A., Out-scaling electrohydrodynamic atomization systems for the production of well-defined droplets. *Powder Technology* **2011**, *214*, 382-387.
14. Meyer, R.; Köhler, J.; Homburg, A., B. In *Explosives*, Wiley-VCH Verlag GmbH & Co. KGaA **2003**; pp 23-48.
15. Radacsi, N.; Ambrus, R.; Szunyogh, T.; Szabó-Révész, P.; Stankiewicz, A.; van der Heijden, A.; ter Horst, J. H., Electrospray Crystallization for

Nanosized Pharmaceuticals with Improved Properties. *Crystal Growth & Design* **2012**, 12, 3514-3520.

16. ter Horst, J. H.; Deij, M. A.; Cains, P. W., Discovering New Co-Crystals. *Crystal Growth & Design* **2009**, 9, 1531-1537.

17. Kadam, S. S.; Kulkarni, S. A.; Coloma Ribera, R.; Stankiewicz, A. I.; ter Horst, J. H.; Kramer, H. J. M., A new view on the metastable zone width during cooling crystallization. *Chemical Engineering Science* **2012**, 72, 10-19.

18. Mullin, J. W., 3 - Solutions and solubility. In *Crystallization (Fourth Edition)*, Mullin, J. W., Ed. Butterworth-Heinemann: Oxford, **2001**; pp 86-134.





Chapter

5

The image shows a laboratory setup for electrospray crystallization. Three glass vials with red caps are suspended vertically by thin wires. Each vial is tilted, and a fine, white, crystalline spray is being emitted from the bottom of each. The background is dark and out of focus, highlighting the vials and the sprays. The text is overlaid on the central part of the image.

Electrospray crystallization:  
challenges in process design,  
operation and control

## Abstract

Electrospray crystallization is a promising technique for the production of (sub)micron sized crystals. For analysis or small dosage purposes it can very well provide the particles with the right size and properties. However, ensuring consistent product quality and narrow size distribution are a challenge. Additionally, the product losses can be high. Here we discuss these challenges and give suggestions to how they might be overcome. The challenges are divided in three topics: (a) Narrow operating window, (b) low yield, and (c) product handling. The narrow operating window is not only inherent to the electrospray process itself, but is limited even more due to the constraint that the solvent must evaporate completely from the droplets before the particles are collected. The low yield has a number of causes, one of which is premature crystallization at the nozzle tips. Product handling involves preventing agglomeration and solvation of the product if so desired. The three challenges are addressed in a comprehensible design tool for solvent selection and equipment design of electrospray crystallization processes, which aims at increasing the efficiency of the experimental and process design phase.

## 5.1. Introduction

As with the entire chemical industry, the field of crystallization perceives the increasing need to fulfill more stringent demands regarding product quality and reduction of carbon footprint and production costs. Especially the product demands, which for crystallization do not only comprise purity, but also properties like polymorphic form, size distribution and mean size, are changing. For example, the trend towards producing nano-sized crystals, e.g. for better dissolution properties e.g. to improve the bio-availability of pharmaceuticals, has become stronger<sup>1-3</sup>. Using confined volumes, such as droplets in microfluidics<sup>4,5</sup> or microwell plates<sup>6,7</sup>, is one way to produce small crystals. Electro spray is another technique that produces small droplets with a narrow size distribution if operated in the cone jet mode. Electro spray, also called electrohydrodynamic atomization (EHDA), is a process where a liquid stream from a nozzle is atomized using a high electric field<sup>8</sup>. The cone jet mode (CJM) is one of the stable modes of operation<sup>9</sup>, in which, due to the electrical charges, the meniscus is drawn into a conical shape, called the Taylor cone. Many parameters (e.g. applied electric potential  $V_N$ , working distance  $d$ , flow rate  $\Phi_v$ ) influence how the CJM is achieved<sup>10</sup>. How these parameters must be chosen relative to each other to achieve the desired spraying mode depends on the fluid properties (e.g. electrical conductivity  $K$ , tension  $\gamma$ , viscosity  $\mu$ ). In the CJM, a small jet emerges from the liquid cone continuously, which breaks up into small droplets of equal size and charge. Due to the charge, the droplets repel each other and no aggregation takes place. Typical droplet sizes are in the lower micron range<sup>10,11</sup>.

Due to their small size, the droplets rapidly evaporate. Adding a solute to the liquid therefore leads to a crystallization step inside each droplet. This integration of EHDA<sup>8</sup> and crystallization<sup>12</sup> is called electro spray crystallization. Due to the small size and narrow size distribution of the droplets, a small size and narrow size distribution of crystals are automatically obtained. Using the EC method, improved material properties as compared to the crystals obtained by more conventional methods, such as cooling crystallization and evaporative crystallization, have been obtained. Radacsi et al.<sup>13</sup> found that their electro sprayed crystals of the explosive compound cyclotrimethylene trinitramine (RDX) had significantly reduced impact sensitivity, and therefore increased safety, as opposed to the starting material, due to the submicron size of the product. IJsebaert et al.<sup>14</sup> produced monodisperse particles of Beclometasone dipropionate (an asthma medicine) in the lower micron range, which significantly increased the therapeutic efficiency of the inhalation drug compared to the particles from the traditional pressurized metered dose inhalers (MDI, conventional asthma inhaler). This way, lower doses could reach the same therapeutic effect. Other benefits of particles produced by electro spray crystallization include those produced by con-

comitant electrospray crystallization, where the (sub)micron sized particles consist of multiple solids, yielding different properties than that of the pure particles<sup>15</sup>. Additionally, the use of polymers in the same process can lead to final formulations of drug particles with controlled release properties<sup>16</sup>.

However, while the previous results show the potential of the EC process for the production of small crystals, the research effort in this specific field still lags behind. The intrinsically low production rate (and difficulties in scale-up) of the EHDA process itself is likely a major cause, since often larger amounts are required than can be produced by a single nozzle. Additionally, the introduction of a crystallization step to the EHDA process poses new challenges, which are not yet widely investigated, but can have an effect on the product quality and the process operation. Here we identify the issues that can arise during operation known so far, along with examples thereof encountered during our experiments, and suggestions of how to overcome them. Additionally, based on our obtained process knowledge we provide a basic design tool for solvent selection and equipment design of electrospray crystallization processes, which aims at increasing the efficiency of the experimental and process design phase.

## 5.2. Materials and methods

Isonicotinamide (INA, >99%), anhydrous caffeine (CAF, >99%) and L-proline (purity >99%) were supplied by Sigma Aldrich. The solvent used for these compounds was 92.5% ethanol. Ethanol (100%) was supplied by Sigma Aldrich and was diluted with ultrapure water. TNT (2,4,6-trinitrotoluene) and class 2 RDX (cyclotrimethylenetrinitramine) were purchased from Chemring Nobel A.S., Norway. Acetone (99.8%), purchased from Merck, was used as solvent for these compounds. For particle visualization a scanning electron microscope (SEM, JEOL JSM5400) was used. X-ray powder diffraction (XRPD) was used for crystal structure analysis. The measurements were performed with a Bruker-AXS D2-Phaser diffractometer, equipped with a Lynxeye detector. The pattern scan was made in the range  $5 \leq 2\theta \leq 50^\circ$ , using a step size of  $0.02^\circ\theta$ . The radiation is  $\text{CuK}\alpha_1$  (0.15406 nm).

### *Electrospray Crystallization setup*

The setup depicted in **Figure 4.3** was used for the electrospray experiments with single nozzle. The setup and the operating parameters are described in **Section 4.3**.

Out-scaling the single nozzle setup led to a setup containing 10 nozzles in an array, where each nozzle was supplied with solution from a separate syringe. All 10 syringes were loaded into one multiple-syringe pump. The same nozzles were used as in the single-nozzle setup. The nozzles were connected by a conductive plate, which was supplied with the electrical potential from

the same power source as the single nozzle setup. The spacing between the center of the nozzles was not less than 45 mm.

## 5.3. Results and discussion

### 5.3.1. Operating window

When EC is successfully operated in the CJM, a monodisperse powder can be obtained with crystal sizes in the lower or sub-micron range. **Figure 5.1A** shows a schematic of EC in the nozzle-plate configuration, operating in the CJM. In the nozzle-plate configuration, which is the most basic configuration of an EHDA process, a nozzle is placed several centimeters away from a grounded plate that acts as counter electrode. The nozzle is provided with a flow rate ( $\sim 1$  mL/h) of solution and a DC electrical potential (several kilovolts) to provide a sufficiently high electric field to achieve the CJM. The meniscus assumes a conical shape and the jet that emerges at the end breaks up into equally sized droplets, that evaporate rapidly due to their size. The evaporation of the solvent creates a supersaturation of the solute, which then crystallizes. Throughout the length from the jet to the counter electrode, the droplets or crystals are equally charged, preventing aggregation. When the solvent evaporates, the charge density on the particle increases, which can lead to Coulomb fission<sup>17</sup>, resulting in even smaller particles. This is a strategy that can be used to create even smaller particles, but is not discussed further here. Due to the potential difference, the droplets are attracted to the grounded counter electrode. There they deposit and lose their charge. In **Figure 5.1B** an example is shown of electrosprayed INA from 92.4% aqueous ethanol. The concentration used was 0.05 g/mL, which is 28% of its equilibrium concentration at 20°C. The flow rate was 1.25 mL/h, the working distance was 7 cm to accommodate the complete evaporation of the solvent. The voltage applied to the nozzle was  $-6.9 \pm 0.2$  kV. The product in **Figure 5.1** is spherical and the size distribution is narrow ( $d_p = 3.3 \pm 0.05$   $\mu\text{m}$ ). In some cases aggregation of two crystals was observed. This occurs because the crystals lose their charge upon contact with the counter electrode, diminishing the repelling action and allowing other crystals to land at the same location. However, mostly the particles are separated from each other.

The technique was also used with multiple solutes. Each resulting particle then contained both solutes that were present in the solution. In **Figure 5.1C** an example is shown of product obtained when spraying INA and CAF together. The distribution of the compounds over each particle depends on the concentrations used<sup>15</sup>. The particle size distribution is also narrow in this sample. Furthermore it is observed from **Figure 5.1B** and **C** that spherical particles are obtained each time, while CAF is needle shaped and INA plate shaped in cooling crystallization. In previous research<sup>15</sup> we found that, while

CAF retains its needle shape and crystallizes as spherulites, TNT loses its needle shape and assumes the shape of the droplets. This is attributed to the fast evaporation of solution.

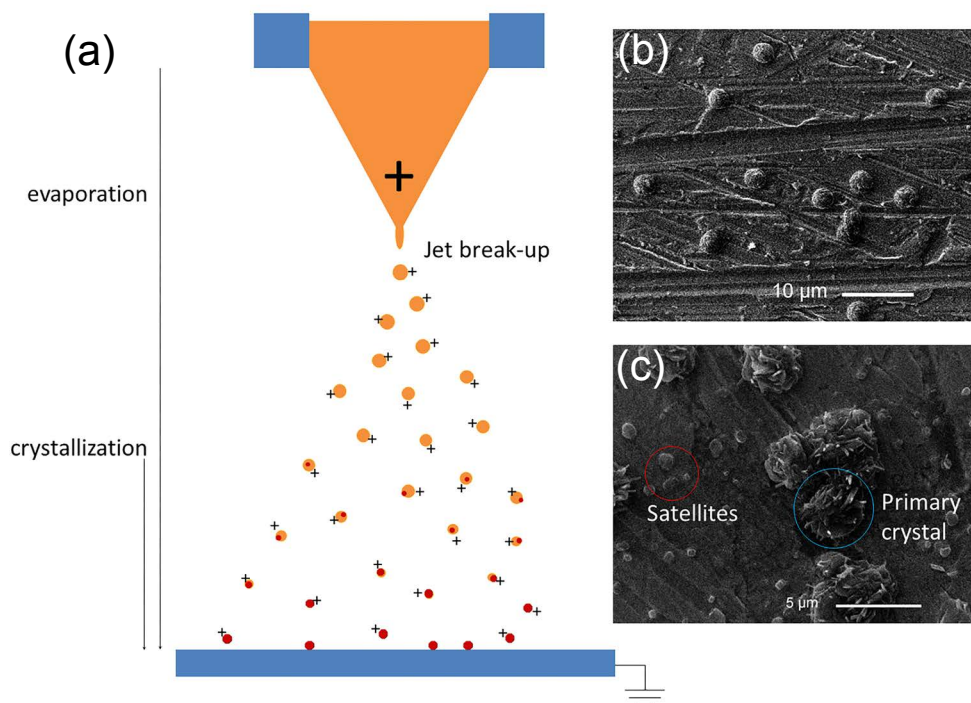


**Figure 5.1:** A: Schematic of EC. The liquid coming through the nozzle is charged, drawn into a conical shape, which emits a jet. After jet breakup small, equally sized and charged droplets are attracted by the grounded counter electrode. Through evaporation of the solvent, supersaturation is reached and crystallization occurs. The charged crystals discharge at the counter electrode. B: SEM image of a crystalline product (INA) from EC. C: SEM image of a crystalline product from concomitant EC with satellite crystals in between.

### 5.3.2. Challenges

One of the advantages of EC is that the electro spray setup is small and simple. The particle size distribution from a setup is inherently narrow if the process is correctly designed and operated. However, complications can arise that generally are related to either one of three major challenges we identified. In this section, first the challenge of finding the narrow operating window is discussed. Second, the potential causes and solutions for the low yield are explored. Third, considerations around the product handling are elaborated.

#### *Narrow operating window*

In the electro spray process, several parameters need to be properly chosen relative to each other to obtain the right spraying mode. Those parame-

ters comprise the working distance, flow rate and electrical potential. How these must be set depends on the fluid properties, like viscosity and electrical conductivity, that must also lie within certain boundaries<sup>9, 10</sup>. This means that for each system, different settings are required to operate in the CJM. The operating window for the combination of these parameters is narrow.

When a solute is added and an EC experiment is performed, this operating window narrows down even further. For the crystallization, it is important to 1) obtain dry crystals and 2) to control the mean crystal size and size distribution.

To obtain dry crystals it is imperative that the solvent completely evaporates before the crystals reach the collector. **Figure 5.2** shows product we obtained from the spraying of CAF from 97.5% ethanol at a working distance of 3 cm. The caffeine needles are seen to grow from the counter electrode in ring shaped configurations. This indicates that wet droplets of solution reached the counter electrode and subsequently dried on the collector plate. The material thus obtained cannot be easily used, since it is stuck to the electrode.

The choice of solvent is a very important step in solving this issue. For a regular electrospay process, the liquid should have a proper electrical conductivity ( $10^{-9} < K < 10^{-1}$  S/m) and the surface tension and viscosity should not be too high<sup>9</sup>. For electrospay crystallization additional requirements are put on the liquid: it must dissolve the solute to some extent to be a good carrier and it should have a high vapor pressure to facilitate the evaporation. Solvents with vapor pressures of  $P^{sat} > 10$  kPa are advised. It is convenient that common solvents, like methanol, ethanol and acetone, are among the suitable solvents for EC.

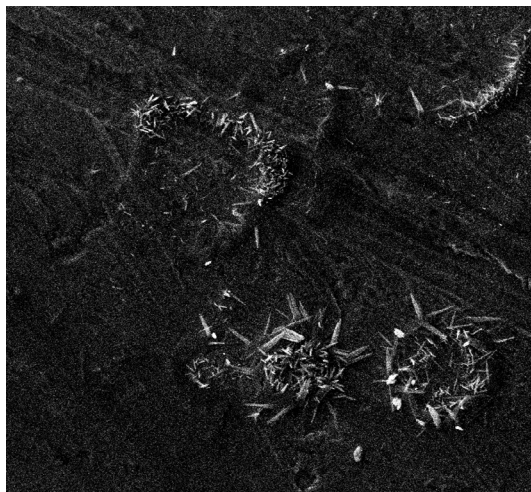


**Figure 5.2:** SEM image of caffeine after EC from 97.5% ethanol at a working distance of 3 cm. The ring shapes in which the crystals are distributed indicate that solvent evaporation was incomplete before the counter electrode was reached.

However, when these solvents do not dissolve the target compound, but a solvent with a lower vapor pressure (e.g. water) should be used, more time is required to reach complete evaporation. This can be arranged by increasing the distance between the nozzle and the collector. In the case of the 97.5% aqueous ethanol, a distance of 7 cm was sufficient to obtain dry material (in the form of needle like spherulites<sup>15</sup>). However, when more water is present, an even larger distance is required, in which case the spray needs to be guided to the collector. In such a case, the nozzle-plate configuration, in which the counter electrode is the collector, is no longer feasible. A charged aerosol can then be made by using a ring-shaped counter electrode close to the nozzle (also called extractor), while applying a relatively small DC potential of the same polarity as the nozzle, i.e. giving it a bias, so that the induced spray will travel through the ring<sup>18, 19</sup>. The spray can then be guided towards the collector by tailoring the external electric field.

Control over the size distribution of the crystals is mainly dependent on a smooth operation (i.e. without instabilities in the jet break-up) of the EC process in the stable CJM. **Figure 5.1B** is an example of product obtained from such a smooth operation. In **Figure 5.1C**, however, smaller particles are observed next to the main particles. Smaller particles can be formed either due to the jet break-up mechanism in an experiment, where satellite droplets are formed between the primary droplets<sup>9</sup>, or due to Coulomb fission of the charged droplets<sup>20</sup>. The size of the particles in **Figure 5.1C** suggests that it is due to the jet break-up mechanism, since fine Coulomb fission would generate much smaller droplets. Due to their small size, the satellite droplets do not make up a large portion of the product and can often be ignored. If this is not the case, they can either be removed from the rest of the spray<sup>21</sup> or prevented from forming by adding disturbances whose frequency approaches the average spontaneous break-up frequency<sup>22</sup>. The operating window for the parameter settings that lead to operation without the creation of satellites is very narrow. Additionally, instabilities of the jet break up, like varicose or kink instabilities<sup>23</sup>, increase the polydispersity of the droplet size. The monodispersity of the droplets sizes can be improved by operating the system close to the onset voltage of the CJM<sup>24</sup>.

The size of the primary crystals resulting from the EC process is directly related to the size of the droplets from which they crystallize. The crystal size increases with the droplet size, as well as with the concentration  $c_i$  of the solute in the solvent. For larger droplet sizes, more solvent needs to be evaporated, for which a larger distance is required. At higher concentrations, more solute is present in each droplet, resulting in a larger particle after complete evaporation of the solvent. The concentration of solute in turn affects the liquid properties, because properties like density and electrical conductivity of a solution are different from that of a pure solvent. Changing fluid properties from pure solvent to solution consequently means changing the electrospray

process. This must be accounted for in achieving operation in the cone jet mode, by adjusting the electric field or other parameters accordingly.

The aforementioned considerations show that the operating window is very narrow, even compared to an electrospray process without a crystallization step, since a balance must be found between solvent choice, concentration of solute and operating distance, in addition to the parameter settings.

#### *Low yield/material loss*

The yield  $Y$  of the electrospray crystallization process is defined as:

$$Y = \frac{M}{c_i \cdot V_{tot}} \cdot 100\% \quad (5.1)$$

where  $M$  is the mass of collected crystals in [mg],  $c_i$  is the concentration of these crystals in the solution being sprayed in [mg/mL] and  $V_{tot}$  is the volume of solution that has emerged from the nozzle in [mL]. The yield, using the TNT/RDX samples and the conventional vertical nozzle-plate setup of our previous work<sup>15</sup>, varied between 25% and 60%. Since it is expected that all particles are charged and thus are attracted to the counter electrode, this yield is dramatically lower than the theoretical yield of 100%. There are several causes for material losses in EC. Apart from the loss of solvent, which is evaporated, the loss is divided into three parts: loss due to encrustation, loss due to degradation and loss due to non-collected material.

#### Encrustation

One type of loss is the crystallization on the nozzle tip. Due to the wetting of the nozzle tips by the solution and subsequent film evaporation of the solvent, the solution can be supersaturated while still in contact with the nozzle. In **Figure 5.3** examples are shown of the crystal formation on the nozzle tips. The encrustation on the nozzle tips in **Figure 5.3** took on average in the order of a minute to form. The crystal deposition on the nozzle in **Figure 5.3 (a)** grew in phases, where first a thin layer of solid material was deposited around the nozzle, from which dendrites formed one at a time. The growth of a single dendrite could be finished in under a second. It was observed that, intermittently, new sprays initiated from the tips of the dendrites. The solvent is drawn to the tips to feed the intermittent sprays that have been observed, which are caused by local peaks in the electric field strength. These peaks are due to the field lines of the electric field focusing on the wet and conductive dendrite tips, creating a high flux of field lines and thus a strong electric field.

Sometimes a single dendrite broke off and fell on the collection plate. On the nozzle of **Figure 5.3 (b)** a ring-shaped deposition can be observed. Given time, on occasion the ring shape grew in the downward direction into a spherically shaped deposition, as seen on the nozzle in **Figure 5.3 (c)**. The

nozzle opening was completely surrounded by the deposition, which occasionally blocked the nozzle entirely. After the crystals have grown to a certain size, they have been observed to fall down from the nozzle onto the collecting plate. After this event, new crystalline material deposited onto the nozzle tips and the process repeated itself. For any type of encrustation, instabilities of the cone-jet occurred, such as multiple or intermittent jets, which was for instance observed by Moerman et al.<sup>25</sup>. In the case of the dendritic crystals in **Figure 5.3 (a)**, smaller pieces of the dendrite broke off prematurely and landed on the collecting plate, in addition to the entire structure falling off. The losses due to encrustation constituted as much as 25 – 50% of the total material loss<sup>15</sup>.

To prevent the encrustation at the nozzle, the first step is to prevent wetting of the nozzle. **Figure 5.3 (d)** shows a schematic of a nozzle tip with several parameters illustrated. There are two aspects that can be optimized separately; the nozzle geometry, i.e. the physical angle  $\phi$  and the wall thickness  $W$  (difference between inner and outer nozzle diameters  $D_{N,in}$  and  $D_{N,out}$ ), and the nozzle material, resulting in a different contact angle  $\theta$  of the solution. The nozzle material and angle must be optimized such, that the solution does not wet the nozzle.

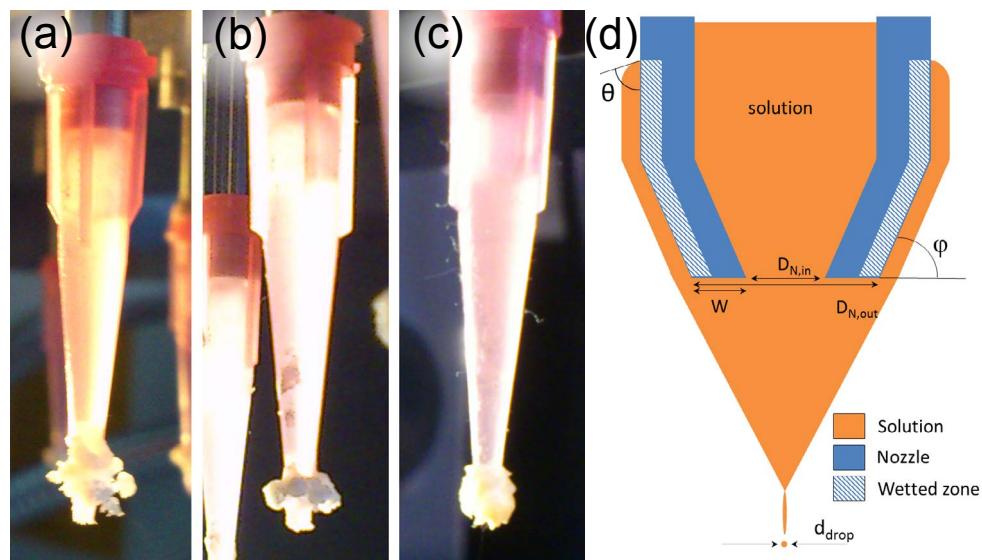


**Figure 5.3:** Examples of crystallization at and wetting profile along the nozzle tip. (a) irregularly shaped encrustation, (b) ring-shaped encrustation, (c) ring-shaped encrustation grown downwards to completely cover and block the nozzle, (d) Schematic of a nozzle tip with several parameters illustrated. The shaded region at the outside of the nozzle represents the 'wetted zone' of the nozzle.  $\theta$  is the wetting angle,  $\phi$  is the nozzle angle,  $D_{N,in}$  is the inner diameter of the nozzle,  $W$  the wall thickness and  $D_{N,out}$  the outer diameter,  $d_{drop}$  is the initial droplet diameter.

Any range of materials is possible, as long as it is resistant to the chemicals used in the process. The material does not need to be conductive, since the liquid carries the charge. Common nozzle materials are stainless steel, PTFE, polyethylene and other polymers. Additionally, coatings or linings can be applied to create a difference between the inside and the outside of the nozzle, e.g. to inhibit crystallization inside the nozzle and prevent wetting outside the nozzle. In our experiments it was found that while stainless steel tips worked well for the CAF-INA system, with the spraying of TNT smooth flow tapered tips made from polyethylene showed less encrustation. Some considerations on nozzle design are given by Lefebvre (1989)<sup>26</sup>. Additionally, the concentration of the solute in the solvent can be lowered to delay the crystallization. However, lowering the concentration also decreases the particle size, which may be undesired. Consequently, a higher flow rate may be required to obtain the desired particle size, which increases the drying distance. A final option for preventing encrustation is by the addition of crystallization inhibitors do delay the crystallization until after the solution is separated from the jet. However, the inhibitor would end up in the final product, which may be undesirable.

Any method to eliminate encrustation of the compound on the nozzle tips leads to an increased yield, as well as more stable operation of the process. Therefore, this is a very important issue to solve.

#### Degradation

**Figure 5.4** shows the loss due to tip encrustation during an electro spray crystallization experiment, clearly showing an imprint of the conical nozzle tip in the encrusted particles. The encrustation in **Figure 5.4**, containing TNT and RDX, is mainly light yellow. However, at some edges the encrustation is pink. This color change from light yellow to pink indicates the degradation of TNT during the experiment. It was found that the solvent, acetone, dramatically increased the decomposition rate of the dissolved TNT. It is likely



**Figure 5.4:** Example of material losses from an EC experiment using TNT and RDX in acetone

that the applied charge increased the decomposition rate even further. Also in other systems the applied electrical charge can cause the solvent or solute to react. The choice of what polarity to use for a spray depends on this, since it effectively determines whether the nozzle acts as a cathode or an anode. Some solvents promote reactions of this kind, as in the case with acetone and TNT, which makes solvent selection a crucial step. Some systems are not suitable for use in an electrospray setup at all, in which case other methods of producing small particles should be considered, such as anti-solvent crystallization, grinding or supercritical processes.

### Collection

A third cause of the loss is due to the particles not reaching the collector plate. Any gas flow present could carry these small particles away from the setup. If nanoparticles are released into open air, they pose a potential threat to the environment. A part of this evacuation is that of satellite droplets. These droplets move away from the center of the spray faster than the larger droplets. Evidence of this evacuation can be found in **Figure 4.3 (insert)**, where beside (above) the main spray, a weaker flow of particles is seen, curving away from the center. In other instances the satellites were observed to curve in the upwards direction and thus away from the counter electrode. This loss type can be reduced by using a closed system and redissolution of the materials deposited on the walls of the closed system. However, a closed system may pose drying issues, since vapor can build up in the direct environment of the spray, decreasing the driving force for solvent evaporation. This can be solved by using a guiding air flow to flush the environment. An added benefit of using a closed system is that also the evaporated solvent can be recovered, which otherwise would be lost to the environment. Additionally, it is easier to work with elevated or reduced temperatures creating an additional process parameter for control. Alternatively, the external electrical field can be tailored to guide the entire spray to the collection area.

### *Product handling*

In the collection of the particles, two important decisions must be made, depending on the demands on the product. It must be decided whether the particles are allowed to aggregate, and whether they are allowed to adsorb ambient water on their surface or even in their crystal structure. Both these choices have implications for the process configuration.

### Aggregation

During electrospray crystallization, the question arises whether aggregation of the crystals is a problem. Batches of submicron-sized particles have a natural tendency to aggregate into clusters of around 30 microns. The clusters do keep an internal nanostructure. With the nozzle-plate configuration in electrospray crystallization this aggregation is promoted, since the aerosol is attracted to the same place and particles will deposit close to, or on top

of each other, as can be seen in **Figure 5.5 (a)**. If this is undesired, a number of options is available to avoid this from happening. In the case that only a small amount of crystals suffices, e.g. in polymorph studies, the nozzle-plate configuration can be used without any changes. Using a short spraying time yields the desired material, like in **Figure 5.5 (b)**. If large amounts need to be produced, the aggregation needs to be actively avoided. How this is done depends on the product requirements. Different solutions are available for deposited materials or uncharged aerosols.

For deposited materials, the deposition substrate can be either solid or liquid. With deposition in a liquid substrate, as seen in **Figure 5.6 (a)**, the particles are collected in a stirred liquid. The liquid must have a low surface tension, so that the crystals can penetrate in the bulk part of the liquid instead of aggregating at the surface. Additionally, the compound must be insoluble in the solvent, to prevent ripening and solvent mediated transformations. When a solid substrate is desired, the substrate must be moving in order to provide a clean surface for the newly deposited particles, as is shown in **Figure 5.6 (b)**. A downside of this is the relatively large surface area of substrate required for only a small amount of material.

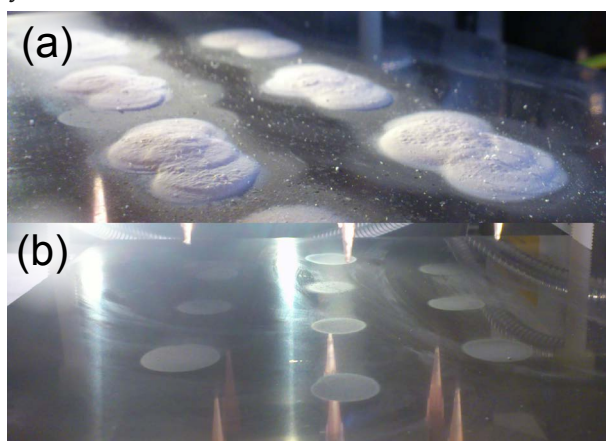


**Figure 5.5:** Collection of charged particles onto a static solid substrate. (a) If the particle density on the surface is large, it possibly results in aggregates, (b) if the particle density on the surface is small, less aggregation occurs and thus less agglomeration.

If an uncharged aerosol is the desired form of the product, e.g. for asthma medicine, the droplets or particles need to be relieved of their charge while still suspended in the air. Globally two discharging methods can be applied: either bipolar coagulation<sup>27</sup>, or corona discharge can be used. Bipolar coagulation can discharge the main spray by introduction of a second spray containing the same solvent, of equal flow rate but of opposite potential, near to the main spray, so that the droplets from each spray attract each other and discharge upon collision (**Figure 5.6 (c)**). Evaporation of solvent continues throughout the process and still for each droplet of the main spray a sin-

gle particle is produced. Corona discharge functions by introducing a sharp, conducting object as counter electrode, charged sufficiently to ionize the air around it<sup>28</sup> (Figure 5.6 (d)).

Variations on these setups may be desirable for stabilization or functionalization, examples of which are described by Hartman<sup>29</sup>. For example, in bipolar coagulation setups a (different) solute may be added to the second spray to induce microencapsulation<sup>30</sup>. Uncharged aerosols have the added benefit that they can be transported by a carrier flow, through which the drying time can be extended. This increases the range of possible solvents. A drawback is that in the uncharged aerosol the particles do not repel each other anymore, which means that the particles can aggregate. However, the extent to which this occurs is very limited, as shown by the measured aerosol size distributions, produced by bipolar coagulation of Borra et al.<sup>31</sup>.

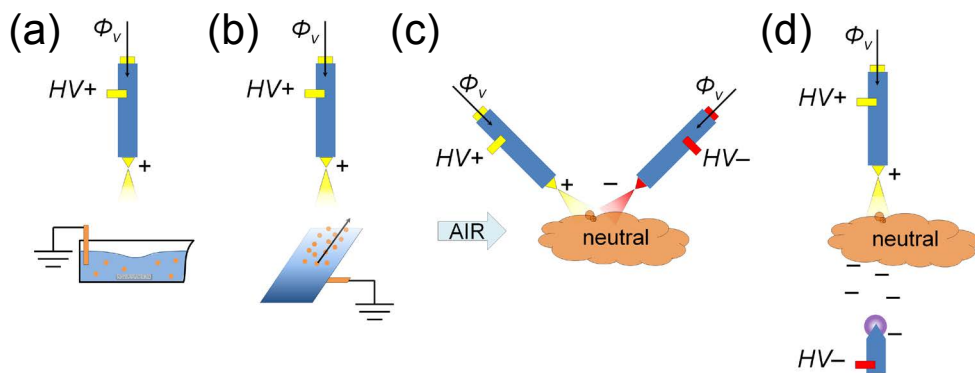


**Figure 5.6:** Different collection mechanisms for EC. (a) collection in a stirred liquid to produce a suspension, (b) collection on a moving substrate to prevent aggregation, (c) discharging the spray by bipolar coagulation and (d) discharging the spray by corona discharge.

### Adsorption

Although the small size of the crystals resulting from EC leads to many benefits, it also has the potential to cause undesired effects. Electro spraying a solution of L-proline in ethanol resulted in the hydrate form of L-proline, as determined by XRPD analysis. However, crystallization of L-proline from ethanol in the bulk usually leads to the anhydrous form. It is most likely that the L-proline initially crystallized in anhydrous form from the ethanol droplets. However, after the full evaporation of ethanol, the crystals were exposed to the air. The moisture content of the environment was most likely sufficient to transform the L-proline into the hydrate form. This transformation was complete within minutes. When more XRPD patterns were recorded of this sample, it was seen that the patterns changed to the anhydrous form over time, due to the hot air flow through the equipment, which takes away the moisture from the sample. The transition takes place within 10 - 30 minutes, indicating that the transitions are quite fast, which is attributed to the small size of the crystals.

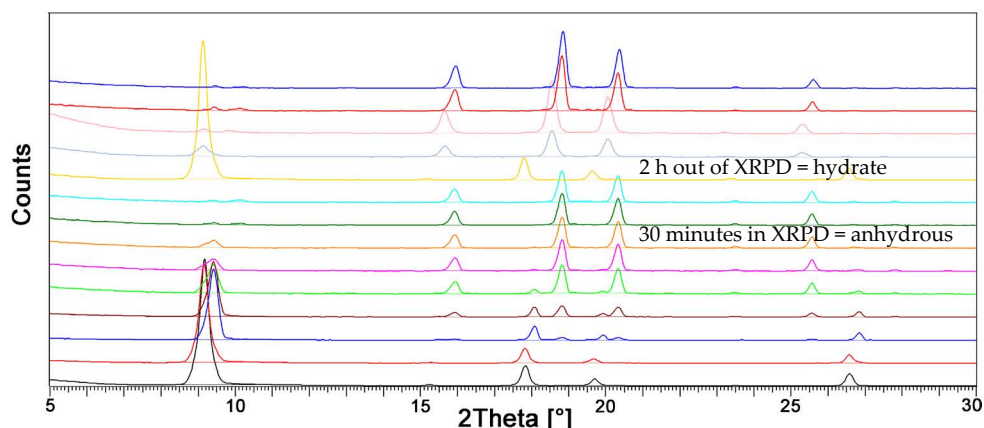


**Figure 5.7:** XRPD patterns of L-proline after electrospay crystallization from ethanol over time. Initially, the hydrate form is measured. Inside the cavity, the hydrate is evaporated out of the structure to reveal the anhydrous form. After leaving it out of the cavity, the hydrate form returns.

Since both the hydration and dehydration of the crystals occur fast, it can be considered to accept that hydration happens, and to dehydrate the crystals before use. When the hydration is undesired at all, for example because the dehydrated crystal structure is very different from the anhydrous structure, or because dehydration causes undesired loss of structural integrity of the crystal, contact of the crystals with air of high relative humidity must be prevented. This can be done by using a closed system, in which a dry environment is used. For the continuous production of crystals, a dry air flow must then be provided to prevent saturation of the environment with solvent. The use of a closed system even allows for other environments than (dry) air to be introduced. The use of e.g. vacuum or  $\text{CO}_2$  environments can be beneficial for liquids that are difficult to spray, for example due to a high surface tension or conductivity. Despite making the process more complex, it has a positive effect on the operating window.

### 5.3.3. Design tool

The solutions to the problems mentioned in **Section 3.2** overlap and need to be balanced against each other to arrive at a properly working electrospay crystallization process. In order to arrive efficiently at an optimal process for the product, where the aforementioned issues are addressed, we provide a diagram that illustrates the sequence of decisions and tests that lead to working solutions in an efficient way. The diagram is based on working with the nozzle-plate configuration with flow rates in the range of  $10^{-2}$  – 10 ml/h and working distances from 1 – 10 cm, where the electrical potential, applied to the nozzle, is adjusted to achieve operation in the cone jet mode (up to 10 kV). Other collection methods can be chosen once the nozzle-plate configuration is optimized. The design tool is shown in **Figure 5.8**, in which

the green blocks represent actions to be taken, orange ones are observations done during testing and the purple blocks are guidelines that aid decision making.

Since the process is designed around producing particles of a certain size of a specific compound, the compound is taken as the starting point of the diagram. From there, eight major design steps are taken to arrive at a properly working system.

### 1. Choosing a solvent

The first important step to be taken is to choose a solvent. The solvent must fulfil three requirements: 1) the compound must be soluble in it, 2) it must be sprayable and 3) it must have a high vapor pressure. For a liquid to be easy to spray, Cloupeau and Prunet-Foch<sup>23</sup> arrived at the following 'low' and 'high' values of the fluid properties:

- Electrical conductivity  $K = 10^{-9} - 10^{-1}$  S/m
- Surface tension  $\gamma = 0.022-0.073$  N/m
- Viscosity  $\mu = 0.4-1,500$  mPa·s

These values can be used as guidelines during solvent selection. The third requirement for the solvent, to have a high vapor pressure, follows from the fact that it needs to evaporate rapidly. It is advised to choose solvents with a vapor pressure of  $P^{sat} = 10$  kPa. Solvents with a lower vapor pressure may also be used, but higher vapor pressures facilitate the operation. Commonly used solvents such as ethanol, methanol and acetone fall within these boundaries and can therefore be used for EC.

### 2. Choosing a concentration

Once the solvent is chosen, a suitable concentration must be determined. The concentration of the compound affects many properties, such as the regular spray behavior, the extent of encrustation and the particle size. To increase throughput and decrease the required amount of solvent, the concentration of the compound should be chosen as high as possible. However, the concentration, in relation to the solubility of the compound, is a factor that greatly influences the extent of encrustation. Since encrustation is identified as one of the major issues, it is important to prevent it. For this reason, a lower concentration is often required. In previous work, an undersaturation ratio ( $y_i$ ) is defined as the concentration of the compound  $c_i$  divided by the equilibrium concentration at 20°C,  $c_i^*$ <sup>15</sup>. During our experiments, it was found that not only the concentration relative to the solubility determines spray behavior. For constant values of the undersaturation ratio  $y_i$ , compounds with a high solubility proved to be more difficult to spray than compounds with a lower solubility. This is attributed to the effect that the solute has on the fluid properties, e.g. conductivity. For the same values of  $y_i$ , the absolute concentration  $c_i$  is much higher for better soluble compounds, causing higher deviations from the preferred range of the fluid properties. There-

fore, it is advised to choose lower undersaturation ratios for better soluble compounds and keep the absolute concentration  $c_i$  low. However, for the particle size and the solid throughput, it can be desirable to use higher concentrations. This leads to the solubility dependent choice of concentration as is given in **Figure 5.8**, which states that for compounds with a low solubility ( $c_i^* = 10 \text{ mg/mL}$ ), the undersaturation ratio can be chosen relatively high ( $y_i = 50\%$ ). For a high solubility ( $c_i^* = 10 \text{ mg/mL}$ ), the undersaturation ratio should be chosen much lower ( $y_i = 10\%$ ). These values are rough guidelines, based on the results of various EC experiments conducted with CAF, INA, RDX, TNT and combinations thereof.

### *Testing*

After the concentration is chosen, the setup can be built in a simple nozzle-plate configuration and the initial test can be performed. During this test, several pieces of information can be gathered and actions can be undertaken to improve the operation.

### **3. Degradation**

Before even trying to obtain a stable CJM, it is advised to determine whether degradation of the product occurs during operation. If this is the case, the polarity can be changed in order to solve the problem. If the product is still subject to degradation after the polarity change, electrospray crystallization is not the most suitable technique for micronizing the product, and other methods should be chosen. In such a case no further investigations are required. In case no degradation occurs, the diagram can be followed to the next step.

### **4. Obtaining stable cone jet mode**

With the chosen solvent and concentration it is now imperative that a stable CJM is achieved to obtain a monodisperse aerosol of (sub-)micron sized droplets of solution. Parameters like the flow rate and electric field strength must be adjusted to achieve the CJM. However, if in all configurations of these parameters a stable CJM is not achieved, it is possible that the concentration of the solute is chosen so high that one of the fluid properties (e.g. electrical conductivity) pass the preferred operating boundaries. In such a case, the concentration needs to be lowered until a stable CJM can be obtained. Once operation in the stable CJM is achieved, there are two requirements that can be assessed simultaneously; obtaining dry particles and avoiding encrustation. However, we treat them in succession here and start with obtaining dry particles.

### **5. Obtaining dry crystals**

A major requirement in EC is that the solvent completely evaporates and dry crystals are obtained. If this is not the case with the basic setup, there are two solutions. Either the drying distance can be increased, or the solvent can be changed. The easiest option is to increase the drying time of the droplets

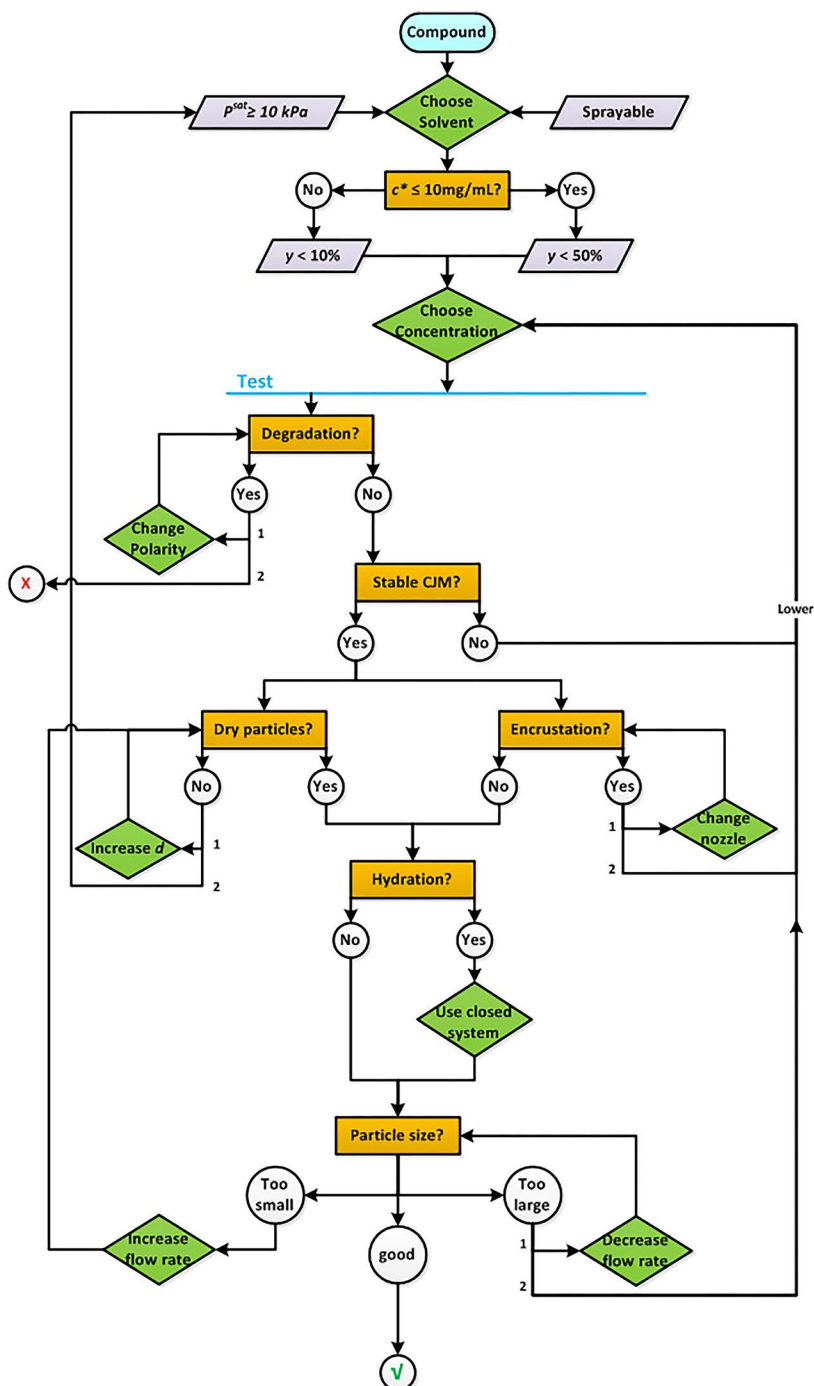


**Figure 5.8:** Design tool for electro spray crystallization in the nozzle-plate configuration. Green blocks are actions, orange ones are observations, the lilac blocks are guidelines that aid decision making. The red cross means that EC is not the most suitable process, the green check mark means an optimized design is achieved.

by creating a longer pathway from the nozzle to the collector. In **Section 5.3.2** suggestions are given how to do that. In the case that very long drying distances still deliver a wet product, the solvent should be changed to one that does fully evaporate. Alternatively, accompanying dry air flows may be utilized to remove the solvent vapor from the spray area.

### 6. Avoiding encrustation

When encrustation is visible on the nozzle, changes are required to enable proper operation. Especially when looking at out-scaling the process, this encrustation must be eliminated. There are several possible actions that help prevent the premature nucleation. The most important is to prevent the solution from wetting the nozzle, like in **Figure 5.3 (d)**. There are several ways to change the nozzle design so that no wetting takes place, which are discussed in **Section 5.3.2**. If encrustation still occurs on the nozzle tips, the concentration of the compound in the solvent can be decreased. In this case, extra attention must simultaneously be given to step 5, since relatively more solvent needs to be evaporated before dry crystals are obtained. In addition to lowering the concentration, crystallization inhibitors may be added to the solution to delay nucleation. When the encrustation issue is solved, the operation of the electrospray process itself is generally feasible. The last two points to be addressed are related to the product quality.

### 7. Hydration of crystals

The crystals obtained from electrospray crystallization are so small, that their specific surface area is very large. For hydrate forming compounds, moisture is quickly taken up in the crystal structure. If, through analysis of the crystals, this hydration is found, it must be decided whether this is undesired or not. If hydration is undesired, it can be prevented by using a closed system and providing an atmosphere in which the concentration of water is very low. If no hydration occurs, or if the product can be dried just before use, no adjustments are required and the last design step can be made.

### 8. Obtaining desired particle size

The diagram in **Figure 5.8** is given to arrive at a process that produces particles of a specific compound having a specific size. To arrive at the desired particle size is the last step in optimizing the EC process. From the basic tests, the particle size can be measured with the aid of either a microscope or a SEM. If the particles are smaller than desired, the flow rate of the solution can be increased to achieve larger droplets and thus larger crystals. Upon increasing the flow rate, the design tool has to be rerun from step 5 to ensure that dry product is still obtained. On the other hand, if they are larger, either the flow rate or the concentration can be decreased. Decreasing the flow rate should have priority, since that will reduce the amount of solvent required for operation. If the concentration is decreased, steps 4 – 8 require repeating. Once the particle size is as desired, a good product is obtained and the EC process is optimized in the nozzle-plate configuration. The most important

parameter settings are determined after completing the design diagram: solvent, concentration of the compound, polarity of the electric potential, minimum sampling distance, nozzle design, open or closed system and the flow rate used. The potential difference between the nozzle and the counter electrode is also determined. Starting from this configuration, the process can be tuned even further. For example, if the yield is too low, the electric field can be customized to guide more crystals toward the collector. From this configuration it is also possible to introduce a discharge mechanism, like in **Figure 5.6 (c)** or **(d)**, so that an uncharged aerosol is generated.

In the case that bipolar coagulation is used, even an encapsulation step can be added. Additionally, the throughput can be increased by using an array of nozzles in this configuration. In this case it is of utmost importance that no encrustation occurs on the nozzles. Such customizations will tailor the process to obtain the product in the desired form. Following the entire flow sheet in **Figure 5.8** the experimental design phase significantly reduces the number of experiments required to achieve a stable EC process that does not suffer from too much material losses. Moreover, the threshold for new investigations of electrospray crystallization as a means to produce (sub)micron-sized crystals with a narrow size distribution, in favor of other methods, is lowered significantly due to the increased efficiency of the design step.

## 5.4. Conclusions

Electrospray crystallization is a promising technique for the production of (sub)micron-sized crystals, since for analysis or high value added purposes it can very well provide the particles with the desired average size and properties. However, apart from scaling up the process, challenges are involved with the design of an experimental setup. From the basis of a regular needle-plate electrospray operation, we identified the added challenges when a crystallization step is combined with this process. Choosing the right solvent and solute concentration were identified as the most important starting steps. Preventing crystallization at the nozzle tips was identified as the most important action in operation. The experimental results have been combined to construct a design tool for electrospray crystallization processes, which aims at increasing the efficiency of the experimental and process design phase and avoiding too much trial and error. The increased efficiency in the design step serves to lower the threshold for new investigations in utilizing this elegant process for the production of (sub)micron-sized crystals with a narrow size distribution.

## 5.5. References

1. Blagden, N.; de Matas, M.; Gavan, P. T.; York, P., Crystal engineering of active pharmaceutical ingredients to improve solubility and dissolution rates. *Advanced Drug Delivery Reviews* **2007**, 59, 617-630.
2. Duhem, N.; Danhier, F.; Pr at, V., Vitamin E-based nanomedicines for anti-cancer drug delivery. *Journal of Controlled Release* **2014**, 182, 33-44.
3. Brough, C.; Williams Iii, R. O., Amorphous solid dispersions and nano-crystal technologies for poorly water-soluble drug delivery. *International Journal of Pharmaceutics* **2013**, 453, 157-166.
4. Vitry, Y.; Teychen , S.; Charton, S.; Lamadie, F.; Biscans, B., Investigation of a microfluidic approach to study very high nucleation rates involved in precipitation processes. *Chemical Engineering Science* **2015**, 133, 54-61.
5. Longuet, C.; Yamada, A.; Chen, Y.; Baigl, D.; Fattaccioli, J., Spatially-controlled protein crystallization in microfluidic chambers. *Journal of Crystal Growth* **2014**, 386, 179-182.
6. Morissette, S. L.; Almarsson,  .; Peterson, M. L.; Remenar, J. F.; Read, M. J.; Lemmo, A. V.; Ellis, S.; Cima, M. J.; Gardner, C. R., High-throughput crystallization: polymorphs, salts, co-crystals and solvates of pharmaceutical solids. *Advanced Drug Delivery Reviews* **2004**, 56, 275-300.
7. Thomas, B. R.; Carter, D.; Rosenberger, F., Effect of microheterogeneity on horse spleen apoferritin crystallization. *Journal of Crystal Growth* **1998**, 187, 499-510.
8. Ciach, T.; Geerse, K. B.; Marijnissen, J. C. M., EHDA in Particle Production. In *Nanostructured Materials, Selected Synthesis methods, Properties and Applications*, Schoonman, P. K. a. J., Ed. Kluwer Academic Publishers **2004**; pp 43-53.
9. Cloupeau, M.; Prunet-Foch, B., Electrostatic spraying of liquids: Main functioning modes. *Journal of Electrostatics* **1990**, 25, 165-184.
10. Grace, J. M.; Marijnissen, J. C. M., A review of liquid atomization by electrical means. *J. Aerosol Sci.* **1994**, 25, 1005-1019.
11. Xie, J.; Jiang, J.; Davoodi, P.; Srinivasan, M. P.; Wang, C.-H., Electrohydrodynamic atomization: A two-decade effort to produce and process micro-/nanoparticulate materials. *Chemical Engineering Science* **2015**, 125, 32-57.
12. Mullin, J. W., *Crystallization. 3 ed.*; Butterworth-Heinemann Ltd.: Oxford, **1993**.
13. Radacsi, N.; Stankiewicz, A. I.; Creighton, Y. L. M.; Heijden, A. E. D. M. v. d.; Horst, J. H. t., Electrospray Crystallization for High-Quality Submicron-Sized Crystals. *Chem. Eng. Technol.* **2011**, 34, 624-630.
14. Ijsebaert, J. C.; Geerse, K. B.; Marijnissen, J. C. M.; Scarlett, B., Electrohydrodynamic spraying of inhalation medicine. *Journal of Aerosol Science* **1999**, 30, S825-S826.

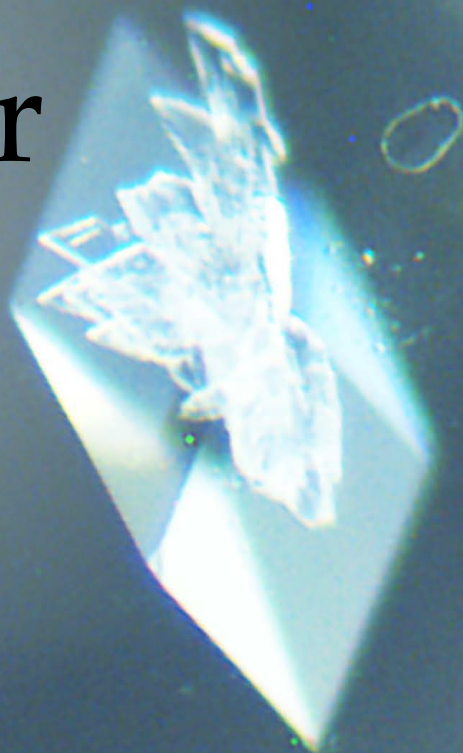
15. Reus, M. A.; Hoetmer, G.; van der Heijden, A. E. D. M.; ter Horst, J. H., Concomitant crystallization for in situ encapsulation of organic materials. *Chemical Engineering and Processing: Process Intensification* **2014**, *80*, 11-20.
16. Xie, J.; Marijnissen, J. C. M.; Wang, C.-H., Microparticles developed by electrohydrodynamic atomization for the local delivery of anticancer drug to treat C6 glioma in vitro. *Biomaterials* **2006**, *27*, 3321-3332.
17. Rayleigh, L., XX. On the equilibrium of liquid conducting masses charged with electricity. *Philosophical Magazine Series 5* **1882**, *14*, 184-186.
18. Rezvanpour, A.; Wang, C.-H., The Effects of Auxiliary Electric Field within the Electrohydrodynamic Atomization Encapsulation Chamber on Particle Size, Morphology and Collection Efficiency. *Chemical Engineering Journal* **2013**.
19. Xie, J.; Lim, L. K.; Phua, Y.; Hua, J.; Wang, C.-H., Electrohydrodynamic atomization for biodegradable polymeric particle production. *Journal of Colloid and Interface Science* **2006**, *302*, 103-112.
20. Gu, W.; Heil, P. E.; Choi, H.; Kim, K., Comprehensive model for fine coulomb fission of liquid droplets charged to Rayleigh limit. *Applied Physics Letters* **2007**, *91*, 064104-1 - 3.
21. Gomez, A.; Tang, K., Charge and fission of droplets in electrostatic sprays. *Physics of Fluids* **1994**, *6*, 404-414.
22. Cloupeau, M., Recipes for use of EHD spraying in cone-jet mode and notes on corona discharge effects. *Journal of Aerosol Science* **1994**, *25*, 1143-1157.
23. Cloupeau, M.; Prunet-Foch, B., Electrohydrodynamic spraying functioning modes: a critical review. *Journal of Aerosol Science* **1994**, *25*, 1021-1036.
24. Tang, K.; Gomez, A., Monodisperse Electrospays of Low Electric Conductivity Liquids in the Cone-Jet Mode. *Journal of Colloid and Interface Science* **1996**, *184*, 500-511.
25. Moerman, R.; Frank, J.; Marijnissen, J. C. M.; Schalkhammer, T. G. M.; van Dedem, G. W. K., Miniaturized Electro spraying as a Technique for the Production of Microarrays of Reproducible Micrometer-Sized Protein Spots. *Analytical Chemistry* **2001**, *73*, 2183-2189.
26. Lefebvre, A. H., Properties of Sprays. *Particle & Particle Systems Characterization* **1989**, *6*, 176-186.
27. Camelot, D.; Marijnissen, J. C. M.; Scarlett, B., Bipolar Coagulation Process for the Production of Powders. *Ind. Eng. Chem. Res* **1999**, *38*, 631-638.
28. Meesters, G. M. H.; Vercoulen, P. H. W.; Marijnissen, J. C. M.; Scarlett, B., Generation of micron-sized droplets from the Taylor cone. *Journal of Aerosol Science* **1992**, *23*, 37-49.
29. Hartman, R. P. A. Electrohydrodynamic Atomization in the Cone Jet Mode. From **Physical Modeling to Powder Production**. Delft University of Technology **1998**.

30. Langer, G.; Yamate, G., Encapsulation of Liquid and Solid Aerosol Particles to Form Dry Powders. *Journal of Colloid and Interface Science* **1968**, 29, 450-455.

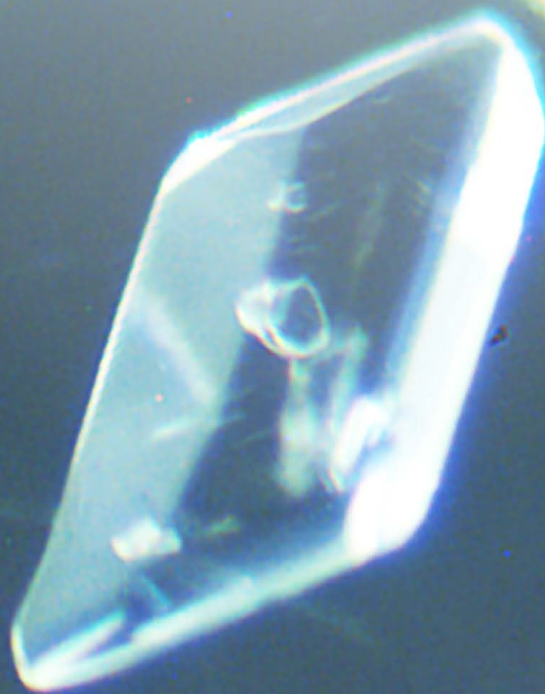
31. Borra, J. P.; Camelot, D.; Chou, K.-L.; Kooyman, P. J.; Marijnissen, J. C. M.; Scarlett, B., Bipolar Coagulation for Powder Production: Micro-mixing Inside Droplets. *J. Aerosol Sci.* **1999**, 30, 945-958.

Chapter

6



Crystal nucleation of  
fenofibrate in encapsulated  
solution droplets



## Abstract

In this paper a method is presented to measure the crystal nucleation rate in small droplets of solution. Thereto, by means of a dripping method, droplets of fenofibrate solution in heptane were encapsulated in a core-shell configuration with a rigid layer of calcium alginate. Due to the transparent nature of the hydrogel encapsulant, the appearance of crystals in the encapsulated solution droplets could be monitored under the microscope. Sets of core-shell particles with solution droplets of 194 and 12 nL were produced, containing high concentrations of fenofibrate in heptane. The encapsulated solution droplets were cooled to a low, constant temperature to induce nucleation, enabling the determination of induction time probability distributions. It appeared that a large fraction of the droplets was inactive, indicating that effective heterogeneous particles were only present in some droplets. Accounting for the presence of heterogeneous particles, the heterogeneous nucleation rate was determined. Also growth rates could be determined which were found to reduce rapidly in time, due to depletion of the solution by the growing crystal.

## 6.1. Introduction

Modern drug discovery techniques produce increasing numbers of active pharmaceutical ingredients (API) with a lipophilic nature, which are poorly water soluble and therefore have a low bioavailability<sup>1-4</sup>. In order to increase the bioavailability of low solubility drugs, a trend is seen towards the production of smaller crystals, with the goal to increase the dissolution rate<sup>5-7</sup>. For the direct production of such small particles in a crystallization process, control, and therefore understanding, of the crystal nucleation and growth are essential. However, to date crystal nucleation is not well understood<sup>8, 9</sup>. Especially primary nucleation mechanisms, both homogeneous and heterogeneous, require more investigation.

Many independent experiments must be performed under well-controlled conditions to capture the stochastic behavior of the nucleation<sup>10</sup>. Both stirred<sup>10-12</sup> and unstirred<sup>13-15</sup> methods are available. Earlier techniques for unstirred small volume crystallization studies employ microfluidics<sup>13, 16-18</sup> or microwell plates<sup>15, 19</sup>. To our knowledge, up to now, encapsulation techniques were not employed to create confined solution droplets for nucleation studies.

We propose a new method of producing small pockets of solution using microencapsulation. Microencapsulation is a technique in which a shell material, mostly solid, completely isolates a core, which can be solid or liquid, yielding small encapsulated droplets ( $< 1 \text{ mm}$ )<sup>20</sup>. Microencapsulation of liquids is widely used for a variety of applications, e.g. to protect a core from oxidizing<sup>21</sup>, for drug delivery<sup>22</sup>, or for capsular perstraction processes<sup>23</sup>. Our aim is to microencapsulate solution droplets with a transparent hydrogel and subsequently measure nucleation rates in these droplets. We used fenofibrate (Fen) in heptane (Hep) as a model system. Fenofibrate is an active pharmaceutical ingredient used to reduce cholesterol and triglyceride levels in the blood. The most commonly used polymorph of fenofibrate is form I, which is the most stable form<sup>24</sup>. Two metastable forms have also been identified: form II, produced by recrystallization from the melt<sup>24</sup> and form III, grown on heterogeneous talc particles<sup>4</sup>. Like many other lipophilic drugs, Fen is an active pharmaceutical ingredient (API) with a very low water solubility ( $0.087 \pm 0.001 \text{ mg/mL}$ )<sup>25</sup>.

## 6.2. Materials and Methods

All materials were used without further purification, unless stated otherwise. Fenofibrate ( $\geq 99\%$ ), heptane (99%), alginic acid sodium salt from brown algae and  $\text{CaCl}_2 \cdot 2\text{H}_2\text{O}$  ( $\geq 99\%$ ) were purchased from Sigma Aldrich.

### 6.2.1. Solubility in stirred solutions

The Crystal16 multiple reactor system (Technobis) was used to determine the solubility and its temperature dependence, as described in Reus et al.<sup>26</sup>. For solubility measurements, concentrations of Fen in Hep between 10 and 120 mg/mL were used.

### 6.2.2. Crystal Nucleation and Growth in Encapsulated droplets

#### *Encapsulation of droplets*

For the production of the droplets the Encapsulator B-390 from Büchi Labortechnik was used (**Figure 6.1**). The sodium alginate ( $c_{Alg} = 16.5$  mg/mL) was dissolved in water and vigorously mixed to form the encapsulating liquid (1). Solutions of Fen in Hep were prepared with concentrations  $c_{Fen} = 55.2$  and 66.2 mg/mL (2) and heated to 60°C to fully dissolve all crystals. The encapsulating liquid and the Fen solution were led through a concentric nozzle (3) with the Fen solution flowing through the inner orifice. Jet break-up into individual droplets was achieved by vibrations received from the vibration coil (4). For each nozzle suitable flow rates were chosen, such that a continuous, concentric jet was emitted from the nozzle. The vibration frequency was optimized for the droplet formation accordingly.

Two sets of concentric nozzles were used; with inner – outer diameters of 200 – 400  $\mu\text{m}$  and 120 – 200  $\mu\text{m}$ . The stroboscope (5), operated at the same frequency as the vibration unit, was used to verify the droplet formation (6).



**Figure 6.1:** Büchi Encapsulator in core-shell configuration, with 1. Pressure bottle with immobilization mixture, 2. Pressure bottle with solution (red for illustration), 3. Concentric nozzle, 4. Vibration coil, 5. stroboscope for visualization, 6. Jet with droplets, 7. Electrostatic dispersion unit, 8. Cross-linking bath, 9. Controls.

The jet passed through a ring (7) that electrostatically disperses the droplets. The resulting droplets fell into a 100 mM solution (8) of  $\text{CaCl}_2$  at room temperature which induced cross-linking in the encapsulate layer around the Fen solution droplet. The cross-linking solution was saturated with Fen to reduce leakage of the Fen through the gel into the water. The air pressure for pumping (varied between  $P = 400 - 500$  mbar), vibration frequency (varied between  $F = 400 - 850$  Hz), nozzle temperature ( $T_N = 65^\circ\text{C}$ ) and electrostatic potential ( $V = 1,000 - 1,600$  V) were controlled using the control panel on the encapsulator (9) to optimize the continuous droplet formation. The flow rate (varied between  $\Phi_V = 2 - 20$  mL/min) was controlled by both the interplay between the applied air pressure and separate regulating valves for the Fen solution and the encapsulating liquid.

#### *Crystal nucleation and growth*

A Leica Nikon Optiphot 200 was used to observe solution and crystals inside the core-shell encapsulated droplets. For the analysis, collapsed droplets were omitted from the dataset. Likewise, droplets with an air bubble inside were not taken into account: the bubble-solution interface is different from the hydrogel-solution interface, which possibly influences the nucleation in that droplet. The large encapsulated droplets (produced with the 200 – 400  $\mu\text{m}$  concentric nozzles) were immersed in a clear crosslinking solution into a Schott crystal growth rate measurement cell suitable for observation under the microscope. The cell was heated in a water bath to  $60^\circ\text{C}$  for a minimum of 30 minutes to dissolve any crystals inside the droplets. Subsequently, the cell was taken out of the water bath and positioned under the microscope. This took less than 3 minutes. The cell was allowed to cool naturally to room temperature. The starting time  $t_0$  for the induction time measurements was taken as 3 minutes after the measurement cell was taken out of the water bath. Using a microscope, it was verified that at that time no crystals were visible in the droplets.

For the small particles (produced with the 120 – 200  $\mu\text{m}$  concentric nozzles), a cuvet, suspended in a cooling cell, was filled with the core-shell particles in their cross-linking solution. This cell was heated to  $60^\circ\text{C}$  to dissolve the Fen. After a period of at least 30 min at this temperature the cell was rapidly cooled to  $5^\circ\text{C}$  and kept at this temperature. The temperature of  $5^\circ\text{C}$  was chosen for the small droplets since at room temperature no crystallization was observed. The reason for the difference in procedure for the small and large droplets was that the large droplets could not be loaded into the cuvet due to their size. The time at which the cooling liquid reached  $5^\circ\text{C}$  was taken as starting time  $t_0$  for the induction time measurements.

In both cases a measurement run was done in which every minute an image, covering  $12 \pm 2$  large droplets or  $60 \pm 11$  small droplets, was recorded. The measurement run continued for at least 4 hours. At the end of each

measurement run images of droplet collections at various locations in the cell were recorded to investigate the total number of crystallization events and the number of crystallization events in droplets that crystallized in earlier measurement runs.

After heating to dissolve the crystals in the droplets, subsequent measurement runs were performed. At least 7 measurement runs were performed for each droplet size and condition.

The induction time was determined by taking the difference between the time a crystal was detected for the first time and the starting time  $t_0$  of the measurement run. The probability distribution of the induction time was determined by plotting the cumulative fraction of crystallized droplets versus the induction times measured.

For each observed crystal the two characteristic sizes (length and width) were recorded. The change in size as a function of time was determined as the growth rate. The crystal size of all crystals after a measurement run was determined by measuring the two characteristic sizes of the crystals. Although the particle shape varied considerably from crystal to crystal, the volume of the crystals  $V_{cr}$  was estimated assuming a spherical particle shape, by using

$$V_{cr} = \frac{\pi}{6} (L_1 \cdot L_2)^{3/2} \quad (6.1)$$

In which  $L_1$  and  $L_2$  are the measured characteristic sizes of the crystal.

### 6.3. Results and discussion

Solubility measurements of solutions of Fen in Hep were performed, in which clear point temperatures were determined for 16 samples with varying fenofibrate concentration ( $10 \leq c_{Fen} \leq 120$  mg/mL). The results are plotted in **Figure 6.2** (♦). Clear point temperatures were fitted to the van 't Hoff equation<sup>27</sup>, modified such that the concentration in mg/mL could be used instead of the mole fraction, via:

$$x_{Fen} = -\frac{a}{T + 273} + b \quad (6.2)$$

And

$$c_{Fen} = x_{Fen} \cdot 10^3 \frac{M_{Fen}}{M_{Hep}} \rho_{Hep} \quad (6.3)$$

In which  $x_i$  is the mole fraction,  $M_i$  is the molar mass and  $\rho_i$  is the density of the compounds. At 5 and 20°C the solubility is  $8.0 \pm 0.6$  and  $21.6 \pm 1.5$  mg/mL, respectively.

The cloud points, determined during the cooling part of the measurements, fluctuated substantially from measurement to measurement. The resulting metastable zone width (MSZW) therefore varied significantly ranging from at least 10 to more than 40°C. The concentrations  $c = 55.2$  and  $66.2$  mg/mL were chosen as the concentration in the encapsulated droplets, to provide a sufficiently high supersaturation ratio for the nucleation measurements. At these concentrations the supersaturation ratio is  $S = c/c^* = 2.55$  and  $3.06$  at room temperature and  $S = 6.90$  and  $8.27$  at 5°C, respectively.

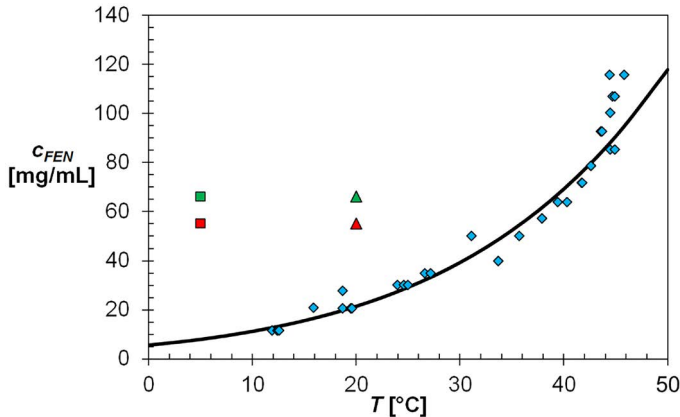


**Figure 6.2:** Temperature dependent solubility (solid black line) of Fen in Hep fitted to the measured clear point temperatures ( $\blacklozenge$ ). Induction times were measured at room temperature in large droplets ( $\blacktriangle$ ) and at 5°C in small droplets ( $\blacksquare$ ) at concentrations of 55.2 (red) and 66.2 mg/mL (green).

### 6.3.1. Encapsulation of solution droplets

The Encapsulator shown in **Figure 6.1** was used for the encapsulation of the Fen/Hep solution droplets. The encapsulated droplet size was influenced by the nozzle diameters, applied flow rate and vibration frequency. In order to produce series of relatively large encapsulated droplets, the concentric nozzle combination 200 – 400  $\mu\text{m}$  was chosen, the combination 120 – 200  $\mu\text{m}$  for the relatively small droplets.

The encapsulated droplets produced with the two different sets of concentric nozzles of 200-400 and 120-200  $\mu\text{m}$  are shown in **Figure 6.3**. The inner diameters of the encapsulated droplets, measured in several experiments, were averaged to  $672 \pm 75$   $\mu\text{m}$  (**a**) and  $295 \pm 45$   $\mu\text{m}$  (**b**), and the corresponding droplet volumes averaged at  $194 \pm 30$  nL (referred to as large droplets) and  $12 \pm 3$  nL (referred to as small droplets), respectively. The corresponding encapsulate layer thicknesses were  $80 \pm 18$   $\mu\text{m}$  and  $44 \pm 7$   $\mu\text{m}$ , respectively. This makes the outer diameter of the encapsulated droplets roughly twice as large as the outer nozzle diameters that were used. For the larger encapsulated droplets, the overall flow rate was approximately 18 mL/min ( $6 \pm 1$  mL/min Fen solution +  $12 \pm 1$  mL/min encapsulating liquid) and the

vibration frequency 400 Hz. For the smaller droplets, the flow rate was approximately 2.3 mL/min ( $0.8 \pm 0.5$  mL/min Fen solution +  $1.5 \pm 0.5$  mL/min encapsulating liquid), while the vibration frequency was 850 Hz.

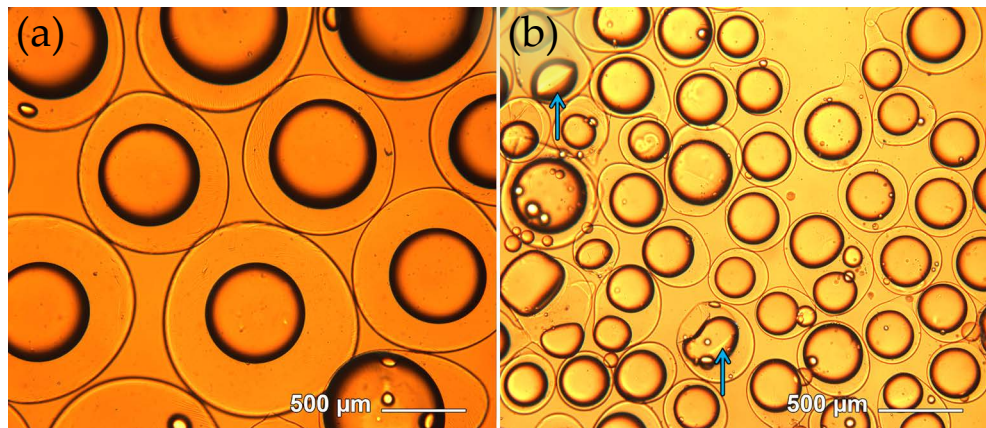


**Figure 6.3:** Droplets of Fen solution in Hep encapsulated by Ca-Alginate, suspended in water. Average inner diameters of these encapsulated droplets are in the range of (a)  $672 \pm 75$   $\mu\text{m}$  and (b)  $295 \pm 45$   $\mu\text{m}$ . The arrows indicate examples of deformed droplets. These deformed droplets were disregarded in the nucleation events.

The jet emerging from the nozzle breaks up into droplets under influence of the vibration applied to it. The encapsulated droplet diameter and shell thickness were mainly influenced by the nozzle diameters, the flow rate of the compounds through the nozzles and the vibration frequency applied to the nozzle. In our experiments, an increase in flow rate caused an increase in droplet and encapsulate size, while an increase in vibration frequency caused a decrease in droplet and encapsulate size. Both these observations are in accordance with the jet break up theory through vibrations by Weber et al.<sup>28</sup> For each nozzle diameter there is an optimum between flow rate and vibration frequency that results in stable, continuous operation and a creation of encapsulated droplets of a specific size. Outside this region, irregular jet break up can occur, resulting in a broad size distribution.

The encapsulated droplets, and in particular the encapsulating layers vary somewhat in size. In addition, sometimes droplets did not break up and ended up as elongated droplet doublets. The width of the size distribution is attributed to the small fluctuations in the flow rates of both liquid feeds (Fen solution and encapsulating liquid) during the encapsulate production. The fluctuations are probably due to fluctuations in the pump action. These fluctuations are more pronounced in the encapsulating liquid due to the higher viscosity. It was further observed that not all droplets are perfectly spherical. Especially in the sets of smaller droplets, some droplets were deformed, examples of which are indicated with arrows in **Figure 6.3(b)**, and were not taken into account. The deformation was most likely caused by the impact

of the droplet with the water surface before cross-linking. However, most droplets were spherical and had similar sizes.

### 6.3.2. Crystallization in droplets

The encapsulated droplets suspended in their cross-linking solution as heating-cooling medium act as separate crystallizers. For the crystallization experiments, the droplets were subjected to a temperature profile. All droplets were assumed to contain the same concentration of Fen as in the feed vessel prior to encapsulation, which was significantly higher than the equilibrium concentration at room temperature. **Figure 6.2** shows the concentrations and temperatures used in the small and large set of droplets. Upon decreasing the temperature after complete dissolution of any crystals in the droplets had taken place at 60°C, supersaturation was created and crystallization could take place inside the droplets. **Figure 6.4** shows an encapsulated droplet in which a single crystal was grown at different times after nucleation. The last picture without a crystal, like the left picture in **Figure 6.4**, was taken as the time  $t = 0$  s.

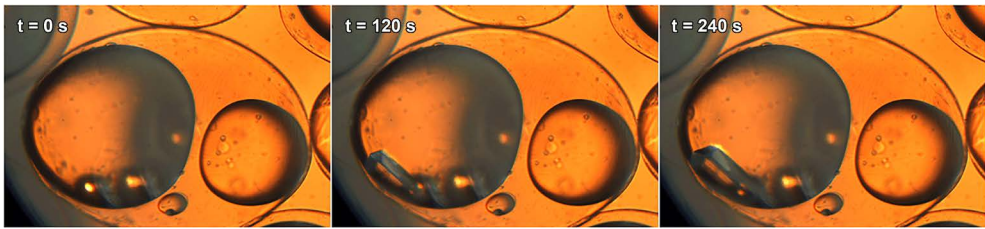


**Figure 6.4:** Growth of a crystal in an encapsulated droplet at different times after nucleation. The concentration of Fen is 55.2 mg/mL. The time  $t = 0$  s is taken as the last picture without a crystal.

#### *Fraction of active droplets*

Preliminary experiments showed that in a time frame of 4 hours only in a small fraction of encapsulated droplets crystallization occurred. It was further noticed in multiple consecutive experiments that previously crystallized droplets had a larger probability of crystallizing in subsequent experiments. **Figure 6.5(b)** shows for instance the single crystals formed in the same droplet after dissolution of the single crystal in the droplet of **Figure 6.5(a)**. This shows that nucleation prefers to occur in specific droplets while other droplets are inactive.

The extent to which such repetitive events occurred was investigated by repeating measurement runs with the same set of droplets. After 4 hours in a measurement run  $i$ , the number  $n_{ce,i}$  of crystallization events was registered as well as the number  $n_{pcd,i}$  of previously crystallized droplets. These lead to the running number  $r_{ce}$  of crystallization events (the total number of crystallization events for run 1 to  $i$  of  $N$  measurement runs) and the running number  $r_{cd}$  of crystallized droplets (the total number of crystallized droplets for run

1 to  $N$ ), corrected for the number of previously crystallized droplets, as a function of the measurement run number:

$$r_{ce,i} = \sum_{i=1}^N n_{ce,i} \quad (6.4)$$

$$r_{cd,i} = \sum_{i=1}^N (n_{ce,i} - n_{pcd,i}) \quad (6.5)$$

These data are plotted for the small droplets with a concentration of 55.2 mg/mL in **Figure 6.5(c)**. From the running number  $r_{ce}$  of crystallization events we can determine an average number  $a$  of crystallization events per measurement run from the slope of the best fitted linear line. The probability to crystallize in a droplet is then:

$$p = \frac{a}{M} \quad (6.6)$$

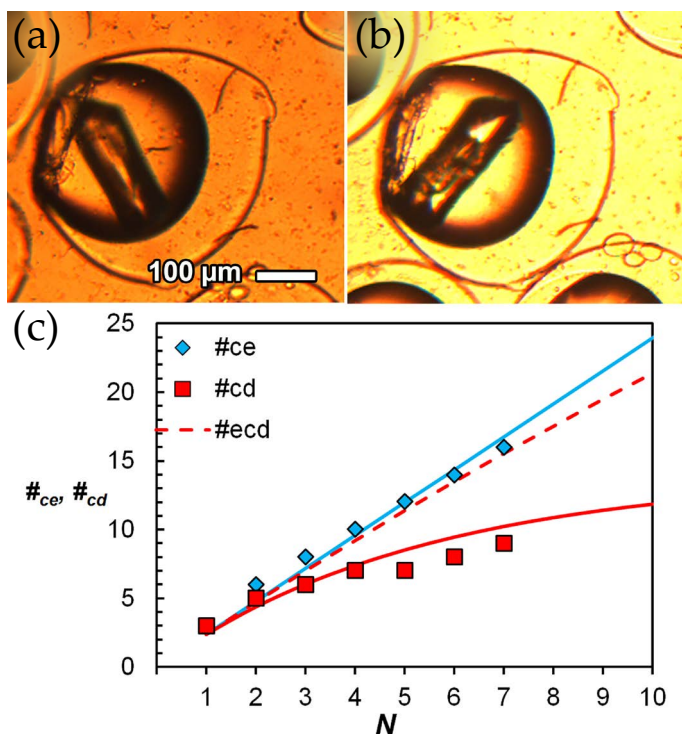


**Figure 6.5:** (a) and (b) A droplet in which nucleation occurred in two consecutive experiments. (c) Number of crystallized droplets  $n_{cd}$  (■) and number of crystallization events  $n_{ce}$  (◆) per measurement run  $i$  in small droplets with a concentration of 55.2 mg/mL, fitted with eq. 6.5 and 6.4, respectively. The number of droplets per measurement run was 94. The expected number of crystallized droplets is also given (---, eq. 6.7).

Where  $M$  is the number of droplets in the set. In the experiment in **Figure 6.5(c)**,  $M = 94$ ,  $a = 2.39$  result in the probability  $p = 0.025$  of a droplet to crystallize. The expected running number  $r_{ecd}$  of crystallized droplets, which assumes that the crystallization events occur randomly in any of the droplets, can be calculated from  $p$  according to:

$$r_{ecd,i} = r_{ecd,i-1} + p(M - r_{ecd,i-1}) \quad (6.7)$$

and  $r_{ecd,0} = 0$ . In **eq. 6.7**, the number of newly crystallized droplets is added to the running number of crystallized droplets from the previous experiment. The expected number of newly crystallized droplets is the difference between the average number of crystallized droplets in measurement  $i$  ( $p \cdot M$ ) and the droplets that are expected to have crystallized in any previous experiments ( $p \cdot r_{ecd,i-1}$ ). The trend is given as a dashed line in **Figure 6.5(c)**. The measured running number of crystallized droplets is significantly lower than that. This means that the number of crystallization events is not randomly distributed over all droplets but prefers to take place in droplets that previously were also crystallized. We attribute this phenomenon to the presence of heterogeneous particles, that apparently are only present in a fraction of the encapsulated droplets. Similar results were obtained for the measurements with higher concentration and in larger droplets.

To determine the concentration of heterogeneous particles, the fraction  $f$  of active droplets containing one or more heterogeneous particles was determined. This fraction was determined to be  $f = 0.15$  for the system in **Figure 6.5(c)**. For the small droplets with  $c_{Fen} = 66.2$  mg/mL the fraction was  $f = 0.20$ . The concentration of heterogeneous particles  $c_{hp}$  was then determined from the number of heterogeneous particles per droplet  $n_{hp}$  and the droplet volume  $V_d$ . Assuming that the heterogeneous particles follow a Poisson distribution over the active droplets, the concentration of heterogeneous particles becomes:

$$c_{hp} = \frac{n_{hp}}{V_d} = \frac{\ln\left(\frac{1}{1-f}\right)}{V_d} \quad (6.8)$$

The concentration of heterogeneous particles amounts to approximately  $(13-19) \cdot 10^3$ /mL. In the large particles with a concentration of 66.2 mg/mL, the fraction of active droplets was determined to be  $f = 0.86$ , yielding a concentration of heterogeneous particles of  $10 \cdot 10^3$ /mL, which is in the same order of magnitude. This supports the hypothesis that the crystallization is driven by heterogeneous particles.

### Final Crystal Size

Leaching of fenofibrate from the droplets through the encapsulation layer could reduce the concentration in the heptane droplets and thereby reduce the likelihood of the formation of crystals in the droplets. Due to the low water solubility of Fen and slow diffusion through the encapsulation layer, it is not expected that fenofibrate escapes from the droplets. To verify that no leaching of fenofibrate takes place, the final size of the crystals was assessed as a measure of initial concentration. At the end of each crystallization experiment, the volume of each crystal  $V_{cr}$  was estimated from the two characteristic sizes ( $L_1$  and  $L_2$ ) visible under the microscope using eq. 6.1.

Additionally, the volume of the droplet in which these crystals were located was estimated. For each of these droplets, the expected crystal volume  $V_{c,t}$  was then calculated based on the concentration and solubility of Fen and the droplet size:

$$V_{c,t} = V_d \frac{c_{Fen} - c_{Fen}^*}{\rho_{Fen}} \quad (6.9)$$

In which the density of fenofibrate  $\rho_{Fen} = 1,180 \text{ kg/m}^3$ . The expected (theoretical) crystal volume was then plotted versus the measured crystal volume in **Figure 6.6**. All data points are scattered around the line  $V_{c,t}/V_{cr} = 1$ , which indicates that the concentration of Fen inside the droplets did not deviate much from that in the feed vessel prior to encapsulation. Additionally, the number of crystallization events in **Figure 6.5(c)** increases linearly with the number of measurement runs, which indicates that the mass fraction of Fen in the droplets is constant over time. From both these findings we conclude that leaching of Fen is not taking place on a regular basis. We assume that this is valid for all droplets. However, it is observed that there is quite a large

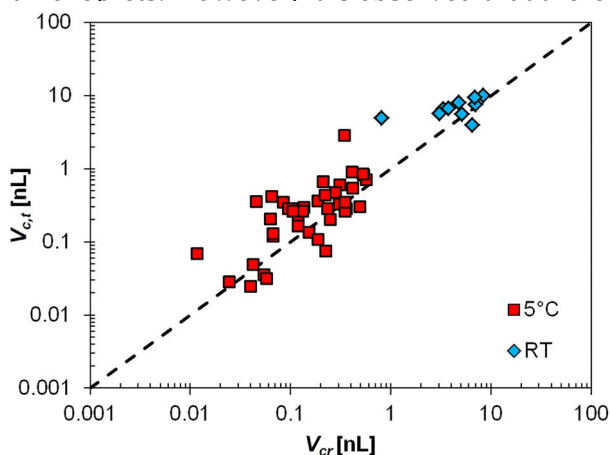


**Figure 6.6:** The theoretical crystal volumes  $V_{c,t}$  (eq. 6.10) inside droplets derived from the solubility versus the experimental crystal volume  $V_{cr}$  (eq. 6.1), estimated from the visual data using a spherical shape factor.

spread among the data points, in some cases deviating more than an order of magnitude from the line. Since only two sides of the crystals could be estimated and the crystal habits varied between plate, cube- and rod-shapes, the error in determining the volume by using a shape factor of  $\pi/6$  can be substantial.

### Crystal Growth

The detection limit of a crystal is estimated to be around  $5 \mu\text{m}$ . In order to estimate the time  $t_g$  from the nucleation event to the detection of the crystal, the growth rates  $G$  of the crystals were determined. After detection of a crystal the two visible characteristic sizes ( $L$ ) were measured every minute, until the lengths remained constant. The sizes of a crystal in a large droplet (■) and in a small droplet (●) with Fen concentrations of  $c_{Fen} = 55.2 \text{ mg/mL}$  are given in **Figure 6.7**.

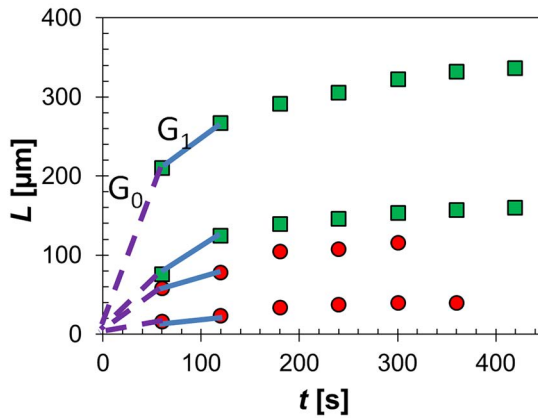


**Figure 6.7:** Characteristic crystal sizes  $L$  in time after detection in the large (■) and small (●) droplets. Growth rates  $G_0$  and  $G_1$  are derived from these data using eq. 6.11.

The growth rates  $G$  in  $\mu\text{m}/\text{min}$  were then determined from these data according to:

$$G = \frac{\Delta L}{\Delta t} \quad (6.10)$$

The growth time until detection  $t_g$  could then be calculated by:

$$t_g = \frac{5}{G} \quad (6.11)$$

Since every minute a picture was taken and the detection limit is  $5 \mu\text{m}$ , this means that a minute before the first observation of the crystal it has a size of less than  $5 \mu\text{m}$ . For the growth rate measurements this was taken as time  $t = 0$ . Two growth rates were determined,  $G_0$  and  $G_1$ . The growth rate  $G_0$  is an estimate of the minimum growth rate between time zero and  $t = 60 \text{ s}$ .

The real initial growth rate cannot be smaller than this value. In addition, for comparison the more accurate growth rate  $G_1$  between  $60 \leq t \leq 120$  s was determined.

It can be seen that the crystals in large droplets grow to larger sizes than those in small droplets, which follows from the fact that in larger solution volumes more molecules of Fen are available for crystal growth than in small solution volumes. Both in the large and small droplets, the growth rate of each face shows the same trend and decreases rapidly. This rapid decrease is attributed to depletion of the supersaturation in the stagnant droplet.

For each of the four datasets in **Table 6.1** the minimum values found for  $G_0$  and  $G_1$ , as well as their corresponding maximum growth times  $t_g$ , are given. From these data it seems that the minimum growth rates  $G_1$  increase with increasing droplet size and increasing concentrations, while such trends are not observed for  $G_0$ . The scattered values for  $G_{0,min}$  are attributed to the unknown time of nucleation, which yield inaccurate values of  $G_0$ . The corresponding growth time for the crystal to reach a size of  $5 \mu\text{m}$  after nucleation is always below 90 s, which can be taken as the maximum growth time  $t_g$ . In our measurements we would detect the crystal at most at 120 s after nucleation.

**Table 6.1:** Minimum growth rates  $G_{0,min}$  and  $G_{1,min}$  and their corresponding growth times until detection ( $t_g$ ) of the crystallization experiments in large droplets with concentrations of 55.2 mg/mL (L55) and 66.2 mg/mL (L66), and in small droplets with concentrations of 55.2 mg/mL (S55) and 66.2 mg/mL (S66).

| Dataset | $G_{0,min}$ [ $\mu\text{m/s}$ ] | $t_g$ [s] | $G_{1,min}$ [ $\mu\text{m/s}$ ] | $t_g$ [s] |
|---------|---------------------------------|-----------|---------------------------------|-----------|
| L55     | 0.08                            | 65.4      | 0.13                            | 39.6      |
| L66     | 1.36                            | 3.6       | 0.19                            | 25.8      |
| S55     | 0.19                            | 26.4      | 0.06                            | 85.8      |
| S66     | 0.06                            | 81.6      | 0.12                            | 42.6      |

### *Nucleation rate*

Nucleation rates can be determined by assessing the variation in the time it takes for nuclei to form after a certain supersaturation is reached. This time is referred to as the induction time of crystallization<sup>29</sup>. Induction time measurements were performed in the droplets to assess the nucleation rate  $J$  and its kinetic and thermodynamic parameters  $A$  in [ $\text{m}^{-3}\text{s}^{-1}$ ] and  $B$ . The nucleation rate is determined from the induction time probability distribution, which is equal to the time dependent fraction of crystallization events in all measurement runs in a dataset according to:

$$P = 1 - \exp\left(-JV_d(t - t_g)\right) \quad (6.12)$$

Where  $P$  is the probability of finding a crystal,  $J$  is the nucleation rate in  $[\text{m}^{-3}\text{s}^{-1}]$ ,  $V_d$  is the droplet volume in  $[\text{m}^3]$ ,  $t$  is the time in  $[\text{s}]$  and  $t_g$  is the time between the formation of the nucleus and detection of the presence of crystals in  $[\text{s}]$ .

The experimental cumulative induction time distribution is plotted versus time for each dataset in **Figure 6.8**. These plots have the same profile as induction time distributions measured in larger volume stirred solution reflecting the stochastic nature of nucleation<sup>11</sup>. However, here they do not approach 1, but level off at a much lower value due to the large fraction of inactive droplets. The experimental distributions were fitted to the cumulative distribution function<sup>11</sup>, which was adapted to account for the fraction  $f$  of active droplets, according to:

$$P = f \left( 1 - \exp \left( -JV_d (t - t_g) \right) \right) \quad (6.13)$$

The supersaturation ratio  $S$ , nucleation rate  $J$ , growth time  $t_g$  and fraction of active droplets  $f$  are given for each dataset in **Table 6.2**. Here it is seen that the growth time  $t_g$  is each time estimated smaller than 1.5 minutes, which is consistent with the data from the growth rate measurements. The error in the growth time  $t_g$  of the experiment in the small droplets with a concentration of 55.2 mg/mL (S55) is substantial. This is attributed to the low number of crystallization events observed in the experiments. From the fitted nucleation rates it is seen that, as expected, higher supersaturation ratios give higher nucleation rates. The fraction of active droplets  $f$  estimated from the induction time experiments is a factor of seven times lower than that from

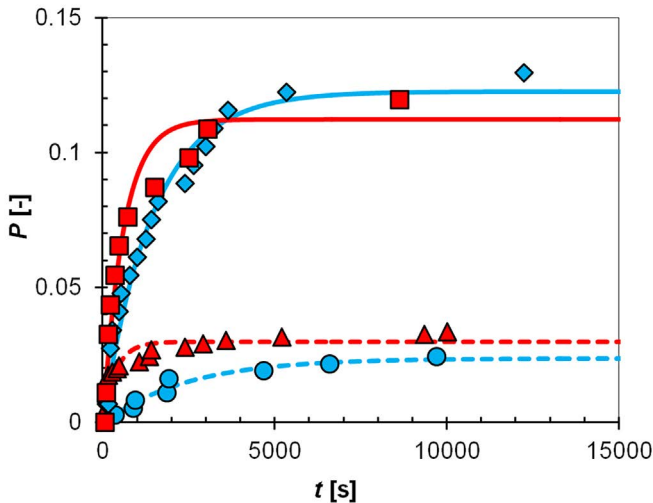


**Figure 6.8:** Fraction of crystallization events over time (●) in small droplets, concentration  $c = 55$  mg/ml, (◆) in large droplets  $c = 55.2$  mg/mL, (▲) in small droplets,  $c = 66.2$  mg/mL and (■) in large droplets,  $c = 66.2$  mg/mL. Each dataset is fitted to the nucleation rate probability function in eq. 6.14.

the recurrent crystallization experiments for each experimental set. This indicates that not all active droplets crystallize within 4 hours in every run.

**Table 6.2:** The droplet volume  $V_d$ , concentration of Fen  $c_{Fen}$ , supersaturation ratio  $S$ , number of droplets per measurement run  $n_{d,i}$ , number of measurement runs  $N$ , nucleation rate  $J$ , growth time  $t_g$  and fraction of active droplets  $f$  determined from the fit of the nucleation probability function (eq. 6.14) to the induction time data in the different sets of droplets.

| Experiment             | L55                        | L66                        | S55                      | S66                       |
|------------------------|----------------------------|----------------------------|--------------------------|---------------------------|
| $V_d$ [nL]             | 194                        | 194                        | 12                       | 12                        |
| $c_{Fen}$ [mg/mL]      | 55.2                       | 66.2                       | 55.2                     | 66.2                      |
| $S$                    | 2.5                        | 3.0                        | 6.9                      | 8.3                       |
| $n_{d,i}$              | 12 ± 2                     | 12 ± 2                     | 60 ± 11                  | 60 ± 11                   |
| $N$                    | 13                         | 10                         | 7                        | 10                        |
| $J$ [ $m^{-3}s^{-1}$ ] | $(3.5 \pm 0.5) \cdot 10^6$ | $(8.8 \pm 1.6) \cdot 10^6$ | $(35 \pm 13) \cdot 10^6$ | $(220 \pm 55) \cdot 10^6$ |
| $t_g$ [s]              | 0 ± 63                     | 21 ± 37                    | 69 ± 242                 | 0 ± 46                    |
| $f$                    | 0.123 ± 0.006              | 0.112 ± 0.004              | 0.024 ± 0.003            | 0.030 ± 0.001             |

The nucleation rate is related to the supersaturation according to the nucleation rate equation<sup>11</sup>:

$$J(t) = A \cdot S \cdot \exp\left(\frac{-B}{\ln^2 S(t)}\right) \quad (6.14)$$

Where  $A$  is the kinetic nucleation parameter in [ $m^{-3}s^{-1}$ ] and  $B$  the thermodynamic nucleation rate parameter. To derive the nucleation rate parameters  $A$  and  $B$ , the quantities  $\ln(J/S)$  and  $1/\ln^2(S)$  were plotted in **Figure 6.9** to give a linear relationship, with a slope of  $-B$  and an intercept of  $\ln(A)$ . The values for the kinetic and thermodynamic nucleation rate parameters following from eq. 6.15 were  $A = (1.9 \pm 0.7) \cdot 10^7 m^{-3}s^{-1}$  and  $B = 2.2 \pm 0.5$ .

Even though the effect of the volume on the nucleation parameters of fenofibrate in heptane could not be accurately assessed due to the different temperatures used in the nucleation events, the experiments conducted in this study show the potential of the encapsulation technique for nucleation studies. The technique is very suitable for further research into the effect of heterogeneous particles on the nucleation, since the hydrogel can be loaded with a known concentration of heterogeneous particles that can have a stimulating or inhibiting effect on the nucleation of the target species. This gives the encapsulation technique an advantage over the microfluidics and microwell techniques.

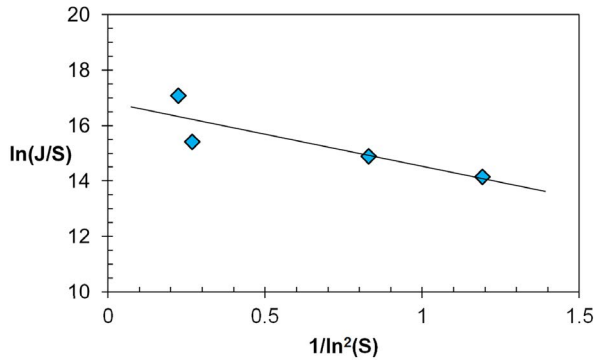


**Figure 6.9:**  $\ln(J/S)$  versus  $1/\ln^2(S)$  of all experiments from **Table 6.2** for determining the nucleation rate parameters according to **eq. 6.15**. The slope of the linear fit is -2.2, the intercept is 16.7.

## 6.4. Conclusions

In this paper we proposed a method to determine nucleation rates in small volumes by encapsulating solution droplets using a hydrogel. The crystallization behavior of fenofibrate in heptane inside the encapsulated droplets is well visible using a microscope, due to the transparent nature of calcium-alginate shell. The repeated crystallization seen in a fraction of the droplets over multiple heating-cooling cycles, in combination with the fraction of droplets that crystallize, indicates that the crystallization is influenced by heterogeneous particles, which most likely are present in the hydrogel surroundings with a concentration in the order of  $(1-2) \cdot 10^4/\text{mL}$ . The growth rate of the crystals inside the droplets was also observed and shown to decrease rapidly due to depletion of the supersaturation in the solution. It is likely that the growth quickly becomes diffusion limited in the stagnant environment of the droplets, which means that in the larger droplets the final crystal size is obtained much later than in the smaller droplets. From the growth rate experiments, a maximum value of  $t_g$  of 90 seconds was determined. It was observed that for increasing supersaturations, increasing nucleation rates were found, regardless of the volume of the droplets. From the nucleation rates, kinetic and thermodynamic nucleation parameters were determined to be  $A = 1.9 \cdot 10^7 \text{ m}^{-3}\text{s}^{-1}$  and  $B = 2.2$ . We showed that performing cooling crystallization in droplets encapsulated with a hydrogel shell is an excellent way to investigate the process at such a small scale. The encapsulation technique shows much promise for the investigation of the effect of heterogeneous particles on the nucleation from solution.

## 6.5. References

1. Beig, A.; Agbaria, R.; Dahan, A., Oral Delivery of Lipophilic Drugs: The Tradeoff between Solubility Increase and Permeability Decrease When Using Cyclodextrin-Based Formulations. *PLoS ONE* **2013**, *8*, e68237.
2. Dahan, A.; Hoffman, A., Rationalizing the selection of oral lipid based drug delivery systems by an in vitro dynamic lipolysis model for improved oral bioavailability of poorly water soluble drugs. *Journal of Controlled Release* **2008**, *129*, 1-10.
3. Lipinski, C. A.; Lombardo, F.; Dominy, B. W.; Feeney, P. J., Experimental and computational approaches to estimate solubility and permeability in drug discovery and development settings1. *Advanced Drug Delivery Reviews* **2001**, *46*, 3-26.
4. Tipduangta, P.; Takiuddin, K.; Fábíán, L.; Belton, P.; Qi, S., A New Low Melting-Point Polymorph of Fenofibrate Prepared via Talc Induced Heterogeneous Nucleation. *Crystal Growth & Design* **2015**, *15*, 5011-5020.
5. Jinno, J.-i.; Kamada, N.; Miyake, M.; Yamada, K.; Mukai, T.; Odomi, M.; Toguchi, H.; Liversidge, G. G.; Higaki, K.; Kimura, T., Effect of particle size reduction on dissolution and oral absorption of a poorly water-soluble drug, cilostazol, in beagle dogs. *Journal of Controlled Release* **2006**, *111*, 56-64.
6. Radacsi, N.; Ambrus, R.; Szunyogh, T.; Szabó-Révész, P.; Stankiewicz, A.; van der Heijden, A.; ter Horst, J. H., Electrospray Crystallization for Nanosized Pharmaceuticals with Improved Properties. *Crystal Growth & Design* **2012**, *12*, 3514-3520.
7. Griffin, D. W.; Mellichamp, D. A.; Doherty, M. F., Reducing the mean size of API crystals by continuous manufacturing with product classification and recycle. *Chemical Engineering Science* **2010**, *65*, 5770-5780.
8. Garetz, B. A.; Matic, J.; Myerson, A. S., Polarization Switching of Crystal Structure in the Nonphotochemical Light-Induced Nucleation of Supersaturated Aqueous Glycine Solutions. *Physical Review Letters* **2002**, *89*, 175501.
9. Nielsen, M. H.; Aloni, S.; De Yoreo, J. J., In situ TEM imaging of  $\text{CaCO}_3$  nucleation reveals coexistence of direct and indirect pathways. *Science* **2014**, *345*, 1158-1162.
10. Kulkarni, S. A.; Kadam, S. S.; Meekes, H.; Stankiewicz, A. I.; ter Horst, J. H., Crystal Nucleation Kinetics from Induction Times and Metastable Zone Widths. *Crystal Growth & Design* **2013**, *13*, 2435-2440.
11. Jiang, S.; ter Horst, J. H., Crystal Nucleation Rates from Probability Distributions of Induction Times. *Crystal Growth & Design* **2011**, *11*, 256-261.
12. Kadam, S. S.; Kramer, H. J. M.; ter Horst, J. H., Combination of a Single Primary Nucleation Event and Secondary Nucleation in Crystallization Processes. *Crystal Growth & Design* **2011**, *11*, 1271-1277.

13. Vitry, Y.; Teychené, S.; Charton, S.; Lamadie, F.; Biscans, B., Investigation of a microfluidic approach to study very high nucleation rates involved in precipitation processes. *Chemical Engineering Science* **2015**, 133, 54-61.
14. Akella, S. V.; Mowitz, A.; Heymann, M.; Fraden, S., Emulsion-Based Technique To Measure Protein Crystal Nucleation Rates of Lysozyme. *Crystal Growth & Design* **2014**, 14, 4487-4509.
15. Thomas, B. R.; Carter, D.; Rosenberger, F., Effect of microheterogeneity on horse spleen apoferritin crystallization. *Journal of Crystal Growth* **1998**, 187, 499-510.
16. Longuet, C.; Yamada, A.; Chen, Y.; Baigl, D.; Fattaccioli, J., Spatially-controlled protein crystallization in microfluidic chambers. *Journal of Crystal Growth* **2014**, 386, 179-182.
17. Hammadi, Z.; Grossier, R.; Zhang, S.; Ikni, A.; Candoni, N.; Morin, R.; Veesler, S., Localizing and inducing primary nucleation. *Faraday Discussions* **2015**, 179, 489-501.
18. Hammadi, Z.; Candoni, N.; Grossier, R.; Ildefonso, M.; Morin, R.; Veesler, S., Small-volume nucleation. *Comptes Rendus Physique* **2013**, 14, 192-198.
19. Morissette, S. L.; Almarsson, Ö.; Peterson, M. L.; Remenar, J. F.; Read, M. J.; Lemmo, A. V.; Ellis, S.; Cima, M. J.; Gardner, C. R., High-throughput crystallization: polymorphs, salts, co-crystals and solvates of pharmaceutical solids. *Advanced Drug Delivery Reviews* **2004**, 56, 275-300.
20. Singh, M. N.; Hemant, K. S. Y.; Ram, M.; Shivakumar, H. G., Microencapsulation: A promising technique for controlled drug delivery. *Research in Pharmaceutical Sciences* **2010**, 5, 65-77.
21. Sun-Waterhouse, D.; Penin-Peyta, L.; Wadhwa, S. S.; Waterhouse, G. N., Storage Stability of Phenolic-Fortified Avocado Oil Encapsulated Using Different Polymer Formulations and Co-extrusion Technology. *Food Bioprocess Technol* **2012**, 5, 3090-3102.
22. Homar, M.; Dreu, R.; Kerc, J.; Gašperlin, M., Preparation and evaluation of celecoxib-loaded microcapsules with self-microemulsifying core. *Journal of Microencapsulation* **2009**, 26, 479-484.
23. Whelehan, M.; Marison, I. W., Capsular perstraction as a novel methodology for the recovery and purification of geldanamycin. *Biotechnology Progress* **2011**, 27, 1068-1077.
24. Heinz, A.; Gordon, K. C.; McGoverin, C. M.; Rades, T.; Strachan, C. J., Understanding the solid-state forms of fenofibrate – A spectroscopic and computational study. *European Journal of Pharmaceutics and Biopharmaceutics* **2009**, 71, 100-108.
25. Yadav, V. B.; Yadav, A. V., Enhancement of solubility and dissolution rate of Fenofibrate by melt granulation technique. *International Journal of PharmTech Research* **2009**, 1, 256-263.

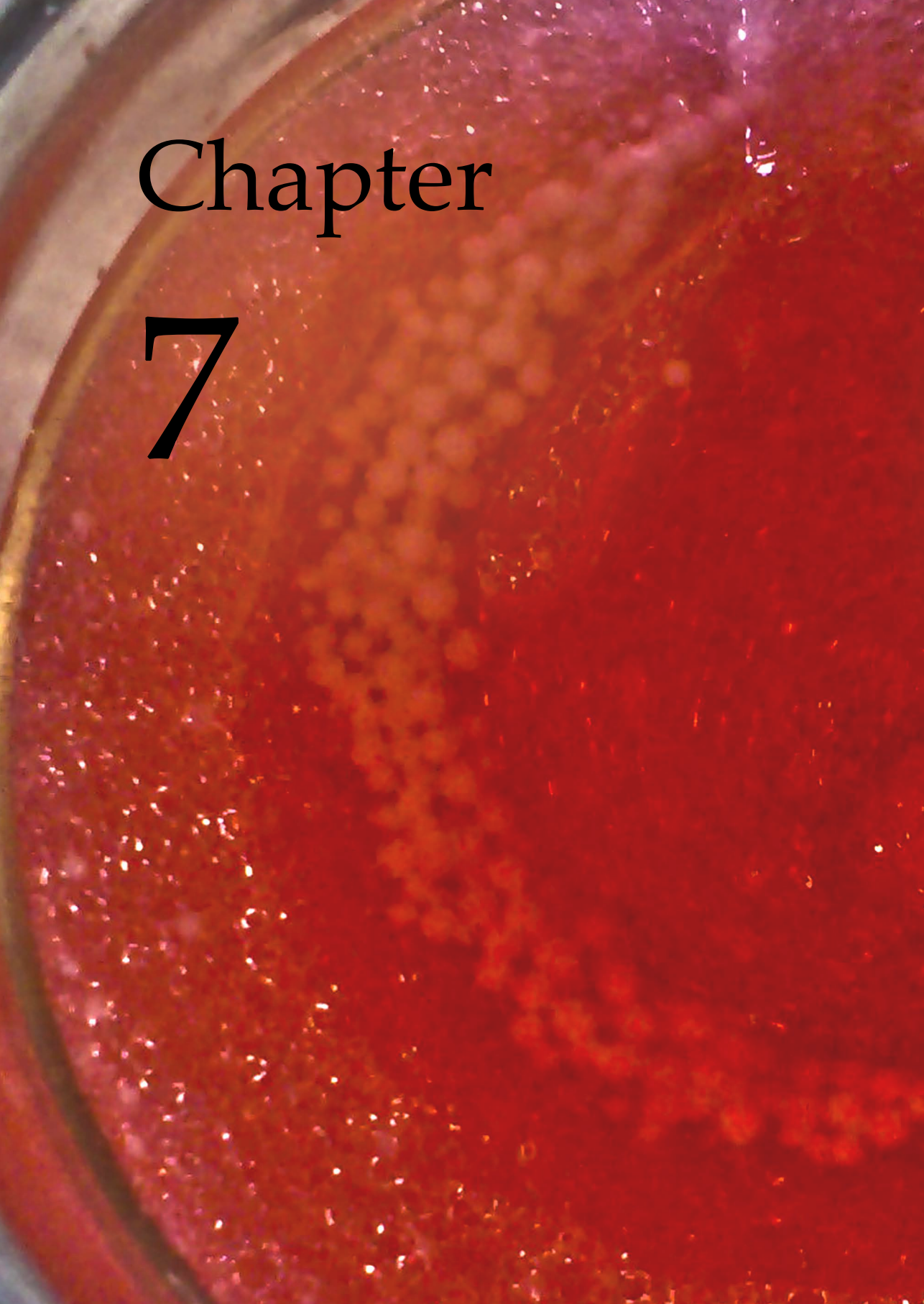
26. Reus, M. A.; Hoetmer, G.; van der Heijden, A. E. D. M.; ter Horst, J. H., Concomitant crystallization for in situ encapsulation of organic materials. *Chemical Engineering and Processing: Process Intensification* **2014**, *80*, 11-20.

27. Mullin, J. W., 3 - Solutions and solubility. In *Crystallization (Fourth Edition)*, Mullin, J. W., Ed. Butterworth-Heinemann: Oxford, **2001**; pp 86-134.

28. Weber, C., Zum Zerfall eines Flüssigkeitsstrahles. *ZAMM - Journal of Applied Mathematics and Mechanics / Zeitschrift für Angewandte Mathematik und Mechanik* **1931**, *11*, 136-154.

29. Kadam, S. S.; Kulkarni, S. A.; Coloma Ribera, R.; Stankiewicz, A. I.; ter Horst, J. H.; Kramer, H. J. M., A new view on the metastable zone width during cooling crystallization. *Chemical Engineering Science* **2012**, *72*, 10-19.





Chapter

7



Immobilization of gluten  
in spherical matrices of  
food -grade hydrogels

## Abstract

In this chapter wheat gluten is encapsulated in a matrix of a food-grade biopolymer for preparing meat analogs. Both sodium alginate and  $\kappa$ -carrageenan were used as encapsulants. Spherical particles of hydrogel-gluten mixtures were produced by means of a dripping method using an encapsulator. While the particle properties of  $\kappa$ -carrageenan surpassed those of alginate in terms of controlled release of the core, the particle production using the encapsulator was more complicated. With  $\kappa$ -carrageenan, a layer of oil on top of the cross-linking bath fluid, as well as through the outer orifice of a concentric nozzle were required to obtain a good sphericity of the particles. For the alginate particles the use of oil was not necessary. Gluten loadings of 7 m% were achieved with 1.5 m% alginate and with 2 m%  $\kappa$ -carrageenan. The water content of the particles can be easily controlled by a subsequent partial drying step. A mixture of soy and particles was sheared in the Couette Cell. Controlled release of the gluten from the alginate particles was not achieved properly by temperature or shear. The controlled release of the gluten was achieved at the processing conditions only with  $\kappa$ -carrageenan. Some fibrilization was observed in the sheared product, but the macrostructure was not yet well developed. However, an optimization of the shearing process for the use of the particles may lead to an improved structure for the meat analogs.

## 7.1. Introduction

Meat analogs are an increasingly welcome alternative to meat for instance in view of animal welfare<sup>1</sup> and sustainability<sup>2</sup>. However, many of the products currently on the market do not reflect the properties of meat to a satisfactory extent<sup>3</sup>: These meat analogs lack the juiciness of meat, which follows from its characteristic fibrous structure.

A novel process was developed for the production of highly fibrous meat analogs, using the lab-scaled Couette Cell device<sup>4</sup>. This process achieves meat-like structure formation by applying simple shear flow and heat to plant protein suspensions, resulting in the formation of fibers, which enhance the structure and mouthfeel of the product<sup>5</sup>. During the mixing step of the ingredients prior to loading of the Couette Cell, soy protein isolate (SPI) is premixed with water and left to rest. However, upon addition of the vital wheat gluten (WG), instant fibrilization takes place<sup>6</sup>, forming a sticky gel and local networks. These effects are undesired, since they lead to material losses, as in gluten sticking to the mixing container and spatula. This can be prevented if the gluten could be immobilized and only be released during processing under simple shear and heat.

Microencapsulation is often used to provide such isolation and release functions<sup>7-9</sup>. Hydrogels form a class of materials that is frequently used as encapsulant in biological and pharmaceutical systems<sup>10-13</sup> and would be able to fit the requirements for the gluten encapsulation. Hydrogels are polymers that can hold a large quantity of water in their three-dimensional structure, due to the hydrophilic parts of the molecules<sup>14</sup>. The open, porous structure does not only allow for the presence of water, but can also provide support to other materials, e.g. cells<sup>15,16</sup>, drugs or peptides<sup>15,17</sup>.

Our aim is to produce spherical encapsulates of gluten in food-grade hydrogel, which release the gluten from the particles at the processing conditions of the meat analog shearing process. The encapsulates should release the gluten inside the Couette Cell, as a result of the higher temperature and shear in the process. Calcium cross-linked alginate and potassium cross-linked  $\kappa$ -carrageenan hydrogels were used for the gluten immobilization. These hydrogels and cross-linkers were chosen because their combinations rapidly form rigid gels, enabling the product to resist the forces exerted on the particles during mixing and loading, and because they are accepted in the food industry<sup>18,19</sup>. The resulting encapsulates are analyzed for particle size, gluten vs. hydrogel loading, and release and fibrilization properties in the actual meat-analog production process.

## 7.2. Materials and Methods

### 7.2.1. Materials

All materials were used without further purification, unless stated otherwise. A blend of soy protein isolate (SPI) (SUPRO EX37 HG IP, Solae, USA) and vital wheat gluten (WG) (VITEN, Roquette, France) was used. In the case of SPI, we determined a protein content of 90 wt%, while gluten had a protein content of 81 wt% based on a nitrogen-to-protein conversion factor of 6.25, measured with the Dumas method. Sodium chloride, referred to as salt hereafter, was also used. Alginic acid sodium salt from brown algae,  $\text{CaCl}\cdot 2\text{H}_2\text{O}$  ( $\geq 99\%$ ),  $\kappa$ -carrageenan – sulfated plant polysaccharide – and KCl ( $\geq 99.0\%$ ) were purchased from Sigma Aldrich. Arachide oil was purchased from a local supermarket; the oil was colored red using a food-grade dye (a mixture of E-numbers E110 sunset yellow FCF, E122 azorubin, E132 indigotine and E151 Brilliant Black BN) for visualization purposes.

### 7.2.2. Methods

#### *Encapsulator*

For the immobilization the Encapsulator B-390 from Büchi Labortechnik was used, as in **Section 6.2**. The sodium alginate and  $\kappa$ -carrageenan were dissolved in water and vigorously mixed to form a liquid hydrogel. The gluten were stirred vigorously into the resulting gels. The hydrogel-WG mixtures were led through a (concentric) nozzle (3), and were cross-linked at room temperature in 100mM solutions of  $\text{CaCl}_2$  or KCl, respectively. The air pressure for pumping was varied between  $P = 400 - 800$  mbar, vibration frequency between  $F = 200 - 1,000$  Hz, the amplitude between  $A = 5 - 9$ , the nozzle temperature between  $T_N = \text{RT} - 65^\circ\text{C}$  and the electrostatic potential, when used, was varied between  $V = 1,000 - 2,500$  V.

#### *Analysis*

Different optical microscopes were used for the analysis of the resulting particles. A Leica Nikon Optiphot 200 was used, as well as a Leica S6D. Closer inspection of the particles and the sheared material was done with a scanning electron microscope (SEM), FEI Nova NanoSEM650. The samples were used as-is under low vacuum (100 Pa) conditions under relatively low (4.0 kV) acceleration voltages, without the need for applying a conductive coating on the particles.

The composition of the particles was checked by determining the amount of water the particles hold after cross-linking and removing the excess cross-linking solution by dabbing with a paper towel. Samples were weighed before and after drying, from which the water content was calculated. The

dry mass was assumed to have the same mass ratio of gluten and hydrogel as initially used before cross-linking.

The melting behavior of the particles was assessed using the Crystalline multiple reactor system (Technobis). The particles were loaded in a vial until the top layer of particles was visible in the camera. The vial was heated to 95°C with a heating rate of 0.3°C/min, pictures were taken every 30 s.

Static stress scans were performed with a PerkinElmer Dynamic Mechanical Analyzer (DMA) 7e with parallel plate geometry, using a range of 0–1,000 mN and a rate of 100 mN/min. When the cylinder, which moves the upper plate, is in the starting position, i.e. resting on the particle without applying force, the height of the particle is 100% of the diameter and the particle is not deformed. When the cylinder is lowered, the particle becomes flatter due to the increasing force applied to it, decreasing the particle height to close to 0% of the particle diameter at the end of the test. A particle is more difficult to deform when the compression force required for a certain displacement of the cylinder is larger. The distance  $h$  between the top and bottom plates is decreased from the initial particle diameter  $d_{p,in}$  to 0. This height, divided by the initial particle diameter ( $h/d_{p,in}$  [%]), represents the deformation of the particle. The bead diameter was used as diameter for the stress and strain calculations. However, the particle diameter is much smaller than the top cylinder of the DMA. This means that the numerical values from the equipment do not represent the true modulus of the materials and the results from the compression tests can only be compared to each other.

#### *Couette Cell*

The release behavior of the particles and fibrilizing capabilities of the released gluten at process conditions were tested in the Couette Cell, which is shown in **Figure 7.1**. It is based on the common concentric cylinder rheometer concept. The device is connected to an electrical motor coupled with a gearbox (Elsto, Voorhout, The Netherlands), which is used to keep the angular velocity of the rotating inner cylinder (#3 in **Figure 7.1**) at a constant value of 30 RPM. The outer cylinder (#1) remains stationary. Both the inner and outer cylinders are heated by means of oil (#2 & #4). The sample material is placed in the space between the two cylinders; this space is called shearing zone (#7). The temperature in the shearing zone is measured in two positions halfway the height of the Couette Cell.

Two oil baths were used; one ‘hot’ oil bath ( $T = 118^\circ\text{C}$ ) to heat up the Couette Cell before and during an experiment and one ‘cold’ oil bath ( $T = 60^\circ\text{C}$ ), to cool down the Couette Cell after shearing. A PT100 temperature sensor (#5) is placed in the wall of the outer cylinder with its tip located at the inner wall of the outer cylinder. The PT100 is connected to the hot oil bath to allow temperature reading and control in the Couette Cell. The temperature of the hot oil bath is controlled by the Lauda Wintherm software (Lauda DR. R.

Wobser GmbH & Co. KG, Lauda-Königshofen, Germany) on a PC connected with the hot oil bath via a R232 connector. A J-type thermocouple is placed at a position closer to the inlet of the heat transfer fluid in the middle of the plug, to seal the filling hole after loading (#6). The J-type thermocouple was calibrated with a dry block calibrator (T 350P, PRESYS) and a high precision thermometer (F252, ASL). The incoming flow of the heat transfer fluid is split before it enters the Couette Cell, so the inner and outer cylinders are heated simultaneously (in parallel). The connection to the heating chamber of the inner cylinder is made using a rotary joint (#8).

Prior to any experiment, the Couette Cell was brought to a temperature of 95°C. The gluten encapsulates were partially dried prior to the preparation of the shearing mixture, to obtain a water-gluten ratio close to that used in experiments without encapsulates. First the meat analog mixture was prepared by mixing 150 g of partially dried encapsulates with 46 g of SPI and 0.5 g of salt, which accounts for the amount of salt in the biopolymer. This mixture was set to rest for 30 minutes and then loaded into the Couette Cell using the loading gun (#6). The shearing was started directly after the loading was completed. During experiments no heating effects from viscous dissipation were measured. It is therefore considered negligible. After 15 minutes the shearing action was stopped and the Couette Cell was actively cooled down.

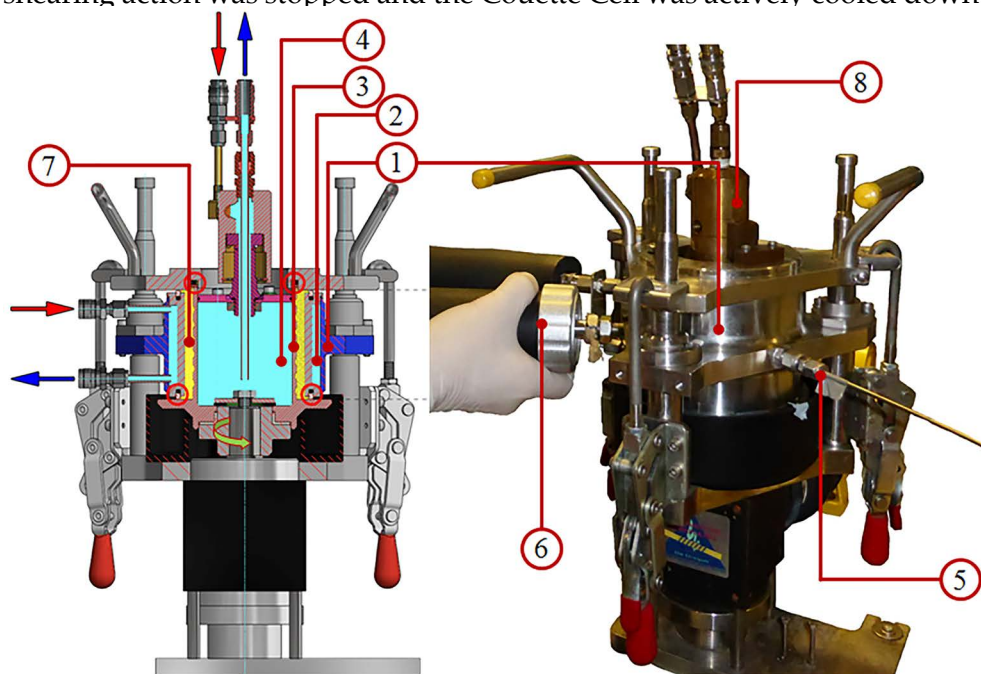


**Figure 7.1:** Couette Cell model (left) and setup (right), with 1. outer cylinder, 2. heating chamber of outer cylinder, 3. inner cylinder, 4. heating chamber of inner cylinder, 5. PT100 temperature sensor, 6. loading gun, 7. shearing zone, 8. rotary joint.

### 7.3. Results and Discussion

For the optimization of the encapsulate production, first the production of spherical beads of hydrogel was optimized. Subsequently, gluten was added to the mixture and the resulting encapsulates of those optimized experiments were tested on their performance.

#### 7.3.1. Particle production

The production of alginate particles was straightforward using the encapsulator. Sodium alginate – water mixtures were led through the single nozzle configuration and cross-linked in a bath containing a  $\text{CaCl}_2$  solution. The flow rate and the vibration frequency were optimized for each nozzle diameter. For example, the particles in **Figure 7.2(a)** were produced using a sodium alginate concentration in water of 1.65 m%. The 300  $\mu\text{m}$  diameter nozzle was used, with a flow rate of alginate  $\Phi_{alg} = 4.1 \text{ mL/min}$  and a vibration frequency of  $F_{vib} = 600 \text{ Hz}$ . This resulted in particles with a diameter of  $606 \pm 12 \mu\text{m}$ . Higher concentrations of sodium alginate in the starting mixture made the mixture more difficult to pump through the nozzle due to increasing viscosity. Additionally, the cross-linked spheres were stronger when higher concentrations of sodium alginate were used, which is undesirable, since too strong particles do not break under the processing conditions. Using lower concentrations of sodium alginate in the starting mixture eventually led to droplets that were mechanically too weak. These droplets disintegrated upon impact with the cross-linking bath and did not produce any microspheres. The lowest feasible concentration was 1.65 m% of sodium alginate in water for the 300  $\mu\text{m}$  nozzle.

For the production of  $\kappa$ -carrageenan particles different settings were required. Mixtures containing 2%  $\kappa$ -carrageenan in water were used. Because of the gelling temperature of the  $\kappa$ -carrageenan solution ( $42^\circ\text{C}$  for 2% solu-

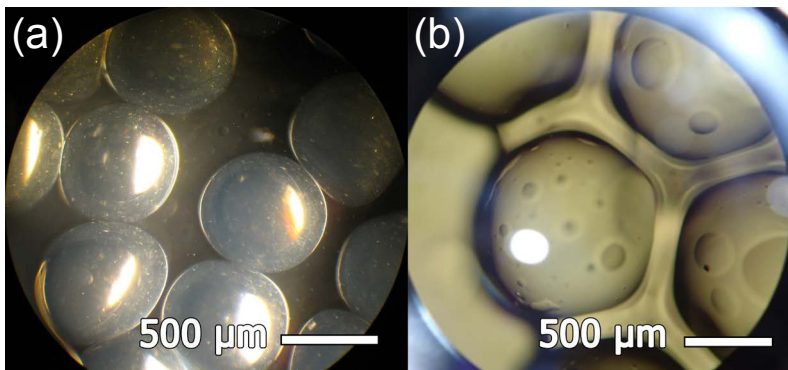


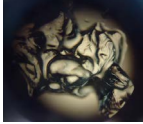
**Figure 7.2:** (a) Alginate particles (3.3 m% alginate, 300  $\mu\text{m}$  nozzle) cross-linked with calcium ions. (b)  $\kappa$ -carrageenan particles (2 m%, concentric nozzles 750 – 900  $\mu\text{m}$ ) cross-linked with potassium ions. The apparent connections between the particles are actually residues of cross-linking solution.

tion<sup>20</sup>), the immobilization mixture was heated to 60°C to facilitate the flow to the nozzle.

With the bead production in the single nozzle configuration and nozzle heating at  $T_N = 50^\circ\text{C}$ , the jet break-up occurred at a larger distance from the nozzle than with the alginate particles. Additionally, the particles were not spherical after cross-linking and not always separated. This is attributed to the droplets losing their spherical shape upon impact with the water or to the long time required for cross-linking.

Several configurations were used to increase the sphericity of the particles, which is beneficial for the flow behavior and therefore aids the loading step. In **Table 7.1** these configurations are shown, together with their results. The nozzle diameters and the liquids flowing through them are mentioned in the 2<sup>nd</sup> and 3<sup>rd</sup> column, the configuration of the cross-linking bath is given in the 4<sup>th</sup> column and the resulting particles in the 5<sup>th</sup>. Keppeler et al.<sup>19</sup> found that dripping the droplets through a layer of oil on top of the cross-linking

**Table 7.1:** Chemicals and nozzle configurations to achieve spherical particles of  $\kappa$ -carrageenan. For the inner and outer nozzles the substance flowing through it and the diameter are given in columns 2 and 3, the solutions used in the hardening bath are given in the 4<sup>th</sup> column and the resulting particle shape in the 5<sup>th</sup>.

| Experiment # | Inner nozzle                            | Outer nozzle                     | Cross-linking bath             | Result   |
|--------------|---|----------------------------------|--------------------------------|--|
| 1            | 2% $\kappa$ -Car,<br>1000 $\mu\text{m}$ | -                                | 150 mM KCl                     | No spherical particles   |
| 2            | 2% $\kappa$ -Car,<br>1000 $\mu\text{m}$ | -                                | 100 mM KCl,<br>with surfactant | No spherical particles   |
| 3            | 2% $\kappa$ -Car,<br>1000 $\mu\text{m}$ | -                                | 100 mM KCl,<br>with oil layer  | More spherical particles, but many broken<br>          |
| 4            | 2% $\kappa$ -Car,<br>750 $\mu\text{m}$  | 100 mM KCl,<br>900 $\mu\text{m}$ | 100 mM KCl                     | One thick agglomerate, despite proper jet break up<br> |
| 5            | 2% $\kappa$ -Car,<br>750 $\mu\text{m}$  | 100 mM KCl,<br>900 $\mu\text{m}$ | 100 mM KCl,<br>with oil layer  | Separate particles, but less spherical and more broken than experiment 3   |
| 6            | 2% $\kappa$ -Car,<br>750 $\mu\text{m}$  | oil,<br>900 $\mu\text{m}$        | 100 mM KCl,<br>with oil layer  | Consistent quality spherical beads   |

bath (like experiment 3 in **Table 7.1**) helped the particles attain a spherical shape. Experiments 1-5 in **Table 7.1** show that the oil was the differentiating factor in the improving the sphericity of the resulting particles. Therefore, it was decided to further employ this feature by using the concentric nozzle configuration and using oil in the outer nozzle around the immobilization mixture in experiment 6. In addition to this, a layer of oil was used on top of the cross-linking mixture. **Figure 7.3** illustrates this configuration. During the experiment, the thickness of the layer of oil on top of the bath increased due to the addition of the oil via the concentric nozzle. The oil separates from the particles after immersion in the cross-linking bath and floats to join the oil layer already present, making it easy to separate and reuse. After cross-linking, the particles were filtered from the salt solution and then washed with demineralized water to remove the oil residues. The result from this configuration is shown in **Figure 7.2(b)**, where it is observed that all particles are spherical and of similar size ( $d_n = (1.02 \pm 0.07) \cdot 10^3 \mu\text{m}$ ).

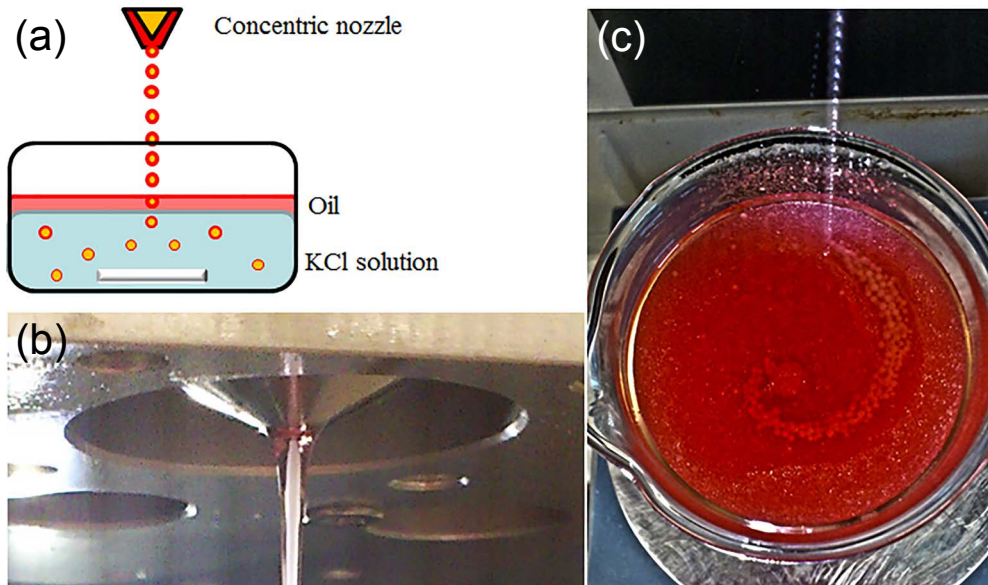


**Figure 7.3:** (a) Schematic of setup using oil in the concentric nozzle as well as on the cross-linking bath. (b) Close up of the immobilization mixture and oil emerging from the concentric nozzle. (c) Droplets entering the cross-linking bath through the layer of oil, which separates the particles from each other.

In this configuration the strength of the spheres was optimized by using lower concentrations of  $\kappa$ -carrageenan. However, at a concentration of 1 m% no particles could be made and particles resulting from a 1.5 m% solution were mechanically very weak. Therefore, a 2 m% solution was considered to provide encapsulates of an acceptable mechanical strength.

Addition of gluten to the particles increased the viscosity of the immobilization mixtures. This required different settings for the bead formation.

For 0.8 m% alginate, 3.7 m% gluten in water, for example, a nozzle diameter of  $D_N = 750 \mu\text{m}$  required a pressure, flow rate and vibration frequency of 456 mbar, 9.8 mL/min and 200 Hz, respectively. In **Figure 7.4 (a)** particles are shown of which the immobilization mixture consisted of 1.65 m% alginate and 1.5 m% gluten. The gluten is clearly visible in the hydrogel, though not evenly distributed. In **Figure 7.4 (b)** the immobilization mixture consisted of 1.65 m% alginate and 3.5 m% gluten. The gluten in this particle is packed much more dense than in **Figure 7.4 (a)**, though the distribution of the gluten inside the particles is not clearly visible anymore.

In the  $\kappa$ -carrageenan mixtures a similar change occurred. However, with appropriate variations of the amplitude, frequency and flow rate, particles loaded with various concentrations of gluten were produced. An example of the optimum mixture (2 m%  $\kappa$ -carrageenan and 7 m% gluten) is shown in **Figure 7.4 (c)**. Settings for the optimum mixture were:  $T_N = 60^\circ\text{C}$ ,  $F_{vib} = 200 \text{ Hz}$ ,  $P = 757 \text{ mbar}$ ,  $D_{NI} = 750 \mu\text{m}$ ,  $D_{NO} = 900 \mu\text{m}$ , with flow rates of the  $\kappa$ -carrageenan-gluten mixture  $\Phi_{cg} = 6.25 \text{ mL/min}$  and of oil  $\Phi_{oil} = 5 \text{ mL/min}$ . After cross-linking, the particles were filtered and washed. The particle size was  $d_p = 1.50 \pm 0.23 \cdot 10^3 \mu\text{m}$  taken from six separate experiments.

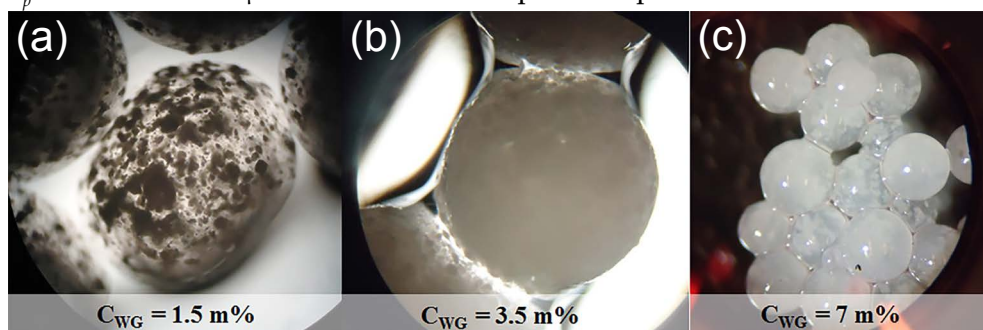


**Figure 7.4:** Alginate particles (a and b) and  $\kappa$ -Carrageenan particles (c) containing various concentrations of gluten.

### Evaluation of particle properties

The suitability of the produced particles to release the encapsulated gluten as a result of shear and elevated temperature in the Couette Cell is assessed by various parameters: the composition in the particles and the behavior of the particles under influence of increasing temperature, simple shear and compression forces are investigated. From the material with the most desirable properties the behavior is also tested in the shear cell. Because the hydrogels can swell in an aqueous environment, the composition of the particles is checked by determining the amount of water the particles hold after cross-linking (as opposed to the initial concentrations used) and removing the excess cross-linking solution by dabbing with a paper towel. **Table 7.2** shows the composition of a selection of particles.

**Table 7.2:** Composition of particles for further testing.

| Initial hydrogel concentration |                 | Gluten %     | Water %         |
|--------------------------------|-----------------|--------------|-----------------|
| Alg %                          | $\kappa$ -Car % |              |                 |
| $1.5 \pm 0.03$                 | 0               | 0            | $96.0 \pm 0.01$ |
| $1.5 \pm 0.03$                 | 0               | $7 \pm 0.01$ | $92.0 \pm 0.01$ |
| 0                              | $2 \pm 0.02$    | 0            | $92.5 \pm 0.01$ |
| 0                              | $2 \pm 0.02$    | $7 \pm 0.01$ | $90.3 \pm 0.01$ |

The results in **Table 7.2** show that some particles have a lower water content than expected from the initial hydrogel concentration used in the immobilization mixture. It is possible that the drying using the paper towel removed more liquid than just the excess cross-linking solution. Due to the porous structures of the biopolymer particles, it is possible that a small amount of water was subtracted from the inner structure. This is especially the case for the particles without gluten. For the particles containing WG the water content is similar to that of the initial immobilization mixture. This indicates that the WG helps the hydrogel to retain the water in its structure.

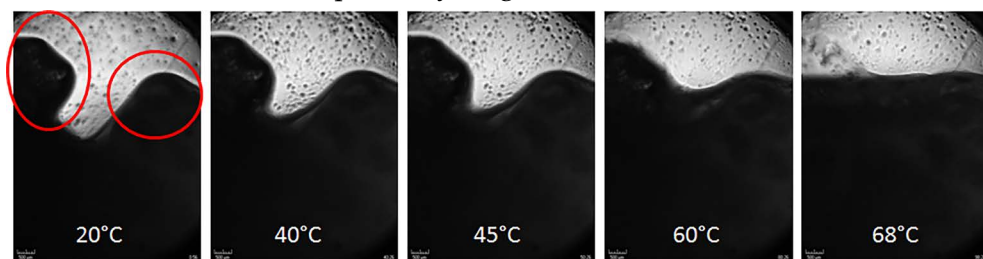


**Figure 7.5:** Melting of  $\kappa$ -carrageenan-gluten particles upon heating. The two top particles are circled in red in the left-most picture. The flattening of the meniscus indicates the melting of these particles.

The particles containing gluten were subjected to a temperature profile to assess the behavior upon heating. In **Figure 7.5**  $\kappa$ -carrageenan particles with gluten are heated to  $95^\circ\text{C}$  with a heating rate of  $0.3^\circ\text{C}/\text{min}$ . At  $T = 20^\circ\text{C}$  the individual particles on top are clearly visible in the circles. Around  $T = 40^\circ\text{C}$  the surface is changing shape, indicating that the particles are melting. Upon increasing the temperature even further, the deformation of the meniscus between particles and air increases, until a flat profile is observed at  $T = 68^\circ\text{C}$  and the particles are completely molten. This means that at the intended processing temperature of  $95^\circ\text{C}$  the particles will melt and release the gluten from their structure. With the alginate particles loaded with gluten this was not the case. These particles remained intact up to  $T = 95^\circ\text{C}$  and showed no change in shape, meaning that the particles would not release the gluten at the intended processing temperature without mechanical action.

Additionally, the particles were compared on their capability to deform under a compression force. In **Figure 7.6** the height divided by the initial

particle diameter ( $h/d_{p,in}$  [%]) represents the deformation of the particle and is plotted versus the force applied to the particles by the upper cylinder of the DMA. These deformation tests were carried out on four different types of particles: Alginate particles of 3 mm diameter loaded with WG,  $\kappa$ -carrageenan particles of 3 mm and 1 mm diameter with WG, and  $\kappa$ -carrageenan particles of 1 mm diameter without WG, to assess both the influence of particle size and type of hydrogel used. In **Figure 7.6** it is observed that larger particles require more force for the deformation. This can be caused either by the ratio of pore size versus particle size, or by the amount of mass to be compressed. It was observed that after compression a puddle of water surrounds the particle. During the deformation the water contained in the particles exits through the pores of the hydrogel. The pore size of the hydrogel is assumed to be independent of the particle size. The larger specific area of the pores in the smaller particles is assumed to allow for easier expulsion of the water and is therefore associated with a smaller compression force.

Between the small particles ( $d_p = 1$  mm) it can be seen that the  $\kappa$ -carrageenan without WG deforms easier than with WG. It was already observed during the production of the particles that the WG provide extra strength to the particles, which remains so after cross-linking, as is seen from **Figure 7.6**. Between the WG loaded particles, it appears that the alginate particles are stronger, while the  $\kappa$ -carrageenan particles are more easily deformed. This gives an indication that they are also easier to break up under influence of a shear force.

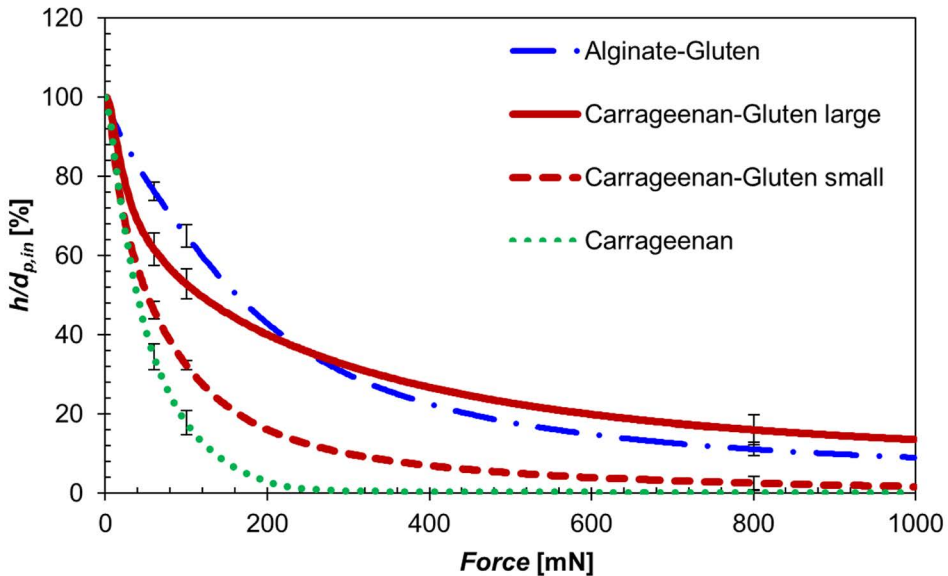


**Figure 7.6:** Deformation of different particles under increasing pressure. Alginate-WG (blue) and  $\kappa$ -carrageenan-WG (red) particles with a diameter of 3 mm and carrageenan-WG (red dashed) and regular  $\kappa$ -carrageenan (green) particles of 1 mm were measured.

## Couette Cell

In other work<sup>4,5</sup> the Couette Cell was used with free gluten powder. The sheared mixtures had a composition like that in **Table 7.3**, but without the hydrogel component and with a higher salt content. In their work, the fibrous structures on both micro and macroscale are clearly visible.

Both the alginate and the  $\kappa$ -carrageenan particles are tested in the Couette Cell to assess whether fiber formation occurs after release of the gluten from their encapsulated environment. Before shearing, the shearing mixture was prepared. The encapsulates were partially dried, until they contained  $88 \pm 1$  m% of water, giving a similar water/gluten ratio as the shearing composition. Subsequently, they were mixed with SPI and salt to arrive at a final composition given in **Table 7.3**.

**Table 7.3:** Composition of shearing mixtures.

| Material                           | m% in shearing composition |
|------------------------------------|----------------------------|
| Water                              | 69                         |
| Gluten                             | 7                          |
| Alginate/<br>$\kappa$ -Carrageenan | 0.83/<br>1                 |
| Soy                                | 23                         |
| Salt                               | 0.5                        |

**Figure 7.7** shows the preparation of the shearing mixture using the particles. The particles were mixed with the SPI and salt and left to rest (a). It was observed that the soy coated both the alginate-gluten and the  $\kappa$ -carrageenan-gluten particles and hydrated by subtracting water from the particles during the resting period (b). The level of hydration of the soy seemed similar to when free water is used.

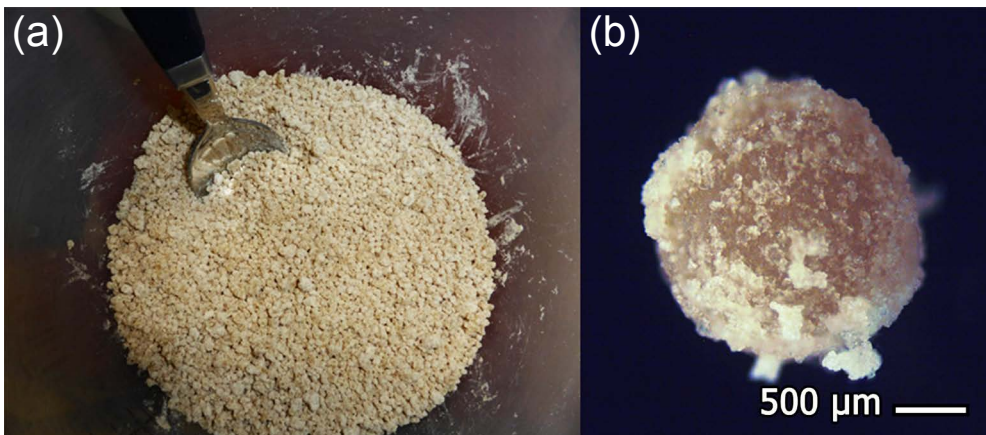


**Figure 7.7:** (a) Preparation of shearing mixture; (b) hydrated soy on a  $\kappa$ -carrageenan particle.

After preparation of the mixture, it was tested how well the mixture loads in the Couette Cell using the loading gun. The loading procedure was completed without complications and the mixture spread well throughout the Couette Cell. Many of the particles were still intact, although some had been broken. Closer inspection of the material showed no evidence of fibrilization at this stage.

**Figure 7.8(a)** shows the alginate-gluten sample after shearing in the Couette Cell. Throughout the sample the particles are still visible and albeit deformed, they were still intact. Microscope images of the material revealed that very limited fibrilization occurred, and only on or surrounding the particles, but nowhere else in the structure. From the entire sample it was also evident that no macrostructure developed. The material falls apart upon movement, since the particles provide break lines in the sample.

**Figure 7.8(b)** shows a sheared sample of  $\kappa$ -carrageenan-gluten particles directly after it is taken from the Couette Cell. No separate particles are visible. All particles have released their gluten and the biopolymer was homogeneously mixed through the sample. The sample did not fall apart like its alginate counterpart, indicating that the macrostructure was more developed. Microscope images of this sample showed numerous gluten fibers throughout the sample.

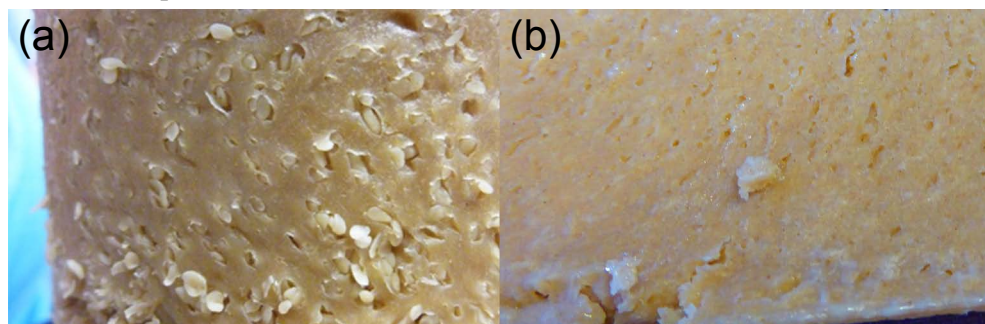


**Figure 7.8:** (a) Alginate-gluten after shearing. Most of the particles are still intact and the macrostructure is not well developed. (b)  $\kappa$ -carrageenan-gluten after shearing. No separate particles are observed and a more cohesive product is obtained.

SEM pictures of the sheared  $\kappa$ -carrageenan sample (**Figure 7.9**) confirm the observations with the optical microscope. In **Figure 7.9(a)** a larger part of the sample is shown with three of the fibers sticking out of the material. In **Figure 7.9(b)**, the three types of material are visible: the gluten fiber, the soy (1) and the surrounding hydrogel (2). The materials were mixed well throughout the sample. The fibers show a wrinkly surface structure, which is also clearly visible in the right picture. This structure is due to the hierarchical nature of the fibers, i.e. the fibers are made up out of smaller fibrils, which was earlier shown for gluten by Ridgley et al.<sup>21</sup>. Changing processing parameters, like temperature, ionic strength and shearing time can influence both the extent of fiber formation, as well as the structure formation. For dif-

ferent sets of processing parameters different structures (e.g. ribbons) were found<sup>21</sup>. It is also observed that the fibers seem to be built up layer by layer from the fibrils, which is most clearly evident from **Figure 7.9(b)** in circle 3. The gluten fibers have various diameters. Larger and smaller fibers were observed next to each other, the larger having diameters of  $20 \pm 3 \mu\text{m}$ , the smaller  $13 \pm 2 \mu\text{m}$ .

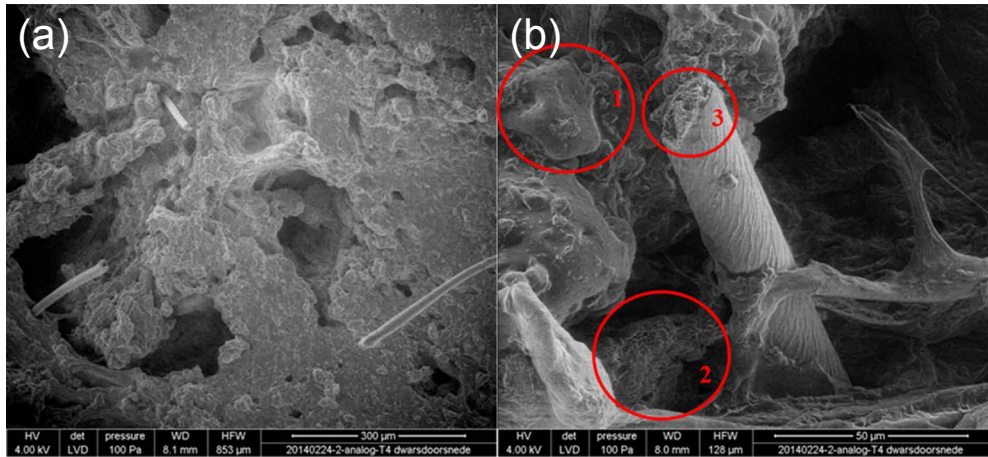


**Figure 7.9:** (a) SEM pictures at different magnifications of fibers in the sheared sample. Multiple fibers were observed. (b) The soy (1) and hydrogel (2) are visible next to the fibril structure at the surface of the gluten fiber (3).

### 7.3.2. Discussion

When immobilizing or encapsulating, the choice of encapsulant is very important. Not only the processing, but also the final composition of the product materials must meet requirements in terms of process conditions and product quality. In the food sector, additional requirements need to be met, which in our case are that the encapsulant is food-grade material and does not alter the ingredient mixture or taste by a significant extent. Requirements for the final product include that the final product is easy to use in the shearing process. This would benefit from spherical particles to make the mixture mix and load easily. These requirements led to our choices of hydrogels, which are easy to process, food-grade materials and tasteless<sup>22, 23</sup>. The dripping technique employed by the encapsulator is particularly suitable for these materials<sup>12, 13, 24</sup>, since it easily leads to spherical particles.

Judging by the melting and compression behavior of the particles it was expected that the  $\kappa$ -carrageenan particles would show better controlled-release properties than the alginate particles, while at room temperature each of them can keep the gluten from cross-linking.

From the results it is clear that the hydrogels used are very well capable of immobilizing the gluten in aqueous environments. The controlled release of the gluten by increased temperature and shear, however, was more easily

achieved from the  $\kappa$ -carrageenan particles than from the alginate particles. In the Couette Cell this behavior was confirmed. The alginate particles are so strong that they do not break or dissolve under the preferred process conditions and thus do not release their gluten for fibrilization. The very limited amount of fibers observed in the sheared sample containing alginate, together with the location of these fibers, i.e. only on top of, or very close to the unbroken particles, are a clear indication that this immobilization material is too strong for the purpose. The  $\kappa$ -carrageenan particles did release the gluten and fibrilization occurred to a much larger extent during the shearing process. However, while comparing the structure sheared from the particles with the structures obtained after shearing the original mixture without particles<sup>4,5</sup>, it was observed that although fibrilization occurs, it is much less than with the original mixture. The macrostructure of the meat analog is not yet well developed. However, both samples were sheared with the settings optimized for the original mixture. The particles take a long time to melt and release their content when the temperature is increased, which was evident from the melting test in **Figure 7.5**. Therefore, it is likely that the shear time must be increased, or that a preheating step must be added to allow for the particles to soften prior to shearing. Additionally, the 2 m% of  $\kappa$ -carrageenan interacts with the mixture, as is also seen in **Figure 7.9(b)**, where the fiber in the picture is partially surrounded with the hydrogel. It is possible that the hydrogel surrounding the fibers actually inhibits the formation of 3D-structures required for a desirable meat analog. Prior to application of immobilized gluten in meat analogs, the settings of the shearing process should be optimized for the new materials used, and the effect of the hydrogel on the mouthfeel of the final meat analog should be assessed.

The successful production of spherical particles of  $\kappa$ -carrageenan with the aid of oil shows that the dripping technique can be used for a wide variety of applications that require the production of spherical encapsulates. For applications such as the immobilization of vitamins, fragrance and pharmaceutical ingredients, the hydrogels are a very suitable encapsulant. However, in other industries the same dripping technique can be used with many other polymers as well, leading to other coating functionalities, e.g. protection from oxygen or moisture from the air. As long as the polymer in question has a low enough melting temperature or suitable cross-linking conditions, the dripping method can be used.

## 7.4. Conclusion

In this paper Wheat Gluten is successfully encapsulated in a matrix of a food-grade biopolymer. Both sodium alginate and  $\kappa$ -carrageenan were used as encapsulants. While the particle properties of  $\kappa$ -carrageenan surpassed those of alginate, the particle production was more complicated. In order

to obtain a good sphericity of the particles, with  $\kappa$ -carrageenan it was required to use a layer of oil on the cross-linking bath, as well as through the concentric nozzle. For the alginate particles no oil phase was required. In the alginate particles a loading of 7 m% gluten was achieved in the particles with 1.5 m% alginate. Controlled release of the gluten from the alginate particles was not achieved properly by temperature or shear. In  $\kappa$ -carrageenan, a loading of 7 m% gluten was achieved in the particles, next to 2 m% of  $\kappa$ -carrageenan. Lower amounts of  $\kappa$ -carrageenan did not lead to separate, spherical particles. The water content of the particles can be easily controlled by a subsequent partial drying step. The controlled release of the gluten was achieved at the processing conditions only with  $\kappa$ -carrageenan. Some fibrilization was observed in the sheared product. However, the shearing process needs to be optimized for the use of the particles to obtain a good structure for the meat analog. The technique used for the immobilization of gluten shows promise for the immobilization or protection of other core materials, in the food industry as well as in other industries, where the food grade biopolymers can be replaced by any polymer with an acceptable melting temperature or cross-linking conditions.

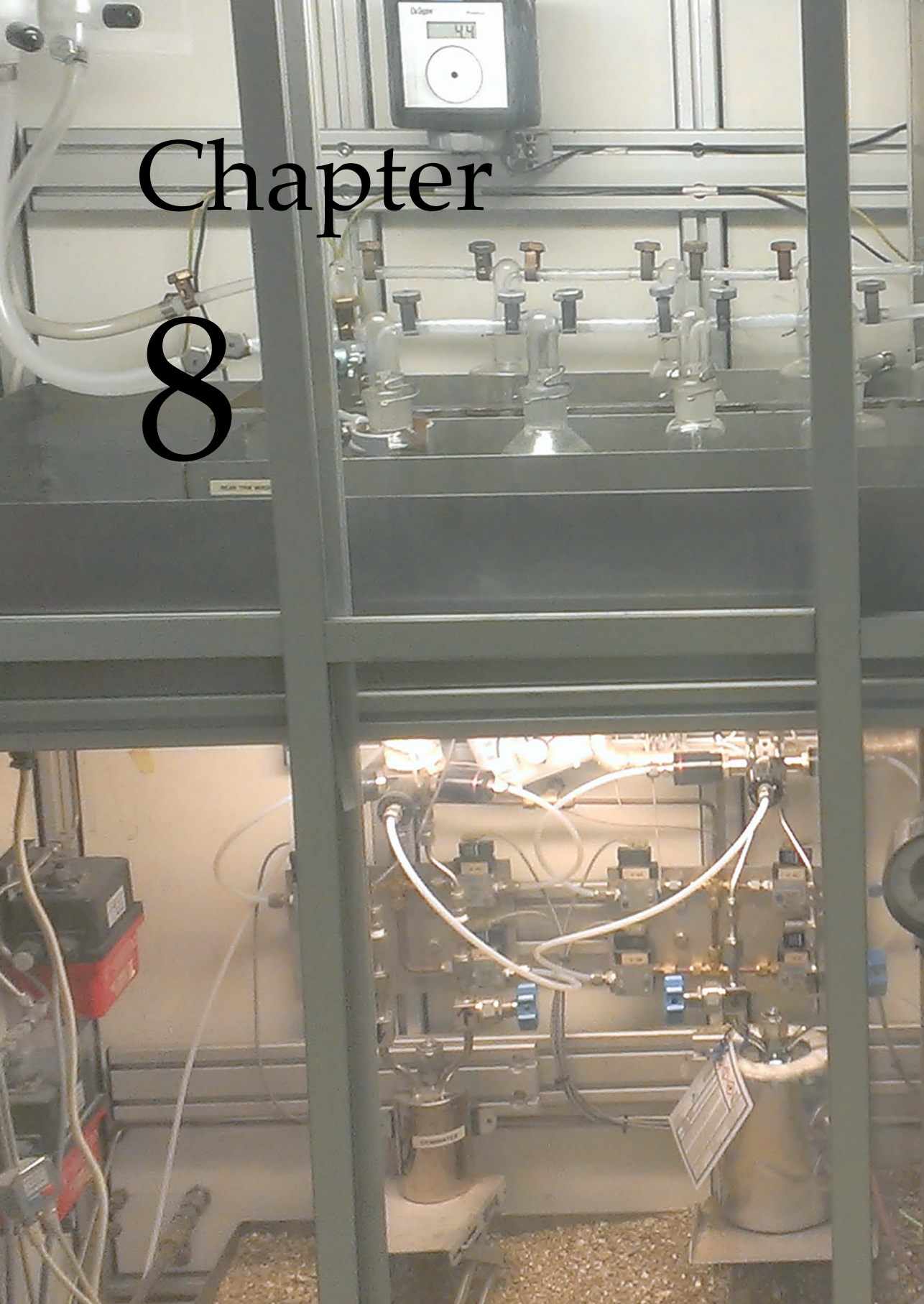
## 7.5. References

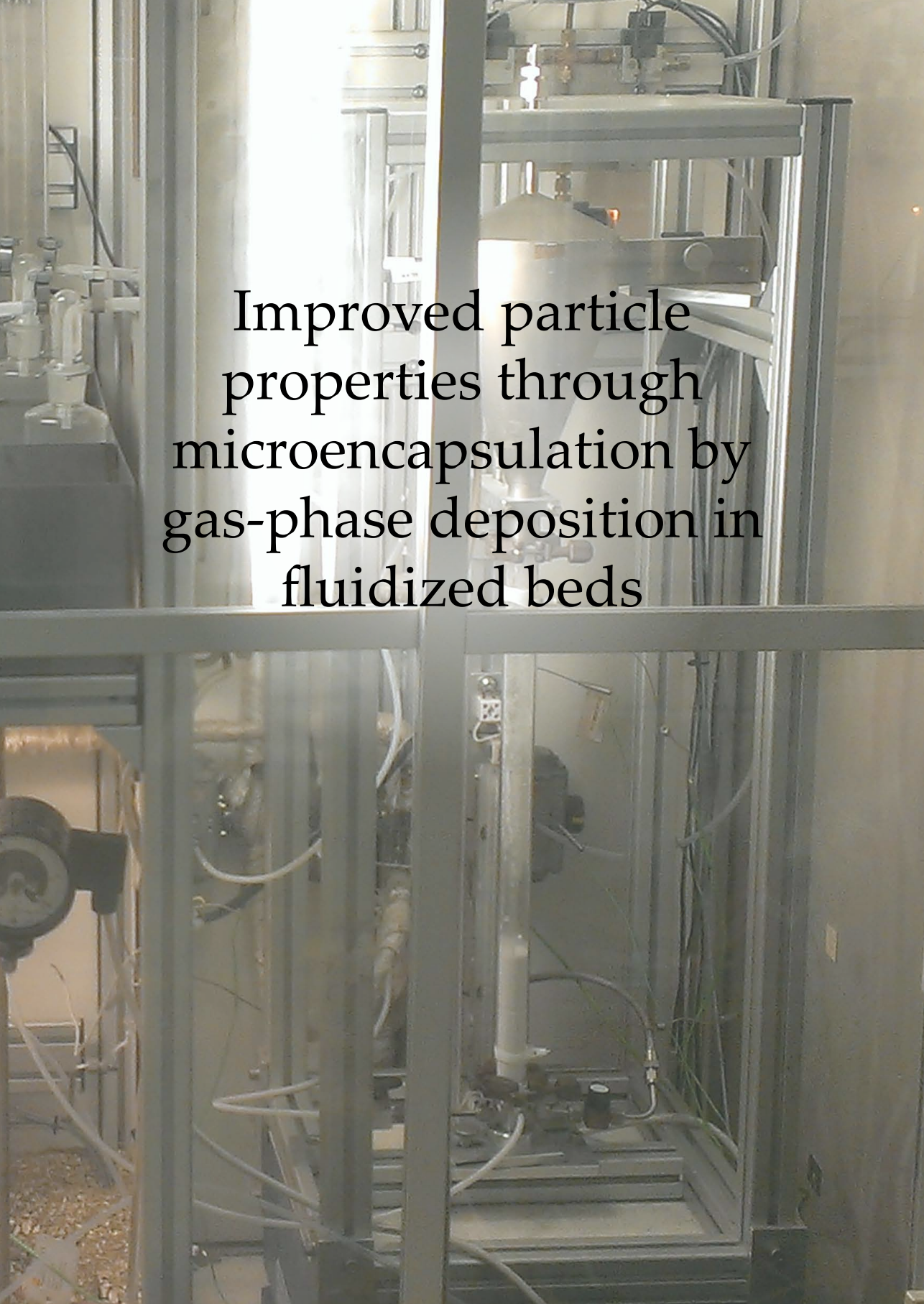
1. Hughes, D., Animal welfare. *British Food Journal* **1995**, 97, 3-7.
2. Steinfeld, H.; Food; Agriculture Organization of the United, N.; Livestock, E.; Development, *Livestock's long shadow : environmental issues and options*. Food and Agriculture Organization of the United Nations: Rome, **2006**.
3. Hoek, A. C.; Luning, P. A.; Weijzen, P.; Engels, W.; Kok, F. J.; de Graaf, C., Replacement of meat by meat substitutes. A survey on person- and product-related factors in consumer acceptance. *Appetite* **2011**, 56, 662-673.
4. Krintiras, G. A.; Göbel, J.; van der Goot, A. J.; Stefanidis, G. D., Production of structured soy-based meat analogues using simple shear and heat in a Couette Cell. *Journal of Food Engineering* **2015**, 160, 34-41.
5. Krintiras, G. A.; Gobel, J.; Bouwman, W. G.; Jan van der Goot, A.; Stefanidis, G. D., On characterization of anisotropic plant protein structures. *Food & Function* **2014**, 5, 3233-3240.
6. Abang Zaidel, D. N.; Chin, N. L.; Abdul Rahman, R.; Karim, R., Rheological characterisation of gluten from extensibility measurement. *Journal of Food Engineering* **2008**, 86, 549-556.
7. Ma, G., Microencapsulation of protein drugs for drug delivery: Strategy, preparation, and applications. *Journal of Controlled Release* **2014**, 193, 324-340.
8. Wieland-Berghausen, S.; Schote, U.; Frey, M.; Schmidt, F., Comparison of microencapsulation techniques for the water-soluble drugs nitenpyram and clomipramine HCl. *Journal of Controlled Release* **2002**, 85, 35-43.
9. Elzoghby, A. O.; Abo El-Fotoh, W. S.; Elgindy, N. A., Casein-based formulations as promising controlled release drug delivery systems. *Journal of Controlled Release* **2011**, 153, 206-216.
10. Doherty, S. B.; Gee, V. L.; Ross, R. P.; Stanton, C.; Fitzgerald, G. F.; Brodtkorb, A., Development and characterisation of whey protein micro-beads as potential matrices for probiotic protection. *Food Hydrocolloids* **2011**, 25, 1604-1617.
11. Li, R.; Shu, C.; Wang, W.; Wang, X.; Li, H.; Xu, D.; Zhong, W., Encapsulation of 10-Hydroxy Camptothecin in Supramolecular Hydrogel as an Injectable Drug Delivery System. *Journal of Pharmaceutical Sciences* **2015**, 104, 2266-2275.
12. Matalanis, A.; Jones, O. G.; McClements, D. J., Structured biopolymer-based delivery systems for encapsulation, protection, and release of lipophilic compounds. *Food Hydrocolloids* **2011**, 25, 1865-1880.
13. Mazzitelli, S.; Tosi, A.; Balestra, C.; Nastruzzi, C.; Luca, G.; Mancuso, F.; Calafiore, R.; Calvitti, M., Production and Characterization of Alginate Microcapsules Produced by a Vibrational Encapsulation Device. *Journal of Biomaterials Applications* **2008**, 23, 123-145.

14. Bai, C.; Zhang, S.; Huang, L.; Wang, H.; Wang, W.; Ye, Q., Starch-based hydrogel loading with carbendazim for controlled-release and water absorption. *Carbohydrate Polymers* **2015**, 125, 376-383.
15. Orive, G.; Hernández, R.; Gascón, A.; Pedraz, J., Encapsulation of Cells in Alginate Gels. In *Immobilization of Enzymes and Cells*, Guisan, J., Ed. Humana Press **2006**; Vol. 22, pp 345-355.
16. Orive, G.; Hernandez, R. M.; Gascon, A. R.; Calafiore, R.; Chang, T. M. S.; Vos, P. D.; Hortelano, G.; Hunkeler, D.; Lacik, I.; Shapiro, A. M. J.; Pedraz, J. L., Cell encapsulation: Promise and progress. *Nat Med* **2003**, 9, 104-107.
17. Zhou, S.; Deng, X.; Li, X., Investigation on a novel core-coated microspheres protein delivery system. *J Control Release* **2001**, 75, 27-36.
18. Tecante, A.; Santiago, M. d. C. N., Solution Properties of  $\kappa$ -Carrageenan and Its Interaction with Other Polysaccharides in Aqueous Media In *Rheology*, Vicente, D. J. D., Ed. InTech **2012**.
19. Keppeler, S.; Ellis, A.; Jacquier, J. C., Cross-linked carrageenan beads for controlled release delivery systems. *Carbohydrate Polymers* **2009**, 78, 973-977.
20. Ogbonna, J., Atomisation Techniques for Immobilisation of Cells in Micro Gel Beads. In *Fundamentals of Cell Immobilisation Biotechnology*, Nedovic, V.; Willaert, R., Eds. Springer Netherlands **2004**; Vol. 8A, pp 327-341.
21. Ridgley, D. M.; Claunch, E. C.; Barone, J. R., The effect of processing on large, self-assembled amyloid fibers. *Soft Matter* **2012**, 8, 10298-10306.
22. Burdock, G. A., *Encyclopedia of Food and Color Additives*. CRC Press **1997**; Vol. 1, p 65.
23. Remington: *The Science and Practice of Pharmacy*. Lippincott Williams & Wilkins **2006**; Vol. 1, p 1073.
24. Danial, E. N.; Elnashar, M. M. M.; Awad, G. E. A., Immobilized Inulinase on Grafted Alginate Beads Prepared by the One-Step and the Two-Steps Methods. *Industrial & Engineering Chemistry Research* **2010**, 49, 3120-3125.

# Chapter

# 8





Improved particle  
properties through  
microencapsulation by  
gas-phase deposition in  
fluidized beds

### Abstract

Atomic Layer Deposition (ALD) is applied in a fluidized bed reactor to encapsulate micron-sized particles. Ammonium chloride is coated with aluminum oxide and zinc oxide to protect it from moisture and other reactive species. Both coatings show island growth with a varying layer thickness. In dissolution experiments the time to dissolve a set amount of core material is increased, indicating a protective function of the coating. However, the coatings applied to the particles are not impervious. Particles coated with zinc oxide show a decrease in mass upon contact with moisture. A side-reaction of ammonium chloride with the zinc oxide forms gaseous ammonia, which escapes the material. Additionally, magnesium and fluorine containing precursors are used to coat aluminum, where the fluorine components function to activate the aluminum. The presence of magnesium and fluorine on the particles is confirmed. However, insufficient fluorine was present to activate the aluminum particles. By TEM-EDX analysis it was shown that coating materials were deposited inside the porous structure of the particles, which shows explicitly the atomic scale at which the ALD process operates.

## 8.1. Introduction

Microencapsulation is widely applied in the food and pharmaceutical industries to improve the stability and functionality (e.g. controlled release) of various materials<sup>1-5</sup>. The encapsulant can act as a barrier, providing protection for its core from moisture or other compounds<sup>5</sup>. However, since any encapsulant can be seen as an impurity, it is often preferred to keep this coating layer as thin as possible.

Using Atomic Layer Deposition (ALD) a very thin coating (<100 nm) can be applied to a material, monolayer by monolayer. **Figure 8.1** shows a typical example of an ALD cycle, where a substrate containing OH-groups is treated with trimethylaluminum (TMA) and water to form one aluminum oxide layer. Hereto, the reactants, transported in an inert gas flow, are exposed to the surface in a consecutive manner, where they react with the available surface groups. The reactions stop when the surface is saturated, making ALD a self-limiting process<sup>6</sup>. The ALD cycle in **Figure 8.1** consists of four steps. First, TMA is exposed to the surface and reacts with the OH-groups on the surface. Second, when all surface groups have reacted, unreacted precursor and produced by-products (methane) are purged. Third, the second precursor (water) is introduced, which reacts with the available methyl groups. Fourth, again unreacted precursor and by-products (methane) are purged. In such a cycle, a layer of aluminum oxide is formed with new hydroxyl groups at the surface, enabling repetition of the process. The number of deposited layers is related to the number of cycles performed, which means that the coating thickness can be controlled by varying the number of ALD cycles<sup>6-9</sup>.

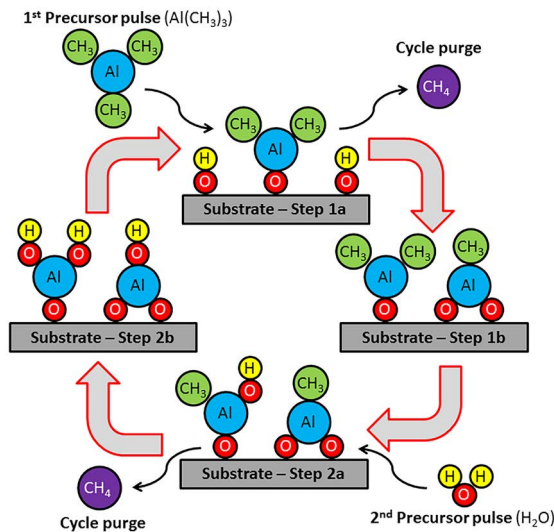


**Figure 8.1:** A typical cycle of atomic layer deposition with TMA (Al(CH<sub>3</sub>)<sub>3</sub>) and water (H<sub>2</sub>O) as precursors.

In order to use ALD for layer deposition on particles instead of flat surfaces, the technique can be applied in a fluidized bed<sup>10-13</sup>. The transportation of reactants and the purging steps are then facilitated by the  $N_2$  flow that is already required for fluidization, making this coating step easy to integrate in the fluidized bed operation. The fluidization action in turn provides good mixing of the core particles and precursors and allows for temperature control during the reactions. However, using ALD as a coating method in a fluidized bed reactor can be hampered by agglomeration of the solid particles due to interparticle forces such as Van der Waals, capillary, and electrostatic forces<sup>14-16</sup>. Too much agglomeration can even lead to defluidization, since the minimum fluidization velocity increases with particle size. However, due to the nature of ALD, the majority of the individual particles within the agglomerates in the fluidized bed reactor is coated<sup>17, 18</sup>.

Coating by means of ALD can be applied to almost any kind of material. For example, energetic materials can be coated using ALD to separate them from their environment. This prevents any unwanted reaction, thereby making the materials easier to handle. We are interested in increasing the manageability of energetic materials such as ammonium nitrate ( $NH_4NO_3$ ), red phosphorus ( $P_4$ ), and metallic aluminum (Al).  $NH_4NO_3$  is used in e.g. propellants. However, it is a hygroscopic material<sup>19</sup> and moisture decreases the performance of the material.  $P_4$  is the compound that produces smoke in smoke grenades<sup>20</sup>. However, in moist air, toxic phosphine gas and various phosphoric acids are produced<sup>20</sup>. Both materials can be protected against moisture by applying a thin, impervious layer to their surface. Aluminum is used as a fuel for different applications in pyrotechnics and rocket propellants<sup>21</sup>. Fluorine activates aluminum in catalytic quantities, improving its burning characteristics<sup>22</sup>. By depositing a fluorine containing film on aluminum, the catalytic effect is brought to the surface where the combustion reactions take place.

The aim of this work is to deposit a thin coating in the order of a few nanometers on various types of microparticles by means of ALD, and investigate if thereby protective or activating effects are achieved on the core particles. Ammonium chloride ( $NH_4Cl$ ) was used as model compound for  $NH_4NO_3$  and  $P_4$ , for safety reasons.  $NH_4Cl$  is coated with aluminum oxide ( $Al_2O_3$ ), using TMA and water as precursors<sup>23</sup>, and with zinc oxide (ZnO), using diethylzinc ( $Zn(CH_2CH_3)_2$ , DEZ) and water as precursors<sup>24</sup>. The number of cycles, reactor temperature, and precursor exposure time were varied to investigate their influence on the coating deposition. The metallic aluminum is coated with magnesium fluoride ( $MgF_2$ ) by using bis(ethylcyclopentadienyl) magnesium ( $Mg(CpEt)_2$ ) and titanium(IV)fluoride ( $TiF_4$ ) as precursors<sup>25, 26</sup>.

## 8.2. Materials and methods

### 8.2.1. Materials

Ammonium chloride (ACS reagent,  $\geq 99.5\%$  purity) was purchased at Sigma-Aldrich. Aluminum (99% purity) was purchased at Acros Organics (Belgium). Trimethylaluminum (select semiconductor grade) and diethylzinc (select semiconductor grade) were purchased from Akzo-Nobel HPMO. Demineralized water was used as second precursor. Bis(ethylcyclopentadienyl)magnesium ( $\geq 98\%$  purity) and titanium(IV)fluoride (98% purity) were purchased from Strem Chemicals.

### 8.2.2. ALD in fluidized beds

**Figure 8.2** shows a schematic representation of the experimental setup used to perform ALD in a fluidized bed reactor (FBR). Nitrogen was used as inert carrier gas, which facilitated the fluidization of the bed as well as the transport and purging of precursors to and from the reactor column. As shown in **Figure 8.2**, valves were used to control the flow of nitrogen through the bubblers to carry precursor to the particles, and through a bypass for purging the system. The TMA and DEZ bubblers were heated to  $30^\circ\text{C}$  and the water bubbler was operated at room temperature. The  $\text{Mg}(\text{CpEt})_2$  bubbler was heated to  $90^\circ\text{C}$ , and the  $\text{TiF}_4$  bubbler to  $225^\circ\text{C}$ . For these temperatures, reasonable precursor vapor pressures were obtained, for which the required precursor exposure time was calculated. A glass reactor was used with an inner diameter of 26 mm and a length of 500 mm. For each experiment, approximately 30 g of powder, sieved to a size fraction of 53 – 75  $\mu\text{m}$ , was loaded in the column. The vibromotors were set to a frequency in the range of 30 – 35 Hz to aid the fluidization. The nitrogen flow ranged from 0.5 to 1 L/min, which corresponds to a superficial flow velocity range of 1.57 to 3.14 cm/s. The hygroscopic  $\text{NH}_4\text{Cl}$  required a superficial velocity of 3.14 cm/s for fluidization. The aluminum powder was fluidized with a superficial velocity of 1.57 cm/s. The number of ALD cycles ranged from 5, 10, 20, to 30 cycles. The cycle times varied from 10 – 600 – 30 – 600 seconds of first precursor, nitrogen purge, second precursor, and nitrogen purge respectively, to 600 – 600 – 600 – 600 seconds. The reactor was heated using an infrared lamp to control the temperature during fluidization. Temperatures ranged from 30 to  $200^\circ\text{C}$ . After the gas flow passed through the reactor, it was cleaned in bubblers filled with mineral oil to remove and stabilize any unreacted precursors. Per precursor, a different set of bubblers was used to prevent precursor reactions inside the bottles. Last, the exhaust gas flow was led through a HEPA filter. The pressure of the outlet gas flow was atmospheric.

For coating  $\text{NH}_4\text{Cl}$  with  $\text{Al}_2\text{O}_3$  and  $\text{ZnO}$ , 30 g of  $\text{NH}_4\text{Cl}$  was used per batch. The number of cycles was varied from 5, 10, to 20. The vibromotors were set

to a frequency of 33 Hz to aid fluidization. Intermediate sampling was done after applying 5 and 10 cycles, each time removing a sample of approximately 10 g from the reactor, after which the experiment was continued. After 20 cycles, the remaining powder was collected from the reactor. For coating aluminum particles with magnesium fluoride, the number of cycles was varied from 5, 10, 20, to 30. After 5, 10, and 20 cycles, about 10 g of sample was removed from the reactor where after the coating procedure was continued. No vibration was required.

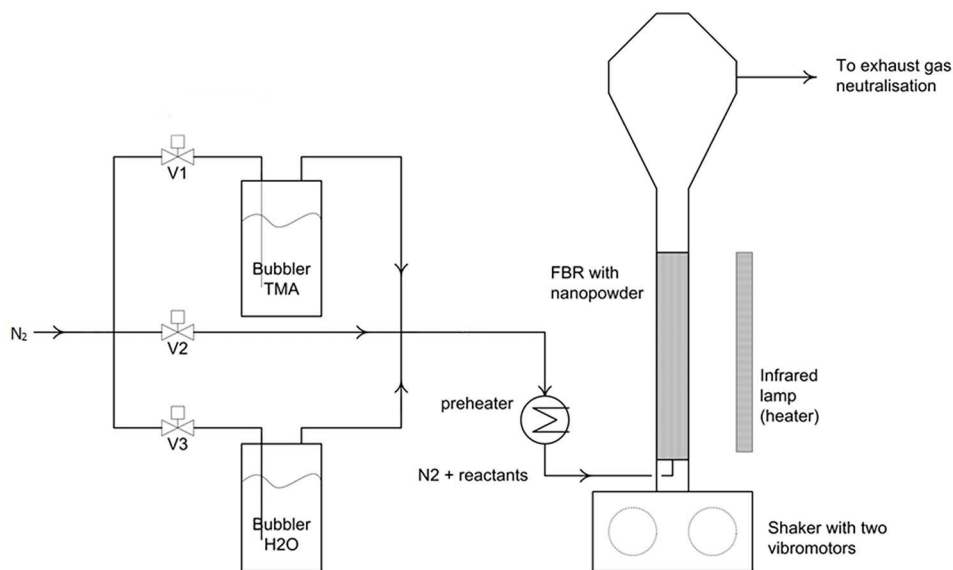


**Figure 8.2:** Schematic of the experimental setup for the coating of particles by ALD in a FBR<sup>23</sup>. Each precursor is transported to the FBR by nitrogen, which acts as carrier flow. Only one valve out of V1 - V3 is opened at a time. V2 is opened for the purge steps between the precursor exposures.

### 8.2.3. Analysis

*Particle visualization / composition* – A Jeol JSM 6500F (SEM) was used to visualize the particles and a Thermo-Fischer Ultradry Solid State Drift (EDX) was used to determine the elemental composition of the particles and coatings. All samples were analyzed as provided. The electron beam had an energy of 10 or 15 keV and a current of 200 pA. All images were acquired in secondary electron image mode (SEI). The EDX results were processed with the accompanying software NORAN System 7 (Thermo-Fischer). The material composition of point measurements were determined using known reference spectra of the pure elements with an acquisition time of 60 seconds.

*Solubility measurements* – To assess the solubility of  $\text{NH}_4\text{Cl}$  solutions at different temperatures, the TV method was used as in **Section 2.2**, with heating and cooling rates of  $0.5^\circ\text{C}/\text{min}$ .

*Particle Size Distribution measurements* – A Microtrac S3500 was used to measure the particle size distribution (PSD) of all core materials. All particle size distributions were measured using dry powder samples. For each measurement, approximately 1 gram of powder was used.

*Elemental concentration measurements* – A Sysmex Spectro Arcos (ICP-OES) was used to measure the concentrations of possible elements from the core materials and coatings. All samples were dissolved using 37% hydrochloric acid (HCl), 70% nitric acid ( $\text{HNO}_3$ ), and water with a volumetric ratio of 3:1:1. Further dilution needed for the sample preparation was done with a 3%  $\text{HNO}_3$  solution.

*Material grinding* – A Pulverisette 7 Premium Line (Fritsch) was used to grind coarse  $\text{NH}_4\text{Cl}$  crystals into smaller particles. Per 15 g of powder, 10 zirconium oxide grinding balls were loaded in a grinding bowl. The bowls were set to a velocity of 1000 rpm for a duration of 5 minutes.

*pH-measurements* – A PHM 95 pH (Radiometer, Copenhagen) was used to measure all pH values. Before each series of measurements, the device was calibrated in aqueous neutral and acidic solutions with a known pH of 7.000 and 4.005. The pH was measured in a range between 3 and 7 (acidic) while the solution was stirred at 300 rpm.

*Mass change measurements* – A Mettler Toledo TGA/DSC 1 was used to measure the mass increase of aluminum powder during oxidation using standard atmospheric conditions and under pure nitrogen. The samples were measured in a temperature range of  $25 - 800^\circ\text{C}$  with a heating rate of  $5^\circ\text{C}/\text{min}$ . The oxidizing atmosphere was supplied at a rate of 50 mL/min. Open aluminum oxide crucibles of 70  $\mu\text{L}$  were used as sample holders.

*TEM-EDX measurements* – A Nova200 cryo-dual beam SEM was used to cut out approximately 0.1  $\mu\text{m}$  thick lamellae from the micro-particles using focused ion beam (FIB) technique. The lamellae were analyzed in a FEI-Tecna F30 equipped with an EDAX EDS system. The Field Emission Gun operated at 300 kV. The images were taken in STEM mode with a HAADF detector.

### 8.3. Results and Discussion

Two core materials were fluidized and subsequently coated with various shell materials. The fluidization of  $\text{NH}_4\text{Cl}$  and coating with  $\text{Al}_2\text{O}_3$  and  $\text{ZnO}$  are discussed in **Section 8.3.1**. In **Section 8.3.2** the results of the fluidization of aluminum powder are presented, together with the deposition of  $\text{MgF}_2$  on its surface.

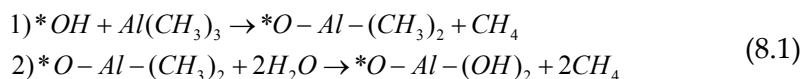
#### 8.3.1. Fluidization and coating of ammonium chloride

The sieved ammonium chloride particles had an average volume based particle size of approximately  $56\ \mu\text{m}$  with a standard deviation of roughly  $29\ \mu\text{m}$ . Because of the hygroscopic nature of  $\text{NH}_4\text{Cl}$ , the powder has the tendency to agglomerate. Therefore, vibration was used to enhance fluidization<sup>27</sup>. At a vibration frequency of 33 Hz, a superficial flow velocity of 2.35 cm/s was the minimum fluidization velocity. For the coating experiments a higher superficial flow velocity of 3.14 cm/s was used to evaporate all moisture present on the  $\text{NH}_4\text{Cl}$  particles. This was necessary, because water was used as second precursor. After fluidizing ammonium chloride for 2.5 h at  $70^\circ\text{C}$ , approximately 2 wt% of the bed material was lost by elutriation. Since a coating experiment takes approximately 8 h, this loss is deemed acceptable. After investigation of the fluidization behavior, the coating experiments were performed.

*Coating with aluminum oxide*

Coating thickness.

The TMA exposure time was varied from 10, 90, to 600 s. The corresponding exposure times for water were 30, 120, and 600 s, respectively. The experiment with a TMA exposure time of 90 s, a water exposure time of 120 s, and a reactor temperature of  $70^\circ\text{C}$  was taken as reference experiment. The reactor temperature was varied from 30, 70, to  $120^\circ\text{C}$ . The two-step ALD mechanism for depositing  $\text{Al}_2\text{O}_3$  is given in **eq. 8.1** where \* denotes the substrate surface as shown in **Figure 8.1**:



ICP measurements on each sample confirmed the presence of Al on the  $\text{NH}_4\text{Cl}$  crystals. **Table 8.1** shows the concentration of aluminum in each sample. The aluminum concentrations differ significantly between the various experiments, where the experiment of  $t_{coat} = 90$  s TMA at a temperature of  $T = 70^\circ\text{C}$  has a significantly higher concentration of aluminum than the others. Between the other experiments trends are seen that higher temperature and longer cycle times lead to higher concentrations of aluminum found in the sample. It is remarkable, though, that in a single experiment, running

more cycles does not necessarily lead to higher aluminum concentrations in a sample.

From these concentrations the layer thickness was estimated. Assuming the  $\text{NH}_4\text{Cl}$  particles to be spherical, the mass of one particle can be estimated using eq. 8.2:

$$m_p = \frac{4}{3} \rho \pi r_p^3 \quad (8.2)$$

Where  $m_p$  is the mass of a particle (kg),  $\rho$  the density ( $\text{kg}/\text{m}^3$ ), and  $r_p$  the radius of a particle (m).

**Table 8.1:** Concentrations and estimated coating thickness of all  $\text{NH}_4\text{Cl}$  samples coated with  $\text{Al}_2\text{O}_3$ , based on ICP analysis.

| Experimental conditions  | Number of ALD cycles | Concentration of Al [ppm]    | Estimated coating thickness [nm] <sup>28</sup> |
|--|----------------------|------------------------------|--|
| $t_{\text{coat}} = 90 \text{ s TMA}$<br>$t_{\text{coat}} = 120 \text{ s H}_2\text{O}$<br>$T = 70^\circ\text{C}$  | 5                    | $(54.2 \pm 2.7) \cdot 10^3$  | $(3.4 \pm 0.3) \cdot 10^3$                     |
|  | 10                   | $(152.5 \pm 7.6) \cdot 10^3$ | $(8.8 \pm 0.9) \cdot 10^3$                     |
|  | 20                   | $(42.5 \pm 2.2) \cdot 10^3$  | $(2.8 \pm 0.3) \cdot 10^3$                     |
| $t_{\text{coat}} = 90 \text{ s TMA}$<br>$t_{\text{coat}} = 120 \text{ s H}_2\text{O}$<br>$T = 30^\circ\text{C}$  | 5                    | $12 \pm 1$                   | $0.8 \pm 0.1$                                  |
|  | 10                   | $13 \pm 1$                   | $0.9 \pm 0.1$                                  |
|  | 20                   | $16 \pm 1$                   | $1.1 \pm 0.1$                                  |
| $t_{\text{coat}} = 90 \text{ s TMA}$<br>$t_{\text{coat}} = 120 \text{ s H}_2\text{O}$<br>$T = 120^\circ\text{C}$ | 5                    | $640 \pm 32$                 | $43 \pm 4$                                     |
|  | 10                   | $772 \pm 39$                 | $52 \pm 5$                                     |
|  | 20                   | $701 \pm 35$                 | $47 \pm 5$                                     |
| $t_{\text{coat}} = 10 \text{ s TMA}$<br>$t_{\text{coat}} = 30 \text{ s H}_2\text{O}$<br>$T = 70^\circ\text{C}$   | 5                    | $33 \pm 2$                   | $2.2 \pm 0.2$                                  |
|  | 10                   | $20 \pm 1$                   | $1.3 \pm 0.1$                                  |
|  | 20                   | $23 \pm 1$                   | $1.6 \pm 0.2$                                  |
| $t_{\text{coat}} = 600 \text{ s TMA}$<br>$t_{\text{coat}} = 600 \text{ s H}_2\text{O}$<br>$T = 70^\circ\text{C}$ | 5                    | $88 \pm 4$                   | $5.9 \pm 0.6$                                  |

For the radius the Sauter mean diameter of the particle size distribution was used. From the sample volume and the aluminum concentration in the sample obtained by ICP, the volume of aluminum oxide was determined using a molar ratio of aluminum to oxide in aluminum oxide of 2:3 and a density  $\rho = 4,000 \text{ kg}/\text{m}^3$ . With the volume of the particle and the coating material, the radius of the coated particle can be estimated using eq. 8.3:

$$t_{cp} = r_c - r_p = \sqrt[3]{\frac{3(V_p + V_c)}{4\pi}} - r_p \quad (8.3)$$

Where  $t_{cp}$  is the thickness of the coating (m),  $r_c$  is the radius of the coated particle (m),  $V_p$  is the volume of the uncoated particle ( $\text{m}^3$ ), and  $V_c$  is the volume of the coating material ( $\text{m}^3$ ). By subtracting the radius of the uncoated particle ( $r_p$ ) from the radius of the coated particle ( $r_c$ ) the coating thickness is approximated, assuming that the coating is evenly distributed on the particle surface.

While it is expected that under normal conditions the layer thickness should increase with the number of cycles, from **Table 8.1** it is observed that this only holds for the case with a reactor temperature  $T = 30^\circ\text{C}$ . For example, in the sample treated with a cycle time of  $t_{coat} = 90$  s TMA at a temperature of  $T = 70^\circ\text{C}$ , much more aluminum was detected after 10 cycles than after 20 cycles. In this particular experiment, the bed was not fluidizing anymore after 10 cycles, but instead converted into a static solid block. Therefore, the 20 cycles sample was performed with a new batch of ammonium chloride particles. These particles were, similar to the first batch for the 5 and 10 cycles samples, not pretreated. It is still consistent with theory that the 10 cycles sample contains more aluminum than the 5 cycles sample. However, almost three times the amount of aluminum was found while it should be doubled.

The larger than expected deposition of  $\text{Al}_2\text{O}_3$  during the first experiment ( $t_{coat} = 90$  s TMA,  $T = 70^\circ\text{C}$ ) is most probably caused by adsorbed moisture on the surface of the particles, since  $\text{NH}_4\text{Cl}$  is hygroscopic<sup>27</sup>. If moisture is present on the sample, the total amount of formed aluminum oxide increases. Therefore, the  $\text{NH}_4\text{Cl}$  samples of all other experiments were dried for 45 minutes in the fluidized bed prior to the coating procedure. This resulted in a significantly lower concentration of aluminum in the samples.

To investigate the effect of temperature on the deposition of the coating, the experiments with ammonium chloride were performed at higher and lower temperatures. The cycle time used for these experiments is  $t_{coat} = 90$  s TMA, which allows for a stoichiometric exposure of precursor to the available particle surface and includes a safety margin, ensuring full surface coverage. During the experiment at  $T = 30^\circ\text{C}$ , the fluidizing bed collapsed during the water cycles, resulting in a low deposition of aluminum oxide since the particles were not mixed for the complete precursor exposure time. The experiment performed at  $T = 120^\circ\text{C}$  yielded a significantly higher deposition of aluminum oxide compared to the experiment at  $T = 30^\circ\text{C}$ . Comparing the concentrations of aluminum in the samples at 30 and  $120^\circ\text{C}$  with those at  $70^\circ\text{C}$ , it follows that the drying of the samples beforehand has a big influence on the amount of reacted TMA. This indicates that the high deposition at

$T = 70^\circ\text{C}$  is indeed due to remaining moisture on the particles at the start of the experiment.

Additionally, the cycle times were varied to allow quantities of precursor to reach the particles between close to stoichiometric values ( $t_{\text{coat}} = 10$  s TMA) and a large excess ( $t_{\text{coat}} = 600$  s TMA). These experiments were conducted at a reactor temperature of  $T = 70^\circ\text{C}$ . The deposition of aluminum oxide onto the particles was larger using an excess amount of precursor ( $t_{\text{coat}} = 600$  s TMA) than for the stoichiometric exposure cycles ( $t_{\text{coat}} = 10$  s TMA). When applying an excess amount of precursor, some of it may condense or adsorb on the surface of the particles and can then still be present after the purging step. Switching to the other precursor causes the condensed or adsorbed material to react, thereby resulting in a thicker coating. This means that to obtain just a monolayer of material per cycle, the cycle time should not be too high. The ALD reactions themselves are self-limiting, but due to adsorption of precursors on the surface when operating at a low temperature, more material can be deposited than with pure ALD.

The particle morphology and surface composition were also assessed by SEM-EDX. **Figure 8.3** shows a SEM-image of uncoated  $\text{NH}_4\text{Cl}$  particles (a) and of  $\text{NH}_4\text{Cl}$  treated with 20 ALD cycles of TMA and water with a cycle time of  $t_{\text{coat}} = 90$  s TMA and  $t_{\text{coat}} = 120$  s  $\text{H}_2\text{O}$  at a temperature of  $T = 70^\circ\text{C}$  (b).

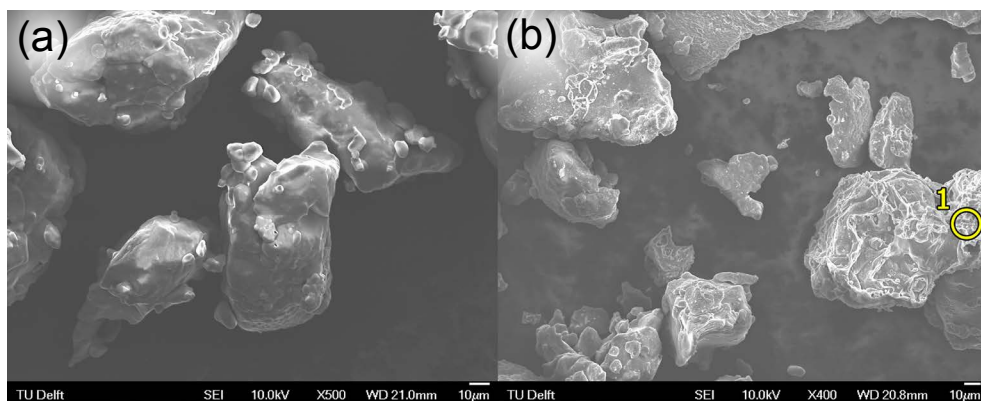


**Figure 8.3:** SEM images of uncoated ammonium chloride (a) and ammonium chloride coated with 20 cycles of TMA and water ( $t_{\text{coat}} = 90$  s TMA,  $t_{\text{coat}} = 120$  s  $\text{H}_2\text{O}$ , and  $T = 70^\circ\text{C}$ ) (b) using a magnification of 400x. Point 1 shows the location of the EDX analysis.

The particle surfaces in **Figure 8.3(a)** and **(b)** show a distinct difference between uncoated and coated particles. While the surface is rather smooth for the uncoated particles, it is rough for the coated ones. This indicates that deposition has taken place on the particles. **Figure 8.4** shows the results of EDX-measurements using uncoated (a) and coated ammonium chloride (b). The EDX measurement was performed at point 1 (**Figure 8.3(b)**). In both figures no peak for nitrogen (N) is shown. To avoid close overlapping of ele-

mental peaks in the EDX plots, nitrogen peaks were removed from the plots. As shown in the table in **Figure 8.4(b)**, both aluminum and oxygen were found. The ratio of Al and O from the EDX analysis indicates that compared to normal  $\text{Al}_2\text{O}_3$  the layer contains a surplus of oxygen, which can be explained by water being adsorbed on the surface. Nevertheless, the amounts of oxygen and aluminum detected on the particle indicate that aluminum oxide was deposited.

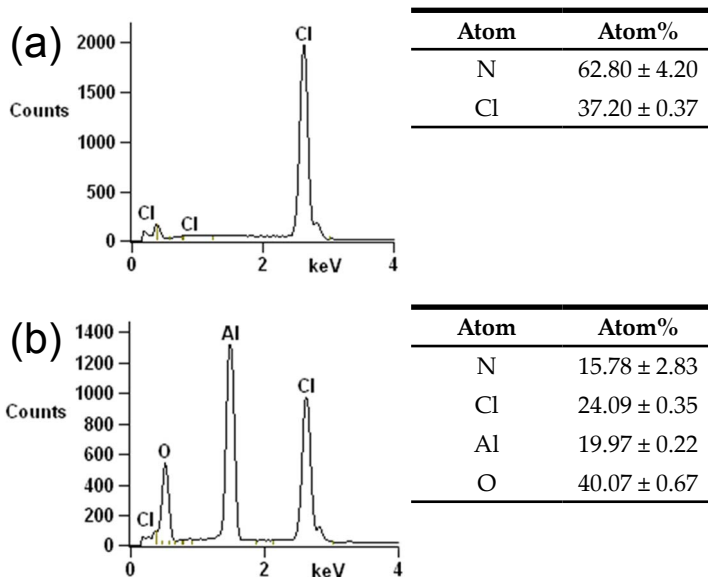


**Figure 8.4:** EDX measurement on uncoated ammonium chloride (a) and coated ammonium chloride (b) with 20 cycles of TMA and water ( $t_{\text{coat}} = 90$  s TMA,  $t_{\text{coat}} = 120$  s  $\text{H}_2\text{O}$ , and  $T = 70^\circ\text{C}$ ) performed at point 1 (**Figure 8.3(b)**).

The EDX measurement on the sample with 20 cycles as shown in **Figure 8.4** is used to estimate the layer thickness. From the concentrations of the elements found by EDX, the number of moles of each species was determined using their molar mass. By using the density of aluminum oxide and ammonium chloride, the total volume of both of these materials in the sample was estimated. With the energy level and materials used, the penetration depth of the EDX analysis is approximately  $1 \mu\text{m}^{29}$ . The coating volume was calculated as a fraction of the total volume. From the penetration depth the volume fraction of coating material was used to estimate its layer thickness. The calculated layer thickness from the EDX analysis in the example is approximately  $496 \pm 27$  nm. The estimated thickness of this sample based on ICP results was  $2,793 \pm 279$  nm. The size of the analyzed particle in **Figure 8.3b** suggests that the measured  $\text{Al}_2\text{O}_3$  is on the surface of the  $\text{NH}_4\text{Cl}$  particle.

In ICP analysis, it was found that the experiment at  $t_{\text{coat}} = 90$  s TMA and  $T = 70^\circ\text{C}$  resulted in a much larger deposition than in all other experiments.

The layer thicknesses are also larger than typical values for ALD deposited coatings. Therefore, the experiment at  $T = 120^\circ\text{C}$  was also investigated in SEM-EDX. In **Figure 8.5(a)** it is observed that the particle surface looks much more like uncoated particles in **Figure 8.3(a)**. However, overlaying an elemental scan showed that all particle surfaces contain quantities of aluminum (red) and oxygen (green), indicating the presence of  $\text{Al}_2\text{O}_3$ . One particle shows up mostly red, instead of containing a mixture of green and red dots. Since ammonium chloride is hygroscopic, moisture can be adsorbed to the particle surface. Subsequently, the moisture can react with water, forming aluminum oxide. This also explains the high amounts of aluminum in the ICP results. Due to the atmospheric pressure and low temperatures, excess precursor molecules can adsorb to the surface and react during the subsequent reaction. The physisorption of unreacted precursor molecules results in a CVD-type (Chemical Vapor Deposition) of growth<sup>30-32</sup>.

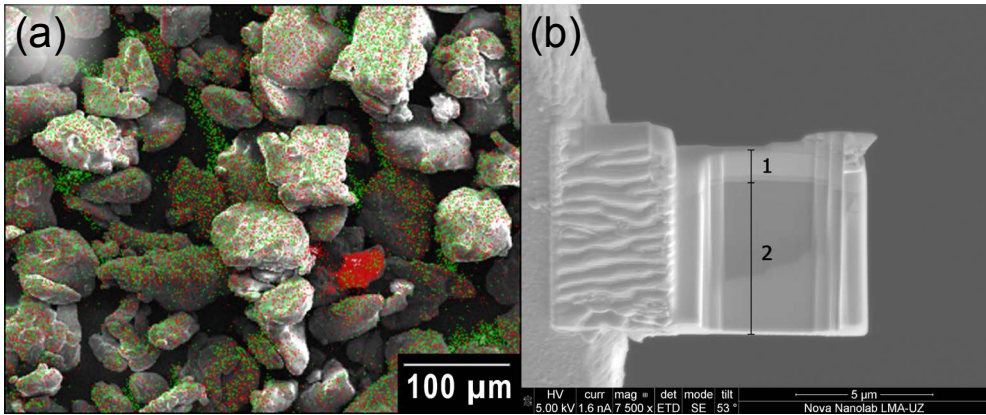


**Figure 8.5:** (a) SEM image of  $\text{NH}_4\text{Cl}$  particles coated with  $t_{\text{coat}} = 90$  s TMA,  $T = 120^\circ\text{C}$ , with an overlay of the EDX elemental scan. Red dots represent aluminum, green dots oxygen. (b) TEM image of a lamella cut out of the same sample. EDX analysis showed that in region 1 aluminum atoms were mixed in the  $\text{NH}_4\text{Cl}$ .

Transmitting electron microscopy (TEM) was used to further analyze the coating thickness. In **Figure 8.5(b)** a lamella is shown, cut from a particle coated with  $t_{\text{coat}} = 90$  s TMA,  $T = 120^\circ\text{C}$ . Layer 1 in this figure is the sputtered layer of Pt that prevents charging of the material, layer 2 is the particle. EDX scans along the height of this particle revealed that the  $\text{Al}_2\text{O}_3$  has diffused inside the porous structure of the particle. In region 2 the aluminum concentration is high, and uniform over the height of the layer. The change in color does not seem to relate to a change of composition. This shows that the precursors penetrate deeply in the particle structure ( $> 5 \mu\text{m}$ ). This explains why the estimated layer thickness is smaller from EDX measurements than from ICP, since the aluminum penetrates deeper than the EDX measurement, so not all deposited aluminum is taken into account. In the ICP measurements, all the aluminum is taken into account. It is likely that due to the deposition

inside the porous structure, there was no full layer on top of the particle. This shows the nature of ALD, which indeed works at the atomic scale and is able to cover nanostructured surfaces.

### Coating performance.

The performance of the coating was tested by dissolution rate experiments. The pH was used as a measure for the concentration. An impervious coating would prevent the core particle ( $\text{NH}_4\text{Cl}$ ) from dissolving in water. However, even if the coating is not impervious, it can still have a protective function. The imperviousness of the coating layer was assessed by measuring the dissolution time of the uncoated and coated  $\text{NH}_4\text{Cl}$  crystals in water. The dissolution time is defined as the time required to reach an equilibrium in terms of pH when a dosage of (coated)  $\text{NH}_4\text{Cl}$  is added to water. **Figure 8.6** shows the dissolution times for two ammonium chloride samples coated with aluminum oxide.

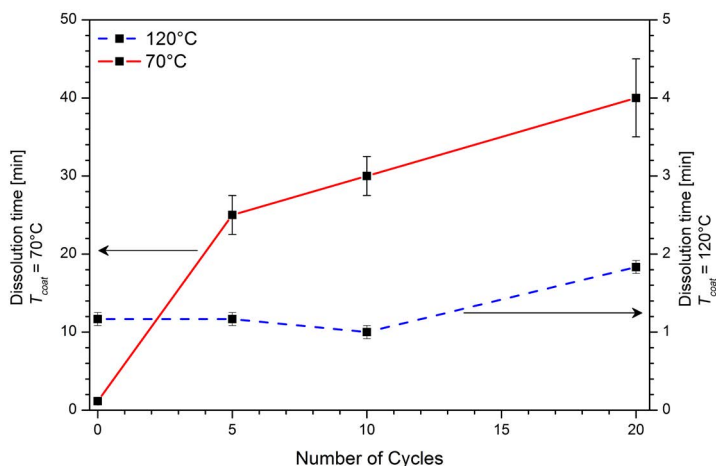


**Figure 8.6:** Dissolution time of  $\text{NH}_4\text{Cl}$  coated with 5, 10, and 20 cycles of TMA and water at two different process conditions:  $t_{\text{coat}} = 90$  s TMA,  $t_{\text{coat}} = 120$  s  $\text{H}_2\text{O}$ , and  $T = 70^\circ\text{C}$  (red, primary y-axis);  $t_{\text{coat}} = 90$  s TMA,  $t_{\text{coat}} = 120$  s  $\text{H}_2\text{O}$ , and  $T = 120^\circ\text{C}$  (blue, secondary y-axis). The dissolution time at 0 cycles corresponds to the dissolution time of uncoated  $\text{NH}_4\text{Cl}$ .

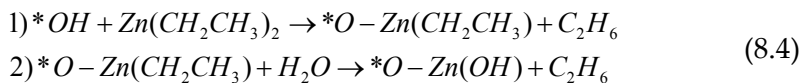
**Figure 8.6** shows a significantly increasing dissolution time with the number of deposited cycles for the experiment with coated  $\text{NH}_4\text{Cl}$  with  $\text{Al}_2\text{O}_3$  with cycle times  $t_{\text{coat}} = 90$  s TMA and  $t_{\text{coat}} = 120$  s water and a reactor temperature  $T = 70^\circ\text{C}$ . For the other experiments the dissolution time remained small and does not show significant changes, meaning that the coating was incomplete, hardly providing any protection against dissolution. The blue line in **Figure 8.6** indicates that the sample shows a delay in dissolution time at 20 cycles. The coatings of the 5 and 10 cycles sample were not sufficient to provide a protective function. This indicates that only after 10 cycles the porous structure is saturated and proper surface coverage commences. In all exper-

iments, eventually all  $\text{NH}_4\text{Cl}$  dissolved, indicating that either the deposited coatings are not impervious, or that the coatings could not withstand the driving forces exerted on them due to the concentration gradient during the dissolution process. A certain amount of reactive surface groups is required to coat a particle with an impervious monolayer. This can be translated to the smallest configuration of a material, the unit cell. The unit cell volume of ammonium chloride is approximately  $57.96 \text{ \AA}^3$ <sup>33</sup>. Each crystallographic surface will have a different number of reactive groups. However, from the perspective of an arbitrary surface, the distance between reactive groups can be relatively large when the concentration of reactive groups is low. This might make it more difficult to make a fully impervious coating, even if an excess of precursors is used. Another explanation would be that the coating grows as islands on the particle surface. Even if the surface has a high density of reactive groups, it depends on how the reaction occurs whether a smooth coating or island growth occurs. If it is more likely that the precursors react far away from a reactive group that has already been reacted, a smooth layer would be the result. On the other hand, if it is more likely that the precursors react close to such a reacted group, island growth occurs. Then, as more coating cycles are applied, the thickness of these islands increases. At the same time, they will grow laterally, finally resulting in a complete layer, when sufficient coating cycles have been applied<sup>34</sup>. According to the functioning and visualization of the  $\text{Al}_2\text{O}_3$  coating on  $\text{NH}_4\text{Cl}$ , a low amount of reactive groups per unit cell area has resulted in the island growth on the ammonium chloride particles. Thus, more ALD cycles should be applied to deposit a thicker and more impervious layer when the coating does not provide the desired effect.

*Coating with zinc oxide*

Coating thickness.

Ammonium chloride was coated with zinc oxide at a temperature  $T = 70^\circ\text{C}$  and a cycle time of  $t_{\text{coat}} = 90 \text{ s}$  DEZ and  $t_{\text{coat}} = 120 \text{ s}$  water. The two-step ALD mechanism for depositing ZnO follows the relations in eq. 8.4 where \* denotes the substrate surface:



The presence of zinc on the particles subjected to the ALD process was confirmed with ICP measurements. **Table 8.2** shows the concentration of zinc on each sample and the estimated layer thickness. A similar approach was used for the estimation of the layer thickness as described for the aluminum oxide coating. The estimated layer thicknesses are much larger than what should be expected with ALD. As with the  $\text{Al}_2\text{O}_3$  layers, this is most likely due to adsorbed water which results in a CVD-type of growth.

**Table 8.2:** Concentration and estimated coating thickness of all  $\text{NH}_4\text{Cl}$  samples coated with ZnO, based on ICP analysis.

| Experimental conditions                       | Number of ALD cycles | Concentration of Zn [ppm]   | Estimated coating thickness [nm] <sup>28</sup> |
|---|----------------------|-----------------------------|--|
| $t_{\text{coat}} = 90 \text{ s DEZ}$          | 5                    | $(9.7 \pm 0.5) \cdot 10^3$  | $126 \pm 13$                                   |
| $t_{\text{coat}} = 120 \text{ s H}_2\text{O}$ | 10                   | $(17.2 \pm 0.9) \cdot 10^3$ | $223 \pm 22$                                   |
| $T = 70^\circ\text{C}$                        | 20                   | $(19.1 \pm 1.0) \cdot 10^3$ | $247 \pm 25$                                   |

According to **Table 8.2**, the amount of deposited zinc increases with the number of applied cycles, as expected. SEM images were used to investigate the surface morphology and EDX was used to determine the elemental composition of the surface. **Figure 8.3(a)** shows a SEM-image of uncoated  $\text{NH}_4\text{Cl}$ . **Figure 8.7** shows a SEM-image of ZnO coated  $\text{NH}_4\text{Cl}$  where small islands on the particle surface can be observed. In comparison with **Figure 8.3(a)**, where the particle surface is smooth, it can be observed that material was deposited on the surface of the particles shown in **Figure 8.7**.

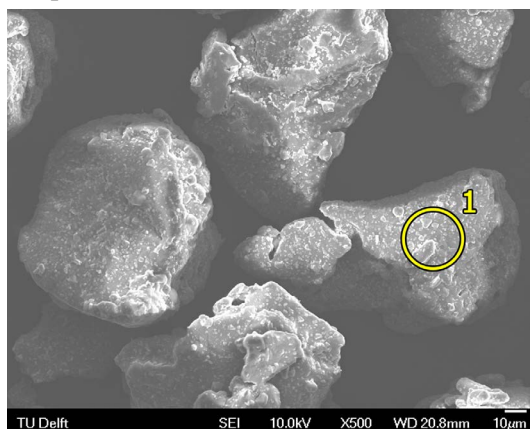


**Figure 8.7:** SEM image of ammonium chloride coated with 20 cycles of DEZ and water ( $t_{\text{coat}} = 90 \text{ s DEZ}$ ,  $t_{\text{coat}} = 120 \text{ s H}_2\text{O}$ , and  $T = 70^\circ\text{C}$ ) using a magnification of 400x. Point 1 shows the location of the EDX analysis.

The surface composition of the coated particles at point 1 in **Figure 8.7** was assessed by EDX, for which the results are shown in **Figure 8.8**. The results of an EDX measurements performed on uncoated  $\text{NH}_4\text{Cl}$  is shown in **Figure 8.4(a)**. From **Figure 8.8** it can be seen that both zinc and oxygen were found on the particles, which indicates the presence of zinc oxide on the  $\text{NH}_4\text{Cl}$  particles. However, while the molar ratio of ZnO is 1:1, the amount of oxygen, compared to the amount of zinc, is not sufficient for all the zinc atoms to be present as ZnO. This means that the zinc atoms must be present in another configuration. Since no other elements than zinc, oxygen and chlorine were detected, either zinc chloride ( $\text{ZnCl}_2$ ) or elementary zinc could

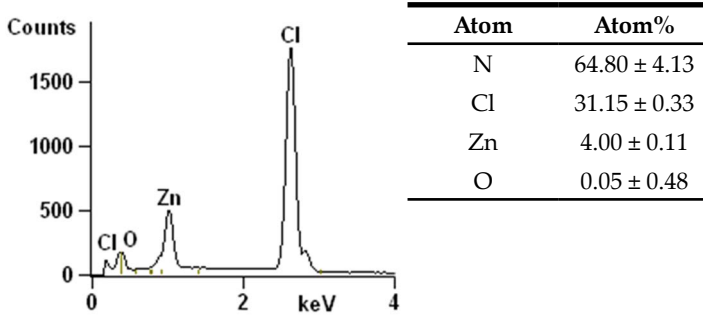


**Figure 8.8:** EDX measurement on coated ammonium chloride with 20 cycles of DEZ and water ( $t_{coat} = 90$  s DEZ,  $t_{coat} = 120$  s H<sub>2</sub>O, and  $T = 70^\circ\text{C}$ ) performed at point 1 in **Figure 8.7**.

have been formed. By using a similar approach for estimating the layer thickness based on EDX analysis, the layer thickness of the ZnO layer for the 20 cycles sample is approximately  $184 \pm 21$  nm which is based on the amount of zinc present. Compared to the estimation from the ICP analysis ( $247 \pm 25$  nm), both approximations for the layer thickness are in the same order of magnitude.

Coating performance.

In order to check the functionality of the zinc oxide coating, moisture absorption experiments were performed, since the ammonium chloride particles coated with aluminum oxide dissolved in water. The amount of moisture absorbed was determined by exposing the sample to ambient air ( $RH = 70\%$ ) and monitoring the weight increase of the different samples (NH<sub>4</sub>Cl uncoated, with 5, 10, and 20 ALD cycles) over time. It is assumed that any mass increase is caused by the absorption of moisture. **Figure 8.9** shows the mass change of the ammonium chloride samples coated with zinc oxide.

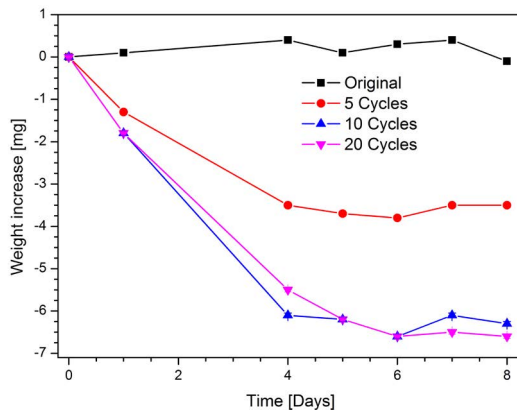


**Figure 8.9:** Mass changes due to moisture absorption for NH<sub>4</sub>Cl uncoated, with 5, 10, and 20 cycles of ZnO with a cycle time  $t_{coat} = 90$  s DEZ and  $t_{coat} = 120$  s water at a temperature  $T = 70^\circ\text{C}$ .

Surprisingly, **Figure 8.9** shows a decrease of mass in time for each sample with coating, although an increase in mass was expected due to the absorption of water. It is possible that elemental zinc is deposited together with some zinc oxide. If an excess of DEZ precursor is used during the coating experiment, elemental zinc can be deposited<sup>24,35</sup>. DEZ is a homo-bifunctional precursor as it has two reactive groups<sup>36</sup>. Both ethyl groups can react with a reactive surface group<sup>24</sup>. In that case there are no ethyl groups available to continue the ALD reactions. However, this principle neither explains the large deposition of elemental zinc, nor the weight loss of the samples when exposed to air.

Another possibility is that DEZ initially reacts with the surface as expected, but that the excess of DEZ reacts with itself. Two ethyl groups can react, forming butane ( $C_4H_{10}$ ). In this case, zinc is deposited on zinc directly and a new ethyl group is available to repeat this action. This phenomenon can be presented as  $(*-O-Zn-Zn-C_2H_5)$  where \* denotes the substrate<sup>24</sup>. Since the amount of deposited Zn is significantly higher than the amount of oxygen, it is most likely that, apart from zinc oxide deposition on the particles, DEZ also reacted with itself, since an excess of precursor is introduced.

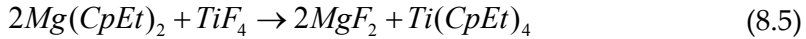
A third possibility comes from Borisov et al.<sup>37</sup>, who found that at elevated temperature (150 to 600°C), zinc oxide can react with ammonium chloride to form a complex, according to  $ZnO + 4NH_4Cl \rightarrow (NH_4)_2ZnCl_4 + H_2O + 2NH_3$ . Through this reaction, a chlorine-containing zinc component ( $(NH_4)_2ZnCl_4$ ) is formed together with water and ammonia ( $NH_3$ )<sup>37</sup>, the latter of which escapes as a gas. The amount of escaped gas roughly translates to the amount of complex formed according to the zinc counts from the EDX measurements. Hence, the formation of a chlorine-containing zinc component with escaping ammonia gas could be a plausible explanation for the mass loss.

### 8.3.2. Fluidization and coating of aluminum

The aluminum particles were fluidized prior to the coating experiment. The particles were sieved to obtain a particle size distribution for the fluidization and coating experiments. The Sauter mean diameter of aluminum was found to be approximately 66  $\mu m$  based on volume with a standard deviation of roughly 21  $\mu m$ . The aluminum particles are covered with a thin impervious oxide layer (2–3 nm)<sup>38</sup>. This oxide layer has hygroscopic characteristics but due to the limited amounts present on the surface, this effect is not translated to the particles to a large extent<sup>39</sup>. To investigate the influence of moisture on the slightly hygroscopic particles, the particles were fluidized at a temperature  $T = 70^\circ C$ . At this temperature and without using the aid of vibration, the aluminum powder fluidized with a superficial velocity of 1.88 cm/s. At the coating temperature ( $T = 200^\circ C$ ) the aluminum particles were fluidized with the same superficial velocity.

Coating Thickness.

Aluminum was coated with magnesium fluoride at a temperature  $T = 200^\circ\text{C}$  and a cycle time of  $t_{\text{coat}} = 60 \text{ s}$   $\text{Mg}(\text{CpEt})_2$  and  $t_{\text{coat}} = 30 \text{ s}$   $\text{TiF}_4$ . The overall reaction for depositing magnesium fluoride ( $\text{MgF}_2$ ) can be found in **eq. 8.5**. Unlike the mechanisms of  $\text{Al}_2\text{O}_3$  and  $\text{ZnO}$  deposition, this reaction follows a path where the precursors adsorb in layers on the surface prior to the reaction<sup>25</sup>. In the past,  $\text{MgF}_2$  has already been deposited using  $\text{TiF}_4$  and a similar Mg precursor<sup>25, 26</sup>.



ICP measurements were used to confirm the presence of magnesium on the coated particles. **Table 8.3** shows the concentration of magnesium for each sample and the corresponding estimated layer thickness calculated from the concentrations. For the layer thickness estimation, a similar approach is used compared to the aluminum oxide layer approximation, which has been explained in **Section 8.3.1** for the ALD process for the coating of the  $\text{NH}_4\text{Cl}$  particles. According to Pilvi et al. the growth per cycle of  $\text{MgF}_2$  is approximately 0.17 nm/cycle<sup>25, 26</sup>. Our layer thickness estimation results in somewhat higher values of ~0.3 nm/cycle.

**Table 8.3:** Concentrations and estimated coating thickness of all aluminum samples coated with  $\text{MgF}_2$ , based on ICP analysis.

| Experimental conditions   | Number of ALD cycles | Concentration of Mg [ppm] | Estimated coating thickness [nm] <sup>28</sup> |
|---|----------------------|---------------------------|--|
| $t_{\text{coat}} = 60 \text{ s}$ $\text{Mg}(\text{CpEt})_2$<br>$t_{\text{coat}} = 30 \text{ s}$ $\text{TiF}_4$<br>$T = 200^\circ\text{C}$ | 5                    | $16 \pm 1$                | $2.3 \pm 0.2$                                  |
|   | 10                   | $22 \pm 1$                | $3.2 \pm 0.3$                                  |
|   | 20                   | $36 \pm 2$                | $5.2 \pm 0.5$                                  |
|   | 30                   | $59 \pm 3$                | $8.6 \pm 0.9$                                  |

The particle morphology and coating composition were assessed by SEM images and EDX analysis. **Figure 8.10(a)** shows uncoated aluminum powder and **Figure 8.10(b)** shows aluminum coated with  $\text{MgF}_2$  (30 cycles). From the SEM images, no clear differences can be observed between the uncoated and coated particles. Since the surface morphology is similar, the particles might be coated with a smooth layer. The unit cell volume of aluminum is approximately  $66.41 \text{ \AA}^3$ <sup>40</sup>. The aluminum particles are covered with a thin layer of aluminum oxide. Hydroxylation occurs at the surface of metal oxides as a result of the reaction between the surface oxides and water to form hydroxyl groups<sup>41</sup>.

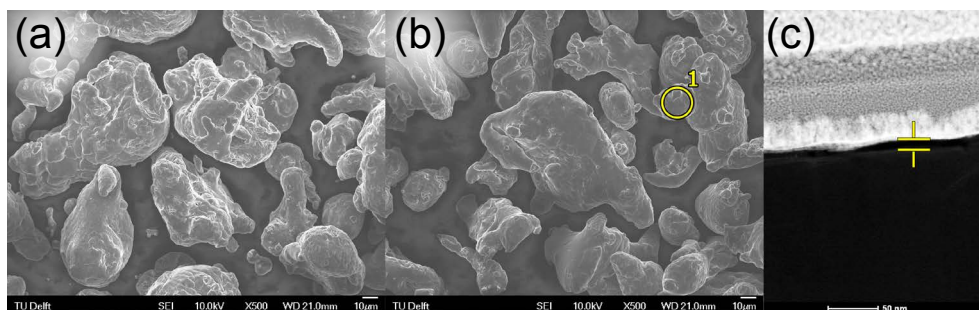


**Figure 8.10:** SEM images of original aluminum (a) and coated with 30 cycles of  $\text{Mg}(\text{CpEt})_2$  and  $\text{TiF}_4$  (b) using a magnification of 500 $\times$  (point 1 shows the location of the EDX analysis), and TEM image of the lamella of aluminum coated with 30 cycles (c) which includes a layer (indicated between the markers) that is rich in the elements F and Mg.

Thus, the number of reactive groups of aluminum particles is probably higher than for ammonium chloride. The EDX results show the presence of fluorine as shown in **Figure 8.11**. The EDX analysis was performed at point 1 of **Figure 8.10(b)**.

By using a comparable approach as for the aluminum oxide, the layer thickness of the coating was estimated to be  $5.2 \pm 3.0$  nm, which is in the same order of magnitude as the layer thickness approximated using the ICP results ( $8.8 \pm 0.9$  nm). The agreement between the values for coating thickness indicates that the aluminum particles did not have a porous structure in which the precursors could easily penetrate. Combining the results from the ICP, which shows the presence of magnesium, and the EDX analyses, which show the presence of fluorine, shows that some deposition took place at the

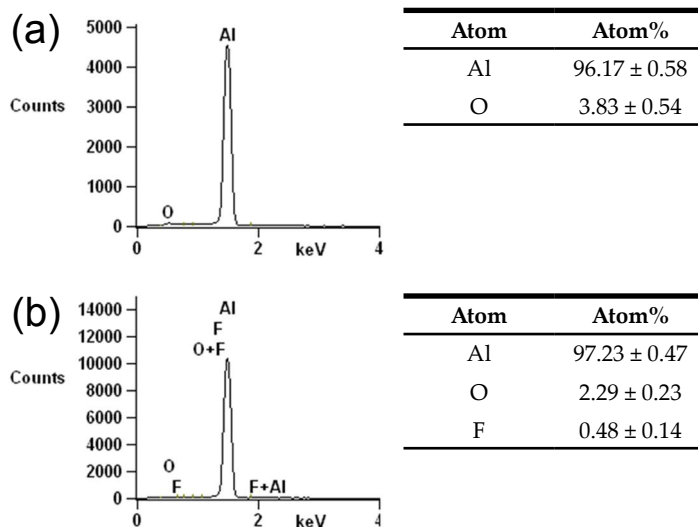


**Figure 8.11:** EDX measurements on uncoated aluminum (a) and on coated aluminum (b) with 30 cycles of  $\text{Mg}(\text{CpEt})_2$  and  $\text{TiF}_4$  ( $t_{\text{coat}} = 60$  s  $\text{Mg}(\text{CpEt})_2$ ,  $t_{\text{coat}} = 30$  s  $\text{TiF}_4$ , and  $T = 200^\circ\text{C}$ ) performed at point 1 (**Figure 8.10(b)**).

aluminum particles. Additionally, a lamella was cut out of the particle and analyzed in a TEM-EDX. **Figure 8.10(c)** shows a detail of this lamella. The white layers on top are the layers of Pt sputtering, comparable to layer 1 in **Figure 8.5(b)**. The dark grey area at the bottom is the aluminum particle. Between these areas, a small black area is visible (between the markers). This layer is rich in both elements Mg and F and was measured to be 5 – 10 nm thick. The thickness is in accordance with the expected values from ICP and SEM-EDX. However, also the aluminum particles were found to be slightly porous, since the grey area on the bottom also contains small quantities of Mg and F. The atomic ratio of F/Mg was larger than 2 at all locations and increased with the depth of the particle, indicating that the  $\text{TiF}_4$  penetrated deeper into the particle than  $\text{Mg}(\text{CpEt})_2$ . This can be explained by the fact that the  $\text{TiF}_4$  is a smaller precursor than  $\text{Mg}(\text{CpEt})_2$ . Deposition of pure fluorine in the pores, without the aid of the magnesium precursor, is possible through a polymerization-like reaction of the  $\text{TiF}_4$ <sup>42</sup>. This penetration of precursors inside the particle reduces the amount of precursor available for deposition on top of the particle, which reduces the layer thickness. However, for the  $\text{MgF}_2$  layer, the effect was only marginal.

#### Coating performance.

A DSC was used to investigate the burning characteristics of the coated and uncoated aluminum particles. **Figure 8.12(a)** shows the DSC-curve for

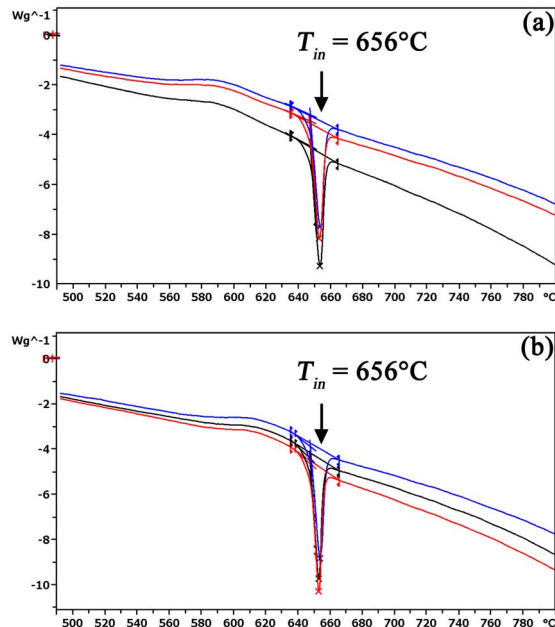


**Figure 8.12:** DSC graphs of uncoated aluminum (a) and aluminum coated with 30 cycles of  $\text{MgF}_2$  (b). Three separate measurements were taken per experimental batch, the graphs show a DSC-curve for each of them.

uncoated aluminum and **Figure 8.12(b)** the DSC-curve of aluminum coated with 30 cycles of  $\text{MgF}_2$ . The initial melting temperature of uncoated aluminum is  $656^\circ\text{C}$ . According to Hahma et al.<sup>22</sup>, a fluorine containing coating starts reacting at a lower temperature than the initial melting temperature of aluminum. If successfully activated, the coated aluminum should have a tendency toward the exothermic direction. However, no significant difference between the DSC-curves of **Figure 8.12(a)** and **(b)** are observed. It is likely that the  $\text{MgF}_2$  coating was not thick enough to have a substantial effect on the burning properties of the aluminum particles.

## 8.4. Conclusions

ALD is applied in fluidized bed reactors to encapsulate micron sized particles of ammonium chloride and aluminum. Ammonium chloride particles were coated with aluminum oxide and zinc oxide. The hygroscopicity of ammonium chloride must be accounted for prior to and during the coating procedure, to prevent a CVD-like deposition mechanism and the collapse of the fluid bed during the water pulse. It was shown that TMA and water penetrate inside the porous structure of the particle and deposit there, reducing the effective layer thickness of coating on the surface of the particle. The protective function of the aluminum oxide layer was shown by reduced dissolution rate of the ammonium chloride. The zinc oxide showed island growth and the coating reacted with the core particle, reducing the mass by the evacuation of gaseous ammonia.

Aluminum particles were successfully coated with  $\text{MgF}_2$  layers of several nanometers thick. Aluminum was also shown to be porous, though while the  $\text{TiF}_4$  precursor was small enough to penetrate into the porous structure, the  $\text{Mg}(\text{CpEt})_2$  precursor was too large to penetrate in significant amounts. Despite the deposition of the materials, no significant changes in tendency toward the exothermic direction for the coated aluminum particles were observed.

## 8.5. References

1. Tikekar, R. V.; Nitin, N., Chapter 27 - Real-Time Analysis of Oxidative Barrier Properties of Encapsulation Systems. In *Microencapsulation in the Food Industry*, Gaonkar, A. G.; Vasisht, N.; Khare, A. R.; Sobel, R., Eds. Academic Press: San Diego, **2014**; pp 353-365.
2. Bou, R.; Cofrades, S.; Jiménez-Colmenero, F., Physicochemical properties and riboflavin encapsulation in double emulsions with different lipid sources. *Food Science and Technology* **2014**, 59, 621 - 628.
3. Kang, A.; Park, J.; Ju, J.; Jeong, G. S.; Lee, S., Cell encapsulation via microtechnologies. *Biomaterials* **2014**, 35, 2651 - 2663.
4. Pérez-Masiá, R.; López-Nicolás, R.; Periago, M. J.; Ros, G.; Lagaron, J. M.; López-Rubio, A., Encapsulation of folic acid in food hydrocolloids through nanospray drying and electrospraying for nutraceutical applications. *Food Chemistry* **2015**, 168, 124 - 133.
5. Feng-Bo, S.; Yu, D.; Yong-Qiang, Y.; Ping, C.; Ya-Hui, D.; Xiao, W.; Dan, Y.; Kai-wen, X., Fabrication of tunable [Al<sub>2</sub>O<sub>3</sub>:Alucone] thin-film encapsulations for top-emitting organic light-emitting diodes with high performance optical and barrier properties. *Organic Electronics* **2014**, 15, 2546 - 2552.
6. Miikkulainen, V.; Leskelä, M.; Ritala, M.; Puurunen, R. L., Crystallinity of inorganic films grown by atomic layer deposition: Overview and general trends. *Journal of Applied Physics* **2013**, 102.
7. Puurunen, R. L., Surface chemistry of atomic layer deposition: A case study for the trimethylaluminum/water process. *Journal of Applied Physics* **2005**, 97, 53.
8. George, S. M., Atomic Layer Deposition: An Overview. *Chemical Reviews* **2010**, 111 - 131.
9. Mittal, V., *Encapsulation Nanotechnologies*. John Wiley & Sons, Inc. **2013**.
10. Yakovlev, S. V.; Malygin, A. A.; Kol'tsov, S. I.; Aleskovskii, V. B.; Chesnokov, Y. G.; Protod'yakonov, I. O., Mathematical model of molecular layering with the aid of a fluidized bed. *Journal of Applied Chemistry USSR* **1979**, vol 52, pp 959 - 963.
11. King, D. M.; Liang, X.; Weimer, A. W., Functionalization of fine particles using atomic and molecular layer deposition. *Powder Technology* **2012**, vol 221, pp 13 - 25.
12. Goulas, A.; Ommen, J. R. v., Scalable production of nanostructured particles using atomic layer deposition. *Powder and Particle Journal* **2014**, vol 31, pp 234 - 246.
13. Longrie, D.; Deduytsche, D.; Detavernier, C., Reactor concepts for atomic layer deposition on agitated particles: A review. *Journal of Vacuum Science Technology A* **2014**, p 32.

14. Yang, C., Fluidization of fine cohesive powders and nanoparticles - a review. *Journal of the Chinese Institute of Chemical Engineers* **2005**, 36, 285 - 299.

15. Seville, J.; Willett, C.; Knight, P., Interparticle forces in fluidisation: a review. *Powder Technology* **2000**, 113, 261 - 268.

16. Hendrickson, G., Electrostatics and gas phase fluidized bed polymerization reactor wall sheetings. *Chemical Engineering Science* **2006**, 61, 1041 - 1064.

17. Ommen, J. R. v.; Yurteri, C. U.; Ellis, N.; Kelder, E. M., Scalable gas-phase processes to create nanostructured particles. *Elsevier* **2010**, 8, 572 - 577.

18. Wank, J. R.; George, S. M.; Weimer, A. W., Nanocoating individual cohesive boron nitride particles in a fluidized bed by ALD. *Powder Technology* **2004**, vol 142, 2004, pp 59 - 69.

19. Luttrell, W. E., Ammonium Nitrate. *Journal of Chemical Health and Safety* **2013**, 20, 38 - 39.

20. Somayajulu, M. R.; Gautam, G. K.; Rao, A. S., Stabilisation of Red Phosphorus to Prevent Moisture Absorption and Suppression of Phosphine Release. *Defence Science Journal* **2007**, 57, 817 - 824.

21. Kappagantula, K. S.; Pantoya, M. L.; Horn, J., Effect of surface coatings on aluminum fuel particles toward nanocomposite combustion. *Surface and Coatings Technology* **2013**, 237, 456 - 459.

22. Hahma, A.; Gany, A.; Palovuori, K., Combustion of activated aluminum. *Combustion and Flame* **2006**, 145, 464 - 480.

23. Beetstra, R.; Lafont, U.; Nijenhuis, J.; Kelder, E. M.; Ommen, J. R. v., Atmospheric Pressure Process for Coating Particles Using Atomic Layer Deposition. *Chemical Vapor Deposition* **2009**, 15, 227 - 233.

24. King, D. M.; Liang, X.; Li, P.; Weimer, A. W., Low-temperature atomic layer deposition of ZnO films on particles in a fluidized bed. *Thin Solid Films* **2008**, 516, 8517 - 8523

25. Pilvi, T.; Hatanpää, T.; Puukilainen, E.; Arstila, K.; Bischoff, M.; Kaiser, U., Study of a novel ALD process for depositing MgF<sub>2</sub> thin films. *Journal of Material Chemistry* **2007**, 17, 5077 - 5083.

26. Pilvi, T.; Ritala, M.; Leskelä, M.; Bischoff, M.; Kaiser, U.; Kaiser, N., Atomic Layer Deposition process with TiF<sub>4</sub> as a precursor for depositing metal fluoride thin films. *Optical Society of America* **2008**, 74, C271 - C274.

27. Hu, D.; Chen, J.; Ye, X.; Yang, X., Hygroscopicity and evaporation of ammonium chloride and ammonium nitrate: Relative humidity and size effects on the growth factor. *Atmospheric Environment* **2011**, 45, 2349 - 2355.

28. Steinfeld, H.; Food; Agriculture Organization of the United, N.; Livestock, E.; Development, *Livestock's long shadow : environmental issues and options*. Food and Agriculture Organization of the United Nations: Rome, **2006**.

29. Cattani Lorente, M.; Scherrer, S. S.; Richard, J.; Demellayer, R.; Amezdroz, M.; Wiskott, H. W. A., Surface roughness and EDS characterization of

a Y-TZP dental ceramic treated with the CoJet™ Sand. *Dental Materials* **2010**, 26, 1035-1042.

30. Profijt, H. B.; Potts, S. E.; Sanden, M. C. M. V. D.; Kessels, W. M. M., Plasma-assisted atomic layer deposition: Basics, opportunities, and challenges. *Journal of Vacuum Science and Technology A: Vacuum, Surfaces and Films* **2011** vol 29.

31. Potts, S. E.; Kessels, W. M. M., Energy-enhanced atomic layer deposition for more process and precursor versatility. *Coordination Chemistry Reviews* **2013**, vol 257, pp 3254 - 3270.

32. Valdesueiro, D.; Meesters, G.; Kreutzer, M.; van Ommen, J., Gas-Phase Deposition of Ultrathin Aluminium Oxide Films on Nanoparticles at Ambient Conditions. *Materials* **2015**, 8, 1249.

33. Forman, R. A.; Jr., W. S. B., Optical spectra of thallium-doped ammonium chloride. *Journal of Luminescence* **1971**, 4, 98 - 104.

34. Daruka, I.; Barabási, A., Dislocation-Free Island Formation in Heteroepitaxial Growth: A Study at Equilibrium. *Physical Review Letters* **1997**, 79, 3708 - 3711.

35. Libera, J. A.; Elam, J. W.; Pellin, M. J., Conformal ZnO coatings on high surface area silica gel. *Thin Solid Films* **2008**, 516, 6158 - 6166.

36. George, S. M.; Yoon, B.; Dameron, A. A., Surface Chemistry for Molecular Layer Deposition of Organic and Hybrid Organic - Inorganic Polymers. *Accounts of Chemical Research* **2009**, 42, 498 - 508.

37. Borisov, V. A.; D'yachenko, A. N.; Kraidenko, R. I., Reaction of Zinc Oxide with Ammonium Chloride. *Russian Journal of Inorganic Chemistry* **2012**, 57, 499 - 501.

38. Zähr, J.; Oswald, S.; Türpe, M.; Ullrich, H. J.; Füssel, U., Characterisation of oxide and hydroxide layers on technical aluminum materials using XPS. *Vacuum* **2012**, 86, 1216 - 1219.

39. Huo, S. H.; Qian, M.; Schaffer, G. B., Aluminium powder metallurgy. *Metals and Surface Engineering* **2011**, 655 - 701.

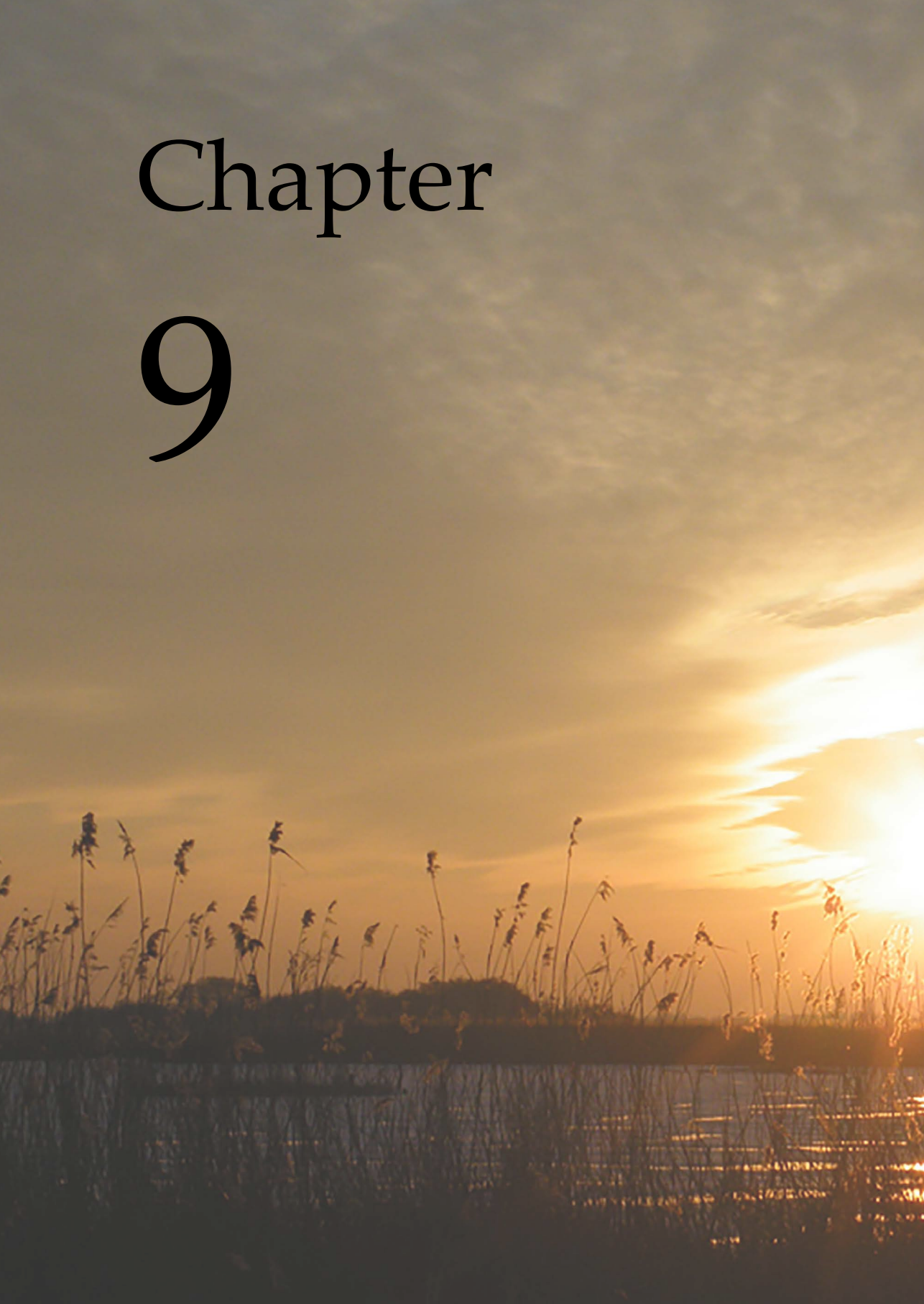
40. Steurer, W., 1 - Crystal Structures of Metallic Elements and Compounds. *Physical Metallurgy (Fifth Edition)* **2014**, 1, 1 - 101.

41. Fierro, J. L. G., *Metal Oxides: Chemistry and Applications*. CRC Press **2005**.

42. Greenwood, N. N.; Earnshaw, A., *Chemistry of the Elements (2nd Edition)*. Elsevier.

Chapter

9



# Conclusions



In this thesis multicomponent particulate products were produced by means of crystallization and microencapsulation processes, and various applications of these products were investigated. The relation between the complex multicomponent mixture, the process conditions and the targeted complex construct were investigated. The knowledge obtained as such is intended to aid in the design of novel crystallization and microencapsulation processes. The findings in this research provide tangible leads for the further development of the processes.

## 9.1. Obtaining multicomponent phase diagrams

The solvent addition technique developed in this work proved to be a valuable technique in the determination of phase diagrams, especially in the case of complex multicomponent mixtures. The reliability of the technique was validated by comparison with the equilibrium concentration method and the temperature variation method. For the dynamic solubility measurement techniques, like the temperature variation method and the solvent addition method, the reliability of the measured data are mainly determined by the rate of change (heating and addition rate, respectively) relative to the kinetics of the system under investigation. Using the solvent addition technique, a co-crystal phase diagram and two solvent mixture phase diagrams (anti-solvent and solvate-hydrate system) were determined.

In the co-crystal phase diagram of isonicotinamide-carbamazepine it was shown that one component greatly influences the pure component solubility of the other. In the solvate-hydrate system, where the compositional regions for formation of various solvated states of p-hydroxybenzoic acid were investigated, three ternary phase diagrams were constructed, using solvents resulting in an anhydrous form (acetic acid), a monohydrate (water) and a hemi-solvate (acetone). Changes in solubility trends were observed when multiple solvated states were possible along the solvent composition. However, the solvent composition where a maximum in solubility was observed was not necessarily the composition at which a change in crystal form was seen. Based on the findings in the co-crystal and the solvate-hydrate phase diagrams, we conclude that the solvent addition technique is very suitable to investigate non-idealities in multicomponent mixtures.

## 9.2. Crystallization in small volumes

In the production of (sub-)micron sized crystals, small solution volumes are used to achieve the size requirement, instead of using a top-down method like grinding. With electrospray crystallization experiments, it was shown that the selection of solvent and the solute concentrations determine the operability of the process and quality of the resulting particulate product to a large extent. Properties like the conductivity, density, viscosity and surface tension determine the sprayability to a large extent. Since it has to be fully evaporated, the vapor pressure determines whether the solvent evaporates fast enough for dry crystals to be obtained at the collection area.

The solute concentration is one of the factors that determine the size of the resulting crystals. Additionally, it is an important variable for the control and smooth operation of the process, since it influences the solution proper-

ties like density and conductivity, as well as the extent of encrustation due to premature crystallization in and on the nozzle. In concomitant electrospray crystallization both solute concentrations determine the distribution of the components throughout the particle. The component with the highest concentration relative to its solubility is found mostly on the outside of the particle, since crystallization starts at the droplet-environment interface.

It was found that the electrospray process has a spherification effect on the particle shape, due to the small initial volume of the droplets, which creates a limited environment for crystal growth, and the rapid evaporation of the solvent, which can lead to high supersaturations.

Another way of producing small droplets is by encapsulating them in a hydrogel by a dripping method. This dripping method is able to generate core-shell particles of a controlled size with solutions inside, by pumping core and shell liquids through a concentric nozzle and achieve jet break-up through vibration of the nozzle. The particles generated as such are used in a newly developed crystal nucleation measurement method. During various cooling crystallization experiments of microencapsulated fenofibrate in heptane under the microscope, we found that only a fraction of the droplets showed a crystallization event. Furthermore it was observed that some droplets crystallized that also crystallized in a previous experiment. Both these observations indicate that the crystallization is driven by heterogeneous particles, that are only present in some of the droplets. The growth rate of the characteristic crystal lengths rapidly decreased, due to depletion of the supersaturation. The fraction of active droplets containing heterogeneous particles was determined and used to determine nucleation rates from the induction time probability distribution. From these nucleation rates, we derived the kinetic and thermodynamic nucleation rate parameters. We showed that performing cooling crystallization in droplets encapsulated with a hydrogel shell is an excellent way to investigate the process at such a small scale.

### 9.3. Protective encapsulants

For the protection of vital wheat gluten against direct fibrilization upon contact with water, the gluten was encapsulated in food-grade hydrogels in a matrix configuration. Both sodium alginate and  $\kappa$ -carrageenan were used as encapsulants and were applied using the dripping technique. With alginate, the particles had a good sphericity. With the  $\kappa$ -carrageenan, the sphericity needed to be improved by applying a layer of oil on the cross-linking bath, as well as around the droplets through the concentric nozzle. The loading of the gluten inside both hydrogels was sufficient for use of the particles in the

Couette Cell after a partial drying step. The controlled release of gluten was not achieved from the alginate particles. From the  $\kappa$ -carrageenan particle the gluten was released at the desired process conditions and fibre formation in the shearing process was confirmed.

For the protection of materials against moisture, as well as for the activation of aluminium powder, we demonstrated the application of very thin layers using the ALD process in fluidized beds. Using this technique, ammonium chloride was coated with  $\text{Al}_2\text{O}_3$  and ZnO layers. At lower temperatures, the fluidized bed collapsed during the water pulse, resulting in a poor deposition of coating materials. This is attributed to the hygroscopic nature of the ammonium chloride. Additionally, using low temperatures and hygroscopic materials leads to adsorption of unreacted precursors on the surface of the particle. When these species react in a subsequent step, a CVD type of deposition is the result and thicker layers are found. Higher temperatures reduce both these effects, leading to good operation of the fluidized bed and proper ALD type deposition.

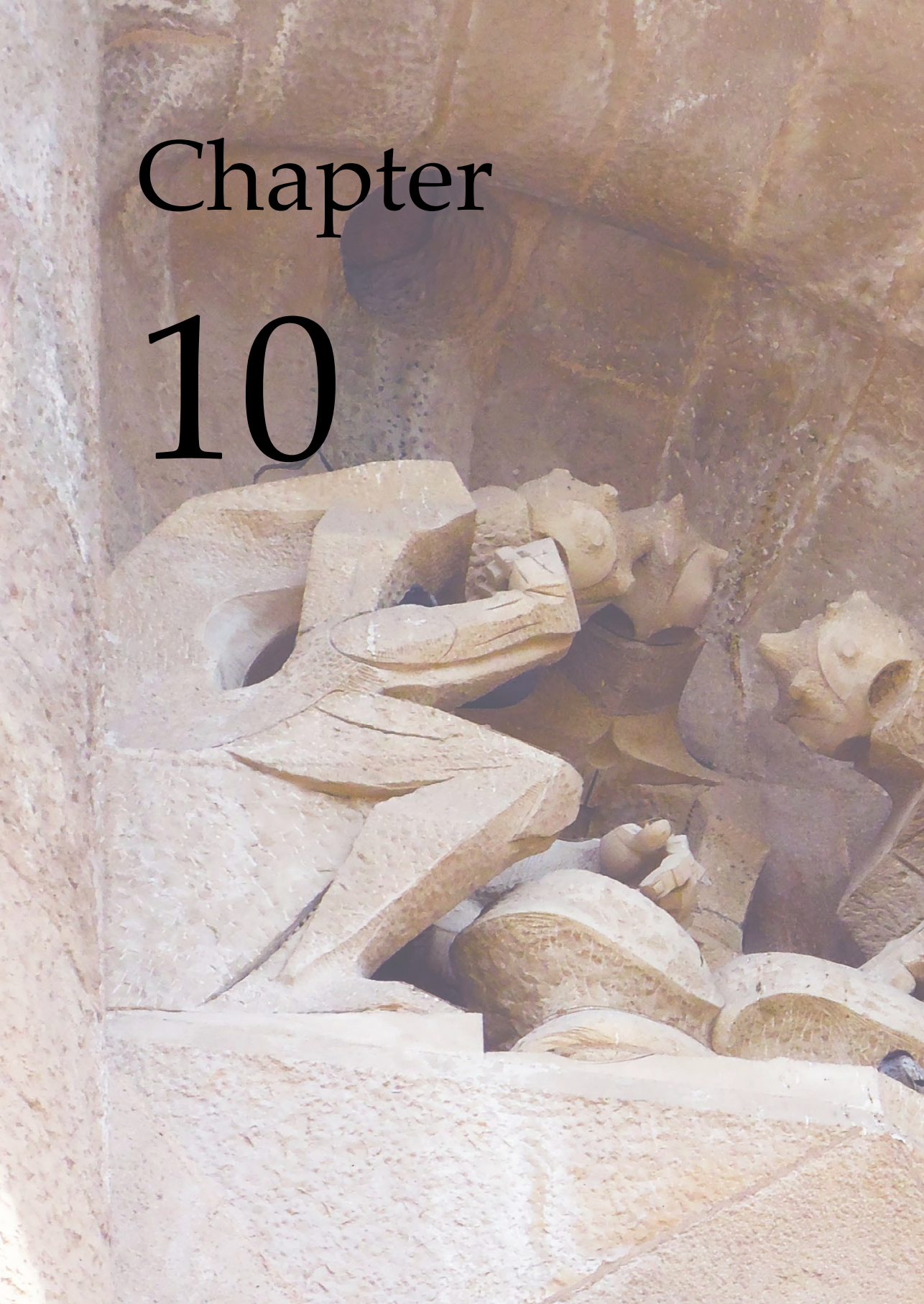
The  $\text{Al}_2\text{O}_3$  layers showed some protection against moisture, as seen by the decreased dissolution rates compared to uncoated material with the same particle size fraction. Exposing the hygroscopic ammonium chloride with ZnO coating to ambient moisture showed a decrease in mass, while an increase in mass was expected due to moisture uptake. This is attributed to a side reaction taking place in which ammonia is formed, which escapes as a gas.

In the coating of metallic aluminum with magnesium fluoride, the aim was to protect the aluminum from moisture, as well as to activate it with the fluoride component to enhance the burning properties. Due to the low vapor pressure of the precursors, a very high temperature was required to reach workable concentrations of precursor in the nitrogen carrier flow. However, not in all parts of the setup could the temperature be controlled, leading to loss of precursor prior to reaching the fluidized bed, due to condensation on the walls. This led to a lower than expected deposition of  $\text{MgF}_2$  on the aluminum particles. The quantity of fluorine was not sufficient to activate the aluminum to a detectable extent.

TEM-EDX measurements showed that the particles were porous and that the precursors diffused deep inside the pores, where they subsequently deposited. This resulted in thinner layers over the particle surface than expected and therefore a lower performance of the coating. However, it clearly shows the atomic scale at which ALD operates.

Chapter

10



The background of the page is a photograph of a stone wall. The wall is composed of large, rectangular stone blocks with visible mortar joints. On the left side of the image, there is a large, jagged opening or hole in the wall, revealing a dark interior space. The lighting is somewhat uneven, with the top right corner appearing brighter than the bottom left.

# Recommendations

The findings in this thesis provide footholds for further research, either into new principles or using different materials from the model compounds that were used. Additionally, enhancements may be considered for some of the setups, to improve their performance or potential.

## 10.1. Applications

### *Automation*

In this thesis, solubility lines were determined by solvent addition. Each time a single experiment was conducted manually. The throughput as such was not high. However, the throughput of this method can be increased dramatically by automating the technique. Multiplexing the number of experiments by using an array of crystallizers, where each crystallizer is fed separately with solvent or solvent mix, allows for a vast increase in measurements done over time.

### *Polymorphism*

In some electrospray crystallization experiments, other polymorphs were found compared to the equivalent cooling crystallization experiments. Due to the rapid evaporation, very high supersaturations are reached, through which metastable forms can crystallize. The effect of the EC process on polymorphism is not studied in depth in this thesis. However, it shows that EC crystallization can be used as a screening tool in polymorph discovery, since very little amounts of material are required to investigate a set of conditions.

### *Particle production*

The spherification technique, used for the production of the gluten as well as the solution encapsulates is a very versatile technique that can be used as a mild processing technique for other applications as well. Using the same technique, spherical particles can be produced of energetic materials that can be melted before decomposition, like TNT. These materials may benefit from a spherical shape to reduce initiation sites. Additionally, by use of the concentric nozzle, a thin protective film of polymer may be added around the TNT particles in the same step. To either the core or the shell, substances may be added that enhance the performance of the composition, e.g. an oxidizer or a fuel. The benefit of such a composition is twofold, since the additive is protected from the environment and is in close contact with the energetic material.

### *ALD with other materials*

The ALD process in the fluidized bed reactor can be applied to many core materials. In some cases surface activation may be required, since the half reactions rely on certain surface groups to react with, e.g.  $-OH$  groups in the case of the TMA precursor. It is important that the particles do not disintegrate in the fluidized bed and that they do not decompose at the reaction conditions. The choice for coating materials is mostly limited to what can be produced from consecutive gas-solid reactions, and whether these reactions can be performed at conditions at which the core particle is stable. Addition-

ally, we found that for higher temperature precursors, like  $\text{TiF}_4$ , the temperature was not sufficiently high in all parts of the setup, leading to deposition of precursor on the walls of the setup. It is advised that all parts of the setup can reach high enough temperatures for the precursors to remain in the gas phase until the fluidized bed is reached.

## 10.2. Research

### *Addition rate*

When using the solvent addition method for determining solubility, the most important variable is the addition rate. It should be chosen low enough for the dissolution to keep up with the change imposed on the system. For systems that have slower kinetics, the addition rate has to be decreased in order to obtain accurate measurements. For faster systems the addition rate can be increased. However, the addition rate should not be increased so far that the dissolution becomes the rate limiting step. In larger volumes (e.g. 1 L or larger), mixing may be less ideal. This can lead to large mixing times relative to the dissolution time, making mixing rather than addition the rate limiting step. In such cases it is advised to decrease the addition rate even further, so that the addition of solvent is once again rate limiting, and accurate data are recorded.

### *Encrustation*

Encrustation is one of the major factors inhibiting stable, smooth operation of the electrospray crystallization process, as well as contributing to material losses to a great extent. It is therefore advised that most efforts are directed towards solving the encrustation issues. Aside from reducing the concentration and changing the nozzle design, crystallization inhibitors could be added to delay the crystallization until after the droplets have broken off the cone jet. However, these inhibitors end up inside the product. If that is undesirable, a co-solvent can be added to the system in such a concentration that the solubility of the compound in the mixture is significantly larger than in the pure solvent. In such a case, the resulting (pseudo-)polymorph may be different, depending on the solvent chosen.

### *Decoupling of properties*

In the concomitant electrospray crystallization process used in this thesis, the absolute concentration of each compound directly determines the relative concentration of that compound through the solubility. The compound with the highest relative concentration crystallizes first and is mostly found on the outside of the particle. This means that the composition of the particle, which is determined by the absolute concentration, is linked to the

distribution of the compounds over the particle, since the solubility does not change. The composition can be decoupled from the distribution when the two compounds are sprayed from a solvent mixture. The solubility of the compounds in the solvent mixture can be adjusted by varying the composition of the solvent mixture. The different evaporation rates of the solvents in the mixture can then either be used to the advantage, or avoided by using azeotropic solvent mixtures.

#### *Water soluble systems*

In the crystallization of fenofibrate inside encapsulated micro-droplets of heptane, the components were chosen such that the solute is insoluble in and the solvent immiscible with water. These constraints were put upon the system since the encapsulant is a hydrogel, which consists of >95% water immobilized in a 3D polymer structure. This polymer structure is porous, which means that components can diffuse in and out of the particle. Due to the immiscibility of the solvent and insolubility of the solute in water, we were able to minimize the communication between the particles. For systems with higher water affinity, this technique can still be used. The cooling liquid should then be exchanged from water to a liquid which the compound does not dissolve in and the solvent does not mix with. For the calculations, the concentration of compounds in the hydrogel shell must be accounted for. Another option is to use a different polymer, one that does not allow leaching.

#### *Functionalization*

In this thesis, pure hydrogel was used for the encapsulation of fenofibrate-heptane solutions. In order to assess the effect of special impurities, like crystallization inhibitors or templates, the hydrogel phase could be enhanced with materials that act as such. This way, the impurity is immobilized in the shell of the encapsulate and not in the solution itself and it is this type of localization that allows for investigation of the effects of said impurity on the crystallization of the compound.

#### *Low shear*

The particles containing immobilized gluten were used in the Couette Cell to assess the controlled release of the core. The extent of fibrilization was found to be less than in uncoated gluten. However, for the shearing of the meat analog with the particles, the same processing conditions and shearing time were used as for the mixture with free gluten. It is recommended that an optimization study is done to arrive at the process conditions and shearing time that accommodate the time for the controlled release of the gluten from the particles. With more optimized conditions, the gluten are allowed to increase the fibre formation, yielding meat analogs with a better fibrous

structure.

*Porosity*

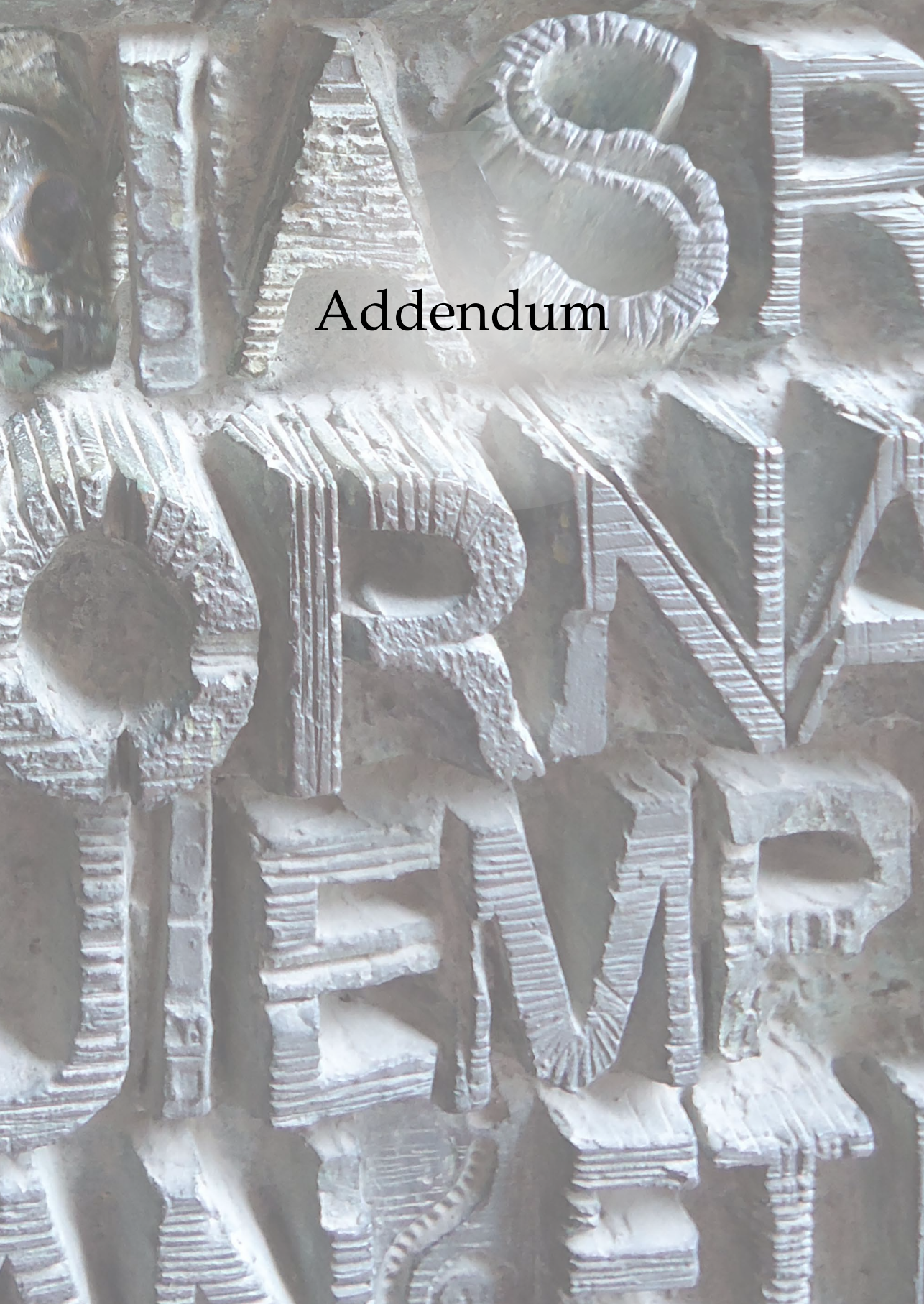
In the ALD coating experiments in this thesis, we found that the particles we encapsulated had a porous structure, and that the precursors diffused quite deep into the particles. This resulted in a thinner layer of coating surrounding the particle than expected and in a lower performance of this coating. We recommend the surface area to be measured before the start of each process (e.g. by BET surface area analysis), and calculate exposure times based on these measurements.

CRYSTALLIZATION

211

ENCAPSULATION



The background of the image is a close-up photograph of ancient Egyptian hieroglyphs. The hieroglyphs are carved into a light-colored stone surface and are arranged in vertical columns. The most prominent hieroglyphs are the 'ankh' (a cross with a loop at the top), the 'djed' (a tall staff with a crossbar), and the 'was' (a staff with a loop at the top). The lighting is dramatic, highlighting the texture and depth of the carvings. The word 'Addendum' is superimposed in the center of the image.

Addendum

---

ENCAPSULATION

214

CRYSTALLIZATION

# Acknowledgements

Well, that's it then.

One of the last things I still get to do is thank the people without whom both this book and me would probably not have turned out the way we are now. Making a PhD thesis is a long process with lots of fun, but also many challenges, some (or perhaps most) of which you cannot hope to tackle alone. Many of those challenges are actually not even related to the thesis, but just pop up at the side, of course at the most inconvenient of times. They have in common that it largely depends on the people around you how well you can cope with them and how much you grow from the experience. I was so fortunate to have a lot of people around me during the years of PhD, maybe even too many, since my hours outside work were often as busy as those in the office. They have all contributed a lot to both my life and this work by supporting me, distracting me and discussing with me about significant and insignificant (or downright ridiculous) things. Although I cannot name everyone, here is my chance to highlight some of the people that made these last five years a truly marvellous experience.

First of all, I would like to thank my promotors, Joop ter Horst and Antoine van der Heijden. I cannot imagine better supervisors than you two. Thank you Joop, for showing me above all that PhD research should not only be serious, but also fun. The endless red corrections to my writings (which showed me that changing your mind back and forth still makes for improvement) were always balanced with some well placed humor in the emails in which you sent them. I also greatly enjoyed organizing the BIWIC'11 conference, while I had no clue yet what conferences were really all about. Antoine, thank you for introducing me to the right people and for helping me find the way around TNO. With just about anything you were always ready to lend a helping hand. I was also very happy to have your help when we moved the encapsulator to about six different locations within half a year. If ever you need a career change... I would like to thank you both for the understanding and support you gave me when things weren't running altogether smoothly. You really tailored the supervision to my needs and managed to motivate me even then, for which I am very grateful. Finally, I'm also delighted to have seen you both rise to full professorship in this time, even though it meant that one of you would not be so closely around anymore. Congratulations!

---

Then also I'd like to thank Andrzej Stankiewicz, who was my promoter from the start, after I finished my master thesis in the same group. Your passion for both innovation and people are indispensable for the IRS group. It is always nice to join the meetings of the Delft Process Technology Institute (DPTI), which largely exists because of your efforts.

Where would I be without the P&E staff? Rob, thank you for arranging so many (financial) things. And the secretaries, Helma, Judith, Eveline, Ilona, for any issues or questions you were always ready to help. And especially Leslie, thanks so much for arranging pretty much everything that was not the research itself. Whatever the requirement, you know a way to arrange it.

Of course you make new friends during your PhD time. Office mates are some of those and they are crucial to the survival. I've been in quite some offices (four, if I'm not mistaken) and each of them had its own inhabitants.

However, I will start with just two: My dear paranymphs and successive office mates, Sayee Prasaad Balaji and Weiwei Li. We've been through some tricky times together, and I could always count on you for support and cheering up. How often didn't I see Sayee crawl under his desk, or Weiwei lose his balance on the office ball? How terrible is our humor and how hard we laugh(ed)! If I need someone to talk about gaming or fantasy books, you are my go-to guys. The Man Utd thing I'll just have to accept. I feel so lucky that also during my defence you'll have my back. Thanks guys, for a wonderful time!

Then for my first office in Delft, in the old API building. Thijs, put your keys in your manpurse and let us know when we can taste some new ice cream. Bernardo, Dr. Bambi, thanks for the relaxed atmosphere you brought to the office. Was that perchance a remnant of your parties? Samir, thank you so much for explaining so many things to me. How you got so many things done while also training everybody on every piece of equipment we had, and keeping that equipment running still amazes me. You were one of my examples at the department, except for your motto, because life really is beautiful! Albert, thank you first for introducing me into the lunch group, a source for a lot of fun. I also like all the pleasant conversations we had. You are truly the furniture of P&E and I hope you keep that up for another while. Sayee, never stop playing, or reading, it's just too much fun. Also, Sara, Lukas, David, Antonio, it was nice having you around.

In the same building, apart from my direct office mates, there were many other people as well: Alondra: there is a life after 30, you live it, you know it! I found it amazing how we think alike on so many topics. Tiemo, all the

best in your life with Alondra! It's great to have you guys around. Guido, I admire the passion with which you work around the clock, but don't forget to take a break now and then. Stephanie, I wasn't going to eat you with the cardboard tube. Thanks for shrinking my 'daddy issues'. Somnath, SoK, our daily conversations in your office were always a bright point of the day. Michel, I finally started using the pixie, can you imagine? Thanks for all your advice. Jurriaan, you are the answer. Thanks for occasionally getting me home safe, you should still come over for whisky, remember. And Sergio (long live the triple birthday parties of you, Alo and Lucie, they were the best), Erin and Kim, Facundo, Clement, Konstantinos Helene, Mariette, Sondre, Ming, Roger, Jessica, Mayte, Lawien, Dennis (thanks for running the candy shop), Norbert, Tomek, Magda, Thijs, Iza, Rene, Aravind, Daniel, Brian, Alex, Onursal, Ernesto, Nafiseh, Bendiks-Jan, Somayeh, Carlos, Mahinder, Herman (your skating and biking skills set an example to us all), Maryam, Antonella, Anamaria, Cristian, George (·x, sorry, I lost count), Alvaro, Enrico, Bart, Eva, Yash, Sowande, Giulia, Marcin, Wiebren, Aditya, Javier, Martina, Theo, Carsten, Alessandro, Gerasimos, Wim, Georgios (you changed the meaning of the word 'crystals' forever), Elif, Widya, Richard, Hrishikesh, Bora, Henry, Almudena thanks for the lunches, coffee breaks, help with the labtours and of course all the fun.

Ruud van Ommen, Mojgan and David, thank you for the cooperation on Jeffrey's project. Professor Santamaria and Teo, thank you for analysing the particles in the dual beam. Caner Yurteri, thank you for teaching me all about electrospray since my BSc thesis. Thanks Kees and Ruud, for the SEM and XRPD analysis at TU Delft. And Danny Stam, it was great how you always came over so quickly to help us out with our crystallization equipment. It's always very nice to talk to you.

Here it was also that I got some help from students. Gerard, you were my first master student. The electrospray crystallization work got published in my first paper and you were a delight to work with. Then Moj, Robert, Debby and Marenka, my LO1 students, and Machiel and Giguru for LO2, I hope you learned something useful during your time at P&E. Moj, you came back to our group for both your Bachelor and Master thesis. It seems we have inspired you to work in a (to my opinion) great field, and I hope you'll keep liking it. Jeffrey, you did a great job on the ALD project and I think it was a lot of fun working with you.

The second office I was introduced to was at TNO in Rijswijk. Well, the lab, really. Willem, thank you for making so much time to analyse my samples with SEM and XRPD. It is always hilarious talking with you. I hope

---

that, by the end of 18 March, I have repaid my debt to you. John Koman, thanks for all the things you taught me and for judging my cookies. I know I still owe you a batch. Also thank you for doing the sensitivity tests on my samples. Charlotte, you are a seriously funny person and no matter my mood in the morning, when I left TNO I was always laughing, also thanks to you. Without the efforts of Bastian, Huub, Ellen, Jamila, Monique (for the IR measurements) and many others, the work would not have been done as 'fast' as it was now. Thanks for all your help and humor. And of course I cannot forget the company and help during work, lunch and drinks of Rob, Reynate, Oscar, Erik, Robin, Wim, Chris, Arien, Gölge, Gerold, Michiel and Rick.

The third office was TNO Ypenburg. Also there I got a warm welcome from everyone and a lot of help, thank you Jacco and Walter, I will never forget how happy you were when you found out I knew what 'Oblivian' was. Rudie, Jos, John Zevenbergen, Dinesh, Joost, Erik, Nico, Martijn, for putting up with all my questions, teaching me loads of stuff and for giving me a great time there.

And the fourth building, the new P&E to which we moved in the last year, contained a lot of the same people as the first one. I got some new office mates there. Fatima, your luck already changed. Congrats on the wedding! Rohit, I'm baffled with how relaxed you are time and again. And Weiwei, the Chinese, or now Dutch, you're a true friend, and I can't imagine a better person to share an office with.

In this building also new people came: Tim, some day you'll know. Karsten, I'm happy there is still someone besides me who can navigate. Metin, best go with Karsten then. Dion, thanks for the history lessons. Daniel, you always have the simplest solutions to everything. Julia, don't change your humor! And of course Meng, Ali, Lalit, Sergio, Martijn, Hassan, Uttiya, Burak (thanks for hiring me), Vincent, Vilbor, Nikolaos, thanks for the fun. I know some of you were already in the old API-building, but I only got to know you better here (better late than never, right).

And what would I do without the guys from DEMO? Jan, Andre, Gerard, Daniel and Martijn, I enjoyed the lookout in the old building and Aad, Bas, Duncan, Jaap, Lennart, thanks for your help in the new. And most of all Michel. Thank you for all your help throughout the entire labwork. Without you it would take so much longer to find everything in the lab and to start up all the work. Thanks for all the support and help.

Not only in the offices, but also at conferences and courses I met quite some people that made my travels great. Margrethe, Ralf, Xiaoguang, Jens-Petter, thanks for adopting me into your Soft family of researchers, it was nice to explore Beijing with you. Erik, Krzysztof, Damon, it was truly fun in Delft and in Enschede. Joris, Kiran, Rene, Mike, thanks for the company. Dear twins Jörn and Ricco, Marcus, Damian, it was great meeting you in various places.

Especially I'd like to thank the Zürich group. Somehow, there is such a click between Delft and Zürich, we always get along well. Perhaps it is related to the drinking habits, Dave, as you said. Thanks also Pawel, Giovanni, Fabio, Ian, Stefan, Matteo, Dorian and Thomas, crystallization meetings are just more fun with you around. And Martin, thanks so much for your friendship. You helped me get through one of the more difficult periods in my PhD, even from such a distance, while it was not always at convenient times for you. It's always great to meet you, and I'm looking forward already to the next time we can catch up.

Not only new, but also old friends were always there for me: Reina and Willem, and now also Femke, thanks for the nice evenings, like Sinterklaas dobbelen (with Arthur, Joost, Mark and Myron), and for so many more. Thanks for the goofyness, it always makes me laugh, and for always being there. Gerdien, Kasia, thanks for being great friends. I wish you all the best in Germany and Canada.

Fabienne and Robert, thanks for the nice dinners and drinks we had, it is always fun to be at your place. And for the great riding holidays! They were truly epic and I'm eagerly waiting for the next. Thank you also for all your support and for understanding me the way you do.

As the horseback riding goes, thanks to everyone at Manege de Wildhoef: Aïde, Fiona and Iris, you really made a lot of good changes. Martine and Sophie, thanks for the great lessons, I learned really a lot. Chell, Pien, Marijn, Lois, Sapphire, Wietske, Janet, Mo, Lieke, bedankt voor de gezelligheid! And of course I should thank the horses. Maybe it sounds a bit weird, but the interaction with them relaxed me and cleared my mind every week, so I was ready for a next one. They're the real therapists here.

To stay a bit longer with the horses: Hillie, Annelies and Bart, you are my oldest friends, in the sense that you are with me the longest of all, over 20 years now. You've seen the best and the worst of the soap that is my life (Hillie's words) and still hang out with me, which is both amazing and heart warming. It is great that we are still in touch after all this time.

---

Also I'd like to thank my liieve clubgenoten. Yop Chagi: Gwan, Sytse, Bas, Thomas, Joost, Misja, Ruben, Laurens, Chris. Even though we don't see each other every week anymore, it's always nice when we meet and the conversation level drops to new depths whether the ladies and kids are there or not. I'm really impressed with where everyone is now and wish you all the best!

And Joost (yes, that's the third one already). It was so nice to meet up again after so many years, and to immediately find the same trust as before. It's great talking to you and laugh some of my worries away. In that sense, facebook isn't half bad.

I would also like to thank Somebody Famous. Mooch (Lucie), Capitaine (David), Gussy (Victor), 12006 (Barbara), Hema (Joelle) and Donna (Alina), breaking out of prison was never so hilarious. Thanks for all the long nights of practice and three great performances, which was some of the most fun I had! Furthermore I'd like to bless Paul (Olindo), Sally (Joelle again), Father Chenille (David again), George... Fazzer George (George), Sister Augusta (Maryam), Sister Philamena (Christina), Sister Mary (Clotilde), it's pity we couldn't make it, but I still had so much fun playing with you! Care for some punch?

Just by chance, or via friends, I met some other great people too. Florian, Sarah and Alex, thank you for all the fun we had, I had great times in Bonnie Scotland. Tophi, Robin, Volker, Nicole, Solene, Chris, Tim, I'm very happy I met you during these years and want to thank you for all the fun we had/have.

You can't, of course, be anywhere without family. Thank you all, opa, oma, aunts, uncles and cousins for the love and support. I would like to thank ome Ton, who always believed in me (see, I wrote it like you requested). Joost, Thijs and Marleen, thank you for your support, especially a small card or phone call now and then always cheered me up. Pap, mam, bedankt voor al jullie steun en advies tijdens dit werk en daarvoor. Zonder jullie was ik hier nooit gekomen. Thank you for inspiring and motivating me since I was just a kid. They say 'you can't choose your family', but even if I could, I would not change it for the world.

# Resume

Marloes Anne Reus was born on the 7<sup>th</sup> of September 1984 in the picturesque village of Heiloo in the Netherlands. After secondary education, Gymnasium, at the Petrus Canisius College in Alkmaar, Marloes was happy to learn about the magic of chemical reactions: in September 2002 she started her BSc study of Chemical Engineering and Biotechnology at Delft University of Technology. During her bachelor thesis she developed a calibration device for nano particle analyzers using electrospray. She continued with the Master of Science study Chemical Engineering at Delft University of Technology. In 2009, she conducted an experimental feasibility study for a new type of battery with her internship at Dr Ten B.V. This included the investigation of the reactions in the cell, as well as the development of the electrodes. Mightily interested in microwaves, she then performed her MSc thesis project on a comparative study on microwave assisted steam reforming of alcohols for hydrogen production.



After graduation in 2010 she felt that Delft University of Technology still held her interest and started her PhD research of the crystallization and microencapsulation in multicomponent mixtures. The main activities were the study of interactions between solid crystalline materials and solvents, the control of multicomponent electrospray crystallization for simultaneous particle formation and encapsulation, the immobilization of solids in polymeric matrices, and finally atomic layer deposition in order to produce inorganic coatings in a fluidized bed. The research was performed at the Process & Energy department of Delft University of Technology, in cooperation with TNO Defence, Safety & Security under supervision of Joop ter Horst and Antoine van der Heijden. The results have been presented at internationally renowned conferences and published in peer reviewed scientific journals. Since December 2015, Marloes has been working as a postdoctoral researcher at the same department, focusing on the selective crystallization of desired polymorphs of highly water-insoluble organic compounds, such as cancer medicines.

*By Fabienne Goosens*

---

# Publications

## Journal publications

1. M.A. Reus, G. Hoetmer, A.E.D.M. van der Heijden, J.H. ter Horst, Concomitant crystallization for in situ encapsulation of organic materials, *Chemical Engineering and Processing: Process Intensification*, Volume 80, 2014, pp 11–20. <http://dx.doi.org/10.1016/j.cep.2014.03.016>
2. M.A. Reus, A.E.D.M. van der Heijden, J.H. ter Horst, Solubility determination from clear points upon solvent addition, *Organic Process Research & Development*, Volume 19 (8), 2015, 1004-1011. <http://dx.doi.org/10.1021/acs.oprd.5b00156>
3. M.A. Reus, G.A. Krintiras, G.D. Stefanidis, J.H. ter Horst, A.E.D.M. van der Heijden, Immobilization of gluten in spherical matrices of food-grade hydrogels (in preparation)
4. J.A. Verbaarendse, M.A. Reus, J.H. ter Horst, J.R. van Ommen, D. Valdesueiro, A.E.D.M. van der Heijden, Improved particle properties through microencapsulation by gas-phase deposition in fluidized beds (in preparation)
5. M.A. Reus, J.H. ter Horst, A.E.D.M. van der Heijden, Electrospray crystallization; Challenges in process design, operation and control (in preparation)
6. M.A. Reus, A.E.D.M. van der Heijden, J.H. ter Horst, Understanding solvate formation in mixed solvents (in preparation)
7. M.A. Reus, A.E.D.M. van der Heijden, J.H. ter Horst, Crystal nucleation of fenofibrate in encapsulated solution droplets (in preparation)

## Conference proceedings (selection)

1. M.A. Reus, A.I. Stankiewicz, A.E.D.M. van der Heijden, J.H. ter Horst, Electrospray crystallization of encapsulated sub-micron particles of energetic materials. In *'Energetic materials - synthesis, characterization, processing', proceedings of the 43rd International Annual Conference of Fraunhofer ICT 2012*, page 1-12.
2. M.A. Reus, A.E.D.M. van der Heijden, J.H. ter Horst, Determining solubility through solvent addition. In *proceedings of 19<sup>th</sup> International Symposium on Industrial Crystallization (ISIC)*, 2014, page 77-79.

### Oral presentations (selection)

1. M.A. Reus, A.I. Stankiewicz, A.E.D.M. van der Heijden, J.H. ter Horst, Electrospray crystallization of encapsulated sub-micron particles of energetic materials. *Energetic materials - synthesis, characterization, processing - 43<sup>rd</sup> International Annual Conference of the Fraunhofer ICT*, June 26-29, 2012, Karlsruhe, Germany.
2. M.A. Reus, A.I. Stankiewicz, A.E.D.M. van der Heijden, J.H. ter Horst, Encapsulation through concomitant crystallization using electrospray and cooling crystallization. *19<sup>th</sup> International Workshop on Industrial Crystallization (BIWIC)*, September 7-9, 2012, Tianjin, China.
3. M.A. Reus, A.E.D.M. van der Heijden, A.I. Stankiewicz, J.H. ter Horst, Using solvent addition to construct solubility diagrams. *3<sup>rd</sup> European Young Engineers Conference (EYEC)*, April 29-30, 2014, Warsaw, Poland. (2nd presentation prize)
4. M.A. Reus, A.E.D.M. van der Heijden, A.I. Stankiewicz, J.H. ter Horst, Using Solvent Addition to Construct Solubility Diagrams. *19<sup>th</sup> International Symposium on Industrial Crystallization (ISIC)*, September 16-19, 2014, Toulouse, France.
5. M.A. Reus, J.A. Verbaarendse, D. Valdesueiro, J.R. van Ommen, J.H. ter Horst, A.E.D.M. van der Heijden, Application of Atomic Layer Deposition to Energetic Materials in Fluidized Beds. *Nederlands Procestehnologie Symposium (NPS)*, November 3-5, 2014, Utrecht, the Netherlands.
6. M.A. Reus, N. Radacsi, A.I. Stankiewicz, J.H. ter Horst, A.E.D.M. van der Heijden, Electrospray Crystallization: producing (sub-)micron sized crystals. *NL-GUTS gathering on crystallisation*, November 25, 2014, 's Hertogenbosch (the Netherlands), invited lecture.
7. M.A. Reus, A.E.D.M. van der Heijden, J.H. ter Horst, Crystal Nucleation and Growth in Encapsulated Droplets. *46<sup>th</sup> Annual BACG Conference*, June 21-23, 2015, London, UK.